Sigurdsson, H., Leckie, R.M., Acton, G.D., et al., 1997
Proceedings of the Ocean Drilling Program, Initial Reports, Vol. 165

4. SITE 999[1]

Shipboard Scientific Party[2]

HOLE 999A

Position: 12°44.639′N, 78°44.360′W (Colombian Basin)

Date occupied: 0030 hr, 6 January 1996

Date departed: 0415 hr, 10 January 1996

Time on hole: 99.8 hr (4 days, 3 hr, 45 min)

Seafloor depth (drill-pipe measurement from rig floor, mbrf): 2838.9

Total depth (drill-pipe measurement from rig floor, mbrf): 3405.0

Distance between rig floor and sea level (m): 11.0

Water depth (drill-pipe measurement from sea level, m): 2827.9

Penetration (mbsf): 566.1

Coring totals:

Type: APC; No: 21; Cored: 197.6 m; Recovered: 206.7 m (104.6%)
Type: XCB; No: 40; Cored: 368.5 m; Recovered: 328.0 m (89.0%)
Total: No: 61; Cored: 566.1 m; Recovered: 534.7 m (94.4%)

Formation:

Nannofossil mixed sediment with foraminifers, nannofossil clayey mixed sediment, clayey nannofossil chalk with foraminifers, and volcanic ash layers

Oldest sediment cored:

Depth (mbsf): 566.1
Nature: Clayey calcareous chalk with foraminifers and nannofossils
Age: early Miocene

HOLE 999B

Position: 12°44.597′N, 78°44.418′W (Colombian Basin)

Date occupied: 0415 hr, 10 January 1996

Date departed: 1700 hr, 24 January 1996

Time on hole: 348.8 hr (14 days, 12 hr, 45 min)

Seafloor depth (drill-pipe measurement from rig floor, mbrf): 2838.9

Total depth (drill-pipe measurement from rig floor, mbrf): 3905.3

Distance between rig floor and sea level (m): 11.1

Water depth (drill-pipe measurement from sea level, m): 2827.8

Penetration (mbsf): 1066.4

Coring totals:

Type: RCB (CC-4 bit); No: 22; Cored: 163.8 m; Recovered: 105.7 m (64.6%)
Type: RCB (PDC bit); No: 40; Cored: 359.2 m; Recovered: 292.1 m (81.3%)
Total: No: 62; Cored: 523.0 m; Recovered: 397.8 m (76.1%)

Formation:

Clayey calcareous limestone, clayey calcareous mixed sedimentary rock, volcanic ash layers, calcareous limestone with clay, claystone, and limestone

Oldest sediment cored:

Depth (mbsf): 1066.4
Nature: Calcareous limestone with clays
Age: late Maastrichtian

Principal results: Site 999 is located on the Kogi Rise, a previously unnamed bathymetric high in the Colombian Basin. Situated northeast of Mono Rise and southeast of the Hess Escarpment, the crest of the Kogi Rise lies some 1000 m above the turbidite-laden floor of the Colombian Basin and is isolated by a saddle from sediments originating from the Hess Escarpment. A continuous Upper Cretaceous to recent record was anticipated; targeted for tropical paleoceanography, including the progressive closure of the Central American Seaway in the late Neogene, as well as an undisturbed Cretaceous/Tertiary (K/T) boundary sequence located relatively proximal to the Chicxulub impact site. With the eventual goal of coring basement and testing the hypothesis of a hot-spot origin for the Caribbean oceanic plateau (i.e., a Large Igneous Province), Site 999 was designated a "legacy site," and a reentry cone and casing were installed in Hole 999B for future reoccupation.

A continuous and apparently complete upper Maastrichtian–Pleistocene section was cored at Site 999. Hole 999A was cored with the APC to a depth of 197.6 mbsf (upper Miocene) with 104.6% recovery, and then cored with the XCB to a depth of 566.1 mbsf with 89.0% recovery. Hole 999A terminated in lower Miocene clayey calcareous chalk. A reentry cone and 62 m of 16-in casing were jetted into the seafloor before Hole 999B was drilled ahead and casing installed to a depth of 524 m. Coring operations resumed with the RCB at a depth of 543.4 mbsf and terminated in upper Maastrichtian limestone with clay at a depth of 1066.4 mbsf. Recovery with the RCB was good, with 76.1% of the drilled interval recovered.

Mixtures of biogenic ooze, nepheloid clays, and volcanic ash are the primary constituents of the sediments on Kogi Rise. Six lithologic units were recognized at Site 999.

Unit I is divided into three subunits. Subunit IA (0.0–150.1 mbsf; Pleistocene–lower Pliocene) consists of nannofossil and foraminiferal clayey mixed sediment with scattered interbedded ash layers. Subunit IB (150.1–229.5 mbsf; lower Pliocene–upper Miocene) is similar to Subunit IA but contains fewer foraminifers. Subunit IC (229.5–265.1 mbsf; upper Miocene) is further distinguished by the presence of siliceous microfossils.

Unit II is divided into two subunits. Subunit IIA (265.1–301.8 mbsf; middle/upper Miocene boundary interval) consists of interbedded clay with nannofossils, clayey nannofossil mixed sediment, and common ash layers. Subunit IIB (301.8–346.9 mbsf; middle Miocene) is similar to Subunit IIA but contains siliceous microfossils and a higher carbonate content.

Unit III (346.9–566.1 mbsf; middle–lower Miocene) consists of clayey calcareous chalk with foraminifers and nannofossils, interbedded with abundant ash layers.

Unit IV is divided into four subunits. Subunit IVA (572.6–644.9 mbsf; lower Miocene–upper Oligocene) consists of clayey calcareous limestone with common thin ash layers, and Subunit IVB (644.9–690.4 mbsf; upper–lower Oligocene) is similar to Subunit IVA but contains more clay.

[1]Sigurdsson, H., Leckie, R.M., Acton, G.D., et al., 1997. *Proc. ODP, Init. Repts.,* 165: College Station, TX (Ocean Drilling Program).
[2]Shipboard Scientific Party is given in the list preceding the Table of Contents.

Subunit IVC (690.4–866.2 mbsf; lower Oligocene–middle Eocene) is also a clayey calcareous limestone, but it contains thicker and more frequent ash layers than Subunits IVA and IVB. Subunit IVD (866.2–887.0 mbsf; middle Eocene) is likewise similar to Subunit IVB but contains more clay.

Unit V is divided into two subunits. Subunit VA (887.0–1033.4 mbsf; middle Eocene–upper Paleocene) is a clayey calcareous mixed sedimentary rock with some interbedded ash layers. Subunit VB (1033.4–1049.3 mbsf; lower Paleocene) is a claystone with some interbedded ash layers. Unit VI (1049.3–1066.4 mbsf) consists of basal Paleocene hard light gray limestone and upper Maastrichtian limestone with clay.

Shipboard biostratigraphy and magnetostratigraphy suggest that the cored section is complete, although the abrupt changes in lithology at the base of the Paleocene may indicate that some of the bedding surfaces recovered in the K/T boundary interval are not conformable or that recovery was incomplete. A comparison of logging records and the cored sediments suggest that a nearly complete boundary sequence was recovered. The position of the boundary has been constrained by shipboard paleontology to within 10 cm, and extensive shore-based research is planned. The K/T boundary is tentatively placed at the base of a limestone in Section 165-999B-60R-1, 10 cm (1050.2 mbsf).

The middle to upper Eocene and the lower to middle Miocene portions of the section include an unexpectedly large number of rhyolitic volcanic ash layers (>1200), most likely derived from distant silicic volcanic centers in Central America. These ash layers define two major explosive volcanic episodes, also recorded in the sediments at Site 998 on the Cayman Rise. Volcanic ash layers account for over 4% of the recovered succession. In addition, solid-phase geochemistry reveals that the dispersed ash comprises ~18% of the total sediment recovered at Site 999, and that a significant amount of clays in the background sediment are the altered products of volcanic glass.

The terrigenous component of the sediment has been quantified through an analysis of chromium variation in the bulk sediment. The composition and quantity of this terrigenous sediment may be closely linked to the history of the Magdalena Fan, which has grown in response to the uplift and erosion of the Andean Cordillera. Growth of the submarine fan has been particularly active since the late Miocene, as evidenced by a marked increase in terrigenous mass accumulation rates (1–2 g/cm^2/k.y.) and an increase in detrital clays.

Below the middle Eocene ash layers is a series of radiolarian and foraminifer-rich layers, caused by winnowing on the seafloor or by productivity events in the upper water column. In either case, changes in oceanic circulation between the Caribbean and eastern Pacific are suspected, perhaps related to tectonically influenced portals or to sources of deep/intermediate water masses during late Paleocene–early Eocene time. An anomalous band of dark laminated claystone in the uppermost Paleocene of Site 999 may represent an expanded tropical record of the widespread oceanographic warming event that occurred during latest Paleocene time (late Paleocene thermal maximum, LPTM).

The transition from the middle to upper Miocene is distinguished by a sharp reduction in carbonate content and a marked increase in magnetic susceptibility and in terrigenous mass accumulation rates. This interval is correlative to the late Miocene "carbonate crash" of the central and eastern equatorial Pacific, and is also recognized at Site 998 on the Cayman Rise. Originally thought to be related to tectonically influenced changes in deep-water exchange between the Pacific and Atlantic, linkages with changes in thermohaline circulation may be responsible for the widespread carbonate crash on both sides of the present-day Isthmus of Panama.

Preliminary evidence for oceanographic changes resulting from the late Neogene (late Miocene–late Pliocene) closure of the Central American Seaway is found in the planktonic foraminifer record at Site 999. Sinistrally coiled *Neogloboquadrina pachyderma,* normally a polar/subpolar species, is found in significant numbers through the upper Miocene–lower Pliocene interval. The termination of this interval is linked to the cessation of regional upwelling in the southwestern Caribbean with the closure of the seaway.

The upper Maastrichtian through Oligocene section accumulated at rates of approximately 9–14 m/m.y. (2.2–3.6 g/cm^2/k.y.), although the lower Paleocene is characterized by sedimentation rates that average <5 m/m.y. (1.2–1.6 g/cm^2/k.y.). A marked rise in sedimentation rates and bulk mass accumulation rates through the lower Miocene (29 m/m.y.; 3.5–6.5 g/cm^2/k.y.) is due in part to the voluminous volcanic ash input. This interval is followed by reduced rates in the middle and upper Miocene (19 m/m.y.; 1.5–2.5 g/cm^2/k.y.), an interval that includes the carbonate crash. The Pliocene–Pleistocene interval is characterized by a return to higher sedimentation and mass accumulation rates (30–33 m/m.y.; 2.6–3.4 g/cm^2/k.y.) in response to increased terrigenous input from the northern Andes.

BACKGROUND AND OBJECTIVES

Site 999 is located in the Colombian Basin, on a small and unnamed rise about 150 km northeast of the Mono Rise. We propose that this rise be named the Kogi Rise, after the Amerindian tribe that inhabits the Sierra Nevada de Santa Marta region in nearby Colombia. The Kogi Rise is elevated nearly 1000 m above the relatively flat and featureless Colombian Plain. Therefore, the Kogi Rise is out of the influence of turbidite deposition of the Magdalena Fan complex that dominates sediment deposition to the southeast on the surrounding plain (Burke et al., 1984; Bowland, 1993). The Hess Escarpment forms a prominent feature to the northwest of the Kogi Rise and is interpreted to be a transcurrent fault (Bowland, 1993). A saddle shields the crest of the Kogi Rise from turbidites originating along the Hess Escarpment.

The acoustic basement horizon beneath the Kogi Rise is at a depth of approximately 1350 m, and it has been correlated with the "smooth" seismic horizon B″ in the Venezuelan Basin, corresponding to the Caribbean Oceanic Plateau of Late Cretaceous age (Bowland and Rosencrantz, 1988). In 1995, the Ocean Drilling Program's Planning Committee recognized the importance of this location for possible deep penetration into the unexplored portion of the Caribbean Oceanic Plateau, which lead to the designation of Site 999 as a "legacy site" to be equipped with a reentry cone and cased down to consolidated sediment.

Our aim at this site was to recover a complete stratigraphic sequence through the Cenozoic and to core into the Cretaceous sequence and underlying igneous basement as far as could be achieved within the time available. The sediments at this site potentially record the deep-water physical and chemical history in the western Caribbean and the effects of the evolving gateways around the basin. Tectonically controlled oceanic gateways include the development of the Aves Ridge and Lesser Antilles arc to the east, the elevation of the Isthmus of Panama to the west, and the possible foundering of the northern Nicaraguan Rise (NNR) to the north. We also aimed to recover a K/T boundary section, which is of particular interest because of the relative proximity of the Kogi Rise to the Chicxulub impact crater. Finally, recovery of basement rocks here would have been the first sampling of the acoustic basement in the entire western Caribbean Sea, west of the Beata Rise, and would have had important implications for the extent and composition of the large igneous province. Unfortunately, time limitations prevented us from reaching this objective, though installation of a reentry cone and casing of Hole 999B has now made this objective a realistic goal of a future Caribbean leg.

SEISMIC STRATIGRAPHY

The seismic stratigraphy of Site 999 on the Kogi Rise (Fig. 1) is known from the analysis of multichannel seismic (MCS) reflection Profile CT1-12a by Bowland and Rosencrantz (1988) and Bowland (1993) (see "Underway Geophysics" section, "Explanatory Notes"

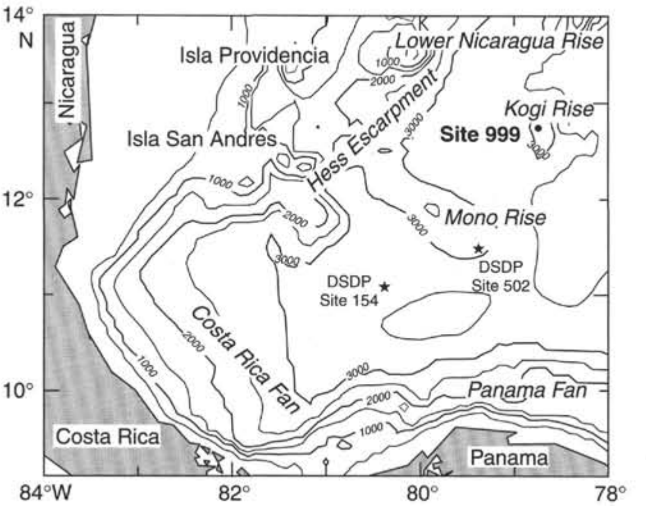

Figure 1. Bathymetric map (500-m contour interval) showing the location of Site 999 and the surrounding major physiographic features of the western Colombian Basin. Site 999 is located on the Kogi Rise 150 km northeast of the Mono Rise and DSDP Site 502. Also shown is DSDP Site 154.

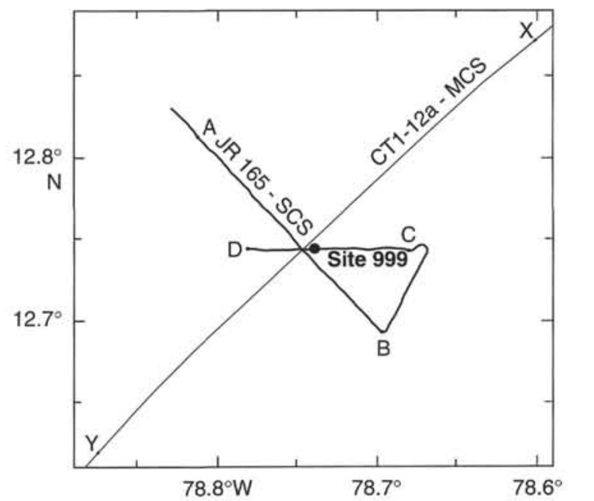

Figure 2. Track chart of a portion of MCS Line CT1-12a acquired during cruise IG2901 and the entire SCS line acquired during Leg 165. Site 999 is located on the east-west JR 165 SCS line, approximately 800 m east of its intersection with MCS Line CT1-12a. This location is within the error limits of the navigation of the 1978 vintage CT1-12a MCS line. A-B, C-D, and X-Y denote portions of each of these lines that are displayed in Figures 3 and 4.

chapter, this volume; Figs. 2, 3). In addition, a short single-channel seismic (SCS) site survey was conducted during this leg (Figs. 2, 4) that confirmed the general seismic character and unit thicknesses observed in the CT1-12a MCS profile.

Acoustic basement in the Colombian Basin was defined as those layers having velocities greater than 4.0 km/s (Bowland and Rosencrantz, 1988). Refraction and gravity studies indicate variable crustal thicknesses in isostatic equilibrium (Ewing et al., 1960; Edgar et al., 1971; Houtz and Ludwig, 1977; Bowin, 1976); that is, the topography of the acoustic basement surface mirrors crustal thickness. The crust is relatively thin (8.5 km) where acoustic basement is deepest and relatively thick (~15 km) beneath basement highs, such as the Mono Rise (150 km southwest of Kogi Rise) (Ewing et al., 1960; Houtz and Ludwig, 1977).

The Colombian Basin displays two primary types of acoustic basement reflections (Ludwig et al., 1975; Bowland and Rosencrantz,1988). The majority of the Colombian Basin is characterized by a smooth, continuous, typically high-amplitude acoustic basement reflection, which is comparable to "smooth" horizon B″ of the Venezuelan Basin. Smooth horizon B″ in the Colombian Basin has never been sampled but may correspond to the top of basaltic sills interbedded with Upper Cretaceous sediments that were cored during Deep Sea Drilling Project (DSDP) Leg 15. Bowland and Rosencrantz (1988) concluded that the thick, elevated crust of the Colombian Basin (including Kogi Rise) represents an oceanic plateau. There are a number of locations in the Colombian Basin east of the Kogi Rise where acoustic basement is deep, appears rough with hyperbolic diffractions, and is associated with thin crust (Ludwig et al., 1975; Houtz and Ludwig, 1977; Bowland and Rosencrantz, 1988). Deep, rough, and thin crust is also observed in the southeast Venezuelan Basin (Biju-Duval et al., 1978; Diebold et al., 1981, 1995a, 1995b). In the Venezuelan and Colombian basins, stratigraphic relations indicate that "rough" acoustic basement predates "smooth" acoustic basement. In the Venezuelan Basin, the unsampled rough acoustic basement (rough horizon B″) is interpreted as the top of the original (proto-Caribbean) oceanic crust, which was extended and thinned contemporaneous with the emplacement of an oceanic plateau (Diebold et al., 1995a, 1995b).

Beneath the Kogi Rise (Site 999), the acoustic basement horizon is smooth and continuous, and has a variable reflection amplitude at approximately 5.0 s two-way traveltime (TWT) (Figs. 3, 4). Bowland and Rosencrantz (1988) propose that acoustic basement beneath the crest of the Kogi Rise forms a horst bounded by normal faults. Although the interpretation of a horst structure is equivocal, it is clear that the continuity of reflections has been disrupted and deformed along the northeast slope of the Kogi Rise (dashed lines, Figs. 3, 5). The only clear vertical offset of reflection continuity occurs at approximately 4.3 s TWT, within sediments of late Miocene age, and indicates a high-angle reverse fault (Fig. 5). The continuation of this fault plane deeper into the section intersects intervals where reflections are disrupted, but with no clear indication of vertical offset (dashed lines, Figs. 3, 5). The uplifted nature of acoustic basement overlain by sediment of uniform thickness could indicate normal faulting of basement before significant sedimentation took place. This zone of weakness apparently remained an active fault zone throughout the late Miocene. DSDP Sites 154 and 502 are also located on proposed uplifted fault blocks where the sediment record indicates significant uplift in the late Miocene to early Pliocene (Prell, Gardner, et al., 1982; Edgar, Saunders, et al., 1973). Regional seismic and gravity profiles provide additional evidence for intraplate deformation in the western Colombian Basin associated with the development of the North Panama Deformed Belt beginning in the middle Miocene (Holcombe et al., 1990). The large-scale offsets of horizon B″ associated with the Beata Ridge and Hess Escarpment are believed to have formed before significant sediment accumulation (Holcombe et al., 1990), and the normal faults offsetting both smooth and rough B″ in the Venezuelan Basin have been interpreted as ongoing crustal extension during, and for some time after, emplacement of an oceanic plateau (Diebold et al., 1995b). It is also clear that faulting has disrupted sediments overlying horizon B″. These faults may have been reactivated during middle Miocene to recent intraplate deformation.

A series of prominent semicontinuous north-dipping reflectors observed beneath acoustic basement are interpreted as basalt lavas, interbedded with volcaniclastic sediments (Fig. 3). The dip of these reflections is opposite to that of overlying reflections and the seafloor, and they have high stacking velocity, indicating that these reflections are not multiple events. Similar subhorizontal reflections are observed in the Venezuelan Basin, where refraction/reflection data indicate a layered velocity structure that has been interpreted as

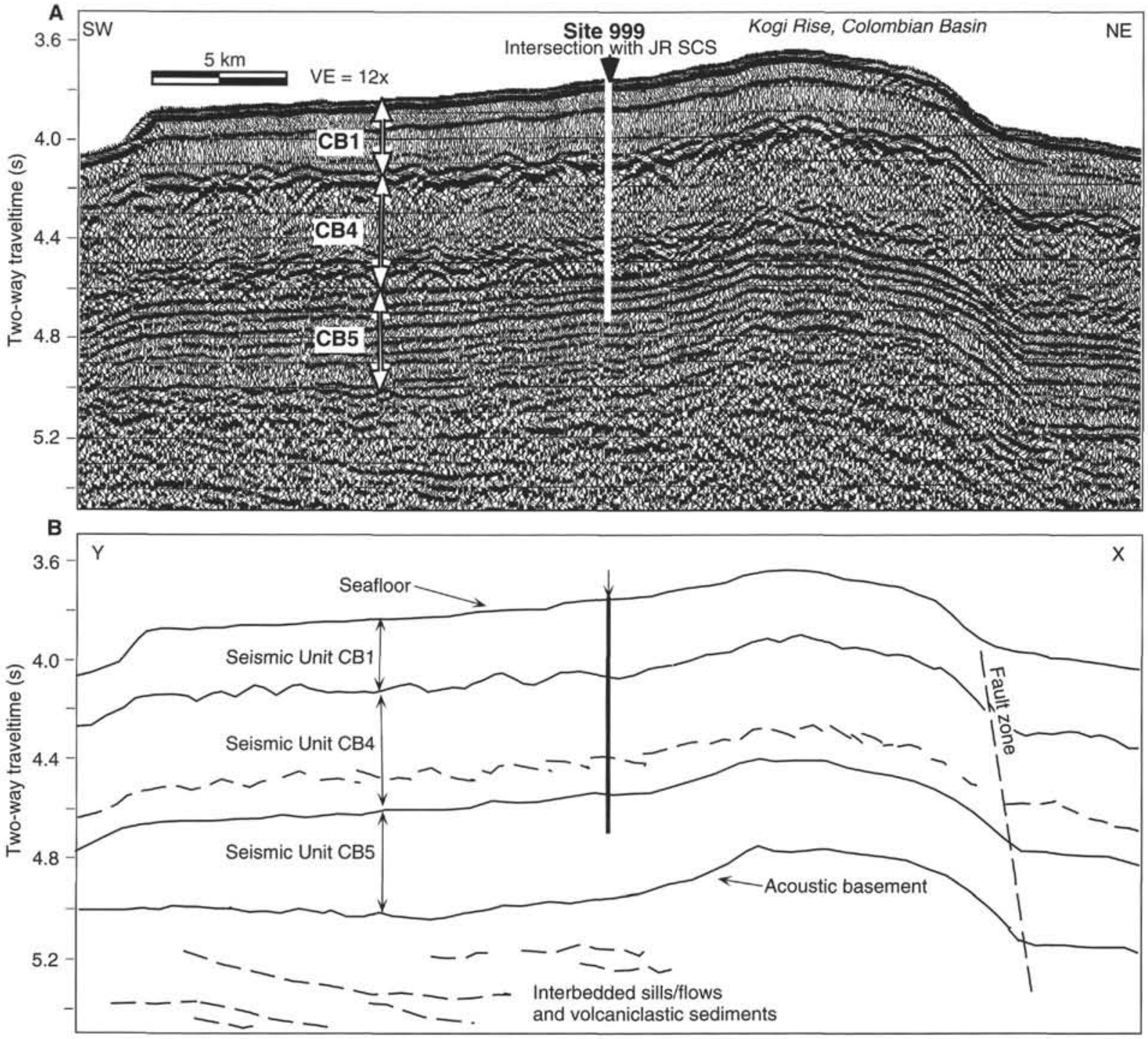

Figure 3. **A.** Portion of IG2901 MCS Line CT1-12a (2 × 1500 in³ air guns) showing the location of Site 999 and the intersection of two JR 165 SCS lines (Fig. 4). Processing parameters and cruise description are given in the "Underway Geophysics" section, "Explanatory Notes" chapter (this volume). VE = vertical exaggeration. **B.** Interpreted seismic stratigraphic correlation for Site 999. The draping character and uniform thickness of seismic Units CB1, CB4, and CB5 are consistent with the pelagic and hemipelagic sediments recovered at Site 999. Disrupted and offset reflections northeast of the Kogi Rise crest indicated by a heavy, high-angle dashed line are interpreted as episodic movement along a pre-existing (but not imaged) basement fault that uplifted acoustic basement before significant sedimentation took place. Points X and Y correspond to identical track chart labels (Fig. 2) marking beginning and end locations.

multiple flow units and/or interbedded massive basalt and volcaniclastic sediments (Stoffa et al., 1981; Diebold et al., 1981, 1995a, 1995b).

The bathymetry of acoustic basement strongly controls depositional character in the Colombia Basin. Basement highs forming the Mono Rise and the Kogi Rise remained isolated from the large influx of terrestrial turbidites that filled in basement lows with up to 6 km of sediment from Eocene through Miocene time. Bowland (1993) identified three principal seismic units in the sedimentary section, all of which drape over the acoustic basement of the Kogi Rise. Seismic Unit CB5 overlying acoustic basement extends from 4.556 to 4.936 s TWT at Site 999 and consists of continuous, high-amplitude reflections concordant with acoustic basement. Seismic Unit CB5 was interpreted as a sheet drape deposit, consisting of biogenic pelagic material, similar to that in the interval between seismic reflectors A″ and B″ in the Venezuela Basin, which are Upper Cretaceous to lower Eocene siliceous claystone, chert, marlstone, chalk, and limestone where sampled during DSDP Leg 15. Seismic reflection and refraction data indicate velocities for the A″–B″ interval that are approximately between 2.5 and 3.5 km/s, with higher velocities associated with greater burial depth and/or carbonate content (Ludwig et al., 1975; Stoffa et al., 1981; Diebold et al., 1981; Edgar, Saunders, et al., 1973). Interval velocities based on an average of approximately 50 semblance analyses at 5-km intervals along CT1-12 were calculated by Bowland (1984, 1993) and were used to estimate unit thicknesses before drilling began. Applying the range of interval velocities of 3.0 ± 0.4 km/s, as reported in Bowland (1993), results in an estimated 494- to 646-m-thick CB5 section (see "Summary and Conclusions" section, this chapter, for post-drilling depth estimates based on logged velocities). The higher interval velocity for this unit was attributed to a higher carbonate content and a deeper burial. This sediment may be of the type that is typical for pelagic sediments overly-

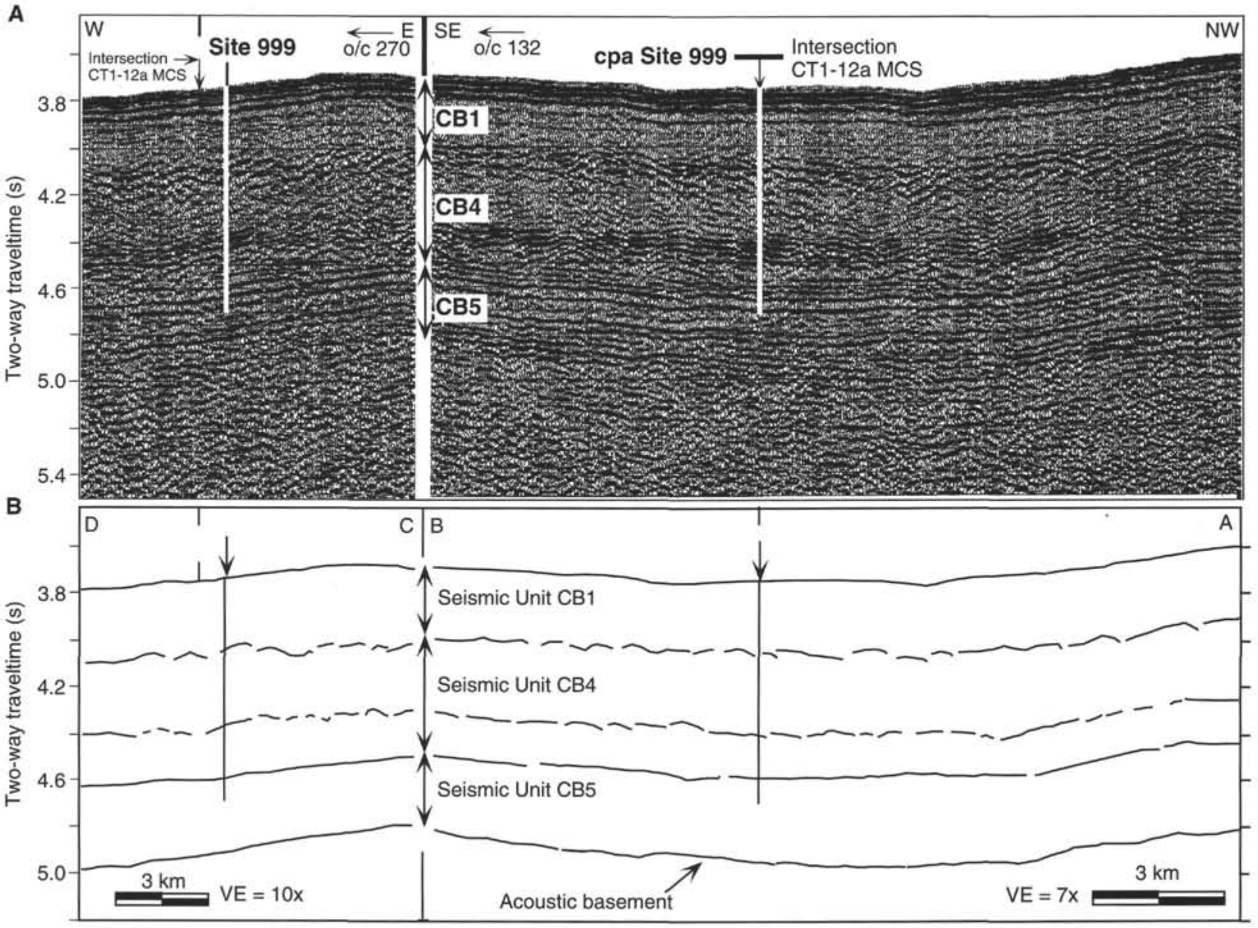

Figure 4. **A.** Two SCS profiles (2 × 200 in³ waterguns) obtained on approach to Site 999 during Leg 165. These SCS lines intersect MCS Line CT1-12a approximately 800 m west of Site 999 location. Processing parameters and cruise description are given in the "Underway Geophysics" section, "Explanatory Notes" chapter (this volume). **B.** The interpreted seismic stratigraphic correlation. The draping character and uniform thicknesses of seismic Units CB1, CB4, and CB5 are consistent with the pelagic and hemipelagic sediments recovered at Site 999. Points A/B and C/D correspond to identical track chart labels (Fig. 2) marking beginning and end locations. VE = vertical exaggeration.

ing oceanic igneous plateaus. In general, the level of the oceanic plateau would be above the carbonate compensation depth (CCD) for much of its early history, resulting in carbonate deposition. Upper Cretaceous calcareous pelagic sedimentary rocks overlying mafic basement in southern Central America (Nicoya Complex, etc.) are probably in part correlative with the CB5 unit (Bowland, 1993).

Seismic Unit CB4 extends from 4.066 to 4.556 s TWT and consists of two subunits separated at 4.4 s TWT, both of which maintain a uniform thickness in the vicinity of Site 999. Both subunits have a hummocky-mounded to chaotic and disrupted seismic facies. The upper subunit displays a high-amplitude upper boundary followed by a relatively transparent interval. The high-amplitude upper boundary of Unit CB4 appears to be offset by a proposed fault along the northeast edge of the Kogi Rise (Figs. 3, 5). The thin lower subunit is characterized by chaotic, discontinuous, and relatively high-amplitude reflections throughout the interval. The upper subunit interval velocity is lower (1.8 ± 0.1 km/s), and the lower subunit interval velocity is 2.6 ± 0.4 km/s. Applying the range of interval velocities of 2.2 ± 0.2 km/s for Unit CB4 as a whole results in an estimated 574–671 m unit thickness. At DSDP Site 502, the HPC acoustic Unit 3 corresponds to calcareous clay with poorly crystallized smectite and siliceous late Miocene microfossils that may correlate with the top subunit of CB4 (Prell, Gardner, et al., 1982). Thus, CB4 is interpreted by Bowland (1993) as mainly hemipelagic and biogenic pelagic deposits, probably laid down above the level of turbidite deposition but not above the influence of nepheloid layers (hemipelagic clay). The widespread hummocky seismic character of the upper subunit was interpreted to be a consequence of postdepositional deformation, related to undercompaction of the open, mechanically interlocked siliceous-microfossil framework of the sediment (Bowland, 1993).

Seismic Unit CB1 extends from the seafloor (3.776 s TWT) to 4.066 s TWT. This unit has a sheet-drape form and a relatively reflection-free seismic character. The upper surface of CB1 (seafloor) is cut by numerous furrows, and significant erosional channels are apparent on the 3.5-kHz record acquired during the pre-site survey. Applying the range of interval velocities of 1.7 ± 0.1 km/s results in an estimated 240–270 m unit thickness. Unit CB1 was also cored on Mono Rise at DSDP Site 502 and found to be composed of foraminifer-bearing nannofossil marl ooze, calcareous clay, and volcanic ash of late Miocene to recent age (Prell, Gardner, et al., 1982). Thus, the unit is a dominantly biogenic pelagic and hemipelagic deposit on this basement high. A 3.5-kHz profile obtained during the approach to Site 999 indicates no major impedance contrasts in the top 30 m of sediment. The seafloor is occasionally disrupted by furrows displaying ~5 m of relief and larger erosional channels ~15–20 m deep and 1–2 km wide.

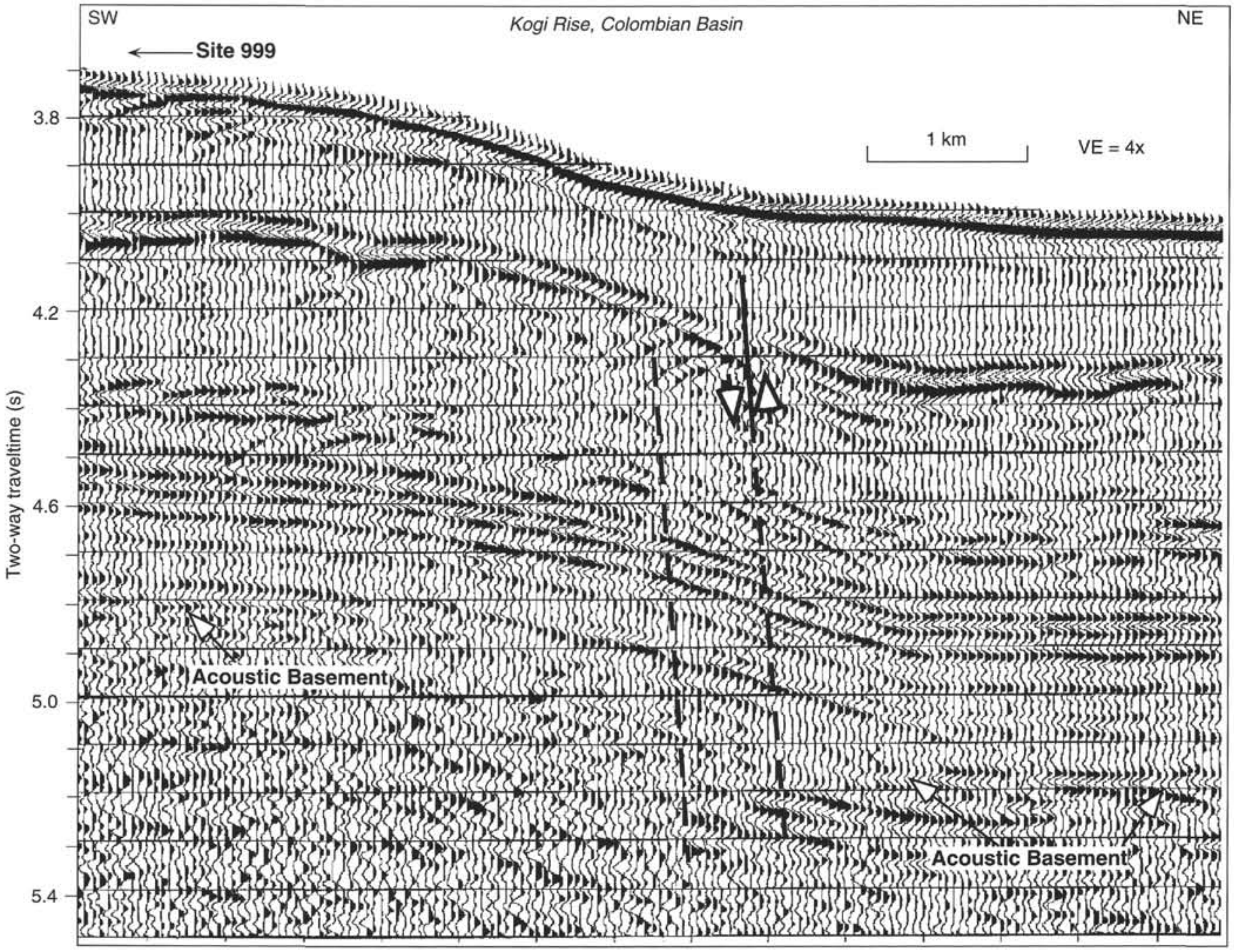

Figure 5. Portion of IG2901 MCS Line CT1-12a displayed at minimal vertical exaggeration (four times) along the northeastern slope of the Kogi Rise. Heavy solid line and arrows indicate the location and vertical component of offset of the otherwise continuous reflection at 4.3 s TWT, which marks the CB1/CB4 seismic unit boundary (late Miocene). Dashed lines indicate disruption of reflection continuity but place no constraints on sense of motion. VE = vertical exaggeration.

Correlations between the seismic stratigraphy and lithology at Site 999 are discussed in the "Summary and Conclusions" section (this chapter).

OPERATIONS

The 468-nmi transit from Site 998 was slower than anticipated owing to the failure of a propulsion motor, subsequently requiring that two motors be taken offline and resulting in a reduced average speed of about 10.7 kt.

A 4-hr single-channel seismic reflection survey was conducted over the site to obtain profiles that crossed the existing multichannel survey. Precision depth recorder data obtained during the survey indicated the presence of a shallow channel at the proposed site location; therefore, the site was moved 900 m to the east.

Hole 999A

Core recovery with the APC was excellent (104.6%; Table 1), whereas the XCB produced very good recovery (89.0%; Table 1) but suffered from core biscuiting (a phenomenon in which the core is broken into many short cylindrical chunks that are surrounded by fine-grained drill cuttings and paste). In an attempt to rectify the problem, several changes were made at the rig floor. After Core 165-999A-33X, the sinker bars were removed, which allowed better control of the flow rates and pressures. Then, the weight on the bit was reduced and the flow rate increased. In addition, coring results at Site 998 had led to the use of a hard-formation cutting shoe and hard-formation core catchers. Together, these changes resulted in better core trimming, more lubrication at the throat of the cutting shoe, and improved core quality.

Coring operations ended in this hole when the formation became indurated enough to provide an acceptable casing seat, which was then used in drill plans for Hole 999B, the reentry hole. Hole 999A was conditioned for wireline logging by circulating sepiolite mud and conducting a wiper trip. Logging activities were abandoned, however, after the initial logging tool encountered an obstruction and then experienced repeated electrical failures (see "Downhole Measurements" section, this chapter).

Hole 998B

Sea-surface currents were negligible while deploying the reentry cone and the conductor pipe (40.6 cm [16 in] diameter) for Hole 999B, though the currents increased to 2.25 kt while running the sur-

Table 1. Coring summary, Site 999.

Core no.	Date (Jan. 1996)	Time (UTC)	Depth (mbsf)	Cored (m)	Recovered (m)	Recovery (%)
165-999A-						
1H	6	1130	0.0–7.6	7.6	7.76	102.0
2H	6	1230	7.6–17.1	9.5	9.90	104.0
3H	6	1315	17.1–26.6	9.5	9.87	104.0
4H	6	1400	26.6–36.1	9.5	9.91	104.0
5H	6	1445	36.1–45.6	9.5	9.77	103.0
6H	6	1515	45.6–55.1	9.5	9.81	103.0
7H	6	1600	55.1–64.6	9.5	9.90	104.0
8H	6	1645	64.6–74.1	9.5	9.96	105.0
9H	6	1755	74.1–83.6	9.5	10.00	105.2
10H	6	1840	83.6–93.1	9.5	10.03	105.6
11H	6	1930	93.1–102.6	9.5	9.97	105.0
12H	6	2030	102.6–112.1	9.5	10.06	105.9
13H	6	2105	112.1–121.6	9.5	9.78	103.0
14H	6	2150	121.6–131.1	9.5	10.00	105.2
15H	6	2245	131.1–140.6	9.5	10.07	106.0
16H	6	2345	140.6–150.1	9.5	9.90	104.0
17H	7	0015	150.1–159.6	9.5	9.86	104.0
18H	7	0105	159.6–169.1	9.5	9.93	104.0
19H	7	0150	169.1–178.6	9.5	9.88	104.0
20H	7	0250	178.6–188.1	9.5	10.07	106.0
21H	7	0330	188.1–197.6	9.5	10.05	105.8
22X	7	0455	197.6–200.6	3.0	6.34	211.0
23X	7	0555	200.6–210.3	9.7	9.85	101.0
24X	7	0650	210.3–219.9	9.6	9.80	102.0
25X	7	0800	219.9–229.5	9.6	9.71	101.0
26X	7	0900	229.5–239.1	9.6	9.69	101.0
27X	7	0940	239.1–248.7	9.6	9.41	98.0
28X	7	1030	248.7–258.4	9.7	9.88	102.0
29X	7	1120	258.4–268.0	9.6	9.87	103.0
30X	7	1215	268.0–277.6	9.6	9.83	102.0
31X	7	1305	277.6–287.2	9.6	9.86	103.0
32X	7	1400	287.2–296.7	9.5	8.78	92.4
33X	7	1500	296.7–306.3	9.6	9.30	96.9
34X	7	1615	306.3–316.0	9.7	9.83	101.0
35X	7	1730	316.0–325.6	9.6	9.62	100.0
36X	7	1915	325.6–335.2	9.6	6.44	67.1
37X	7	2045	335.2–344.8	9.6	9.25	96.3
38X	7	2200	344.8–354.4	9.6	9.67	101.0
39X	7	2325	354.4–364.0	9.6	9.83	102.0
40X	8	0040	364.0–373.7	9.7	9.35	96.4
41X	8	0200	373.7–383.4	9.7	9.77	101.0
42X	8	0320	383.4–393.0	9.6	7.74	80.6
43X	8	0430	393.0–402.5	9.5	6.08	64.0
44X	8	0545	402.5–412.1	9.6	9.86	103.0
45X	8	0710	412.1–421.8	9.7	9.43	97.2
46X	8	0810	421.8–431.4	9.6	9.56	99.6
47X	8	1000	431.4–441.1	9.7	9.77	101.0
48X	8	1115	441.1–450.7	9.6	9.80	102.0
49X	8	1230	450.7–460.3	9.6	7.15	74.5
50X	8	1400	460.3–469.9	9.6	9.85	102.0
51X	8	1515	469.9–479.5	9.6	9.80	102.0
52X	8	1635	479.5–489.1	9.6	5.09	53.0
53X	8	1800	489.1–498.7	9.6	9.49	98.8
54X	8	1950	498.7–508.3	9.6	7.96	82.9
55X	8	0030	508.3–512.9	4.6	0.23	5.0
56X	8	2300	512.9–517.9	5.0	1.17	23.4
57X	9	0050	517.9–527.6	9.7	0.68	7.0
58X	9	0230	527.6–537.2	9.6	9.05	94.3
59X	9	0410	537.2–546.8	9.6	1.40	14.6
60X	9	0545	546.8–556.5	9.7	9.59	98.8
61X	9	0730	556.5–566.1	9.6	8.26	86.0
Coring totals				566.1	534.52	94.4
165-999B-						
****Drilled from 0.0 to 543.4 mbsf*****						
1R	14	1830	543.4–553.2	9.8	0.00	0.0
2R	14	2100	553.2–562.9	9.7	0.00	0.0
3R	14	2310	562.9–565.5	2.6	0.00	0.0
4R	14	0120	565.5–572.6	7.1	0.00	0.0
5R	15	1745	572.6–577.2	4.6	2.28	49.5
6R	15	1930	577.2–582.2	5.0	5.71	114.0
7R	15	2230	582.2–591.8	9.6	9.98	104.0
8R	16	0450	591.8–601.5	9.7	7.24	74.6
9R	16	0940	601.5–611.1	9.6	9.88	103.0
10R	16	1230	611.1–620.7	9.6	1.16	12.1
11R	16	1515	620.7–630.3	9.6	6.15	64.0
12R	16	1815	630.3–639.9	9.6	10.02	104.4
13R	16	2045	639.9–649.5	9.6	7.96	82.9
14R	16	2300	649.5–659.1	9.6	9.72	101.0
15R	17	0150	659.1–668.8	9.7	3.54	36.5
16R	17	0415	668.8–672.4	3.6	9.93	276.0
17R	17	0720	672.4–678.4	6.0	0.00	0.0
18R	17	1100	678.4–681.9	3.5	0.01	0.3
19R	17	1345	681.9–684.9	3.0	1.30	43.3
20R	17	1530	684.9–687.9	3.0	3.07	102.0
21R	17	1930	687.9–697.6	9.7	9.10	93.8
22R	18	0040	697.6–707.2	9.6	8.82	91.9
23R	18	1830	707.2–716.9	9.7	8.22	84.7
24R	18	2030	716.9–726.6	9.7	7.56	77.9
25R	18	2230	726.6–736.3	9.7	9.15	94.3
26R	19	0030	736.3–746.0	9.7	8.21	84.6
27R	19	0230	746.0–755.7	9.7	8.38	86.4
28R	19	0440	755.7–765.4	9.7	8.85	91.2
29R	19	0800	765.4–775.1	9.7	8.61	88.7
30R	19	1010	775.1–784.9	9.8	6.45	65.8
31R	19	1215	784.9–794.8	9.9	5.81	58.7
32R	19	1445	794.8–804.7	9.9	1.76	17.8
33R	19	1830	804.7–814.5	9.8	7.68	78.3
34R	19	2100	814.5–824.1	9.6	7.28	75.8
35R	19	2300	824.1–833.7	9.6	4.91	51.1
36R	20	0130	833.7–843.3	9.6	5.03	52.4
37R	20	0350	843.3–852.9	9.6	5.16	53.7
38R	20	0630	852.9–862.6	9.7	5.62	57.9
39R	20	0910	862.6–872.2	9.6	7.55	78.6
40R	20	1130	872.2–881.9	9.7	9.07	93.5
41R	20	1330	881.9–886.5	4.6	4.22	91.7
42R	20	1450	886.5–891.5	5.0	4.35	87.0
43R	20	1745	891.5–901.1	9.6	6.21	64.7
44R	20	2045	901.1–910.7	9.6	8.71	90.7
45R	20	2330	910.7–920.3	9.6	9.30	96.9
46R	21	0200	920.3–930.0	9.7	8.64	89.1
47R	21	0435	930.0–939.6	9.6	9.06	94.4
48R	21	0645	939.6–949.2	9.6	9.68	101.0
49R	21	0910	949.2–958.8	9.6	9.52	99.1
50R	21	1200	958.8–968.4	9.6	8.73	90.9
51R	21	1440	968.4–978.1	9.7	8.51	87.7
52R	21	1745	978.1–987.7	9.6	8.46	88.1
53R	21	2100	987.7–997.4	9.7	9.89	102.0
54R	22	0015	997.4–1007.1	9.7	7.94	81.8
55R	22	0400	1007.1–1016.7	9.6	9.50	98.9
56R	22	0720	1016.7–1026.3	9.6	9.79	102.0
57R	22	1000	1026.3–1035.9	9.6	7.90	82.3
58R	22	1300	1035.9–1045.5	9.6	6.89	71.8
59R	22	1530	1045.5–1050.1	4.6	3.92	85.2
60R	22	1845	1050.1–1055.1	5.0	4.40	88.0
61R	23	0215	1055.1–1064.8	9.7	9.32	96.1
62R	23	0430	1064.8–1066.4	1.6	1.78	111.0
63B	23	1300	1066.4–1066.4	0.0	0.11	0.0
Coring totals				523.0	398.00	76.1
Drilled				543.4		
Total				1066.4		

Note: An expanded version of this coring summary table that includes lengths and depths of sections, location of whole-round samples, and comments on sampling disturbance is included on CD-ROM in the back pocket of this volume.

face casing (29.8 cm [11.75 in] diameter). A centralizing ring was used in the moonpool to help keep the casing vertical, and no other current-imposed problems arose.

While jetting in the reentry cone and conductor pipe, pump pressures were lower than predicted and the jetting process (total time 4.5 hr) took longer than anticipated based on the jetting test results. After landing the reentry cone at the seafloor, a 540-m-deep hole was drilled with a 37.5 cm (14.75 in) diameter tricone drill bit. Upon recovering the drilling assembly, the tricone bit was found to have one of three jets missing, thus explaining the earlier jetting difficulties.

Casing operations went smoothly and without delay even with two minor complications. First, the plastic thread protectors on nearly every other casing joint had to be removed by cutting them off with a torch, probably because of their age. Second, the riser bridge crane jumped a sheave, damaging the line. Fortunately, the calmness of the weather and sea allowed us to use the #3 crane safely. After reentering Hole 999B, the casing was landed without incident, placing the bottom of the casing pipe (the casing shoe) at 526.2 mbsf. The casing was cemented into place with 300 barrels of 15.8 lb/gal cement and the drill pipe was tripped to the surface in preparation for RCB coring.

A CC-4 tungsten carbide roller cone insert bit was selected for RCB coring because the formation was expected to get progressively harder, eventually grading into silicified limestone and chert. The bit repeatedly clogged with aluminum debris from the cementing dart, resulting in no core recovery for the first four cores. The debris was removed after tripping the drill string back to the surface, which resulted in a delay of ~14 hr. Coring progressed well from Core 165-999B-5R until retrieval of Core 165-999B-8R, during which the forward sand-line broke and the core barrel, sinker bars, and 464 m of sand line fell to the bottom of the hole. This was fished out of the hole successfully on the first try and coring resumed. The rate of penetration (ROP) rapidly deteriorated with depth; the ROP for the last two cores was 3.2 and 2.4 m/hr, respectively, compared with 4.7 m/hr for the previous 100-m interval. At these rates, we would not have been able to reach the depth objectives, and so a decision was made to switch to a polycrystalline diamond compact (PDC) antiwhirl core bit. The bit change required another trip to the surface with the drill string, another reentry into the hole, and another ~15 hr delay.

The new PDC bit proved to be worth the extra time as there was a slight improvement in core quality and a significant increase in the ROP, which averaged 8.9 m/hr over the first 100-m interval, or 2–4 times that achieved by the CC-4 bit. Even when the formation became a well-indurated limestone, the ROP only dropped to 6.9 m/hr for the PDC bit.

The ROP only began to decrease significantly at a depth of about 1046 mbsf while Core 165-999B-59R was being drilled, which was also marked by a increase in drill pump pressure from 500 psi to about 750 psi. Core 165-999B-59R was potentially the core that would contain the K/T boundary interval. Our primary concern was that the increased pump pressures would wash away part or all of the critical interval, and thus a joint decision was made to retrieve the core after advancing only 4.6 m. The ROP dropped even further, to about 1.5 m/hr, during coring of the next three cores (165-999B-60R through 62R), which indicated bit degradation. Perhaps because of luck, or to the extra care taken while drilling through the critical interval, the overall recovery (92.9%; Table 1) for the last four cores was over 10% higher than achieved for the other part of the hole cored with the PDC bit.

Having determined that we were about 15 m into the Upper Cretaceous section and realizing that further coring at the very slow ROP would gain us little given the time constraints, we ended coring operations at a depth of 1066.4 mbsf. The hole was then prepared for logging with sepiolite mud sweeps without using a wiper trip. Hole conditions were excellent for logging, which resulted in very smooth logging operations and high quality logs, as discussed in the "Downhole Measurements" section (this chapter).

LITHOSTRATIGRAPHY

The 1066.4-m-thick sedimentary sequence recovered at Site 999 ranges in age from Late Cretaceous (Maastrichtian) to late Pleistocene and consists dominantly of pelagic sediments and sedimentary rock with significant, though variable, input of clays and volcanic ash. A K/T boundary interval was recovered near the base of the Site 999 sequence. High density measurements (5-cm sample spacing) of color reflectance (see Appendix tables on CD-ROM in the back pocket of this volume for the complete data set) and magnetic susceptibility, in addition to shipboard data on carbonate content and sedimentological criteria (percentage of microfossils and minerals in smear slides, depositional textures, sedimentary structures, and XRD bulk analyses), form the basis for dividing the recovered sequence into six lithologic units (I–VI) and a number of subunits. The stratigraphic distribution of these units and subunits is summarized in Figure 6.

Description of Lithologic Units

Unit I

Intervals: Core 165-999A-1H through Section 165-999A-29X-5, 74 cm
Age: Pleistocene to late Miocene
Depth: 0.0–265.1 mbsf, Hole 999A

Unit I consists of 265.1 m of nannofossil clayey mixed sediment with foraminifers, foraminiferal clayey mixed sediment with nannofossils, nannofossil clayey mixed sediment with foraminifers and pteropods, clayey nannofossil mixed sediment, and clayey nannofossil ooze. This unit includes the transition from soft to firm sediments in Core 165-999A-22X at 197.6 mbsf. Sediments of Unit I are massive and structureless, and they exhibit slight to heavy bioturbation, leading to common olive gray to gray mottling of the core surface. Volcanic ash occurs both as dispersed ash and as discrete layers. Unit I is divided into three subunits (IA, IB, and IC), based on variations in the abundance of foraminifers and the occurrence of siliceous microfossils (Fig. 6).

Subunit IA

Intervals: Core 165-999A-1H through Section 165-999A-16H-CC
Age: Pleistocene to early Pliocene
Depth: 0.0–150.1 mbsf

Sediments of Subunit IA consist predominantly of nannofossil clayey mixed sediment with foraminifers and foraminiferal clayey mixed sediment with nannofossils. They are medium to thick bedded, and the contacts between lithologies are gradational. Major constituents of Subunit IA include abundant nannofossils, foraminifers, and clay minerals. The XRD analyses indicate that the clay mineral assemblages consist of smectite, minor amounts of chlorite, kaolinite, and more rarely illite(?) (Table 2). Clear, volcanic glass shards are a common minor constituent along with quartz, feldspar, zeolites, and opaque minerals. Downhole variations in the relative abundance of quartz and clay have been determined by XRD analyses (Fig. 7). There is a maxima in quartz and clay abundances in Cores 165-999A-2H through 5H, underlain by an interval of near-constant abundance. Traces of feldspar are also present within the uppermost core sections. Pyrite is a ubiquitous minor component that increases in abundance downcore through Subunit IA and occurs as infillings of millimeter- to centimeter-sized burrows. The most common forms of pyrite include framboidal (spheroidal), irregular, and "worm" tube casts.

Carbonate contents in Subunit IA range from 32% to 72% (Fig. 6). The variations in carbonate content show higher frequency changes from 0 to 60 mbsf compared with the interval from 60 to 150 mbsf. Near the base of Subunit IA, the carbonate content variations are more similar to the upper part of the hole (Fig. 6). Magnetic susceptibility varies in a similar, but inverse manner to the carbonate record (Fig. 6). In Cores 165-999A-1H to 13H (0.0–121.6 mbsf), the sediment lithologies consist of decimeter-scale alternations between gray, light olive gray, and olive gray nannofossil clayey mixed sediment with foraminifers, and foraminiferal clayey mixed sediment with nannofossils. The boundaries between these two lithologies are gradational on a scale of a few centimeters. Within Cores 165-999A-1H through 3H, some differences exist: (1) nannofossil clayey mixed sediment with foraminifers and pteropods occur within the lower 100 cm of Sections 165-999A-1H-1 and 1H-4, 80–120 cm; and (2) they are dominated by light olive brown, light brownish gray, grayish brown, and olive gray colored sediments. Cores 165-999A-14H and 15H are dominated by clayey nannofossil mixed sediment with foraminifers.

Several volcanic ash layers occur within Subunit IA in Cores 165-999A-6H and 17H. Typically, they have sharp basal contacts and bioturbated tops, and they are normally graded. The dominant components are clear silicic glass shards with minor amounts of plagioclase, biotite, hornblende, and opaque minerals. Most are moderately to well sorted and range in average grain size from fine sand to fine silt. In the lower portion of Unit I, some of the ash layers contain pyrite as framboidal overgrowths on glass shards (see "Igneous Petrology and Volcanology" section, this chapter).

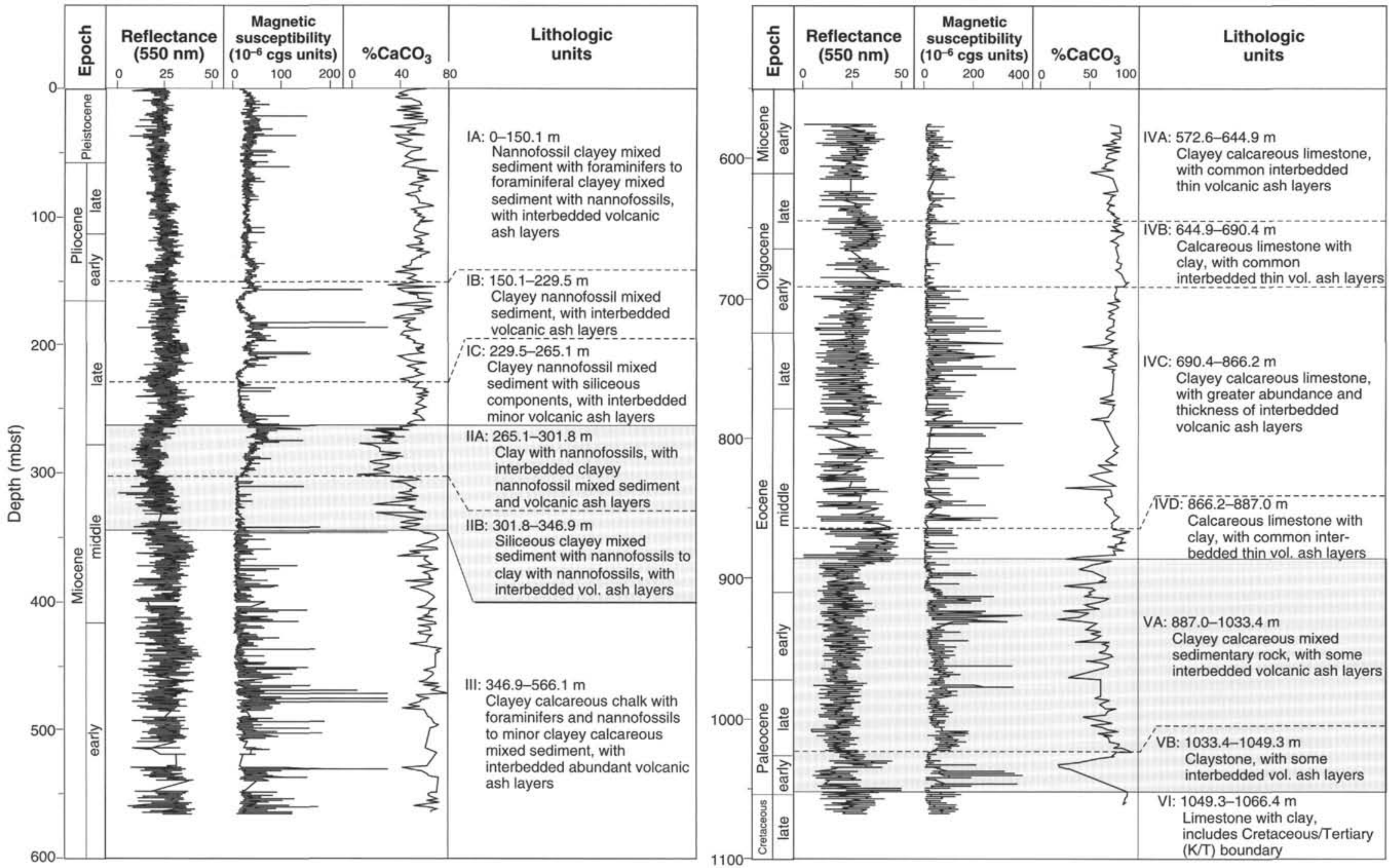

Figure 6. Lithologic units of Site 999 (Holes 999A and 999B) and their relationship to downcore variations in color reflectance (550 nm), magnetic susceptibility, and %$CaCO_3$.

Table 2. XRD bulk mineralogical analyses for Site 999.

Unit	Subunit	Core, section interval (cm)	Depth (mbsf)	Mineralogy														
											Zeolites			Clays				
				Calcite	Feldspar	Quartz	Opal CT	Apatite	Pyrite	Dolomite	Clinoptilolite	Heulandite	Phillipsite	Clay minerals (when not known)	Chlorite	Kaolinite	Illite	Smectite
I	A	999A-2H-1, 88–89	8.48	P	Tr?	P									Tr	Tr		P
		999A-4H-3, 101–103	30.61	P	Tr	P									Tr	Tr		P
		999A-5H-3, 100–101	40.10	P	Tr?	P									Tr	Tr	Tr?	P
		999A-6H-3, 91–92	49.51	P		P					Tr?				Tr	Tr	Tr?	P
		999A-9H-2, 81–82	76.41	P		P									Tr	Tr	Tr?	P
		999A-10H-1, 20–22	83.80	P		P									Tr	Tr		P
		999A-12H-5, 10–11	108.70	P		P									Tr	Tr	Tr?	P
		999A-14H-3, 127–128	125.87	P		P									Tr?	Tr?	Tr?	P
		999A-15H-3, 80–82	134.90	P		P									Tr	Tr	Tr	P
	B	999A-18H-3, 59–61	163.19	P		P									Tr	Tr?		P
		999A-20H-1, 28–29	178.88	P		P									Tr	Tr?		P
		999A-20H-6, 60–62	186.70	P		P									Tr?	Tr?		P
		999A-21H-7, 82–83	197.10	P	Tr	P									Tr	Tr		P
		999A-22X-3, 129–130	201.89	P		P									Tr?	Tr?		P
		999A-24X-1, 121–122	211.51	P		P									Tr?	Tr?		P
		999A-24X-4, 90–91	215.70	P		P									Tr?	Tr?		P
		999A-24X-6, 101–102	218.81	P		P												P
		999A-25X-4, 50–51	224.90	P		P												P
	C	999A-26X-3, 90–91	233.40	P		P												P
		999A-27X-3, 100–102	243.10	P		P												P
		999A-28X-2, 51–52	250.71	P		P												P
		999A-28X-5, 61–62	255.31	P		P												P
		999A-29X-2, 81–83	260.71	P		P												P
		999A-29X-4, 69–71	263.59	P		P												P
II	A	999A-30X-2, 138–141	270.88	P		P												P
		999A-30X-7, 20–21	277.20	P		P					Tr?		Tr?					P
		999A-31X-1, 87–89	278.47	P		P									Tr?			P
		999A-31X-5, 68–70	284.28	P		P									Tr?		Tr?	P
		999A-31X-5, 137–138	284.97	Tr	Tr	P												P
		999A-31X-6, 133–135	286.43	P	Tr?	P												P
		999A-32X-1, 59–60	287.79	P		P					Tr?		Tr?					P
		999A-32X-5, 82–83	294.02	P		P					Tr?		Tr?					P
	B	999A-34X-2, 91–92	308.71	P		P					Tr?		Tr?					P
		999A-35X-3, 78–80	319.78	P		Tr												P
		999A-36X-2, 59–60	327.69	P		P												P
III		999A-38X-3, 79–81	348.59	P		Tr												P
		999A-40X-3, 80–82	367.80	P		Tr												P
		999A-44X-2, 32–33	404.32	P		Tr												P
		999A-45X-1, 35–36	412.45	P	Tr	Tr												P
		999A-46X-3, 106–107	425.86	P		Tr												P
		999A-48X-4, 66–68	446.26	P		Tr												P
		999A-49X-4, 98–100	456.18	P	Tr	Tr												P
		999A-50X-3, 78–79	464.08	P		Tr												P
		999A-52X-2, 108–110	482.08	P		Tr												P
		999A-53X-5, 81–82	495.91	P		Tr												P
		999A-54X-3, 99–100	502.69	P		Tr												P
		999A-56X-1, 58–59	513.48	Tr	Tr	Tr												P
		999A-60X-4, 57–58	551.87	P		Tr												P
		999A-61X-3, 99–100	560.49	P		Tr												P
IV	A	999B-5R-2, 21–22	574.27	P		Tr?					Tr							P
		999B-7R-4, 101–102	587.23	P		Tr?					Tr							P
		999B-8R-3, 82–83	595.62	P	Tr?	Tr?					Tr							P
		999B-10R-1, 60–61	611.70	P		Tr?					Tr							P
		999B-11R-1, 31–32	621.01	P		Tr?					Tr							P?
		999B-11R-5, 25–26	626.42	Tr	Tr		?				Tr							P
		999B-12R-3, 26–27	632.21	P			P?				Tr?							P?

Table 2 (continued).

Unit	Subunit	Core, section interval (cm)	Depth (mbsf)	Mineralogy														
											Zeolites			Clays				
				Calcite	Feldspar	Quartz	Opal CT	Apatite	Pyrite	Dolomite	Clinoptilolite	Heulandite	Phillipsite	Clay minerals (when not known)	Chlorite	Kaolinite	Illite	Smectite
	B	999B-16R-4, 56–61	672.65	P		Tr?					Tr?							P?
		999B-19R-1, 44–46	682.34	?	?	?	?				Tr							P
		999B-20R-1, 76–77	685.66	P			P?											Tr?
	C	999B-22R-4, 48–49	702.58	P			P?											Tr?
		999B-24R-4, 66–67	721.86	P			P?				Tr							Tr
		999B-26R-5, 78–79	743.08	P			P?				Tr							Tr?
		999B-30R-2, 68–70	777.28	P			P?				Tr?							Tr?
		999B-31R-4, 47–48	790.47		Tr?		P?				Tr							P
		999B-32R-2, 40–42	796.20	P			P?				Tr							Tr?
		999B-34R-2, 87–88	816.87	P			P?				Tr							Tr?
		999B-36R-2, 91–93	836.11	P		Tr	P?				Tr?							Tr?
		999B-38R-2, 142–144	855.82	?	P	?					P							P
		999B-38R-4, 50–52	857.90	P		P					Tr			Tr				
		999B-39R-2, 110–112	865.20	P		P								P				
	D	999B-40R-1, 19–21	872.39	P		P					Tr			Tr				
V		999B-42R-1, 65–66	887.15	P		P								P				
		999B-44R-5, 59–61	907.69	P		P								P				
		999B-44R-5, 64–66	907.74	P	Tr?	P					Tr			P				
		999B-47R-5, 46–49	936.46	P	Tr	P		Tr	Tr		P	P		P				
		999B-48R-4, 71–72	944.81	P		P												P
		999B-49R-4, 57–59	954.27	P		P												P
		999B-50R-1, 44–45	959.24	P	Tr	P												P
		999B-53R-5, 87–88	993.24	P	P	P												P
		999B-54R-4, 43–44	1002.33	P	P	P												P
		999B-55R-3, 75–76	1010.85	P	P	P												P
		999B-56R-4, 63–64	1021.83	P	Tr	P												P
VI		999B-61R-3, 62–63	1058.72	P	P	P			Tr									P
		999B-61R-5, 5–6	1061.15	P	P	P			Tr				Tr?					P

Notes: The precise identification of chlorite and kaolinite is not possible due to the low intensities of diagnostic peak reflections. Sample intervals with asterisks are volcanic ashes. P = present, Tr = trace quantities, and Tr? = presence of mineral uncertain.

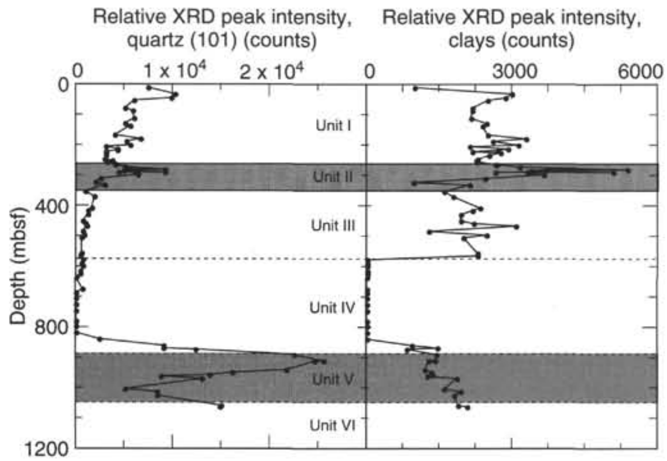

Figure 7. Variations in the relative downcore abundance of quartz and clay in sediments from Site 999 based on XRD bulk sediment analyses.

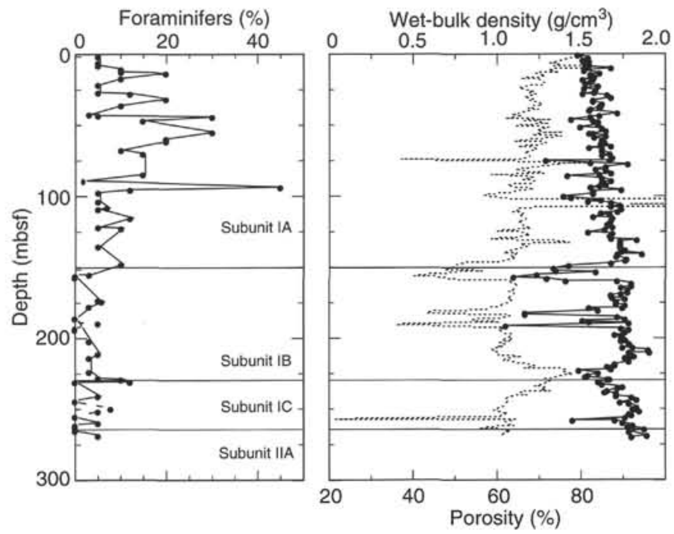

Figure 8. Foraminifer abundance based on smear slide analysis as well as variations in sediment wet-bulk density (solid line) and porosity (dashed line) as a function of depth in Hole 999A. No apparent correlation exists between foraminifer abundance and sediment porosity.

Subunit IB

Intervals: Sections 165-999A-17H-1 through 25X-CC
Age: early Pliocene to late Miocene
Depth: 150.1–229.5 mbsf

Subunit IB is distinguished from Subunit IA by a lower abundance of foraminifers (<10%; Fig. 8). The dominant lithology is homogenous, olive gray, clayey nannofossil mixed sediment, and the overall texture of the sediment is finer grained than in Subunit IA. In addition, a minor amount of clayey nannofossil ooze is present. Major components in the clayey nannofossil mixed sediment include abundant nannofossils, clays, and foraminifers. The clay assemblages are dominated by smectite, with minor quantities of chlorite and kaolinite detectable down to Core 165-999A-24X (Table 2). Clear, silicic glass shards are also common minor constituents along with quartz, feldspar, and opaque minerals. The relative abundance of quartz decreases downcore through this subunit (Fig. 7). Pyrite is a common component in the sediment and occurs as small dispersed framboids up to 100 µm in diameter. Pyrite is also locally concentrated within burrows. In addition, Subunit IB contains several volcanic ash layers, although most have been altered to zeolites and/or clay minerals.

Cores 165-999A-17H through 26X (150.1–229.5 mbsf) are comprised of greenish gray and light greenish gray clayey nannofossil mixed sediment. Within the APC cores (165-999A-16H through 21H), there is a discernible color variation on a decimeter scale; this is not seen, however, in the XCB-cored sediments. Carbonate contents in Subunit IB range from 30% to 70%, and significant fluctuations are evident throughout the subunit (Fig. 6). The magnitude and frequency of the fluctuations is greatest in the upper part of the unit and decreases downcore.

The use of foraminifer abundance as a criterion for the division of Subunit IA from Subunit IB (Fig. 8) was done to facilitate lithologic comparisons between Site 999 and DSDP Site 502, located approximately 150 km to the southwest in the Colombian Basin. This criterion was used at Site 502 to mark the boundary between lithologic Subunits IB and IC, which occurred at a depth of 110 mbsf (Prell, Gardner, et al., 1982). At Site 999, the boundary occurs at a depth of 150 mbsf and is thus offset by about 40 m from Site 502.

A distinctive sequence of volcanic ashes that includes a light gray ash layer followed by an ash doublet in Section 165-999A-6H-3, 10–14 cm, and in Sections 165-999A-17H-4, 112–116 and 128.5–131 cm (Fig. 9), respectively, is likely to be correlated to a similar sequence of ash layers found at DSDP Site 502 (Prell, Gardner, et al., 1982). The sequence of ashes at Site 999 occurs at 47.7, 155.7, and 155.9 mbsf, whereas at DSDP Site 502 they are found at 30.2, 131.4, and 131.7 mbsf, respectively. The offset of 17–24 m between the sites is possibly the result of the higher sedimentation rate at Site 999. This offset is generally consistent with the offset inferred by the reduction in foraminifer abundance described above.

Subunit IC

Intervals: Section 165-999A-26X-1 through 29X-5, 74 cm
Age: late Miocene
Depth: 229.5–265.1 mbsf

Subunit IC consists dominantly of well-indurated, light greenish gray to greenish gray, clayey nannofossil mixed sediment. The sediment is massive, homogenous, and moderately to heavily bioturbated. It is distinguished from sediment in Subunit IB by the presence of a significant amount of biogenic siliceous material such as sponge spicules, radiolarians, and diatoms (Fig. 10). Carbonate contents show less variation than in Subunits IA and IB, ranging from 52% to 62% (Fig. 6). Nannofossils and clays (only smectite detected; see Table 2) are the major components of the sediment, with minor amounts of volcanic glass, pyrite, quartz, and feldspar. The abundance of quartz and clay, as determined by XRD, shows little change from that of Subunit IB (Fig. 7). The presence of biogenic silica appears to correlate well with changes in the wet-bulk density and porosity of the sediment (see "Physical Properties" section, this chapter; Fig. 10). Additional support for the correlation of the upper portions of Sites 999 and 502 comes from the location of the significant downcore increase in the amount of radiolarians, sponge spicules, and diatoms marked by the boundary between Subunits IB and IC. At Site 999, this increase occurs in Core 165-999A-26X at 230 mbsf, whereas at Site 502 this increase was noted at 210 mbsf, indicating an offset of about 20 m between the two sites. This offset is generally consistent with both the offsets inferred from the correlation of volcanic ash layers and the change in lithology from sediments with greater than 10% foraminifers to those with less than 10% (Subunit IA to Subunit IB boundary).

Volcanic ash layers occur intermittently throughout Subunit IC and are generally 2–10 cm thick. Unlike many of the layers in Subunits IA and IB, the layers in Subunit IC contain abundant clear glass shards (see "Igneous Petrology and Volcanology" section, this chapter). However, a significant number of the layers contain glass shards

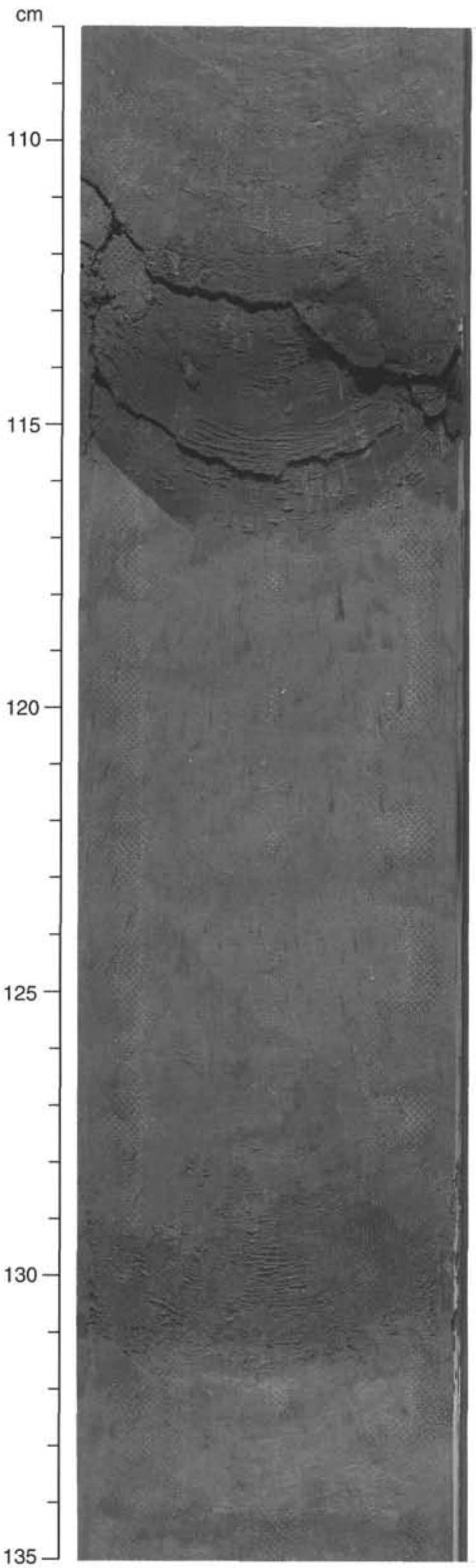

Figure 9. Pair of volcanic ash fall layers from Section 165-999A-17H-4, 108–135 cm. This ash layer doublet is correlated with a similar pair occurring at approximately 131 mbsf at DSDP Site 502 in the southwest Colombian Basin.

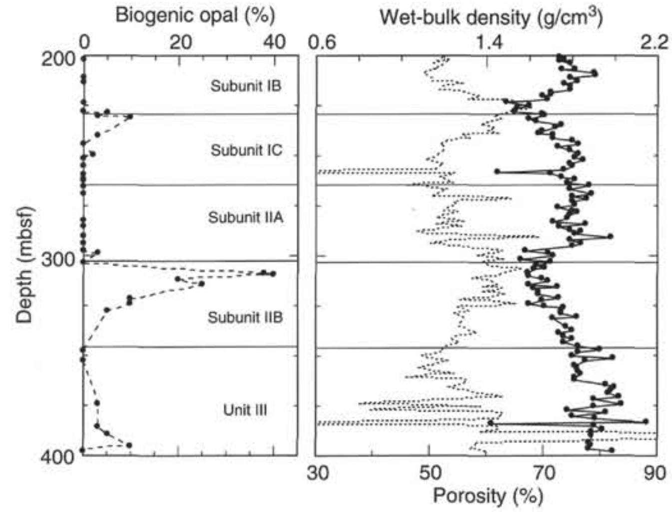

Figure 10. Biogenic opal abundance based on smear slide analyses as well as variations in sediment wet-bulk density (solid line) and porosity (dashed line) as a function of depth in Hole 999A. Note the correlation between biogenic opal and (1) increased sediment porosity and (2) decreased wet-bulk density (see "Physical Properties" section, this chapter, for further discussion).

that have overgrowths of pyrite. These layers are often dark gray to black.

The lower boundary of Subunit IC occurs at Sample 165-999A-29X-5, 74 cm (265.1 mbsf), and is marked by the abrupt appearance of a dark greenish gray clay with nannofossils (Fig. 11). This boundary also coincides with a rapid decline in sediment carbonate values, an increase in relative quartz and clay abundance (Fig. 7), a large-amplitude increase in magnetic susceptibility, and a change in color reflectance (Fig. 6).

Unit II

Intervals: Sections 165-999A-29X-5, 74 cm, through 38X-2, 63 cm
Age: late to middle Miocene
Depth: 265.1–346.9 mbsf, Hole 999A

Lithologic Unit II at Site 999 consists of sediments ranging in composition from indurated (carbonate- and siliceous-bearing) mixed sediments to indurated clays with nannofossils. Unit II ranges in age from middle to late Miocene. The upper boundary of Unit II is defined by the first downhole transition from indurated mixed sediments into indurated clays and an initial reduction in mean carbonate content to less than 30%. The lower boundary of Unit II is defined by the downhole transition from clayey mixed sediments into clayey chalk and an increase in carbonate content to more than 60%. Based upon differing proportions of foraminifers, nannofossils, radiolarians, and clays, the sediments of Unit II can be classified as nannofossil clayey mixed sediment, nannofossil clayey mixed sediment with radiolarians, siliceous clayey mixed sediment, and clay with nannofossils. Silicic volcanic ash layers are common throughout Unit II.

Unit II is divided into Subunits IIA and IIB. The subdivision is based upon the abundance of siliceous microfossils as well as upon variations in the carbonate content, magnetic susceptibility, and color reflectance data (Fig. 6).

Subunit IIA

Intervals: Sections 165-999A-29X-5, 74 cm, through 33X-4, 62 cm
Age: late to middle Miocene
Depth: 265.1–301.8 mbsf

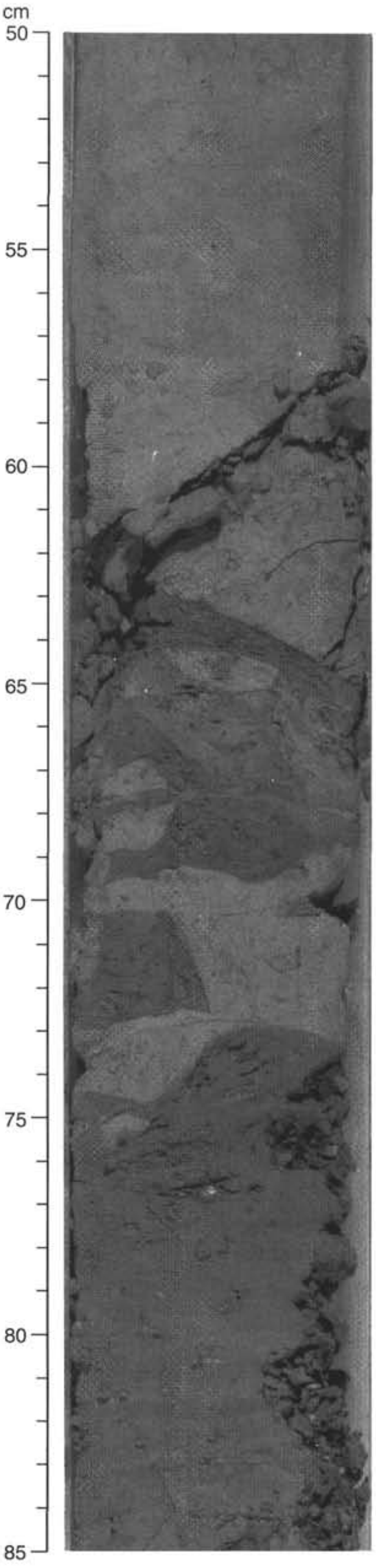

Figure 11. The abrupt transition between lithologic Unit I and Subunit IIA is noted by the first occurrence of indurated clay with nannofossils in Section 165-999A-29X-5, 50–85 cm, otherwise composed of clayey nannofossil mixed sediment farther downcore.

Major lithologies in Subunit IIA consist of clay with nannofossils interbedded with clayey nannofossil mixed sediment. Volcanic ash layers occur as minor lithologies. The upper boundary of Subunit IIA is defined by the first occurrence of indurated clay with nannofossils (Fig. 11), which corresponds to an abrupt decline in carbonate content and an increase in magnetic susceptibility. A change in lithology from indurated clay with nannofossils to indurated clayey nannofossil mixed sediment defines the lower boundary of Subunit IIA, coinciding with a sharp increase in carbonate content and lower magnetic susceptibility values (Fig. 6). The 550-nm color reflectance data show a marked decrease in association with the upper boundary of Subunit IIA and a return downhole toward higher values at the boundary with Subunit IIB. A comparison of magnetic susceptibility and carbonate data shows a marked offset between the interval of minimum carbonate values and the interval of maximum susceptibility within Subunit IIA (Fig. 12).

Bulk XRD analyses reveal quartz and smectite clay as important constituents, after calcite. Chlorite, illite, and zeolites (clinoptilolite? and philipsite?) are at or above the limit of detection for Cores 165-999A-30X and 31X (Table 2). Large fluctuations in clay and quartz abundances occur within this subunit, most likely in response to changes in carbonate content (Fig. 7).

The average carbonate content of Subunit IIA is 29%, with values ranging from 4% to 44%. Subunit IIA stands out from the rest of the sediments drilled at Site 999 in that carbonate contents decrease dramatically, recording a shoaling of the CCD above or close to seafloor depth at this site during late middle to early late Miocene time. This event has been referred to as the carbonate crash (see "Lithostratigraphy" section, "Site 998" chapter, this volume) and has been recognized also at Site 998 (Fig. 13).

The indurated clays with nannofossils of Subunit IIA are typically dark greenish gray. Clayey nannofossil mixed sediments are typically light greenish gray to greenish gray. Both lithologies are massive as

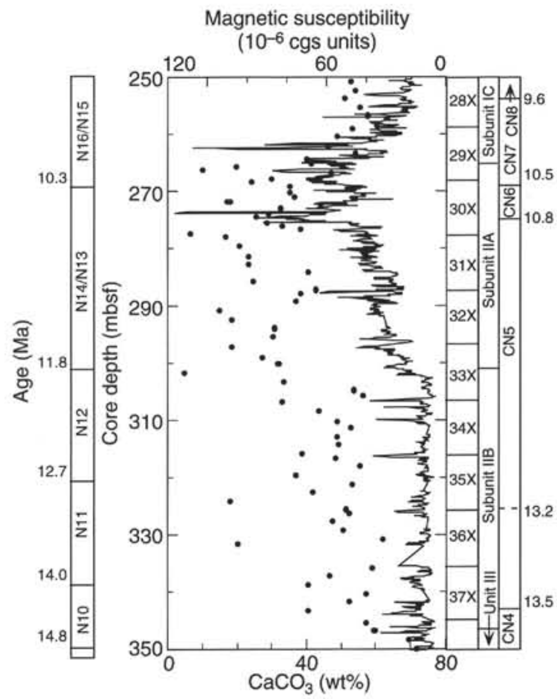

Figure 12. Variation in carbonate content (solid circles) and magnetic susceptibility (dashed line) in lithologic Subunits IC, IIA, and IIB, and Unit III in Hole 999A. Boundaries of the lithologic units and nannofossil zonal data are shown on the right, and the foraminifer zonal data are shown on the left.

well as moderately to heavily bioturbated. *Zoophycos* bioturbations are common and often well preserved. Dark gray (N4), pyritic(?) concentric rims commonly occur around burrows because of the localized, suboxic degradation of organic matter.

A few volcanic ash layers occur as minor lithologies in Subunit IIA. They are generally brownish gray in color and reach a few centimeters in thickness. Their upper and lower boundaries are usually gradational because of reworking by benthic organisms.

Subunit IIB

Intervals: Sections 165-999A-33X-4, 62 cm, through 38X-2, 63 cm
Age: middle Miocene
Depth: 301.8–346.9 mbsf

Major lithologies in Subunit IIB consist of dark greenish gray clay with nannofossils, and light greenish gray siliceous clayey mixed sediment with nannofossils, nannofossil mixed sediment with radiolarians, and nannofossil clayey mixed sediment. Volcanic ash layers occur as minor lithologies. The transition downhole between Subunits IIA and IIB is marked by an abrupt increase in carbonate content to an average of 48.3%, a decrease in magnetic susceptibility to some of the lowest values for the entire section, and an increase in color reflectance at 550 nm (Fig. 6). The 550-nm color reflectance data show a gradual increase downhole throughout Subunit IIB. Magnetic susceptibility in Subunit IIB is lower for a given carbonate content than it is for most of Unit I, probably as a result of the relatively high biogenic silica component of this unit (see below).

The XRD bulk sediment analyses indicate smectitic clay, minor quartz, and possible traces of zeolites. Within this subunit, relative abundances of quartz and clay are significantly lower than within Subunit IIA and Unit I (Fig. 7). Also contained within the massive, background sediments of this unit is a significant component of siliceous microfossils, including diatoms, radiolarians, and siliceous sponge spicules. Bioturbation is moderate to heavy throughout, *Zoophycos* is common, and both *Chondrites* and *Planolites* were observed. The early stages of silicification (incipient chert) are present in Section 165-999A-36X-3, 47 cm, and microfaulting with displacements typically on the order of several centimeters or less is evident in Cores 165-999A-33X and 34X. Several well-preserved volcanic ash layers occur in Subunit IIB. They are generally brownish gray to light brownish gray in color and a few centimeters thick. Their lower boundaries are generally sharp, and their upper boundaries gradational due to reworking by benthic faunas.

Unit III

Intervals: Section 165-999A-38X-2, 60 cm, through Core 165-999A-61X
Age: middle to early Miocene
Depth: 346.9–566.1 mbsf, Hole 999A

Sediments of Unit III consist predominantly of clayey calcareous chalk with foraminifers and clayey nannofossil chalk with foraminifers. Calcareous chalk with foraminifers and clayey nannofossil mixed sediment are interbedded as minor lithologies, whereas volcanic ash layers are ubiquitous and distributed throughout the section. The top of Unit III is marked by a relatively sharp downhole increase in the carbonate content of the sediment and by the first appearance of sediment indurated enough to be called chalk. The bottom of Unit III is taken as the base of the stratigraphic sequence recovered in Hole 999A, giving this unit a total thickness of 219.2 m. The sediments of Unit III range in age from early to middle Miocene.

In addition to the rise in carbonate content, the transition to Unit III from the overlying mixed sediments of Subunit IIB is marked by a pronounced increase in color reflectance at the 550-nm (green) wavelength and a distinct change to increased variability in magnetic susceptibility values (Fig. 6). These changes accompany the lithologic transition from unconsolidated oozes and mixed sediments above to well-indurated chalks below. Shipboard measurements indicate carbonate contents in Unit III that range from about 38% to 79%, with a mean of 63%. The clayey calcareous chalks and clayey nannofossil chalks that dominate the unit are generally massive and vary in color between light greenish gray and dark greenish gray, with the hue largely dependent on carbonate content. XRD bulk sediment analyses indicate minor quartz in the background sediment, which decreases with increasing depth (Fig. 7). The relative abundance of clay minerals (smectite) is reduced relative to Unit I and also decreases downhole (Fig. 7). Siliceous biogenic material (radiolarians, diatoms, and spicules) is a minor but persistent contributor to the sediments.

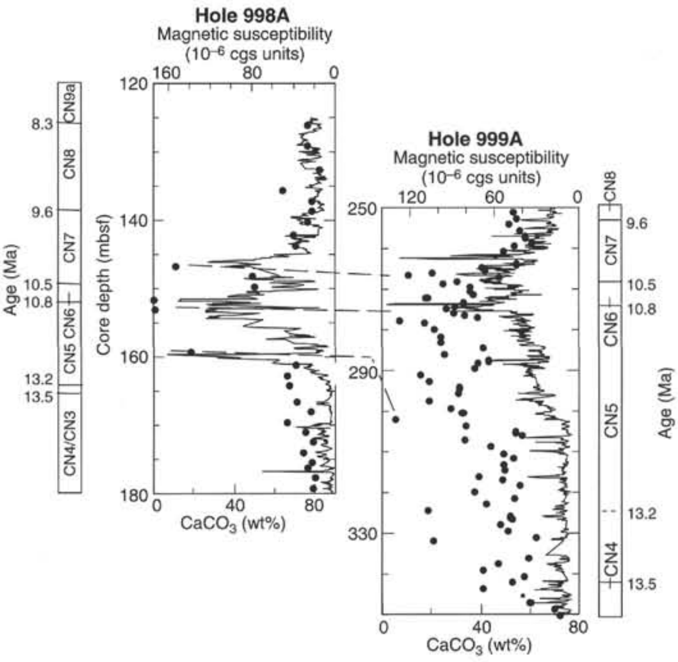

Figure 13. Comparison of carbonate content (solid circles) and magnetic susceptibility (solid line) data in Holes 998A and 999A in the middle/late Miocene carbonate crash interval. The nannofossil biostratigraphic zones for each hole are shown on the right- and left-hand sides of the figure. Note difference in scale of SI units from Hole 998A to Hole 999A.

Unit III chalks are moderately to heavily bioturbated throughout. Burrows are commonly pyritized, especially in the lower half of the unit. Pyrite here occurs as clusters of irregularly shaped grains or as framboids. A distinct *Chondrites*-type burrow is observed in Section 165-999A-41X-6. With the increase in lithification comes increased evidence at this site for microfracturing and faulting, which is particularly evident in Cores 165-999A-43X and 58X.

Volcanic ash is an extremely common component of Unit III sediments, occurring both in discrete ash layers and in disseminated form throughout the sequence. Ash layers are numerous and are typically graded with sharp basal contacts and bioturbated tops. Their colors range from brownish gray to dark gray or very dark gray. Pyrite is commonly associated with ash layers in the lower portion of the unit. Although most ash layers show evidence of at least partial alteration to clays and zeolites, many are surprisingly fresh with high proportions of clear to pale brown glass shards. Magnetic susceptibility peaks that rise above background values (Fig. 6) are generally associated with individual ash layers. Further discussion on the origin and character of these Miocene ashes can be found in the "Igneous Petrology and Volcanology" section (this chapter).

Lithologic Unit III ends at the base of Hole 999A at a depth of 566.1 mbsf. Hole conditions at this level were judged to be suitable for the installation of casing, and the drill string was tripped to begin drilling operations at Hole 999B.

Unit IV

Intervals: Core 165-999B-5R through Section 165-999B-42R-1, 50 cm
Age: early Miocene to middle Eocene
Depth: 572.6–887.0 mbsf

Lithologic Unit IV is 314.4 m thick and consists of thick-bedded clayey calcareous limestone, calcareous limestone with clay, and volcanic ash layers. The limestones are well indurated and slightly to moderately bioturbated; they often show color banding from shades of light greenish gray to greenish gray on a decimeter scale. Volcanic ash layers consist of glass shards (fresh and altered) with minor amounts of plagioclase, biotite, amphibole, and opaque minerals. Significant variations in the frequency of ash layers occur throughout the unit and represent major episodes of explosive volcanism from sources to the west of Site 999 (see "Igneous Petrology and Volcanology" section, this chapter). Unit IV has been divided into four subunits based on the carbonate content of limestones and the abundance of interbedded volcanic ash layers (Fig. 6).

Subunit IVA

Intervals: Core 165-999B-5R through Section 165-999B-13R-4, 50 cm
Age: early Miocene to late Oligocene
Depth: 572.6–644.9 mbsf

The major lithology in Subunit IVA consists of thick-bedded clayey calcareous limestone with common thin-bedded volcanic ash layers. The light greenish gray calcareous limestone is often characterized by an alternation from light greenish gray to greenish gray on a decimeter scale. Transitions between such color bands are gradational on a scale of a few centimeters. Bioturbation ranges from slight to moderate; with increasing depth, the burrows are flattened as a result of compaction. In Core 165-999B-12R, there are *Zoophycos* trace fossils. A common feature of the calcareous limestone is the presence of wispy laminations that are dark greenish gray, usually less than 1 cm thick, undulatory, and sometimes showing laminae bifurcation.

The major biogenic constituents of the clayey calcareous limestone are common nannofossils and foraminifers, together with small carbonate fragments. The mineralogy of the subunit includes traces of quartz within Cores 165-999B-5R through 11R, together with clays, which are most likely smectitic (alteration products of volcanic glass; Table 2). Several meters above the base of the subunit, the first occurrence of opal-CT is detected in Section 165-999B-12R-3 (Table 2). Fresh volcanic glass shards are minor constituents along with zeolites (clinoptilolite), feldspar, opaque minerals, and pyrite.

Carbonate contents in Subunit IVA range from 50% to 80%, but with the majority falling between 60% and 80% (Fig. 14). With increasing depth in the subunit, the carbonate contents decrease to a broad minimum between 580 and 630 mbsf.

Subunit IVA contains numerous volcanic ash layers and dispersed ash zones (see "Igneous Petrology and Volcanology" section, this chapter). The layers are gray to greenish gray to dark gray, with sharp basal contacts and bioturbated tops. Most layers are less than 10 cm thick and contain abundant altered volcanic glass with minor amounts of phenocryst phases such as feldspar, biotite, and opaque minerals. Fresh glass is also present in amounts that vary from trace to over 90%. Dispersed, bioturbated ash zones are also common within Subunit IVA. They consist of continuous to discontinuous bands of gray to dark gray ash with bioturbated basal and upper contacts. Most are less than a few centimeters in thickness.

Subunit IVB

Intervals: Sections 165-999B-13R-4, 50 cm, through 21R-2, 100 cm
Age: late to early Oligocene
Depth: 644.9–690.4 mbsf

Subunit IVB consists of thick-bedded calcareous limestone with clay interbedded with common thin-bedded volcanic ash layers. This subunit is distinguished from Subunit IVA by a shift in the predominant lithology from clayey calcareous limestone to limestone with clay (Fig. 14). The light greenish gray limestone with clay shows alternations in color from light greenish gray to greenish gray on a decimeter scale, as observed in Subunit IVA. Transitions between such color bands are gradational on a scale of a few centimeters. Bioturbation ranges from slight to moderate, and most burrows are flattened as a result of compaction. A common feature of the calcareous limestone is the presence of wispy laminations that are dark greenish gray, usually less than 1 cm thick, and undulatory as well as sometimes showing laminae bifurcation.

The major biogenic constituents of the calcareous limestones are common nannofossils and foraminifers, together with small carbonate fragments. The mineralogy of the subunit includes traces of quartz, together with minor clays that are most likely smectitic (alteration products of volcanic glass). Fresh volcanic glass shards are minor constituents along with zeolites, feldspar, opaque minerals, and pyrite. Carbonate contents in Subunit IVB range from 75% to 90% (Fig. 14).

Subunit IVB also contains common volcanic ash layers and dispersed ash zones. The layers are gray to greenish gray to dark gray, with sharp basal contacts and bioturbated tops. Most layers are less than 10 cm thick and contain abundant altered volcanic glass with minor amounts of phenocryst phases such as feldspar, biotite, and Fe-Ti oxides. Fresh glass is also present in amounts that vary from trace to over 90%. Dispersed, bioturbated ash zones also occur within Subunit IVB. They consist of continuous to discontinuous bands of gray to dark gray ash with bioturbated basal and upper contacts. Most are less than a few centimeters in thickness. A small chert nodule occurs in Core 165-999B-16R.

Subunit IVC

Intervals: Sections 165-999B-21R-2, 100 cm, through 39R-3, 55 cm

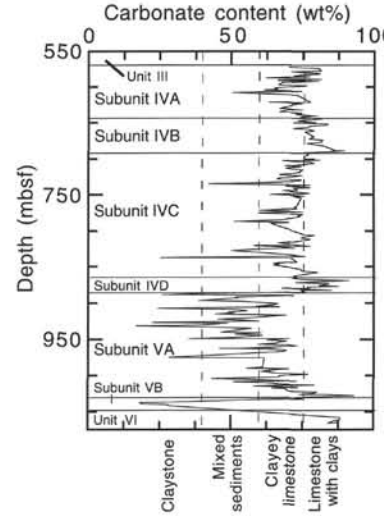

Figure 14. Downcore variation in carbonate content within lithologic Units III, IV, V, and VI.

Age: early Oligocene to middle Eocene
Depth: 690.4–866.2 mbsf

Subunit IVC consists of thick-bedded light greenish gray clayey calcareous limestone with abundant thin- to-medium-bedded dark gray volcanic ash layers. It is distinguished from Subunit IVB by the much greater abundance and thickness of ash layers, and a change in the amount of clay in the limestone. In some core sections, volcanic ash constitutes a major lithology. The clayey calcareous limestone is similar to that found in Subunit IVA and is slightly to moderately bioturbated with flattened burrows.

The major constituents of the clayey calcareous limestone include nannofossils, foraminifers, abundant silt-sized carbonate fragments, and clay. Identification of microfossils in smear slides is more difficult in this subunit because of the greater degree of lithification. Volcanic glass shards and their alteration products (smectitic clay) remain as minor constituents along with feldspar, opaque minerals, and traces of pyrite. Opal CT is present within this subunit, from its upper boundary to approximately 835 mbsf. From this depth to the lower boundary of the subunit, quartz is observed in the sediments. Its relative abundance increases very rapidly to levels far in excess of those observed uphole. Also at this depth, there appears to be a slow, but steady downhole increase in relative clay abundance (Fig. 7).

Carbonate contents in Subunit IVC range from 25% to 81%, but with the majority falling between 50% and 80% (Fig. 14). Compared with Subunit IVB, the majority of the carbonate values in Subunit IVC are lower. The drop in carbonate content in this subunit correlates with the occurrence of abundant ash layers. Shipboard sampling avoided discrete ash layers for carbonate sampling, but the high frequency of ash layers in many cores is likely to have contributed substantial bioturbated ash into the background sediment. Geochemical modeling confirms a relatively high (up to 30%) content of volcanic ash (see "Inorganic Geochemistry" section, this chapter).

A distinguishing feature of Subunit IVC is the very large number of volcanic ash layers and dispersed ash zones that are interbedded with calcareous limestone (see "Igneous Petrology and Volcanology" section, this chapter). The maximum number of ash layers per core occurs in Core 165-999B-33R, where 39 ash fall layers were identified. The layers are gray to greenish gray to dark gray, with sharp basal contacts and bioturbated tops (Fig. 15). Most layers are less than 15 cm thick, but Core 165-999B-38R has a layer that is 32 cm thick. As in Subunits IVA and IVB, the major constituents of the ash layers include abundant altered volcanic glass with minor amounts of phenocryst phases such as feldspar, biotite, and opaque minerals. Fresh glass is also present in amounts that vary from trace to over 90%. Dispersed, bioturbated ash zones are also common within Subunit IVB. They consist of continuous to discontinuous bands of gray to dark gray ash with bioturbated basal and upper contacts. Most are less than a few centimeters in thickness.

A relatively minor lithology of Subunit IVC is dark green claystone. Thin beds, usually less than 10 cm thick, occur in Cores 165-999B-31R and 34R. In Core 165-999B-31R, the claystone has a fissile structure and is very friable. Portions of the core with this lithology are typically eroded by the drilling process and consequently are of smaller diameter than the more lithified enclosing sediments.

In Core 165-999B-28R, there is a zone of incipient silicification. This zone is about 3 cm thick and has an irregular shape with smooth edges. It is highly lithified and translucent.

Subunit IVD

Intervals: Sections 165-999B-39R-3, 55 cm, through 42R-1, 50 cm
Age: middle Eocene
Depth: 866.2–887.0 mbsf

Sediments in Subunit IVD consist predominantly of thick-bedded calcareous limestone with clay interbedded with common thin-bedded volcanic ash layers. This subunit is distinguished from Subunit

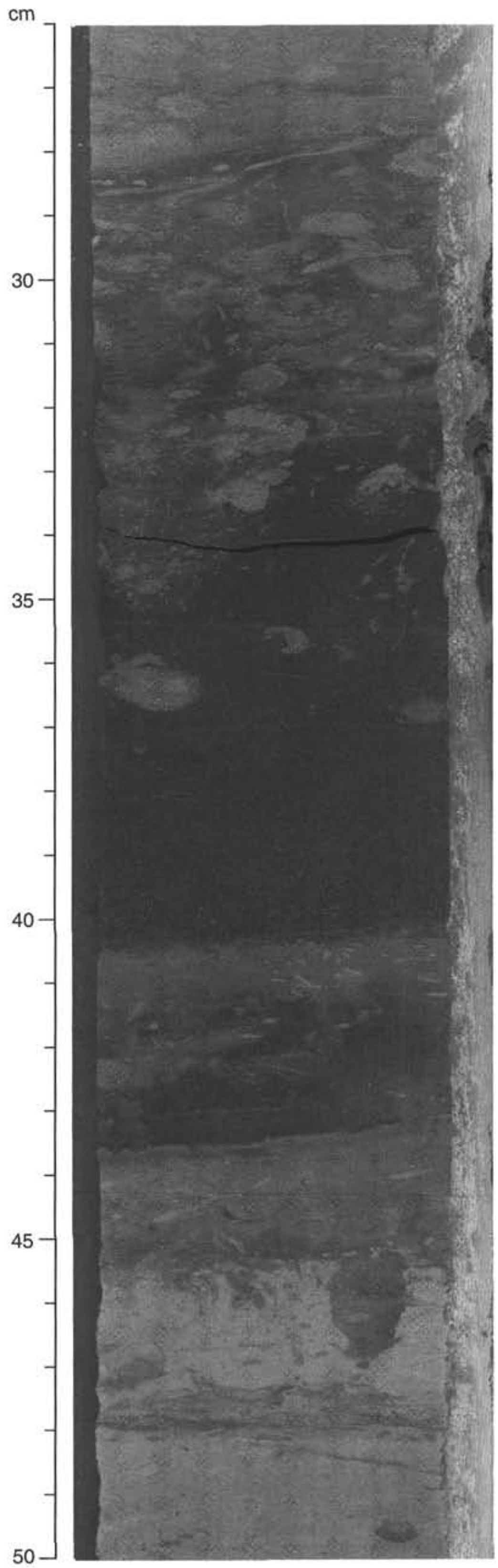

Figure 15. Pair of dark gray volcanic ash fall layers in lithologic Subunit IVC (Section 165-999B-26R-1, 26–50 cm). Note the sharp basal contacts and bioturbated tops of each layer.

IVC by a significant reduction in the frequency and thickness of volcanic ash layers and by an increase in the carbonate content of the limestone. Bioturbation ranges from slight to moderate, and most burrows are flattened as a result of compaction. As in Subunit IVC, wispy laminations are common.

The major biogenic constituents of the calcareous limestone with clay are small carbonate fragments, nannofossils, and foraminifers. In terms of bulk mineralogy, Subunit IVD resembles Subunit IVC (Table 2). Fresh volcanic glass shards are minor constituents along with feldspar, opaque minerals, and pyrite. Carbonate contents in Subunit IVD range from 41% to 91%, with the majority falling between 68% and 85% (Fig. 14).

Unit V

Intervals: Sections 165-999B-42R-1, 50 cm, to 59R-CC, 5 cm
Age: middle Eocene to early Paleocene
Depth: 887.0–1049.3 mbsf

Unit V at Site 999 consists of lithologies that range in composition from clayey calcareous limestone to nearly pure claystone as end-members. It ranges in age from middle Eocene to early Paleocene. The upper boundary of Unit V is defined by the downhole transition from clayey calcareous limestone into clayey calcareous mixed sedimentary rock, with carbonate contents down to 25% (Fig. 14). The upper boundary coincides with a transitional downhole rise in magnetic susceptibility values and with an abrupt shift in the reflectance values at the green (550 nm) wavelength (Fig. 6). The lower boundary is defined by the downhole transition from claystone into clayey calcareous limestone, denoted by a sharp decrease in magnetic susceptibility and a decrease in the reflectance values at the green (550 nm) wavelength (Fig. 6).

Unit V is divided into two subunits (VA and VB), based upon variations in carbonate contents, as well as upon distinct patterns in magnetic susceptibility and color reflectance data (Fig. 6).

Subunit VA

Intervals: Sections 165-999B-42R-1, 50 cm, to 57R-5, 110 cm
Age: middle Eocene to early Paleocene
Depth: 887.0–1033.4 mbsf

The major lithology identified in Subunit VA is clayey calcareous mixed sedimentary rock interbedded with minor foraminifer- and radiolarian-rich layers and volcanic ash layers. The clayey calcareous mixed sedimentary rock is well lithified, homogenous, and slightly to moderately bioturbated light greenish gray to dark greenish gray clay interlayered with thin intervals of claystone and clayey calcareous limestones. Claystone layers often display wispy laminations (Fig. 16). Carbonate contents vary from 38% to 82%, and tend to shift toward higher values downhole (Fig. 14). Within this subunit, a distinctive mineral assemblage is recognized below the radiolarian-rich layers (see below), composed of feldspar, quartz, and an interstratified smectite(?). The relative abundance of clays decreases up the sequence (Fig. 7).

Foraminifer- and radiolarian-rich layers are characterized by distinctive sandy textures and range in thickness from 1 to 13 cm. Both their upper and lower boundaries are characterized by an abrupt grain-size change, but they are not erosive. Often a less than 1-cm-thick, clay-rich interval bounds both the top and base of the sandy layers. Smear-slide data indicate that the sandy layers consist of a mixture of foraminifers, radiolarians, crystalline carbonate grains, and clay minerals. The above sedimentological observations indicate that they are not redeposited turbidite events, but rather that they were probably formed by intensified winnowing conditions and/or by an increased flux of foraminifers and radiolarians to the sediment. These sand-rich layers have been observed in the interval between 910 and 1065 mbsf, and are most abundant between 920 and 1010 mbsf (Fig. 17). The relative abundance of radiolarians vs. foraminifers decreases downhole, as foraminifers become the major components of the layers in the lower part of Subunit VA. However, more radiolarians are likely to occur dispersed within the background sediment. The occurrence of these radiolarian-rich layers also correlates with a peak in the relative abundance of quartz, as determined from XRD analysis (Fig. 7). This quartz peak immediately follows the disappearance of opal-CT (Table 2).

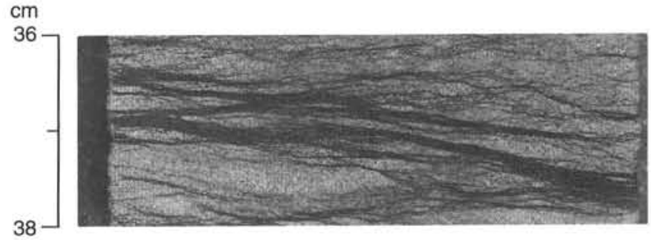

Figure 16. Wispy claystone laminations in lithologic Subunit VA (Section 165-999B-57R-1, 36–38 cm).

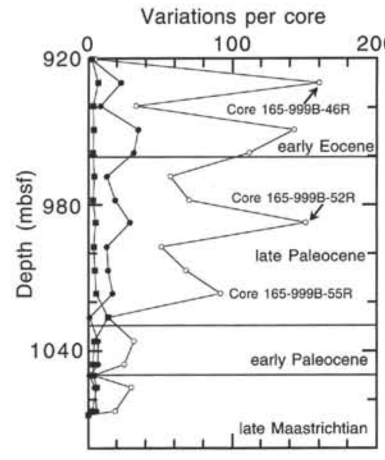

Figure 17. Downhole variations per core in the number (solid circles), thickness (open circles, cm), and average thickness (solid squares, cm) of foraminifer- and radiolarian-rich sandy layers in lithologic Unit V.

A number of intervals with carbonate contents less than 40% occurs in the upper part of Subunit VA and coincides with high magnetic susceptibility values (Fig. 18). These could reflect either higher volcanic ash or radiolarian contents. In general, samples for carbonate content measurements were chosen in background lithologies, and ash layers were avoided. However, these low values could reflect dispersed ash within background sediment. Data on the accumulation rates of volcanic ash (Fig. 7) show that one of the major peaks of ash accumulation spans the interval between the middle and the upper Eocene, suggesting that if the low carbonate values occurring at the top of Subunit VA were related to dispersed ash, we should expect to see the same patterns also in Unit IV. However, this relationship is not observed. Comparison of carbonate data with physical properties parameters, such as porosity and wet-bulk density (Fig. 19), shows that the lower carbonate content values between 887 and 950 mbsf coincide with increased porosity and lowered wet-bulk density values. By analogy with results for Hole 999A (Fig. 8), this relationship is interpreted to reflect higher contents of biogenic silica within the background sediment.

Another distinctive feature observed in Subunit VA is a claystone interval, occurring in Section 165-999B-51R-5, 70–135 cm (Fig. 20).

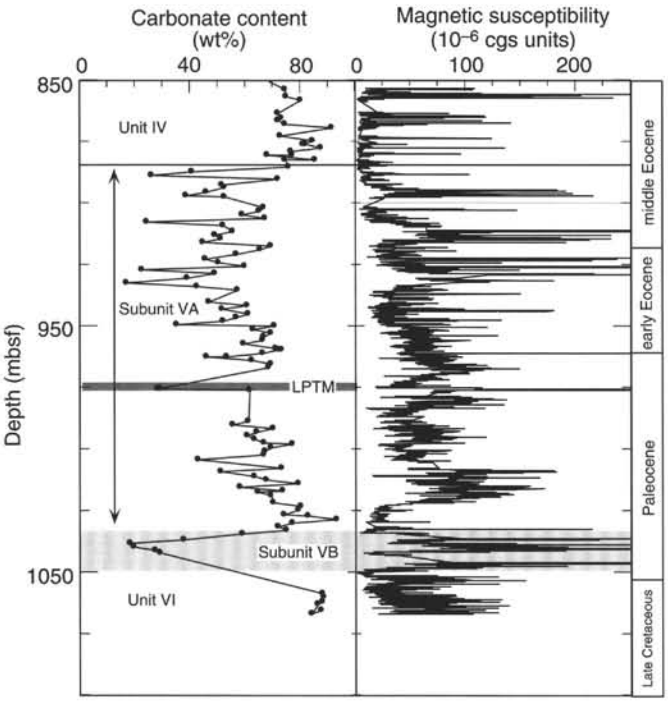

Figure 18. Downcore variations in carbonate content (solid circles) and magnetic susceptibility (solid line) data within lithologic Units IV, V, and VI. LPTM refers to the late Paleocene thermal maximum (see text for further details). Magnetic susceptibility data obtained using the multisensor track (MST).

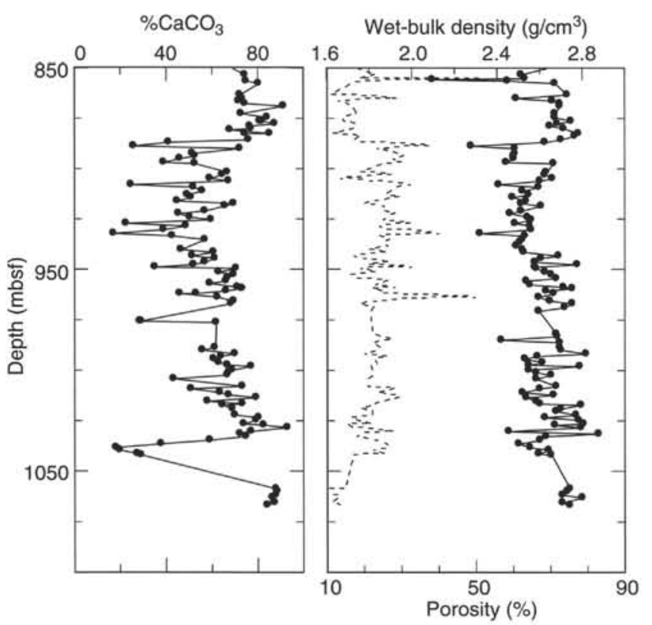

Figure 19. Comparison of %CaCO$_3$, porosity (dashed line), and wet-bulk density (solid line) data for the lower part of Hole 999B.

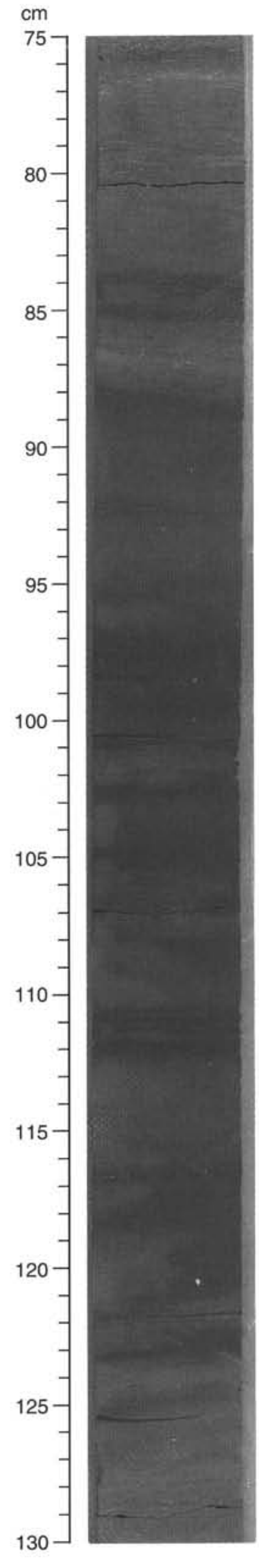

Figure 20. Core photograph showing the claystone interval in Section 165-999B-51R-5, 75–130 cm, defined as the late Paleocene thermal maximum (LPTM).

The spacing of samples for carbonate data is too low to show the extent of this event on the carbonate content curve. However, its boundaries have been indicated in Figure 20. Biostratigraphic data indicate that this event falls within the late Paleocene (see "Discussion," this section).

Volcanic ash layers also occur as a minor lithology in Subunit VB. They are very thin- to medium-bedded layers and can be recognized by their greenish to gray color and distinctive lithology. Within the subunit, they occur (1) as discrete layers with sharp bases and tops, (2) as discrete layers with sharp bases and transitional bioturbated tops, or (3) as bioturbated but visible patches of dispersed ash in the background sediment, reworked together with carbonate grains.

Subunit VB

Intervals: Sections 165-999B-57R-5, 110 cm, to 59R-CC, 5 cm
Age: early Paleocene
Depth: 1033.4–1049.3 mbsf

The lithologies identified in Subunit VA are predominantly clayey nannofossil mixed sedimentary rock and claystone with interbedded volcanic ash layers. The boundary between Subunits VA and VB is marked by a decrease in carbonate content and by an increase in the magnetic susceptibility and color reflectance values at the green (550 nm) wavelength. Subunit VB is characterized overall by low carbonate contents, ranging from 18% to 59%, and by high magnetic susceptibility values (Fig. 18). The major lithologies consist of well-lithified, homogenous and slightly to moderately bioturbated, light greenish gray to dark greenish gray clayey calcareous mixed sedimentary rock interbedded at the decimeter-scale with claystones. Bands of darker color coincide with claystone layers and are typically 1–3 cm thick.

Volcanic ash layers occur as a minor lithology in Subunit VB. They are characterized by their distinctive lithology and their greenish to gray color. They occur mainly as discrete layers with sharp bases and transitional bioturbated tops, and as bioturbated patches of ash dispersed in the background sediment by bioturbation.

Unit VI

Intervals: Sections 165-999B-59R-CC, 5 cm, to 62R-CC, 30 cm
Age: earliest Paleocene to late Maastrichtian
Depth: 1049.3–1066.4 mbsf

Lithologic Unit VI at Site 999 consists of calcareous limestone with clay, characterized by some of the highest values of carbonate content (84%–88%) observed in Site 999. It ranges in age from earliest Paleocene to late Maastrichtian and includes a K/T boundary interval. The upper boundary of Unit VI is defined by the occurrence of a 21-cm-thick bed of very hard, light gray limestone with some clay that spans the interval between Sections 165-999B-59R-CC, 5 cm, and 60R-1, 10 cm (Fig. 21). This limestone bed corresponds to earliest Paleocene lithology overlying Late Cretaceous limestone with clay and forms a critical part of the K/T boundary sequence at Site 999. Unit VI extends down to the bottom of Hole 999B and is 16.4 m in thickness.

The majority of Unit VI consists of massive, hard, light greenish gray to light gray calcareous limestone with clay, characterized by weak bioturbation and frequent subhorizontal wispy laminations. These limestones are interbedded with numerous, dark gray to greenish gray clay-rich layers, usually marked by sharp lower and upper boundaries. These layers are a few centimeters thick, and one is rich in altered volcanic ash. However, unlike other discrete volcanic ash fall layers, these layers often lack very sharp bases and bioturbated tops. They also contain higher proportions of carbonate compared with altered ash layers from younger units. As in Unit V, the limestones are also interbedded with several centimeter-thick coarser

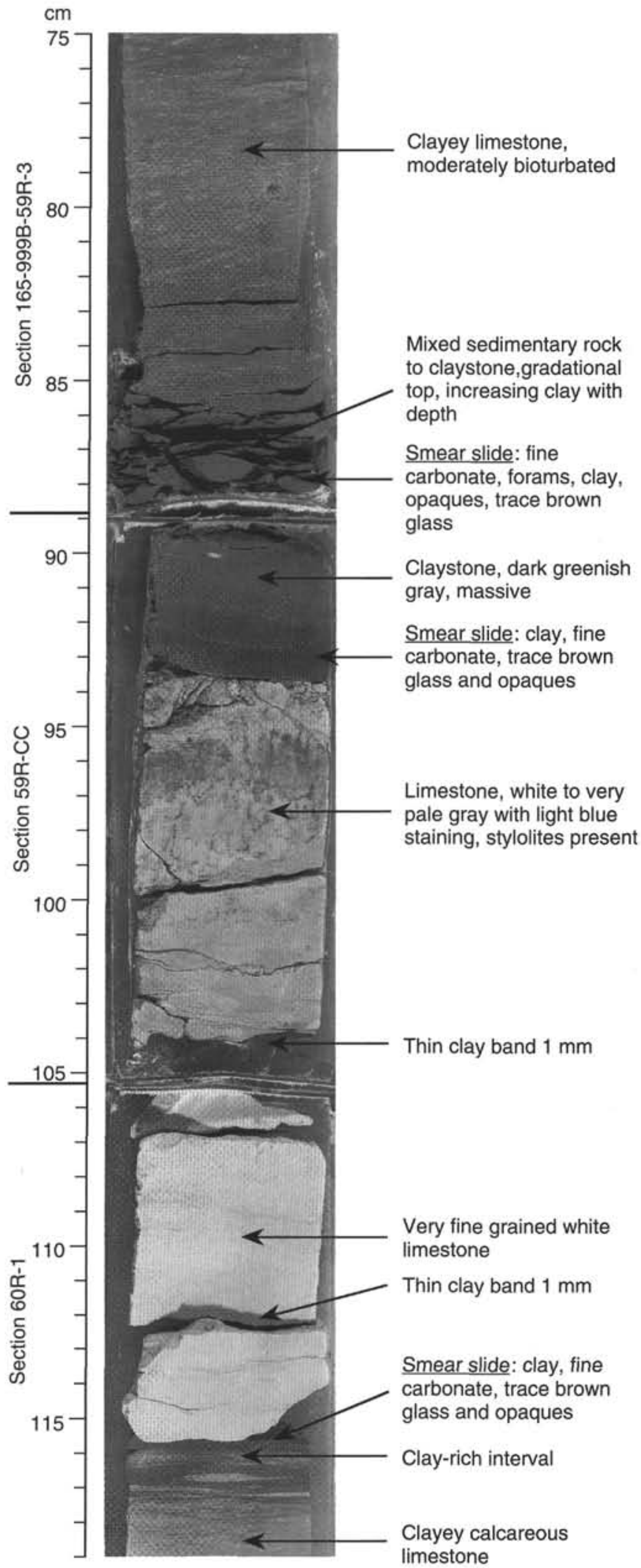

Figure 21. Composite core photograph of the K/T boundary interval in Hole 999B (Section 165-999B-59R-3, 75–119 cm).

greenish gray intervals rich in recrystallized foraminifers and radiolarians.

Cretaceous/Tertiary Boundary Sequence

Shipboard biostratigraphical studies indicate that the K/T boundary lies within the uppermost part of Unit VI in Section 165-999B-60R-1, between 1 and 21 cm. Figure 21 shows a composite core photograph of the basal portion of Section 165-999B-59R-3, the core catcher of Core 165-999B-59R, and the top of Section 165-999B-60R-1, which encompasses the interval around the boundary. A clayey calcareous limestone of late Maastrichtian age occurs at the base. This limestone is very well indurated and is light greenish gray in color; it has wispy green laminations and is slightly bioturbated. Moving up the section, there is a gradational transition into a clayey mixed sedimentary rock that is greenish gray and exhibits compacted burrows. Above this point, the core is broken and there is an abrupt change to very light gray massive limestone in the top of Section 165-999B-60R-1 (three pieces; Fig. 21). This limestone is quite distinctive from any limestones observed within Unit VI or the overlying Unit V. At the base of the lower piece is a thin, 4-mm-thick, gray claystone. A smear slide of this material indicates that it consists of abundant clay, fine carbonate grains, and trace amounts of brown glass and opaque minerals. Another thin, ~1-mm-thick claystone band occurs between the basal and middle limestone pieces. The upper piece of limestone is dated as earliest Paleocene.

At the base of Section 165-999B-59R-CC, the sediment begins with a thin discontinuous claystone band that is approximately 1 mm thick. This band is in sharp contact with an overlying 10-cm-thick sequence of white to very pale gray limestone (Fig. 21). The upper part of the limestone is mottled with a light bluish gray staining and resembles a piece of "Roquefort blue cheese." This limestone has also been dated as earliest Paleocene. It is in sharp contact with a dark greenish gray massive claystone above. This claystone is darker at its base and exhibits some faint parallel laminations. A smear slide of the claystone indicates that it consists of abundant clay, fine carbonate grains, and trace amounts of brown glass and opaque minerals. The contact between this claystone and the pale gray limestone below marks the boundary between Units V and VI.

In Section 165-999B-59R-3, the claystone continues and is in gradational contact with an overlying interval of well-indurated greenish gray clayey limestone (Fig. 21). A smear slide from the claystone at the base of Section 165-999B-59R-3 indicates the presence of abundant clay, fine carbonate grains, foraminifers, and trace amounts of brown glass and opaque minerals.

Discussion

Drilling at Site 999 penetrated 1066.4 m of a section extending from the Pleistocene to the upper Maastrichtian. The oldest material collected is approximately 66–67 Ma and consists of massive limestone with clay, representing deep-water pelagic deposition at this site. Within these limestones are numerous thin intervals of carbonate-bearing claystones that contain some altered volcaniclastic material. These layers appear to differ from altered volcanic ash fall layers in the nature of their contacts with surrounding sediment, the abundance of carbonate, and the presence of bifurcating structures. Magnetic susceptibility records of cores containing these carbonate-bearing claystones indicate a marked periodicity in their distribution, and they are likely to represent Milankovitch-driven oscillations in carbonate dissolution similar to those observed below the K/T boundary at DSDP Site 146 (King and D'Hondt, unpubl. data, 1996).

The K/T boundary occurs within Unit VI and represents an abrupt transition to the deposition of a thin (21 cm), distinctive, very light gray limestone with a blue-gray mottling. Formation MicroScanner logs across the boundary, coupled with magnetic susceptibility records of recovered cores, suggest that several centimeters of a boundary deposit may be unaccounted for, but it is unlikely that a thick boundary deposit, in excess of 10 cm, was not recovered by drilling. This deposit may be associated with a short-term oceanographic response to the proposed impact of a large bolide with the Earth (see "Summary and Conclusions" section, this chapter).

Following deposition of the light gray limestone sequence, there was an abrupt transition to the deposition of relatively carbonate-poor sediments in the earliest Paleocene (Subunit VB). Deposition of progressively more carbonate-rich sediment took place over about 2–4 m.y., but was then followed by an extended period throughout the rest of the Paleocene and into the middle Eocene when carbonate content gradually decreased (Subunit VA; Fig. 18). A short interval of decreased carbonate deposition resulted in the deposition of a thin claystone layer in the latest Paleocene. The timing of this event suggests a possible correlation with the dramatic short-term paleoenvironmental phenomenon observed at Hole 690B, on the Maud Rise in the Southern Ocean, coinciding with benthic foraminifer extinction (Thomas, 1990) and abrupt carbon and oxygen isotope excursions (Kennett and Stott, 1991). This event has been interpreted to reflect an abrupt, short-term warming event, and has been referred to as the late Paleocene thermal maximum (LPTM; Zachos et al., 1993). A similar event has been described at ODP Site 865 on Allison Guyot in the equatorial Pacific where the benthic extinction was found synchronous with the carbon excursion (Bralower et al., 1995). However, at that Pacific location, planktonic foraminifer oxygen isotope values do not record any change, suggesting that as the deep oceans and high-latitude surface waters rapidly warmed, low-latitude surface temperatures remained more or less constant (Kennett and Stott, 1991).

During the time interval between the late Paleocene and the early Eocene, there was also another distinctive type of facies deposited at Site 999. Pelagic mixed sedimentary rocks and limestones are found to be interbedded with numerous thin (centimeter-scale), foraminifer- and radiolarian-rich sand layers with relatively sharp upper and lower contacts (Fig. 17). These layers are interpreted to represent the winnowing of bottom sediments by deep current activity. Formation of this feature may have been facilitated by the existence of a deep passage linking the Pacific and Caribbean areas and the existence of enhanced bottom currents during this time.

In the middle Eocene, the facies at Site 999 shifted rather abruptly from mixed sedimentary rock to clayey limestone (Unit IV). The occurrence of foraminifer- and radiolarian-rich layers greatly diminished and was replaced by the beginning of a massive influx of volcaniclastic material by ash fallout from explosive eruptions to the west of the site. These changes most likely represent the initiation of intense subduction-related volcanism in the Central American region and may have been associated with the restriction of deep circulation between the Pacific and Caribbean areas by uplift and volcanic activity along the southern margins of the subduction complex.

From the middle Eocene to the middle Miocene, pelagic deposition of carbonate sediment (Units III and IV) was superimposed by volcanic ash deposition in two major pulses, culminating in the latest Eocene and late early Miocene to early middle Miocene (see "Igneous Petrology and Volcanology" section, this chapter). This activity led to the formation of hundreds of discrete ash fall layers ranging in thickness from less than 1 cm to as much as 32 cm.

As the middle Miocene pulse of explosive volcanism waned, volcanic ash fall deposition greatly decreased and an interval of siliceous clayey mixed sediment was deposited (Subunit IIB). The appearance of siliceous components in the sediment may reflect enhanced preservation resulting from increased silica contents in sediment pore waters associated with the great abundance of buried silicic ash layers (see "Inorganic Geochemistry" section, this chapter).

At a level approximating the middle to late Miocene boundary interval, sediments at Site 999 record a pronounced decrease in carbonate deposition that correlates to the carbonate crash previously documented at Site 998 on the Cayman Rise. A substantial reduction in carbonate accumulation rates (see "Sedimentation Rates" section, this chapter) and the poor preservation of calcareous microfossils in smear slides and washed paleontology samples suggest that carbonate dissolution and a shoaling of the lysocline and CCD are responsible for the observed patterns. An effort was made at Site 999 to generate additional shipboard carbonate data and to refine biostratigraphic age determinations in this interval. Figure 12 shows the resulting carbonate data plotted for comparison with magnetic susceptibility data using the refined stratigraphic framework. The initial abrupt drop in carbonate content used to identify the boundary between lithologic Subunits IIA and IIB occurs within calcareous nannofossil Zone CN5 and is matched by an increase in magnetic susceptibility, though of lesser relative magnitude. Low carbonate values (<20%) persist until somewhere after 10.5 Ma in a pattern directly comparable to that found at Site 998 (Fig. 13). Further shore-based studies of this interval, and comparisons with sites elsewhere that record this profound change in the carbonate system (e.g., Leg 138 sites in the eastern equatorial Pacific; Lyle et al., 1995), should help to identify the origins of the middle/late Miocene carbonate crash.

From the late Miocene to the present, the sediments at Site 999 indicate that deposition remained predominantly pelagic with occasional influxes of volcaniclastic material by fallout from explosive eruptions. However, throughout this interval there is a progressive increase in the amount of quartz being deposited (Fig. 7). Associated with the increase is a change in the clay mineral assemblage from one dominated by smectitic clays to one containing smectite, with lesser quantities of chlorite, kaolinite, and illite. These shifts indicate an increase in the terrigenous flux to the site that may be associated with the development of the Magdalena submarine fan.

BIOSTRATIGRAPHY

Calcareous Nannofossils

We prepared standard smear slides in every core section recovered, but concentrated on determining standard nannofossil datums (see Table 2 in "Explanatory Notes" chapter, this volume) as precisely as possible. The theoretical depth uncertainty for datums is about 1.5 m throughout Holes 999A and 999B. However, the actual uncertainty increases significantly as preservation deteriorates in the lower part of the section. Approximately 750 slides were examined to determine nannofossil datums and zonal boundaries of Okada and Bukry (1980) at Site 999 (Table 3; Figs. 83, 84).

Nannofossil preservation is good to excellent from the Pleistocene through the Pliocene (Cores 165-999A-1H to 15H), moderate in the upper Miocene (Cores 165-999A-16H to 31X), moderate to poor in the middle Miocene (Cores 165-999A-32X to 38X), and generally poor in the lower Miocene (Cores 165-999A-39X to 165-999B-9R). Abundance decreases significantly in intervals of the lower Miocene. Preservation in the Oligocene and upper Eocene (Cores 165-999B-9R to 29R) section is mostly poor and nannofossils are common to abundant. A noticeable deterioration in preservation and decrease in relative abundance is noted in the middle and lower Eocene (Cores 165-999B-29R to 50R) where nannofossils are rare, having been almost entirely replaced by micrite. An interval of slightly improved preservation and increased abundance was observed in the upper Paleocene (Cores 165-999B-51R to 56R). Preservation in the lower Paleocene sediments (Cores 165-999B-57R to 59R), however, is extremely poor and very few nannofossils were observed. A significant improvement in preservation and increase in abundance was observed in Maastrichtian sediments (Cores 165-999B-60R to 62R). In poorly preserved assemblages of all ages, specimens are heavily overgrown, moderately etched, and fragmented. We observed that preservation in the bioturbated upper parts of the middle and upper Eocene ash horizons was markedly superior, and nannofossil abundances are an order of a magnitude higher than they are in the surrounding limestones. This phenomenon likely results from buffering of bicarbonate in the ash horizons during the alteration of feldspars to smectite (for complete discussion, see "Inorganic Chemistry" section, this chapter). For this reason, samples were taken in the upper part of ash horizons wherever possible.

The tropical location of Site 999 resulted in a diverse nannofossil assemblage where preservation is good throughout the upper part of the Neogene section. The Neogene section was deposited at moderately high sedimentation rates (averaging 25 m/m.y.) and appears to be largely continuous. Sedimentation rates decline below the lower Miocene; however, the Paleogene and uppermost Cretaceous section also appear to be largely complete to within biostratigraphic resolution. Most of the Cenozoic zones and subzones of Okada and Bukry (1980) can be recognized (Table 3; Figs. 83, 84).

Pleistocene

A thick and continuous Pleistocene section was recovered from Hole 999A (Table 3). Sedimentation rates are over 30 m/m.y. All of the Pleistocene nannofossil zones and subzones can be defined in the uppermost part of Hole 999A (Table 3; Fig. 83). Most of the additional Pleistocene nannofossil datums of Takayama and Sato (1987) and Sato et al. (1991) can be detected also. *Reticulofenestra asanoi* was observed between Samples 165-999A-4H-4, 100 cm, and 4H-CC. Samples 165-999A-5H-4, 100 cm, through 6H-4, 100 cm, contain large *Gephyrocapsa* specimens. The LO of *Helicosphaera sellii* is placed between Samples 165-999A-5H-7, 30 cm, and 5H-CC.

Pliocene

The Pliocene/Pleistocene boundary, which lies close to the boundary of Subzones CN13b/CN13a at the FO of *Gephyrocapsa caribbeanica,* is placed between Samples 165-999A-7H-1, 100 cm, and 7H-2, 100 cm. This corresponds to the base of medium-sized (>4 µm) *Gephyrocapsa* defined by Raffi et al. (1993). Pliocene sedimentation rates are variable but average about 30 m/m.y. All of the Pliocene zones and subzones of Okada and Bukry (1980) can be accurately defined at Site 999 (Table 3; Fig. 83).

Miocene

The Miocene/Pliocene boundary is approximated to lie between the LO of *Discoaster quinqueramus* and the FO of *Ceratolithus acutus* between Samples 165-999A-18H-7, 30 cm, and 18H-2, 100 cm. Sedimentation rates in the Miocene average about 22 m/m.y., but they decrease in the interval surrounding the carbonate crash in the upper part of Zones CN5 and CN6. Most of the zones and subzones of Okada and Bukry (1980) can be delineated (Table 3; Fig. 83) with the following exceptions. We did not observe *Discoaster loeblichii,* the FO of which defines the base of Subzone CN8b, and therefore cannot divide Subzones CN8a and CN8b in Hole 999A. This marker is also rare in sediments from the Ceara Rise (Curry, Shackleton, Richter, et al., 1995). The base of Subzone CN5b cannot be precisely determined because of the rarity of the marker taxon, *Discoaster kugleri.* Samples 165-999A-30X-5, 100 cm, down to 37X-5, 100 cm, therefore, are placed in Zone CN5 based on the absence of *Catinaster coalitus* and *Sphenolithus heteromorphus. Helicosphaera ampliaperta,* the LO of which defines the base of Zone CN4, is observed below Sample 165-999A-39X-CC in Hole 999A. *Discoaster druggii,* the FO of which defines the boundary between Subzones CN1c and CN1b, is difficult to identify because common overgrowth in the lower Miocene interval tends to obscure specimens of *Discoaster.* Although *Cyclicargolithus abisectus* is observed in the lower Mio-

Table 3. Nannofossil datums, absolute ages, and depths at Site 999.

Event	Zone (base)	Age (Ma)	Core, section, interval (cm)	Depth (mbsf)
Hole 999A:				
B *Emiliania huxleyi*	CN15	0.248	2H-1, 100 to 2H-2, 100	9.35
T *Pseudoemiliania lacunosa*	CN14b	0.408	2H-7, 30 to 2H-CC	17.20
T *Reticulofenestra asanoi*		0.88	4H-3, 100 to 4H-4, 100	31.35
B *Gephyrocapsa parallela*	CN14a	0.94	4H-6, 100 to 4H-7, 30	35.50
B *Reticulofenestra asanoi*		1.17	4H-CC to 5H-1, 100	36.70
T Large *Gephyrocapsa* spp.		1.23	5H-3, 100 to 5H-4, 100	40.85
T *Helicosphaera sellii*		1.26	5H-7, 30 to 5H-CC	45.55
B Large *Gephyrocapsa* spp.		1.48	6H-4, 100 to 6H-5, 100	51.85
B *Gephyrocapsa oceanica*		1.64	6H-CC to 7H-1, 100	55.65
T *Calcidiscus macintyrei*		1.64	6H-CC to 7H-1, 100	55.65
B *Gephyrocapsa caribbeanica*	CN13b	1.71	7H-1, 100 to 7H-2, 100	56.85
T *Discoaster brouweri*	CN13a	1.95	7H-CC to 8H-1, 100	65.20
T *Discoaster pentaradiatus*	CN12d	2.36	9H-4, 100 to 9H-5, 100	81.85
T *Discoaster surculus*	CN12c	2.51	10H-1, 100 to 10H-2, 100	85.35
T *Discoaster tamalis*	CN12b	2.82	11H-1, 100 to 11H-2, 100	94.85
T *Sphenolithus* spp.		3.62	13H-1, 100 to 13H-2, 100	113.85
T *R. pseudoumbilicus*	CN12a	3.83	13H-6, 100 to 13H-7, 30	121.00
T *Amaurolithus* spp.	CN11	4.50	16H-6, 100 to 16H-7, 10	149.40
B *Ceratolithus rugosus*	CN10c	5.046	16H-CC to 17H-1, 100	150.80
T *Ceratolithus acutus*		5.046	17H-5, 100 to 17H-6, 100	157.85
B *Ceratolithus acutus*	CN10b	5.089	18H-2, 100 to 18H-3, 100	162.85
T *Discoaster quinqueramus*	CN10a	5.537	18H-6, 100 to 18H-7, 30	168.53
B *Amaurolithus* spp.	CN9b	7.392	22X-1, 100 to 22X-2, 100	199.85
B *Discoaster berggrenii*	CN9a	8.281	26X-3, 100 to 26X-4, 100	234.25
T *Discoaster hamatus*	CN8a	9.635	28X-3, 100 to 28X-4, 100	253.45
B *Discoaster hamatus*	CN7	10.476	29X-CC to 30X-1, 100	268.64
B *Catinaster coalitus*	CN6	10.794	30X-4, 100 to 30X-5, 100	274.25
T *Cyclicargolithus floridanus*		13.23	35X-7, 20 to 35X-CC	325.40
T *Sphenolithus heteromorphus*	CN5a	13.523	37X-5, 100 to 37X-6, 100	342.95
T *Helicosphaera ampliaperta*	CN4	15.6	39X-7, 30 to 39X-CC	363.97
B *Sphenolithus heteromorphus*	CN3	18.2	48X-CC to 49X-1, 100	451.30
T *Sphenolithus belemnos*		18.3	49X-3, 100 to 49X-4, 30	454.95
B *Sphenolithus belemnos*	CN2	19.2	51X-CC to 52X-1, 100	480.10
T *Reticulofenestra bisecta*	CN1a	23.9	Below base of section	
Hole 999B:				
T *Reticulofenestra bisecta*	CN1a	23.9	10R-CC to 11R-1, 92	617.08
T *Sphenolithus ciperoensis*		25.5	11R-1, 92 to 11R-2, 122	622.26
T *Sphenolithus distentus*	CP19b	27.5	14R-4, 106 to 14R-5, 25	654.42
B *Sphenolithus ciperoensis*	CP19a	29.9	18R-CC to 19R-1, 21	680.26
B *Sphenolithus distentus*	CP18	31.5	21R-CC to 22R-1, 15	697.37
T *Reticulofenestra umbilicus*	CP17	32.3	23R-4, 18 to 23R-5, 85	712.97
T *Ericsonia formosa*	CP16c	32.8	23R-CC to 24R-1, 39	716.36
T *Discoaster saipanensis*	CP16a	34.2	25R-4, 100 to 25R-5, 46	731.18
T *Discoaster barbadiensis*	CP16a	34.3	25R-5, 100 to 25R-6, 53	732.71
T *Chiasmolithus grandis*	CP15	37.1	29R-5, 59 to 29R-CC	773.1
B *Reticulofenestra bisecta*		38.0	31R-3, 11 to 31R-4, 18	788.54
T *Chiasmolithus solitus*	CP14b	40.4	30R-CC to 31R-1, 130	783.91
B *Reticulofenestra umbilicus*	CP14a	43.7	35R-3, 36 to 35R-CC	828.24
T *Chiasmolithus gigas*	CP13c	44.5	36R-4, 10 to 36R-CC	838.52
B *Chiasmolithus gigas*	CP13b	46.1	39R-1, 140 to 39R-2, 68	864.39
B *Discoaster sublodoensis*	CP12	49.7	45R-5, 18 to 45R-CC	918.44
B *Discoaster lodoensis*	CP10	52.0	48R-CC to 49R-1, 130	949.89
T *Fasciculithus tympaniformis*		55.3	51R-2, 119 to 51R-3, 118	971.84
B *Discoaster multiradiatus*	CP8	56.2	54R-2, 112 to 54R-3, 119	1000.81
B *Discoaster mohleri*	CP6	57.5	54R-4, 17 to 54R-4, 125	1002.61
B *Heliolithus kleinpellii*	CP5	58.4	55R-1, 110 to 55R-2, 126	1009.03
B *Fasciculithus tympaniformis*	CP4	59.7	56R-CC to 57R-1, 26	1026.53
B *Fasciculithus* spp.		59.9	57R-2, 102 to 57R-3, 60	1029.36
B *Sphenolithus primus*		60.6	57R-2, 102 to 57R-3, 60	1029.36
B *Sullivania danica*	CP2	63.8	58R-CC to 59R-1, 110	1044.70
T Cretaceous spp.	CP1a	65.0	59R-CC to 60R-1, 10	1049.81
B *Micula murus*		66.2	Below base of section	

Notes: T = top of species range (last appearance datum), B = base of species range (first appearance datum). This entire table also appears on CD-ROM (back pocket).

cene section, poor preservation prevents changes in the abundance of this species from being observed clearly. Thus, the boundary between Subzones CN1a and CN1b cannot be delineated.

Oligocene

The Oligocene section was deposited at markedly lower rates (~13 m/m.y.) than the overlying Neogene; nevertheless, preliminary observations suggest that the section is largely complete. Some uncertainty exists in the placement of the Oligocene/Miocene boundary in Hole 999B based on nannofossils. This boundary has been correlated with the LOs of *Reticulofenestra bisecta* and *Sphenolithus ciperoensis* (e.g., Perch-Nielsen, 1985). These events are separated by 1.6 m.y. in Berggren et al. (1995), but only by a few meters at Sites 998 and 999. In most low-latitude sites, the LO of *S. ciperoensis* is used to approximate the boundary (e.g., Curry, Shackleton, Richter, et al., 1995). We use the LO of *R. bisecta* because it lies closer to the FO of the planktonic foraminifer, *Paragloborotalia kugleri,* which lies between Samples 165-999B-8R-CC and 9R-CC, and is traditionally used to define the Oligocene/Miocene boundary. As at Site 998, we note that *Reticulofenestra bisecta* is considerably smaller in the uppermost part of its range than the standard size of this species (at least 10 µm in most definitions). The LO of *Zygrhablithus bijugatus* was found to lie between Samples 165-999B-11H-4, 122–123 cm, and 11H-5, 66–68 cm. We did not observe any *Sphenolithus delphix* at Site 999, probably as a result of poor preservation. Subdivision of the Oligocene proved to be somewhat problematic as we had difficulty distinguishing consistently between *Sphenolithus ciperoensis, S. distentus,* and *S. predistentus,* which are the major Oligocene zonal markers (Table 3; Fig. 83). As in numerous other studies (e.g., Aubry, 1989; Curry, Shackleton, Richter, et al., 1995), considerable overlap exists between these species, and we also observed many transitional specimens in Hole 999B. Thus, although we applied the guidelines proposed by Aubry (1989) and these datums are consistent with Site 998, they may be difficult to correlate with other sequences. We did not observe a pronounced acme of *Ericsonia subdisticha* and therefore could not determine the boundary between Subzones CP16a and CP16b.

Eocene

Sedimentation rates in the Eocene are variable but average about 10 m/m.y. Several datums lie in the Eocene/Oligocene boundary interval. The LOs of *Reticulofenestra umbilicus, Ericsonia formosa,* and *Discoaster barbadiensis* have been determined with confidence (Table 3). We are less confident about the placement of the LO of *D. saipanensis* due to overgrowth. However, the Eocene/Oligocene boundary lies between the LOs of *D. barbadiensis* and *E. formosa* (i.e., between Samples 165-999B-23R-CC and 25R-6, 53 cm). We could determine events based on *Chiasmolithus grandis, C. gigas, C. solitus, Discoaster sublodoensis,* and *D. lodoensis* relatively precisely because of their abundances. We were unable to determine the FO of *Cribrocentrum reticulatum* because this species is very rare in the lower part of its range, and the FO of *Blackites inflatus* because no specimens of this species were observed. *Nannotetrina fulgens* and *Tribrachiatus orthostylus* occurred sporadically, and thus the base of Zone CP13 and Subzone CP9b could not be defined accurately. We did not observe the species *Coccolithus crassus,* the FO of which defines the base of Zone CP11.

We used minimum sizes of 10 and 14 µm to define *Reticulofenestra bisecta* and *R. umbilicus* (e.g., Backman and Hermelin, 1986), respectively, but we note that slightly smaller specimens extend 10–20 m below the ranges determined here. The FO of *R. bisecta* lies just below the LO of *C. solitus,* the opposite order to the scheme of Berggren et al. (1995). A similar result was found at Site 998.

Paleocene

No specimens of *Tribrachiatus bramlettei* and *T. contortus* were observed. We are not sure whether these absences result from overgrowth on these species rendering them unrecognizable, from extreme rarity in sparse nannofossil assemblages, or from a limited paleobiogeographic distribution. Neither species was observed at Site 865 (central Pacific), which also was deposited in a tropical, pelagic setting (Bralower and Mutterlose, 1995), or in Caribbean sites drilled during DSDP Leg 15 (Hay and Beaudry, 1973). Because of the absence of *T. contortus,* we could not approximate the Paleocene/Eocene boundary with nannofossil biostratigraphy. The absence of *T. bramlettei* and *Discoaster diastypus* prevented us from delineating the base of Zone CP9. Other markers suggest that the latest Paleocene interval at Site 999 is relatively complete. The FO of *Fasciculithus tympaniformis* lies some 4 m above the suspected benthic foraminifer extinction event. At Site 865, where a minor unconformity is suspected above the benthic foraminifer extinction event, these events are separated by 2 m (Bralower et al., 1995).

Several events in the upper Paleocene appear to be clustered stratigraphically with respect to other sites (Table 3). These include the FOs of *Discoaster multiradiatus* (56.2 Ma), *D. mohleri* (57.5 Ma), and *Heliolithus kleinpellii* (58.4 Ma), which define the bases of Zones CP8, CP6, and CP5, respectively. Further work is necessary to observe whether the close spacing of these events is a result of the presence of slow sedimentation rates or minor unconformities in the section. *Discoaster nobilis,* the FO of which defines the base of Zone CP7, was not identified in our preliminary observations of this interval. Nannofossil preservation in the lower Paleocene (Cores 165-999B-57R to 59R) deteriorates markedly and abundance declines, preventing accurate delineation of Zones CP1 to CP3. No specimens of *Ellipsolithus macellus,* the FO of which defines the base of Zone CP3, were observed in Hole 999B. In addition, the lowermost occurrence of *Cruciplacolithus tenuis,* the FO of which defines the base of Subzone CP1b, lies in the same sample (165-999B-58R-CC) as the FO of *Sullivania danica,* which defines the base of Zone CP2. Thus, we place the base of the latter zone at this level and cannot subdivide Zone CP1. Core 165-999B-59R appears to lie in Zone CP1, but the only nannofossil specimens observed include reworked Cretaceous species (*Cribrosphaerella ehrenbergii, Cylindralithus* sp., *Micula decussata,* and *Watznaueria barnesae*), fragments of *Thoracosphaera,* and exceptionally rare, questionable shields of *Biscutum romeinii.* Because of their exceptionally small size (1–2 µm), the latter species, the range of which is limited to Subzone CP1a (Perch-Nielsen, 1985), require documentation in the scanning electron microscope. Blooms of the calcareous dinoflagellate *Thoracosphaera* have often been observed in lowermost Danian sediments (e.g., Perch-Nielsen et al., 1982). No specimens of *Biantholithus sparsus,* the FO of which is often used to define the K/T boundary (e.g., Perch-Nielsen, 1985), were observed.

Cretaceous

The Cretaceous section at Site 999 lies within the uppermost zone of the Maastrichtian, the *Nephrolithus frequens* Zone (CC26), or the uppermost part of the underlying *Arkhangelskiella cymbiformis* Zone (CC25) of Sissingh (1977) based on the presence of *Micula murus. M. murus* has been observed in the uppermost Cretaceous sample observed (Sample 165-999B-60R-1, 10 cm) as well as in the lowermost sample taken in Hole 999B (Sample 165-999B-62R-CC). Although most specimens of *M. murus* lack typical extensions, this species can be clearly differentiated from other species of *Micula* (e.g., *M. decussata*) by its characteristic arrangement of elements. A few tentative specimens of *M. prinsii,* the FO of which lies at 65.4 Ma, closer than any other event to the K/T boundary, have been observed in Sample 165-999B-60R-1, 10 cm. Nannofossil preservation in the Maastrichtian section appears to be better in the thin claystone beds than in the limestone. However, diversity in both lithologies tends to be low. All of the Maastrichtian zonal marker species, such as *Tranolithus orionatus, Reinhardtites levis, Quadrum gothicum,* and *Q. trifidum,* are absent, confirming the latest Maastrichtian age. Due to the currently inconclusive identifications of *Micula prinsii, Biantholithus sparsus,* and *Biscutum romeinii,* it is not possible to determine whether the K/T boundary at Site 999 is complete from a nannofossil biostratigraphic viewpoint.

Planktonic Foraminifers

Central American Seaway

Site 999 lies ~200 km north-northeast of DSDP Sites 154 and 502 (11°29′N; 79°23′W). Keigwin (1978, 1982b) described the unusual occurrence of sinistrally coiled *Neogloboquadrina pachyderma* in significant numbers in the upper Miocene to lower Pliocene (4.5–8.0 Ma) at Site 502. This faunal event is not found at DSDP Site 503 (4°03′N; 95°38′W) in the Pacific. Keigwin (1982b) noted that the *N. pachyderma* specimens at Site 502 are associated with warm-water faunal elements, which suggests that their presence indicates seasonal upwelling rather than generally cold water. This low-latitude *pachyderma* event is also found at Site 999 (12°43′N; 78°46′W) between Samples 165-999A-15H-CC and 23X-CC. *Globigerina bulloides,* another species associated with upwelling (e.g., Cullen and Prell, 1984), is also found in most of the samples that include *N. pachyderma.* In the modern Pacific Ocean, a band of upwelling is associated with the boundary between the westward-flowing North Equatorial Current (NEC) and the eastward-flowing North Equatorial Countercurrent (NECC). In the late Miocene to early Pliocene, an open Central American Seaway would have permitted the extension of this current boundary into the western Caribbean (Emiliani et al., 1972; Kaneps, 1979). In the modern Pacific the latitude of the boundary, which moves seasonally, is ~10°–12°N. Although the NEC/NECC boundary may have been in a different location in the late Miocene, it is presently at the latitude of Caribbean Sites 502 and 999, but it is several degrees north of the latitude of Pacific Site 503.

Neogloboquadrina pachyderma are predominantly sinistrally coiled between Samples 165-999A-18H-CC and 23X-CC. Between Samples 165-999A-15H-CC and 17X-CC, the ratio of dextrally to sinistrally coiled specimens increases until the taxon is represented by rare dextral specimens at the top of this event. Assemblages at Site 999 during the "*pachyderma* event" are dominated by neogloboquadrinid species. Above the event, the dominance shifts to the menardii-form globorotaliids and the Pliocene Atlantic radiation of that group begins. Parker and Berger (1971) described a successive dominance of assemblages by different thermocline-dwelling taxa across the modern equatorial Pacific. In the eastern Pacific, where the thermocline is shallowest and productivity is highest, neogloboquadrinids dominate. In the central equatorial region, where the thermocline is slightly deeper and productivity commensurately less, the globorotaliids dominate. In the western Caribbean, the early Pliocene closing of the Central American Seaway may have created a temporal analogy to this geographic phenomenon in the Pacific. Disruption of surface currents through the seaway ended regional upwelling and led to the local extinction of *Neogloboquadrina pachyderma,* followed by the expansion and diversification of the menardii-form globorotaliid plexus. Although *Globigerina bulloides* persists in low numbers in the upper Pliocene portion (Samples 165-999A-7H-CC, 8H-CC, and 10H-CC) of the section, the sinistrally coiled *N. pachyderma* is not found again (cf. Keigwin, 1978).

Pleistocene and Pliocene

Only core-catcher samples were processed and examined in the upper Neogene section of Hole 999A. *Globigerinoides fistulosus* was observed only in Sample 165-999A-9H-CC; specimens are rare and not sensu stricto. Therefore, this datum could not be constrained. However, the LO of *Globigerinoides obliquus* at 1.3 Ma (Chaisson and Pearson, in press) is located between Samples 165-999A-4H-CC and 5H-CC. *Globoconella triangula,* a tropical ecophenotype of *Globoconella inflata* (Weaver and Raymo, 1989), is present only rarely at Site 998, but it is found in most core catchers between Samples 165-999A-3H-CC and 7H-CC in Hole 999A.

Menardella menardii is more abundant in the Pleistocene and latest Pliocene sections of Hole 999A than it was at Site 998. In Sample 165-999A-3H-CC, a broad range of *M. menardii* morphotypes are present, varying from extremely robust to finely perforate and delicate forms. The latter forms echo the Pliocene menardii-form species (e.g., *M. exilis*) endemic to the tropical Atlantic and Caribbean. Members of the *menardii* plexus are more consistently present in the Pleistocene and Pliocene section of Hole 999A than they were at Site 998.

The base of Zone N22 is marked by the FO of *Truncorotalia truncatulinoides* between Samples 165-999A-7H-CC and 8H-CC. Specimens of *T. truncatulinoides* are all dextrally coiled in Samples 165-999A-1H-CC, 2H-CC, 6H-CC, and 7H-CC, and all sinistrally coiled in Samples 165-999A-4H-CC and 5H-CC. There is a mixed coiling ratio (dextral dominant) only in Sample 165-999A-3H-CC, whereas at Site 998 mixed coiling was the prevailing condition. *T. tosaensis* is present only in Sample 165-999A-9H-CC; therefore, the base of Zone N21 could not be constrained at this site. *T. crassaformis* is consistently present in Hole 999A down to its FO between Samples 165-999A-14H-CC and 15H-CC.

The Pliocene radiation of the finely perforate menardii-form globorotaliids begins in Sample 165-999A-13H-CC with the FO of *M. exilis.* The FO of *M. miocenica* marks the base of Zone N21/N20 between Samples 165-999A-10H-CC and 11H-CC. *M. pertenuis* appears only in Sample 165-999A-9H-CC. The radiation of the normally perforate subgroup begins with the development of the *M. limbata/M. pseudomiocenica* morphotypes in the late Miocene (Kennett and Srinivasan, 1983). The FO of *M. limbata/M. pseudomiocenica* is between Samples 165-999A-19H-CC and 20H-CC. *M. multicamerata* first occurs between Samples 165-999A-13H-CC and 14H-CC in the lower Pliocene; its LO, along with that of *Dentoglobigerina altispira,* falls between Samples 165-999A-10H-CC and 11H-CC.

The transition from *Hirsutella margaritae* to *H. hirsuta* occurs in the mid-Pliocene as the *evoluta* type of *H. margaritae* grows increasingly robust. The datum event in Hole 999A is placed between Samples 165-999A-10H-CC and 11H-CC with *H. margaritae* to *H. hirsuta* present in Samples 165-999A-11H-CC. The distinction is drawn based on the development of a hirsute surface texture.

Pulleniatinids are quite rare at Site 999. The "Atlantic hiatus" (Bolli and Saunders, 1985) extends between Samples 165-999A-8H-CC and 13H-CC. *Pulleniatina primalis* is found only in Samples 165-999A-14H-CC and 15H-CC; it is sinistrally coiled in both samples.

Miocene

The base of Zone N19 is found between Samples 165-999A-17H-CC and 18H-CC. The marker species, *Sphaeroidinella dehiscens,* is not found in the lower Pliocene and uppermost Miocene samples in Hole 999A, and is quite rare in the two core catchers just above its FO. *Sphaeroidinellopsis kochi* (= *S. multiloba*), which was observed frequently at Site 998, is found only rarely in Hole 999A samples.

The FO of *Hirsutella margaritae* is found between Samples 165-999A-17H-CC and 18H-CC. The total range of *H. cibaoensis* seems to conform to the limits set by the Berggren et al. (1995) datums; its FO is between Samples 165-999A-23H-CC and 24H-CC and its LO is between Samples 165-999A-14H-CC and 15H-CC. This contrasts with the range of this morphotype at Ceara Rise (western tropical Atlantic), where it ranged both above and below levels associated with its FO and LO datum ages (Chaisson and Pearson, in press); and at Ontong Java Plateau (western tropical Pacific), where it was found down to mid-Zone N16 (8.2–10.0 Ma) (Chaisson and Leckie, 1993).

The FO of *Globigerinoides conglobatus,* assigned an absolute age (6.2 Ma) by Chaisson and Pearson (in press), is between Samples 165-999A-19H-CC and 20H-CC. The first occurrence of this readily identifiable taxon seems to be a sound datum event to add to the datum-poor late Miocene interval, at least in the tropical Atlantic and Caribbean region. This form is readily distinguished from *Globigerinoides extremus* by its more globose shape, more closely appressed chambers, and greater tendency to be encrusted with secondary calcite. The FO of *G. extremus* is located between Samples 165-999A-25H-CC and 26H-CC. The distinction between *G. extremus* and *G. obliquus* is made by adhering to a narrow definition of the descendant species and accepting more variation in the morphology of the ancestor species.

Globorotalia tumida is not found below the upper Pleistocene in samples examined from Hole 999A. The base of Zone N18 could not be delimited, therefore. The base of a combined Zone N18/N17 is between Samples 165-999A-25H-CC and 26H-CC, constrained by the FO of *Globorotalia plesiotumida.* Drilling disturbance mixes younger sediments down to Core 165-999A-29R, causing small and rare *G. plesiotumida* to be found in the core catcher.

Sinistrally coiled *Neogloboquadrina pachyderma* are found in Samples 165-999A-19H-CC, 20H-CC, and 23X-CC. This occurrence, unusual for both its low-latitude location and its late Miocene timing, was noted by Keigwin (1982a) at DSDP Site 502 (~200 km south-southwest of Site 999) through the same stratigraphic interval. The lower *S. dehiscens* to upper *G. plesiotumida* Zones of Jenkins and Orr (1972) employed by Keigwin are equivalent to the lower Zone N19 to upper Zone N17 of Blow (1969) used for this study. The FO of *Neogloboquadrina acostaensis,* which marks the base of Zone N16, is between Samples 165-999A-27X-CC and 28X-CC. Above its FO, it is sinistrally coiled. It switches to dextral coiling between Samples 165-999A-24X-CC and 25X-CC and returns to sinistral coiling between Samples 165-999A-23X-CC and 24X-CC. Where it occurs with *N. pachyderma,* it is most often sinistrally coiled, which was also noted by Keigwin (1982a). The base of Zone N15, marked by LO of *Paragloborotalia mayeri,* is between Samples 165-999A-30X-1, 42–44 cm, and 30X-2, 43–45 cm.

Temperate to warm-subtropical species in the *Globoconella* plexus are present at Site 999 between Samples 165-999A-30X-2, 43–45 cm, and 31X-5, 42–44 cm. This coincides with the middle Miocene interval at Site 998 where *Globoconella conoidea* and *G. miozea* were found. At Site 998, *G. miozea* is also present, but the more prevalent species are *Globoconella praescitula* and *G. panda.* These taxa are more common in samples from Hole 999A than the related taxa were at Site 998. This may be, in part, a result of the better preservation of specimens found at Site 999 compared with Site 998, but there may also be a paleohydrographic explanation.

Globoturborotalita nepenthes, which marks the base of Zone N14, is found only sporadically in the Miocene section of Hole 999A; it does not occur at all below Sample 165-999A-28X-CC. For this reason, Zones N14 and N13 are combined. The base of Zone 13 is marked by the LO of the genus *Fohsella* between Samples 165-999A-32X-CC and 33X-CC. This interval is disturbed by drilling and samples include taxa from Zone N17 through N13. Preservation is also poor and planktonic foraminifers are rare. The only fohsellids identified in Sample 165-999A-33X-CC were assigned to *Fohsella peripheroacuta.* Single specimens of apparently reworked *Fohsella fohsi robusta* were found in Samples 165-999A-32X-4, 43–45 cm, and 32X-5, 42–44 cm. Good *Fohsella fohsi* are found only in Sample 165-999A-34X-CC, placing the base of Zone N12 between this sample and Sample 165-999A-35X-CC. The bases of Zones N11 and N10 are marked by the FOs of *F. praefohsi* and *F. peripheroacuta,* respectively. Both of these events are between Samples 165-999A-37X-CC and 38X-CC. Preservation in these samples is poor-to-moderate, and there is much volcanic ash (glass) present.

Orbulina universa is regularly present in Hole 999A down to the middle Miocene part of the section. In the middle Miocene the whorled portion of the test on many specimens is embedded in the wall of the final spherical chamber. The suture between the whorl and the terminal chamber is not perforated in the manner of the praeorbulines, and the entire specimen is more delicate than praeorbuline test. The FO of *O. universa,* which should mark the base of Zone N9, is between Samples 165-999A-33X-CC and 34X-CC in Zone N12. Poor preservation may have eliminated *O. universa* below this level. However, a similar stratigraphic pattern for *O. universa* was observed at Site 806 on Ontong Java Plateau (Chaisson and Leckie, 1993), where preservation was superior to that at Site 999. *Praeorbulina sicana* was the only praeorbuline species definitively identified in Hole 999A, and its FO between Samples 165-999A-44X-CC and 45X-CC marks the base of the combined Zone N9/N8.

The lowermost zone delimited in Hole 999A was the base of Zone N7, marked by the LO of *Catapsydrax dissimilis* between Samples 165-999A-48X-CC and 49X-CC. *Globigerinatella insueta* with areal apertures are found in Sample 165-999A-61X-CC, the bottom sample of Hole 999A. This datum, which has been used to mark the base of Zone N6 (Blow, 1969), proved to be problematic at Site 998 and at western tropical Atlantic sites (see "Biostratigraphy" section, "Site 998" chapter, this volume; Curry, Shackleton, Richter, et al., 1995).

Oligocene

Documentation of Paleogene and Cretaceous planktonic foraminifer zones at Hole 999B is complicated by the deep burial depth of this sequence (605.96–1066.58 mbsf) and the consequent strong lithification and poor foraminiferal preservation throughout the entire Paleogene and Cretaceous interval at this site. Nonetheless, most of the Paleogene and Cretaceous was successfully zoned, albeit at slightly coarser zonal resolution in a few intervals (i.e., Eocene Zones P16–P17 and P8–P10).

There was no sediment recovered in the first four cores of Hole 999B due to drilling difficulties, and any overlap with Hole 999A was lost. The first datum identified in Hole 999B is the base of Zone N4 (and the base of the Miocene), marked by the FO of *Paragloborotalia kugleri* between Samples 165-999B-8R-CC and 9R-CC (Table 4). Preservation is poor throughout Hole 999B and planktonic foraminifers were rare in most samples, so even semiquantitative estimates of abundance were rarely attempted. Consequently, the first "common occurrence" of *Globigerinoides primordius* could not be determined. However, the FO of this species and the base of Zone P22, which is marked by the LO of *Paragloborotalia opima,* are between Samples 165-999B-11R-CC and 12R-CC.

The base of Subzone P21a is marked by the last common occurrence of *Chiloguembelina cubensis.* We reason that the taxon would have to be common to be found at all in sediments with such poor preservation; therefore, we tentatively place the base of Subzone P21a above the LO of *C. cubensis,* between Samples 165-999B-15R-CC and 16R-CC.

Globigerina angulisuturalis, a morphologically distinct species that is resistant to dissolution, was observed frequently at Site 998. However, in Hole 999 this species is found in only one sample (165-999B-14R-CC), and there it is found only in the <150-μm fraction. Therefore, the base of Subzone P21a could not be delimited. The base of Zone P20 is marked by the LO of *Turborotalia ampliapertura.* No sediment was recovered in Core 165-999B-17R, and only rare specimens of *T. ampliapertura* were found in Sample 165-999B-18R-CC. The base of combined Subzone P21a/Zone P20 is placed, therefore, between Samples 165-999B-16R-CC and 18R-CC. The FO of *Paragloborotalia opima* is also in this interval.

The base of Zone P19 is marked by the LO of the genus *Pseudohastigerina.* This datum event is between Samples 165-999B-22R-CC and 23R-CC. No *Hantkenina* spines were found in any samples examined in Hole 999B, and the LO of this genus, which closely approximates the Eocene/Oligocene boundary, could not be delimited. Rather, the base of Zone P18, which is marked by the LO of *Turborotalia cerroazulensis,* is used to approximate the base of the Oligocene between Samples 165-999B-25R-CC and 26R-CC, although nannofossil biostratigraphy indicates that the Eocene/Oligocene boundary lies within Core 999B-25R.

Eocene

As at Site 998, neither *Cribrohantkenina inflata* nor *Turborotalia cunialensis* was observed at this site. The absence of these species rendered Zones P16 and P17 inseparable and required us to approximate the base of the combined Zone P16/P17 with the LOs of *Turborotalia pomeroli* and *Porticulasphaera semiinvoluta.* Both of these datums lie between Samples 165-999B-27R-CC and 28R-CC.

The zonation of the middle Eocene is generally straightforward at Hole 999B. The base of Zone P15 is defined by the FO of *P. semiinvoluta* between Samples 165-999B-28R-CC and 29R-CC, and the base of Zone P14 occurs between Samples 165-999B-29R-CC and 30R-CC at the LO of *Globigerapsis beckmanni.* The FO of *G. beckmanni* marks the base of Zone P13 between Samples 165-999B-30R-CC and 31R-CC, and the base of Zone P12 is marked by the LO of *Morozovella aragonensis* between Samples 165-999B-36R-CC and 37R-CC. The base of Zone P11 is defined by the FO of *Globigerapsis kugleri* between Samples 165-999B-40R-CC and 41R-CC. Unfortunately, as at Site 998, poor microfossil preservation precluded recog-

Table 4. Planktonic foraminifer datums, absolute ages, and depths at Site 999.

Event	Zone (base)	Age (Ma)	Core, section, interval (cm)	Depth (mbsf)
Hole 999A:				
LO *Globigerinoides obliquus*		1.3	4H-CC to 5H-CC	41.19
FO *Truncorotalia truncatulinoides*	N22	2.0	7H-CC to 8H-CC	69.78
LO *Menardella miocenica*		2.3	8H-CC to 9H-CC	79.33
LO *Menardella multicamerata*		3.0	10H-CC to 11H-CC	98.35
LO *Dentoglobigerina altispira*		3.0	10H-CC to 11H-CC	98.35
FO *Menardella miocenica*	N21/N20	3.6	10H-CC to 11H-CC	98.35
LO *Hirsutella margaritae*		3.6	10H-CC to 11H-CC	98.35
LO *Globorotalia plesiotumida*		4.4	13H-CC to 14H-CC	126.91
FO *Menardella exilis*		4.5	13H-CC to 14H-CC	126.91
FO *Truncorotalia crassaformis*		4.7	14H-CC to 15H-CC	136.43
LO *Hirsutella cibaoensis*		5.0	14H-CC to 15H-CC	136.43
FO *Sphaeroidinella dehiscens*	N19	5.6	17H-CC to 18H-CC	164.76
FO *Hirsutella margaritae*		6.0	17H-CC to 18H-CC	164.76
FO *Globigerinoides conglobatus*		6.2	19H-CC to 20H-CC	183.88
FO *Hirsutella cibaoensis*		7.7	23X-CC to 24X-CC	215.28
FO *Globigerinoides extremus*		8.0	25XCC to 26X-CC	234.40
FO *Candeina nitida*		8.0	25XCC to 26X-CC	234.40
FO *Globorotalia plesiotumida*	N18/N17	8.2	25XCC to 26X-CC	234.40
FO *Neogloboquadrina acostaensis*	N16	10.0	27X-CC to 28X-CC	253.55
LO *Paragloborotalia mayeri*	N15	10.3	30X-1, 42–44 to 30X-2, 43–45	269.19
LO *Fohsella fohsi*	N14/N13	11.8	32X-CC to 33X-CC	300.99
FO *Fohsella fohsi*	N12	12.7	34X-CC to 35X-CC	320.88
FO *Fohsella praefohsi*	N11	14.0	37X-CC to 38X-CC	349.46
FO *Fohsella peripheroacuta*	N10	14.8	37X-CC to 38X-CC	349.46
FO *Orbulina universa*		15.1	33X-CC to 34X-CC	311.07
FO *Praeorbulina sicana*	N9/N8	16.4	44X-CC to 45X-CC	416.95
LO *Catapsydrax dissimilis*	N7	17.3	48X-CC to 49X-CC	454.38
Hole 999B:				
FO *Paragloborotalia kugleri*	N4	23.8	8R-CC to 9R-CC	605.96
FO *Globigerinoides primordius*		26.7	11R-CC to 12R-CC	633.59
LO *Paragloborotalia opima*	P22	27.1	11R-CC to 12R-CC	633.59
LO *Ch. cubensis* (common)	P21b	28.5	15R-CC to 16R-CC	670.69
LO *Turborotalia ampliapertura*	P21a/P20	30.3	16R-CC to 18R-CC	675.57
FO *Paragloborotalia opima*		30.6	16R-CC to 18R-CC	675.57
LO *Pseudohastigerina* spp.	P19	32.0	22R-CC to 23R-CC	710.92
LO *Turborotalia cerroazulensis*	P18	33.8	25R-CC to 26R-CC	740.14
LO *Turborotalia pomeroli*		35.3	27R-CC to 28R-CC	759.47
LO *Porticulasphaera semiinvoluta*		35.3	27R-CC to 28R-CC	759.47
LO *Morozovella spinulosa*		38.1	33R-CC to 34R-CC	817.08
FO *Porticulasphaera semiinvoluta*	P15	38.4	28R-CC to 29R-CC	769.28
LO *Acarinina primitiva*		39.0	28R-CC to 29R-CC	769.28
LO *Globigerapsis beckmanni*	P14	40.1	29R-CC to 30R-CC	777.78
FO *Globogerapsis beckmanni*	P13	40.5	30R-CC to 31R-CC	786.13
FO *Globigerapsis index*		42.9	42R-CC to 43R-CC	894.28
LO *Morozovella aragonensis*	P12	43.6	36R-CC to 37R-CC	843.60
FO *Globigerapsis kugleri*	P11	45.8	40R-CC to 41R-CC	883.70
FO *Acarinina pentacamerata*	(P8)	50.8	48R-CC to 49R-4, 68–70	951.84
FO *Morozovella aragonensis*	P7	52.3	48R-CC to 49R-4, 68–70	951.84
LO *Morozovella marginodentata*		52.5	48R-CC to 49R-4, 68–70	951.84
LO *Morozovella lensiformis*		52.7	49R-4, 68–70 to 49R-CC	956.56
LO *Morozovella aequa*		53.6	48R-CC to 49R-4, 68–70	951.84
FO *Morozovella formosa*	P6b	54.0	49R-CC to 50R-CC	963.14
FO *Morozovella lensiformis*		54.0	49R-CC to 50R-CC	963.14
LO *Morozovella velascoensis*	P6a	54.7	49R-CC to 50R-4, 82–84	961.41
LO *Morozovella acuta*		54.7	48R-CC to 49R-4, 68–70	951.84
FO *Morozovella gracilis*		54.7 (54.9)	51R-6, 12–14 to 51R-CC	976.47
FO *Igorina broedermanni*		54.7	51R-CC to 52R-1, 26–28	977.64
FO *Morozovella subbotinae*		55.9	52R-1, 26–28 to 52R-2, 144–146	979.71
LO *Globanomalina pseudomenardii*	P5	55.9	54R-CC to 55R-CC	1010.97
LO *Acarinina nitida*		56.3	52R-CC to 53R-CC	992.08
FO *Acarinina soldadoensis*	P4c	56.5	53R-CC to 54R-CC	1001.47
FO *Morozovella aequa*		56.5	55R-CC to 56R-CC	1021.56
FO *Morozovella velascoensis*		60.0	55R-CC to 56R-CC	1021.56
FO *Igorina albeari*	P4b–P3b	60.0	55R-CC to 56R-CC	1021.56
FO *Morozovella angulata*	P3a	61.0	56R-CC to 57R-CC	1030.35
FO *Praemurica uncinata*	P2	61.2	57R-CC to 58R-CC	1038.50
FO *Praemurica inconstans*		63.0	57R-CC to 58R-CC	1038.50
FO *Subbotina triloculinoides*	P1b	64.3	58R-CC to 59R-2, 122–123	1044.87
LO *Parvularugoglobigerina eugubina*	P1a	64.7 (64.9)	59R-2, 122–123 to 59R-CC	1048.75
FO *Woodringina claytonensis*		64.97	59R-2, 122–123 to 59R-CC	1048.75
LO Most Cretaceous taxa	Pα/P0	65.0	60R-1, 0–1 to 60R-1, 21	1050.21

Notes: Zone names in parentheses indicate that a secondary taxon is approximating age of the base. FO = first occurrence, LO = last occurrence. This entire table also appears on CD-ROM (back pocket).

nition of the P9 and P10 zonal markers. Consequently, Zones P8, P9, and P10 were not differentiated at Site 999. The FO of *Acarinina pentacamerata* and the FO of *Morozovella aragonensis,* respectively, mark the bases of Zones P8–P10 and P7. Both datums occurred between Samples 165-999B-48R-CC and 49R-4, 70 cm. The base of Subzone P6b is defined by the FO of *Morozovella formosa,* which occurs between Samples 165-999B-49R-CC and 50R-CC. The base of Subzone P6a, as defined by the LO of *Morozovella velascoensis,* lies between Samples 165-999B-49R-CC and 50R-4, 82–84 cm. This places the Paleocene/Eocene (P5/P6a of Berggren et al., 1995) boundary at approximately 961 mbsf in Hole 999B.

Paleocene

The base of foraminiferal Zone P5 tentatively is located using the LO of *Globonomalina pseudomenardii* between Samples 165-999B-

54R-CC and 55R-CC; this species was rarely identified in Hole 999B core-catcher samples. The base of Subzone P4c could not be determined in Hole 999B because the marker species, *Acarinina soldadoensis,* was not observed below Sample 165-999B-53R-CC, which is above the provisional base of Zone P5. The marker species for the base of Subzone P4b, *Acarinina subsphaerica,* was not found at all in Hole 999B, and the rarity of *Globonomalina pseudomenardii* made locating the base of Subzone P4a impossible. Therefore, these zones were grouped, and the FO of *Igorina albeari,* which defines the base of Subzone P3b, was used to delimit a combined Zone P4b–P3b between Samples 165-999B-55R-CC and 56R-CC. The FO of *Morozovella angulata* marks the base of Subzone P3a between Samples 165-999B-56R-CC and 57R-CC. The base of Zone P2 is placed between Samples 165-999B-57R-CC and 58R-CC at the FO of *Praemurica uncinata.* Because *Globanomalina compressa* was not consistently found in this Paleocene sequence, Subzones P1c and P1b were not differentiated in Hole 999B. The base of the combined Subzone P1c/P1b is at the FO of *Subbotina triloculinoides,* between Samples 165-999B-58R-CC and 59R-2, 123 cm. The base of Subzone P1a was placed at the LO of *Parvularugoglobigerina eugubina,* between Samples 165-999B-59R-2, 122 cm, and 59R-CC.

Cretaceous/Tertiary Boundary

Because of the very well-indurated nature of the lowermost Paleocene and uppermost Cretaceous limestones, the level of the K/T boundary was determined primarily by thin-section analyses of planktonic foraminifer assemblages. As defined by planktonic foraminifers, the K/T boundary occurs in Section 165-999B-60R-1. The LO of most Maastrichtian species occurs between Samples 165-999B-60R-1, 1 cm, and 60R-1, 21 cm. Thin sections of Sample 165-999B-60R-1, 21 cm, and underlying samples contain abundant and relatively diverse Maastrichtian assemblages. In contrast, Samples 165-999B-60R-1, 1 cm, and 59R-CC, 15 cm, contain few foraminifers. The foraminiferal assemblages of the latter two samples are dominated by the K/T survivor, *Guembelitria cretacea,* but also contain trace numbers of unidentified tiny trochospiral specimens. Given the possibility that some of those tiny trochospirals are *Parvularugoglobigerina eugubina,* Samples 165-999B-60R-1, 1 cm, to 59R-CC, 1 cm, were assigned to Zone P0/Pa (undifferentiated).

Maastrichtian

Abathomphalus mayaroensis, the uppermost Cretaceous zonal marker, was not observed at Site 999. However, the presence of other latest Cretaceous planktonic foraminifers (i.e., *Pseudoguembelina palpebra* and *Planoglobulina multicamerata*) indicates that the interval from Samples 165-999B-60R-1, 21 cm, to 165-999B-62R-CC is late Maastrichtian in age (*A. mayaroensis* Zone or upper *Gansserina gansseri* Zone). Given the presence of the latest Maastrichtian nannofossil, *Micula murus,* in this interval, it appears that the absence of *A. mayaroensis* in Samples 165-999B-60R-1, 21 cm, through 62R-CC probably results from the difficulty of extracting and recognizing rare taxa from these heavily indurated limestones.

PALEOMAGNETISM

Whole- and Split-Core Measurements

The remanent magnetization of the archive-half sections of APC and XCB cores from Hole 999A and RCB cores from Hole 999B were measured using the pass-through cryogenic magnetometer at a 10-cm interval. After measuring the natural remanent magnetization (NRM), most sections were partially demagnetized in peak alternating fields (AF) of 10 mT, and all the sections were partially demagnetized at 20 mT.

The NRM intensities (Fig. 22) range from 5 to 20 mA/m within the top 60 mbsf and increase fairly linearly downcore to about 210 mbsf, where they are 35–50 mA/m, with the exception of one low at 162–175 mbsf, which could be caused by a low in the dispersed volcanic ash and an absence of discrete volcanic ash layers. The NRM intensity decreases abruptly below 210 mbsf, probably owing to reduction diagenesis. The intensity then ranges from 1 to 10 mA/m between 160 and 890 mbsf, except for three intervals of higher intensity at 250–280, 460–580, and 705–875 mbsf, which correspond to the carbonate crash, the Miocene volcanic episode, and the Eocene volcanic episode, respectively (see "Igneous Petrology and Volcanology" section, this chapter). The intensities also increase in the lower part of Hole 999B, probably reflecting the increase in clay content (Fig 45). The overall intensity signal varies in a similar fashion to the whole-core susceptibility signal, particularly below 160 mbsf (Fig. 22).

The NRM inclinations (Fig. 23) are strongly biased toward high positive inclinations (50°–80°), which is inconsistent with the 42° inclination of the present-day geomagnetic field and inconsistent with the 24° inclination expected for a present-day axial dipole field. The observed directions indicate that a strong drilling-induced magnetization is present as previously identified at Site 998. AF demagnetization to 10 mT and subsequently 20 mT removes a large part of the secondary overprint, as suggested by the observed sharp decrease of the NRM intensity in some parts of Hole 999A, but the removal of this relatively soft component is incomplete (Fig. 23). At the 20-mT step, the inclinations are mostly positive and scattered. Only the top 150 mbsf cored with the APC tool displays intervals of negative inclinations, indicating the presence of a primary remanent magnetization. Additional problems caused by drilling disturbance in the section cored with the XCB system were encountered farther down Hole 999A.

The secondary overprint, reported in many ODP legs, is characterized by steep inclinations and is probably acquired during drilling. The acquisition of this overprint seems dependent on the lithology and the nature of the magnetic mineral fraction. It is likely that the magnetic mineral fraction becomes coarser downhole at Site 999 because of the loss of the high surface-to-volume fine-grained magnetite, which results from reduction diagenesis. The residual coarse-grained, multidomain magnetite would be more prone to acquiring a drill-string overprint.

As expected, the NRM inclinations of Hole 999B are also biased toward positive values. Upon demagnetization to 10 and 20 mT, we observed a significant decrease in intensity and a shift toward less steep inclinations, but the secondary overprint was not completely removed. This overprint precluded any magnetostratigraphic interpretation on whole-core measurements of Hole 999B. Instead, the polarity data have been obtained from discrete sample analysis.

Discrete Sample Analysis

Oriented samples (6-cm^3 plastic cubes), collected from almost every core from Holes 999A and 999B, were subject to stepwise AF demagnetization to try to remove the secondary magnetization. Two or three samples were also collected per section on some cores of special interest. All the samples were measured using the Molspin magnetometer and demagnetized on a Schondstedt GSD-1 AF-demagnetizer. A total of 151 samples were analyzed from Hole 999A and 90 samples from Hole 999B (see Appendix tables on CD-ROM, back pocket, this volume).

Results from Hole 999A

We began our analysis by further testing the reliability of the AF-demagnetizer, given that the acquisition of a spurious magnetization component has been reported in previous ODP legs, which used the

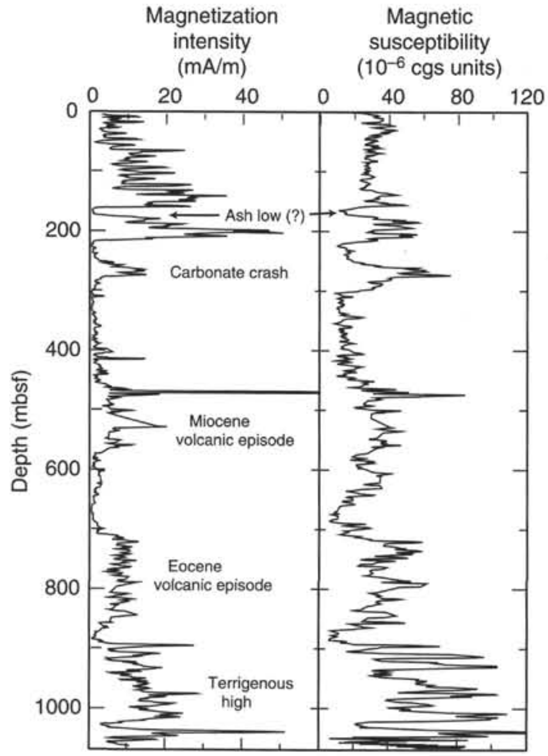

Figure 22. NRM intensities from Site 999 compared with whole-core susceptibility measurements.

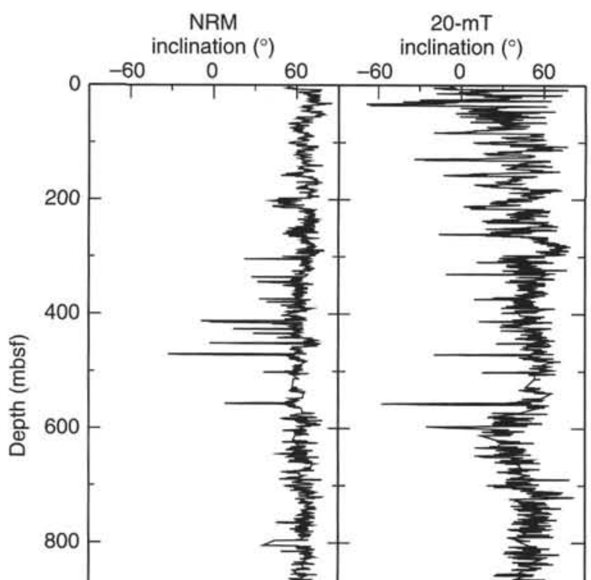

Figure 23. Inclinations of NRM directions before and after demagnetization at 20 mT from Site 999, which illustrate the strong drill-string overprint that is only partially removed by AF demagnetization at 20 mT.

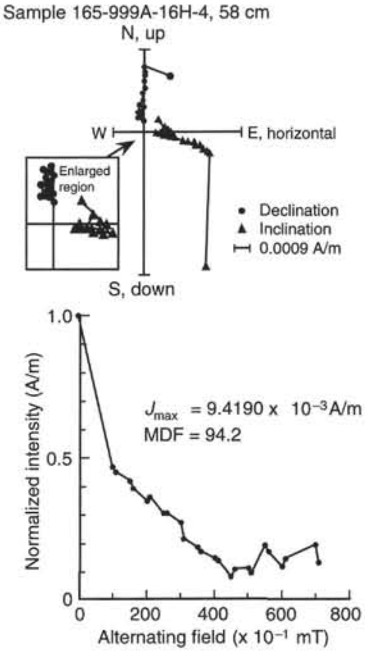

Figure 24. Vector demagnetization diagram for a pilot discrete sample from Hole 999A. Acquisition of spurious magnetization caused by an anhysteretic remanent magnetization effect during AF demagnetization occurs above 45 mT.

same instrument. Two samples (165-999A-16H-4, 58–60 cm, and 17H-4, 60–62 cm) were progressively demagnetized with 5-mT increments up to 70 mT. At each step the sample was demagnetized along the X, Y, and then Z axis, measured, demagnetized again at the same step along the Z, Y, and then X axis, and measured again. A very steep downward component is removed at 10 mT and a second component that trends toward the origin of the orthogonal vector-plot is stable up to high fields. On Sample 165-999A-17H-4, 60–62 cm, this stable component is also of steep inclination, indicating that the induced drilling component is only partially removed even at high demagnetization fields. On Sample 165-999A-16H-4, 58–60 cm, the stable component has a low inclination and is likely the primary component (Fig. 24). At high fields, the remanent magnetization displays scattered directions and erratic intensity variations. These effects are most probably the result of an anhysteretic remanent magnetization (ARM) produced by the demagnetizer. These spurious magnetizations occur for demagnetizations steps above 45–50 mT, and so analysis of magnetic components carried by high-coercivity magnetic grains will have to be made in shore-based studies with better analytical conditions.

Given these results, most discrete samples were demagnetized at three to five steps up to 40–50 mT. As observed from pilot-sample studies, a soft component is removed at 10 mT on all samples. A stable component of low inclination is isolated in some samples; it has positive or negative inclination and thus is most probably a primary magnetization (Fig. 25; Samples 165-999A-3H-4, 63–65 cm, and 6H-3, 63–65 cm). On most samples, a steep positively inclined component persists to AF levels higher than 40 mT (Fig. 25; Samples 165-999A-11H-2, 61–63 cm, and 30X-2, 104–106 cm), which hampered our attempts to establish a magnetostratigraphy for most of Hole 999A.

Comparison of whole-core measurements at 20-mT AF demagnetization with results of discrete samples at the same demagnetization step show good agreement (Fig. 26), indicating that the steep inclination measured by the cryogenic magnetometer is not instrument related, but a true overprint. Even when the discrete samples are demagnetized in higher peak fields (typically 40 mT), they correlate well

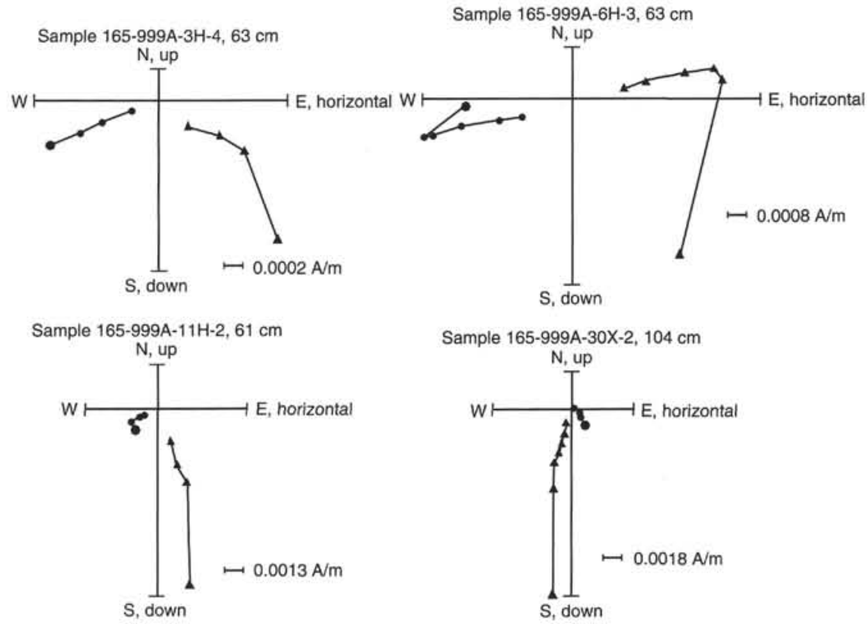

Figure 25. Vector demagnetization diagrams for four representative samples from Hole 999A. Samples with a stable component with low inclinations display normal (Sample 165-999A-3H-4, 63–65 cm) or reversed (Sample 165-999A-6H-3, 63–65 cm) polarity. Many samples, however, display a stable component with steep positive inclination induced by drilling (Samples 165-999A-11H-2, 61–63 cm, and 30X-2, 104–106 cm), which we were unable to remove by AF demagnetization using peak fields of 40–50 mT. Circles = declination, and triangles = inclination.

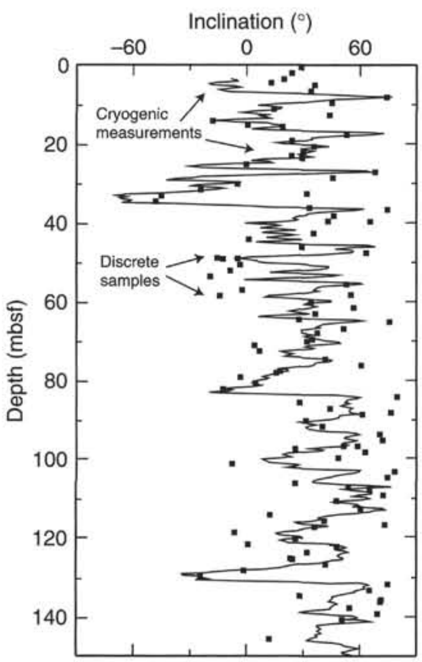

Figure 26. Comparison of results from whole-core measurements of inclination after AF demagnetization at 20 mT (solid line) with results from discrete samples demagnetized at 20 mT (black squares) for the top 150 mbsf of Hole 999A.

with cryogenic magnetometer results at 20 mT. This indicates, at least for the cores from the upper 150 mbsf, that higher demagnetization fields have been ineffective at removing the overprint. Because we are limited to fields of about 45 mT, shipboard removal of the overprint is not possible for these samples.

Results from Hole 999B

Results from discrete sample analyses of Hole 999B sediments are quite similar to those obtained from Hole 999A (see Appendix tables on CD-ROM, back pocket, this volume). A special emphasis was placed on analysis of the numerous volcanic ash layers from Core 165-999B-31R through to the bottom of the hole. It was expected that these ash layers would be less affected by the secondary overprint and thus better recorders of a stable characteristic remanent magnetization. Forty discrete samples from these layers were analyzed. The NRM of ash layers is of somewhat higher intensity than the clayey limestones and the contribution of the secondary overprint to the whole NRM seems less important. In general, the overprint is removed in peak fields of 5 or 10 mT, and a stable component with a shallow positive or negative inclination (normal or reversed polarity) is isolated for all ash layer samples. Comparisons between discrete sample measurements and whole-core measurements show less agreement for Hole 999B, owing to the good results obtained from these ashes and a few other samples from the lower ~30 m of the hole (Fig. 27).

Preliminary analysis from the incomplete demagnetization paths of the ash samples gives a crude estimate of 6° for the mean paleolatitude of the site for the interval between 45 and 60 Ma. This latitude is consistent with several models for the formation of the Caribbean Plate, including one in which the Caribbean Plate forms over the Galapagos hot spot and then migrates to the northeast, as proposed by Duncan and Hargraves (1984).

Magnetic Stratigraphy

Possible polarity assignments were difficult to establish at Site 999 given the difficulty of completely removing the secondary magnetization overprint. A polarity interpretation (Table 5) was attempted, however, on specific intervals of special interest based on the analysis of numerous discrete samples (one or two from each section). Using biostratigraphic data (see "Biostratigraphy" section, this chapter), the main Pliocene–Pleistocene chrons were identified and the boundaries of Chron C5n were also tentatively identified. The latter interval corresponds to a rapid change in the deep water chemistry at the transition of middle to late Miocene. This interval referred to as the late Miocene carbonate crash was recognized in Site 998 (see "Lithostratigraphy" section, "Site 998" chapter, this volume) and was also identified in Hole 999A (see "Lithostratigraphy" section, this chapter).

Polarity assignments for Hole 999B should be of great interest, especially at the base of the hole where the K/T boundary occurs in

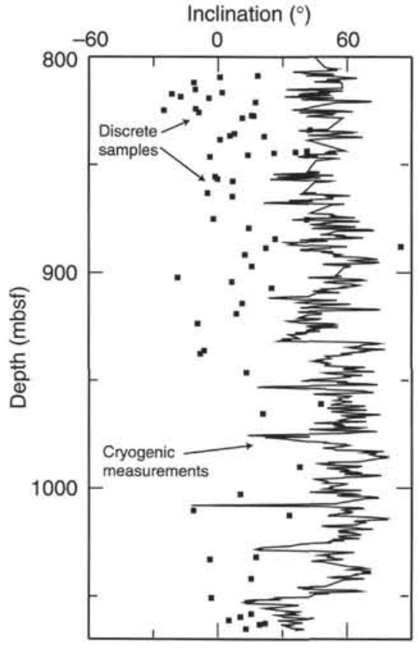

Figure 27. Comparison of results from split-core measurements of inclination after AF demagnetization at 20 mT (solid line) with results from discrete samples demagnetized at 20 mT (black squares) from the lower portion of Hole 999B.

Table 5. Depths of polarity chron boundaries in Hole 999A.

Magnetochron	Age (Ma)	Core, section, interval (cm)	Depth (mbsf)
C1n	0.78	4H-1, 83	27.43
C1r1n (t)	0.99	4H-6, 125	35.35
C2n (t)	1.77	7H-4, 10	59.7
C2n (o)	1.95	8H-1, 5	64.65
C2An.1n (t)	2.6	10H-2, 40	85.5
C2An.1r (t)	3.04	11H-5, 63	99.73
C2An.2r (o)	3.33	12H-4, 63	107.73
C2Ar (t)	3.58	13H-2, 62	114.22
C3n.1n (t)	4.18	15H-1, 62	131.72
C3n.1n (o)	4.29	15H-2, 62	133.22
C3n.2n (t)	4.48	15H-6, 63	139.29
C5n.1n (o)	9.775	28X-4, 138, to 28X-6, 115	254.58–257.35
C5n.2n (t)	9.185	29X-2, 95, to 29X-3, 94	260.85–262.34
C5n.2n (o)	10.839	32X-1, 17, to 32X-3, 126	287.67–291.46

Note: (t) = termination, (o) = onset.

Core 165-999B-59R. We present only a preliminary interpretation (Fig. 83) based on analyses of discrete samples and using biostratigraphic age assignments (see "Biostratigraphy" section, this chapter). Our results indicate, however, that post-cruise studies using numerous discrete samples should be able to produce a fairly high-resolution magnetostratigraphy.

SEDIMENTATION RATES AND MASS ACCUMULATION RATES

Sedimentation rates obtained from major planktonic foraminifer and calcareous nannofossil datums (Tables 3, 4) are illustrated in an age-depth plot (Fig. 28). Select nannofossil datums (the same as at Site 998) are used to estimate average sedimentation rates through time (Fig. 29). Uncertainties are relatively minor in the upper Miocene to Pleistocene, where microfossil preservation tends to be moderate to good, but they increase significantly in the middle and lower Miocene and in the Paleogene, where microfossil preserva-

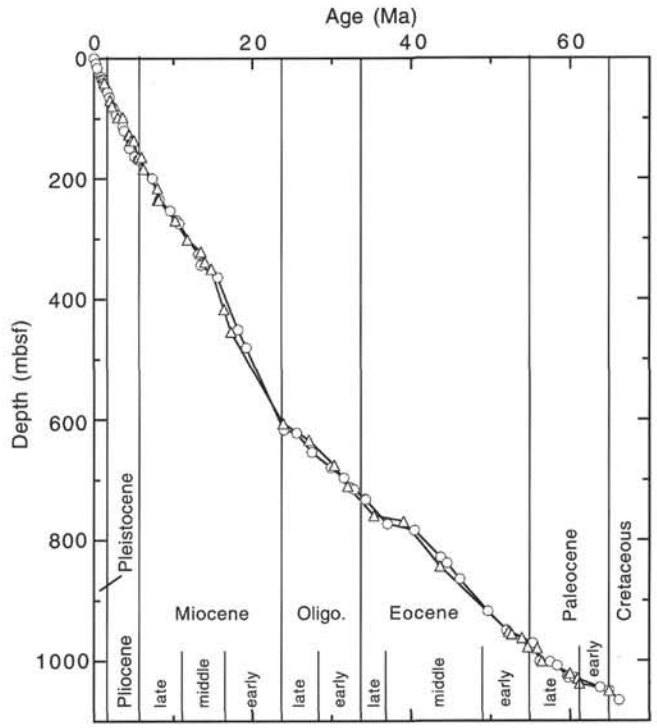

Figure 28. Age-depth plots for planktonic foraminifer (triangles) and calcareous nannofossil (circles) datums at Site 999.

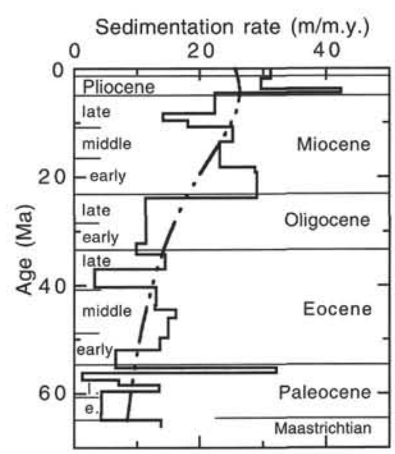

Figure 29. Sedimentation rate calculated from selected nannofossil datums plotted vs. age. The dotted curve is a third-order polynomial fitted to the data, with correlation coefficient $r = 0.99914$.

tion deteriorates. Negligible differences in age-depth plots between nannofossils and foraminifers (Fig. 28) are likely to have resulted from differences in sampling densities for the two fossil groups (only core-catcher samples have been studied for foraminifers vs. every section for nannofossils).

Age-depth plots illustrate largely continuous sedimentation at Site 999 (Fig. 28) for the past 66 m.y., but with rates varying by more than a factor of three (Fig. 29). Sedimentation rate history at Site 999 can be divided into 10 separate parts (Fig. 28):

1. 0–94.8 mbsf (upper Pliocene–Pleistocene),
2. 94.8–162.8 mbsf (lower–upper Pliocene),
3. 162.8–364.0 mbsf (middle Miocene–basal Pliocene),
4. 364.0–606.0 mbsf (lower–middle Miocene),

Table 6. Interpolated ages and mass accumulation rate data from Site 999.

Core, section, interval (cm)	Depth (mbsf)	Age (Ma)	DBD (g/cm^3)	LSR (cm/k.y.)	Bulk MAR (g/cm^2/k.y.)	$CaCO_3$ (wt%)	$CaCO_3$ MAR (g/cm^2/k.y.)	Noncarbonate MAR (g/cm^2/k.y.)
165-999A-								
1H-1, 32–34	0.32	0.01	0.67	3.36	2.25	61.14	1.38	0.87
1H-2, 32–34	1.82	0.05	0.71	3.36	2.38	45.73	1.09	1.29
1H-3, 32–34	3.32	0.10	0.73	3.36	2.45	37.73	0.92	1.53
1H-4, 32–34	4.82	0.14	0.78	3.36	2.62	45.98	1.21	1.42
1H-5, 32–34	6.32	0.19	0.79	3.36	2.65	35.32	0.94	1.72
1H-6, 32–34	7.32	0.22	0.79	3.36	2.64	39.65	1.05	1.59
2H-1, 32–34	7.92	0.24	0.78	3.36	2.61	48.56	1.27	1.34
2H-2, 32–34	9.42	0.28	0.82	3.36	2.74	51.06	1.40	1.34
2H-3, 32–34	10.92	0.33	0.78	3.36	2.63	55.48	1.46	1.17
2H-4, 32–34	12.42	0.37	0.84	3.36	2.83	57.23	1.62	1.21

Note: DBD = dry-bulk density, LSR = linear sedimentation rate, MAR = mass accumulation rate.

Only part of this table is produced here. The entire table appears on CD-ROM (back pocket).

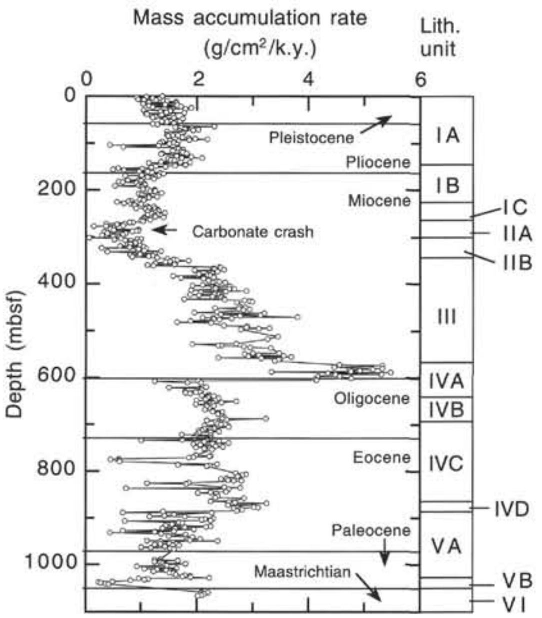

Figure 30. Mass accumulation rates for carbonate fraction vs. depth at Site 999. Lithologic unit boundaries are on the right (see "Lithostratigraphy" section, this chapter).

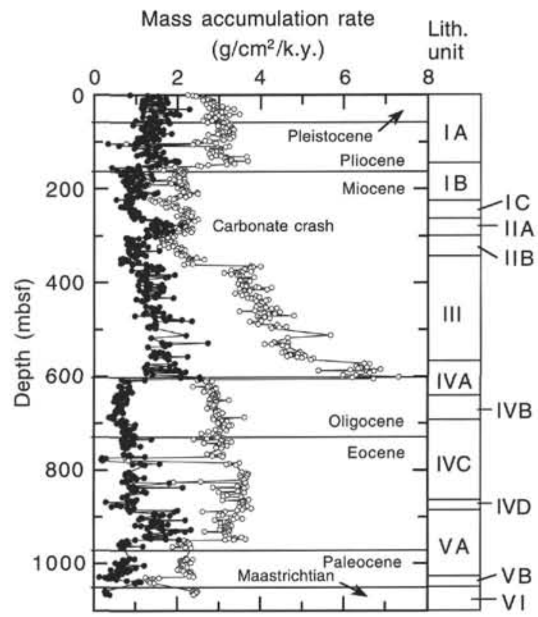

Figure 31. Mass accumulation rates for bulk sediment (open circles) and noncarbonate (solid circles) fraction vs. depth at Site 999. Lithologic unit boundaries are on the right (see "Lithostratigraphy" section, this chapter).

5. 606.0–773.1 mbsf (upper Eocene–Oligocene),
6. 773.1–783.9 mbsf (upper middle Eocene),
7. 783.9–949.9 mbsf (lower–middle Eocene),
8. 949.9–1029.4 mbsf (upper Paleocene–lower Eocene),
9. 1029.4–1050.2 mbsf (lower Paleocene), and
10. 1050.2–1066.4 mbsf (upper Maastrichtian).

Mass accumulation rates (MARs) for carbonate and noncarbonate fractions (Table 6) were calculated from dry-bulk density and carbonate percentage data through ten linear sedimentation rate segments (see "Physical Properties" section, this chapter) (Figs. 30–34). MARs of the detrital terrigenous and ash components of the bulk sediment are calculated from their absolute concentrations (see "Inorganic Geochemistry" section, this chapter), the dry-bulk density values, and the linear sedimentation rates.

Late Maastrichtian sedimentation rates (and bulk sediment accumulation rates, in parenthesis) were 14 m/m.y. (2.4 g/cm^2/k.y.) and early Paleocene rates averaged 6 m/m.y (1.4 g/cm^2/k.y.). Sedimentation rates (and accumulation rates) increased to an average of 9 m/m.y. (2.2 g/cm^2/k.y.) in the late Paleocene to earliest Eocene. From the early to middle Eocene, rates averaged 14 m/m.y. (3.3 g/cm^2/k.y.); rates decreased to 3 m/m.y. (0.8 g/cm^2/k.y.) in the late middle Eocene, then increased to 13 m/m.y. (2.9 g/cm^2/k.y.) for the late Eocene through Oligocene, and increased to 30 m/m.y. (6.5 g/cm^2/k.y.) in the early Miocene. Sedimentation rates averaged about 19 m/m.y. (4.4 g/cm^2/k.y.) through the middle and late Miocene but decreased to about 15 m/m.y. (2.0 g/cm^2/k.y.) in the interval surrounding the carbonate crash (see "Lithostratigraphy" section, this chapter) between 10 and 11 Ma (Fig. 29), in which nannofossil and planktonic foraminifer preservation reflects dissolution. Finally, in the Pliocene–Pleistocene interval, rates averaged about 32 m/m.y. but were quite variable with bulk MARs decreasing through late Pliocene and Pleistocene time (Fig. 29).

The sharp increase in sedimentation rates near the Oligocene/Miocene boundary (~24 Ma) corresponds in part to a marked upcore increase in ash layer frequency and the relative proportion of dispersed ash in the sediments (Fig. 52). The sharp drop in carbonate MARs within the lower Miocene marks the abrupt change in lithifi-

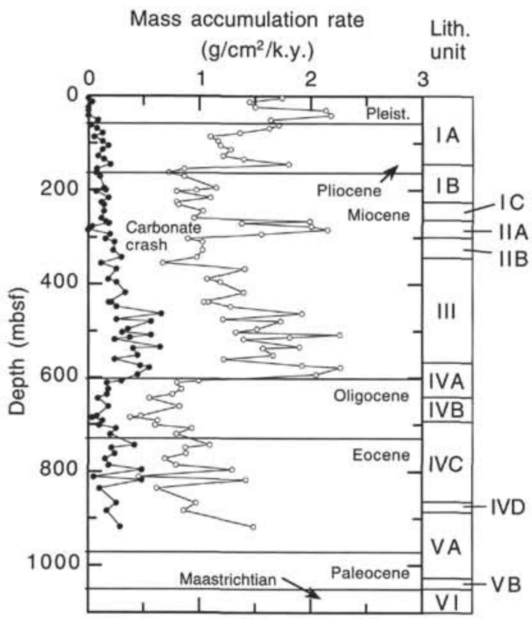

Figure 32. Mass accumulation rates for noncarbonate (open circles) and ash (solid circles) components as determined from trace element ratios (see "Inorganic Chemistry" section, this chapter).

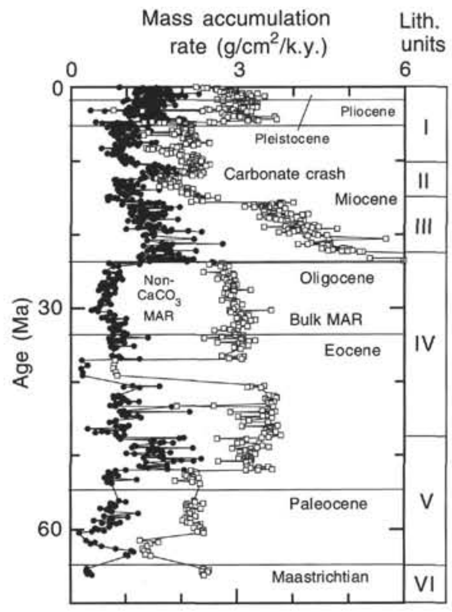

Figure 34. Mass accumulation rates for bulk sediment (open squares) and noncarbonate (solid circles) fraction vs. age at Site 999.

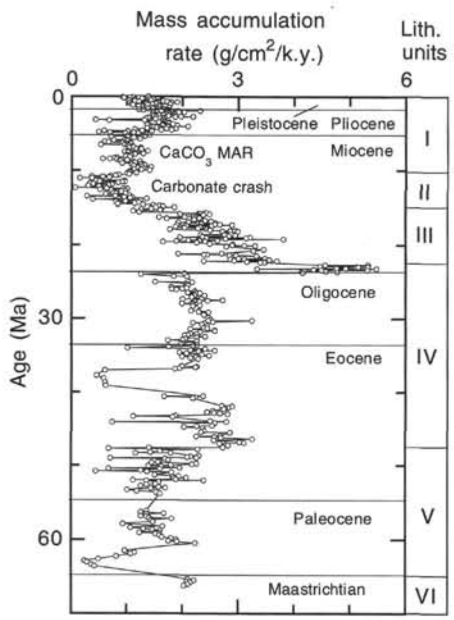

Figure 33. Mass accumulation rates for carbonate fraction vs. age at Site 999.

cation from clayey limestone (lithologic Subunit IVA) to clayey chalk and mixed sediment (lithologic Unit III). Changes in sedimentation rates in the Eocene show no correlation with the interval of increased ash frequency in the middle and upper Eocene.

ORGANIC GEOCHEMISTRY

Introduction

Concentrations of inorganic carbon ($CaCO_3$) were measured at a frequency of one sample per section for each core collected in Holes 999A and 999B (~650 total analyses). Total organic carbon (TOC) values were determined for approximately one sample per core in Hole 999A and approximately one sample per every other core in Hole 999B. In conjunction with the measurement of total carbon, from which TOC values were determined, additional data were generated for concentrations of total nitrogen (N_T) and total sulfur (S_T). Finally, headspace gases were monitored routinely in compliance with drilling safety requirements (one sample/core). Analytical details are provided in the "Organic Geochemistry" section of the "Explanatory Notes" chapter (this volume).

Despite broad similarities to the diagenetic profiles at Site 998, the sediments at Site 999 are characterized by slightly greater concentrations of TOC. Although very subtle, the increased burial of reactive organic phases has facilitated greater rates and extents of suboxic to anoxic diagenesis. These differences are recognized most readily in the pore-water profiles for sulfate, ammonium, manganese, and iron; in addition, the concomitant production of alkalinity during microbial degradation of organic matter appears to drive precipitation of calcium carbonate in the uppermost intervals of the section (see "Inorganic Geochemistry" section, this chapter).

Concentrations of Inorganic and Organic Carbon, Total Nitrogen, and Total Sulfur

Concentration trends for inorganic carbon are discussed and graphically presented in the "Lithostratigraphy" section of this chapter. Results for $CaCO_3$, along with data for TOC, N_T, and S_T, are provided in Table 7. Holes 999A and 999B are characterized by low concentrations of TOC. Unlike the low levels at Site 998, however, the majority of the TOC concentrations in Hole 999A are within analytical resolution, yielding a mean TOC value of 0.11 ± 0.11 wt%. In deeper portions of the section (i.e., Hole 999B), the vast majority of the TOC concentrations are below analytical resolution (reported as values of 0.00 in Table 7). The values for TOC in Hole 999A show a significant degree of downcore scatter, reflecting the effects of varying degrees of $CaCO_3$ dilution and, when viewed on long time scales, the overall non-steady-state nature (historical variability) of the system. The magnitude of the latter effect is corroborated by evaluations of the data on a $CaCO_3$-free basis.

Table 7. Concentrations of inorganic carbon, calcium carbonate, total carbon, total organic carbon, total nitrogen, and total sulfur, Holes 999A and 999B.

Core, section, interval (cm)	Depth (mbsf)	C_{inorg} (wt%)	$CaCO_3$ (wt%)	Total C (wt%)	TOC (wt%)	Total N (wt%)	Total S (wt%)
165-999A-							
1H-1, 34–35	0.34	7.34	61.1				
1H-2, 34–35	1.84	5.49	45.7				
1H-3, 34–35	3.34	4.53	37.7	4.60	0.07	0.05	0.09
1H-4, 34–35	4.84	5.52	46.0				
1H-5, 34–35	6.34	4.24	35.3				
1H-6, 34–35	7.34	4.76	39.7				
2H-1, 34–35	7.94	5.83	48.6				
2H-2, 31–32	9.41	6.13	51.1				
2H-3, 31–32	10.91	6.66	55.5	6.72	0.06	0.04	0.06
2H-4, 34–35	12.44	6.87	57.2				
2H-5, 31–32	13.91	4.73	39.4				
2H-6, 34–35	15.44	6.81	56.7				
2H-7, 32–33	16.92	4.39	36.6				
3H-1, 32–33	17.42	5.91	49.2				
3H-2, 31–32	18.91	7.02	58.5				

Notes: Data are reported as weight percent (wt%). C_{inorg} = inorganic carbon, $CaCO_3$ = calcium carbonate, TOC = total organic carbon.

Only part of this table is produced here. The entire table appears on CD-ROM (back pocket).

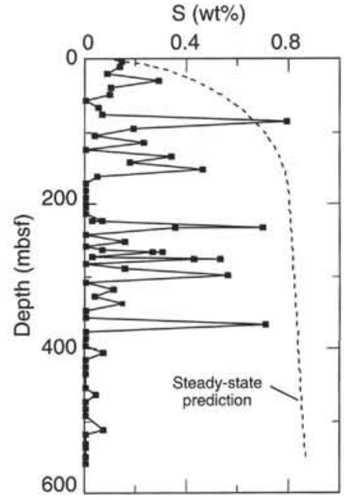

Figure 35. Downcore distribution of total sulfur concentrations for Hole 999A reported as weight percent on a noncarbonate basis. A schematic representation of the predicted distribution of pyrite sulfur, assuming a steady-state diagenetic model, has been included for comparison.

When viewed on a total sediment basis, the most enriched interval of TOC is found between ~260 and 340 mbsf, with values approaching 0.4 wt%. This subtle enrichment coincides with a pronounced minimum in concentrations of $CaCO_3$ (i.e., the carbonate crash), thus further illustrating the effects of carbonate dilution. When the data are viewed on a carbonate-free basis, any apparent relationship with regard to the carbonate minimum breaks down and the scatter is further emphasized. The overall low levels of organic matter (OM) are a product of oxic degradation within the water column and at the sediment-water interface, in combination with $CaCO_3$ dilution and comparatively low rates of OM primary production. Furthermore, extensive bioturbation, particularly that observed for the lower Pliocene through Miocene section (see "Lithostratigraphy" section, this chapter), would have the effect of exacerbating the processes of oxic decay. The low concentrations of N_T are consistent with the low levels of TOC. In light of the scarcity of organic carbon, no effort was made to further characterize the organic matter using either Rock-Eval pyrolysis or C/N values.

Diagenetic redox pathways at Site 999 are dictated largely by the limited availability of labile organic matter. Although smoothed by diffusion, the pore-water profile for sulfate shows a systematic decrease that extends to approximately 150–200 mbsf (see "Inorganic Geochemistry" section, this chapter). The corresponding increase in pore-water ammonium over the same depth interval reflects the degradation of OM during dissimilatory sulfate reduction (DSR), as well as during microbially mediated reduction of Fe and Mn. Although interpretations are constrained by the somewhat limited resolution provided by the sampling strategy, concentrations of TOC are sufficiently large that no clear distinction (i.e., observable vertical separation) can be made between suboxic (Mn- and Fe-dominated) and anoxic (DSR-dominated) diagenetic regimes (Froelich et al., 1979).

The slightly more reducing system that characterizes Site 999, when compared with Site 998, may be the product of a greater flux of organic carbon. Conversely, the greater bulk sediment accumulation rates at Site 999 favor the rapid burial of labile organic phases and, hence, increased availability for anaerobic respiration (e.g., sulfate reduction). Under conditions of slower sediment accumulation, a larger percentage of the metabolizable fraction is lost through processes of aerobic degradation. Consequently, data compilations from a wide range of marine environments show a strong positive correlation between sedimentation rate and organic reactivity (Toth and Lerman, 1977; Berner, 1978).

Despite the observed trends for sulfate consumption, production of hydrogen sulfide was still comparatively minor. Furthermore, reaction with the readily available Fe delivered as detrital- and ash-related mineral phases would maintain the pore-water sulfide at essentially negligible levels. Pending shore-based analyses with an emphasis of S speciation, the S_T data in Table 7 are assumed to represent FeS_2. The low concentrations of pyrite-S are perhaps the most obvious characteristic of these data, particularly in the lower portion of the section. As with TOC, the highest values of S_T coincide commonly with the lowest values of $CaCO_3$ (e.g., within the carbonate minimum occurring between ~260 and 340 mbsf), once again highlighting the effects of dilution by carbonate sediment.

The errors in the S_T determination are such that it is impossible to interpret downcore trends that exceed first-order variability; the lowest values and the smaller scale fluctuations are within error. Somewhat surprisingly, total sulfur concentrations in Hole 999A fail to show systematic variation, whether reported on a bulk sediment basis or normalized to the noncarbonate fraction (Fig. 35). A schematic representation of progressive diagenetic pyrite formation under typical steady-state marine conditions has been included for comparison in Figure 35. Similarly, accumulations of OM and S_T are strongly decoupled, which is unexpected given the strong degrees of carbon limitation that characterize this system. To some degree, the observed scatter reflects the state of analytical precision. However, future studies will address the possibility of external sources of dissolved sulfide that are not linked to local deposition of organic matter (e.g., basement-derived fluids moving along permeable zones such as faults and porous ash layers). The distribution of S_T in Figure 35 is reminiscent of the downcore variability that characterizes distributions of ash dispersed within the bulk sediment and ash found as discrete layers. Interestingly, the ash layers in the upper part of Hole 999A are highly altered and commonly display dramatic enrichments in pyrite-S and Ni (see "Volcanology and Igneous Petrology" section, this chapter). These enrichments may be linked mechanistically to externally derived fluxes of sulfur and metals into the host sediments; post-cruise sulfur isotopic analyses will address this hypothesis.

Volatile Hydrocarbons

As part of the shipboard safety and pollution monitoring program, hydrocarbon gases were measured continuously in the sediments of

Table 8. Interstitial water composition, Holes 999A and 999B.

Core no.	Depth (mbsf)	pH	Alkalinity (mM)	Salinity (g/kg)	Cl^- (mM)	Na^+ (mM)	Mg^{2+} (mM)	Ca^{2+} (mM)	SO_4^{2-} (mM)	PO_4^{3-} (µM)	NH_4^+ (µM)	$Si(OH)_4$ (µM)	K^+ (mM)
165-999A-													
1H	4.5	7.3	3.571	35	560	470	50.8	10.60	27.09	1.2	50	144	11.85
3H	21.6	7.36	4.625	34.5	567	477	49.5	9.38	24.20	0.7	268	165	11.65
6H	50.5	7.42	5.014	34.3	566	480	46.1	8.88	20.85	0.9	436	260	10.84
9H	78.6	7.38	5.154	34.2	566	485	43.3	7.69	17.94	0.9	588	202	10.24
12H	107.1	7.4	5.055	34.1	573	486	40.9	8.65	15.72	0.7	551	196	10.22
15H	135.6	7.72	4.746	34	573	474	37.9	9.03	14.13	0.4	706	236	10.06
18H	164.1	7.54	3.814	34	577	479	35.0	10.62	13.02	0.9	614	285	9.38
21H	192.6	7.45	3.67	34	575	486	32.2	12.41	12.46	0.8	739	263	10.29
25X	224.4	7.63	3.842	34	578	482	31.0	15.08	13.85	2.5	638	875	10.74
28X	253.2	7.67	4.503	34	574	483	26.9	17.56	12.41	1.5	568	543	9.25
31X	282.1	7.8	2.544	32.5	561	470	24.8	20.42	12.45	BDL	656	220	9.83
34X	310.8	7.23	4.06	34	589	491	21.2	21.49	12.09	2.2	604	1139	10.82
37X	339.7	7.38	3.262	34	590	484	21.0	22.34	14.39	2.2	423	1016	10.80
40X	368.5	7.42	2.694	34	585	493	17.1	24.77	12.42	2.2	453	995	11.39
43X	397.5	7.65	3.284	34	588	497	15.9	26.76	12.95	2.1	624	1136	11.33
46X	426.3	7.32	2.06	34	579	498	14.2	28.96	12.89	2.2	565	1059	10.66
49X	455.2	7.59	0.955	34	587	492	12.4	30.21	12.88	2.0	351	921	9.93
53X	493.6	7.6	1.329	34	592	502	12.0	32.47	12.95	3.3	508	1130	9.61
58X	532.1	8.23	1.374	34	586	507	10.4	35.91	13.17	2.3	413	856	8.75
60X	549.8	7.76	0.828	34	589	509	10.6	37.01	13.48	2.0	473	1071	8.44
165-999B-													
5R	574.0				590	511	8.2	37.50	13.31			232	7.32
8R	593.0				589	512	8.2	40.00	13.81			220	6.17

Notes: Missing data in Hole 999B indicate "not measured." BDL = below detection limit. This entire table also appears on CD-ROM (back pocket).

Table 8 (continued).

Core no.	Depth (mbsf)	Fe (µM)	Mn (µM)	Sr (µM)	Rb (µM)	Li (µM)
165-999A-						
1H	4.5	31	112	91	2.7	23
3H	21.6	39	41	119	2.2	26
6H	50.5	26	27	172	2.2	33
9H	78.6	43	21	235	1.9	43
12H	107.1	37	17.5	308	2.0	59
15H	135.6	19	15.5	381	1.9	83
18H	164.1	1	12.5	446	2.0	110
21H	192.6	7	20.5	520	2.2	136
25X	224.4	3	12	584	2.8	156
28X	253.2	9	14.5	691	2.2	197
31X	282.1	BDL	14	824	2.6	216
34X	310.8	3	8	979	3.5	227
37X	339.7	3	4.5	1098	3.6	201
40X	368.5	1	2.5	1227	3.6	200
43X	397.5	7	2.5	1283	3.6	185
46X	426.3	4	2.5	1434	3.4	176
49X	455.2	2	2	1466	3.1	154
53X	493.6	3	2	1558	2.9	136
58X	532.1	3	2	1452	2.8	111
60X	549.8	3	2.5	1398	2.6	105
165-999B-						
5R	574.0			1223		
8R	593.0			1154		

Holes 999A and 999B (one analysis/core) using the headspace technique. Consistent with the low levels of organic carbon and the presence of dissolved sulfate at concentrations of 10–15 mM at a depth of ~550 mbsf, methane concentrations were found to range between trace levels and 12 ppm throughout the entire section recovered in Hole 999A. The extremely low concentrations of TOC and S_T in Hole 999B, for which pore-water data are not available, argue for a persistence of the very low rates of sulfate reduction inferred from the deeper portions of the sulfate profile from Hole 999A (see "Inorganic Geochemistry" section, this chapter). As expected, the methane concentrations in Hole 999B were low and ranged from 2 to 23 ppm. Although the data are scattered, there appears to be an overall increase in methane concentration with increasing depth at Site 999. The scarcity of methane is expected given the low levels of TOC, the likely persistence of sulfate over the complete section, and the common observation that significant methanogenesis occurs only after sulfate is depleted and sulfate reduction has progressed essentially to completion (Martens and Berner, 1974). The slightly elevated levels of methane in the lower portions of Hole 999B reflect either production within organic-rich microenvironments or diffusion from below. Additional hydrocarbon gases were not observed.

INORGANIC GEOCHEMISTRY

Interstitial Water Chemistry

Introduction

Twenty-two interstitial water samples were collected at Site 999: 20 from Hole 999A at depths from 4.5 to 549.8 mbsf, and two from Hole 999B at depths of 574 and 593 mbsf (Table 8). Negligible yields from 5-cm whole rounds collected at greater depths prevented further sampling. Analytical methods are detailed in the "Inorganic Geochemistry" section of the "Explanatory Notes" chapter (this volume). Samples were analyzed for pH, salinity, chlorinity, alkalinity, sulfate, phosphate, ammonium, silica, Na^+, Fe, Mn, Mg^{2+}, Ca^{2+}, K, Sr, Rb, and Li. Pore-water profiles were not normalized to Cl^- concentrations because of the small (~5% relative) variation in Cl^- abundance and because of the uncertainty concerning the conservative behavior of Cl^- throughout the section. Data for volcanic ash thickness, degree of alteration, mineralogy, and frequency (see "Igneous Petrology and Volcanology" section, this chapter) are used to evaluate the relationship between ash distribution and downcore geochemical trends in both pore waters and sediments. Reference seawater values, derived from mean ocean-bottom-water compositions (Millero and Sohn, 1992), are plotted as arrows on the axes of the various diagrams.

Despite a broadly similar depositional environment, some chemical signatures observed for the interstitial waters from Site 999 contrast with those of Site 998. The upper portions of the section contain a higher reactive organic component, which is manifested by greater rates of sulfate reduction. This observation, together with a greater abundance of pyrite, indicates a more reducing environment than at Site 998. The increased availability of organic matter relative to Site 998 is related to the more rapid sediment accumulation at Site 999, although total organic carbon (TOC) remains low in Hole 999A (mean = 0.11 ± 0.11 wt%) and is essentially zero in Hole 999B. Chemical signatures that mimic most closely the distribution of ash in discrete layers are associated with the minor interval of increased

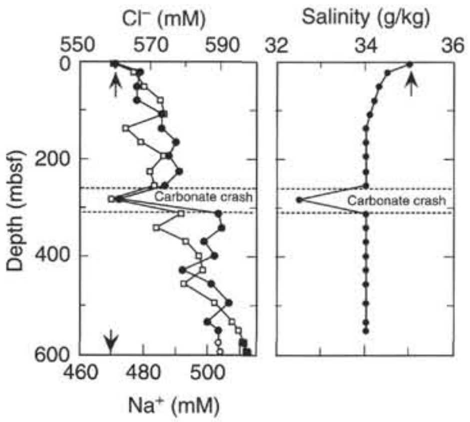

Figure 36. Depth profiles of Na^+ (squares), Cl^- (circles), and salinity in Site 999 interstitial waters. The transition from open to closed or closed to open symbols on a single profile differentiates between Hole 999A and Hole 999B. Arrows indicate mean ocean-bottom-water composition taken from Millero and Sohn (1992).

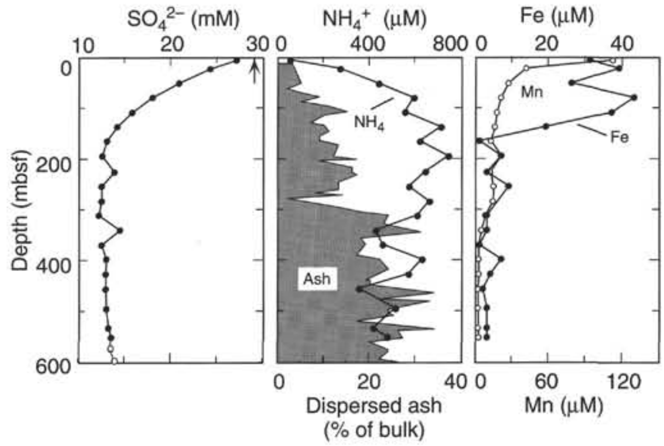

Figure 37. Depth profiles of sulfate, ammonia, iron (solid circles), and manganese (open circles) in Site 999 interstitial waters. The transition from open to closed or closed to open symbols on the sulfate profile differentiates between Hole 999A and Hole 999B. The fraction of bulk sediment composed of dispersed volcanic ash (shaded area) is also plotted with depth on the ammonium profile to permit evaluation of the effect of ash on pore-water chemistry. Arrow indicates mean ocean-bottom-water sulfate composition taken from Millero and Sohn (1992).

ash deposition at ~170–270 mbsf. These ashes are altered to a greater degree than those within the main interval of Miocene ash centered at ~400–500 mbsf (Fig. 57). The less obvious relationship between pore-water chemistry and the presence of volcanic material at 400–500 mbsf may be a function of the freshness of the ashes in this lower interval, combined with a greater component of terrigenous matter and, most importantly, contributions from the abundant dispersed ash. Despite the smoothing effects of diffusion, pore-water signatures of local-scale processes are retained. Large volumes of Eocene ash at depths that exceed the pore-water sampling may exert greater control than basement on the distribution of some elements such as Mg^{2+}.

pH, Salinity, Sodium, and Chlorinity

Values for interstitial pH increase in a nonsystematic manner from values of 7.3 close to the sediment-water interface to ~7.8 at ~280 mbsf (Table 8). Although sampling resolution is low, the pronounced pH maximum at this depth is broadly coincident with the carbonate crash (see "Lithostratigraphy" section, this chapter). Values generally increase, albeit with noise, in the deeper parts of the pore-water profile below the $CaCO_3$ minimum, to a maximum pH value in excess of 8.2. This relationship reflects the alteration of ash layers found in this part of the profile (see below). Concentration trends for Na^+ and Cl^- show strongly similar patterns and increase with depth from surficial values characteristic of seawater to ~500 and 600 mM, respectively (Fig. 36). The minima for both species at 280 mbsf correspond precisely with the carbonate crash. The decrease in Na^+ and Cl^- within the $CaCO_3$ minimum may be caused by dilution from water released from interlayer sites within the abundant associated clay minerals. As expected, a similarly sharp decrease in salinity occurs in the same interval (Fig. 36).

Sulfate, Ammonium, Iron, Manganese, and Phosphate

Concentrations of these species measured in pore waters from the upper levels of Site 999 show classic redox-controlled reaction profiles that are readily explained by the progressive breakdown of labile phases of organic carbon. Levels of pore-water sulfate decrease from values close to those of seawater to ~12–13 mM over the uppermost 170 m of the section and remain at this lower value with increasing depth (Fig. 37). The morphology of the sulfate profile is controlled by rates of reaction associated with organic degradation, but it is diffusionally smoothed and becomes asymptotic at depth. This asymptotic relationship reflects the gradual depletion of original reactive organic phases, according to the general reaction:

$$1/53(CH_2O)_{106}(NH_3)_{16}(H_3PO_4) + SO_4^{2-} \rightarrow$$

$$2HCO_3^- + HS^- + 16/53NH_3 + 1/53H_3PO_4 + H^+. \quad (1)$$

An absence of complete sulfate consumption is consistent with the low ambient levels of methane observed throughout the section (see "Organic Geochemistry" section, this chapter). The more rapid decline in sulfate abundance with increasing depth in this profile compared with that of Site 998 (compare Fig. 37), together with the greater extent of sulfate reduction over comparable stratigraphic thicknesses, is likely a function of an increased flux of reactive organic matter in combination with more rapid rates of sediment accumulation. Greater bulk accumulation rates, although having a dilution effect, facilitate a more rapid removal of organic matter from the overlying source of oxygen and, thus, favor a greater relative consumption by way of anaerobic respiration (see "Organic Geochemistry" section, this chapter).

Organic remineralization is also reflected in the ammonium pore-water profile, which, as expected from Equation 1, rapidly increases over the same depth interval that sulfate decreases. The gradual decline in ammonium below 200 mbsf could record a waning contribution from organic degradation in combination with clay-mineral alteration and authigenesis. Detrital clay minerals may form an ammonium sink through incorporation as either a trace cation or through exchange with K (Stevenson and Cheng, 1972). The downcore decrease in ammonium is approximately coincident with the appearance of abundant ashes, many of which contain biotite. However, a relatively high level of pore-water ammonium is maintained with increasing depth, suggesting that release of ammonium by weathering of micas present within the ash layers may balance consumption. Mass balance considerations based on the reaction stoichiometry for bacterial sulfate reduction (assuming a Redfield C:N ratio) indicate that uptake of biologically liberated ammonium by way of silicate alteration may be important in the uppermost sediment layers.

The microbial breakdown of organic matter and the concomitant reductive dissolution of Mn oxides (oxyhydroxides) can be invoked to explain the elevated pore-water Mn content (~110 μM) in the up-

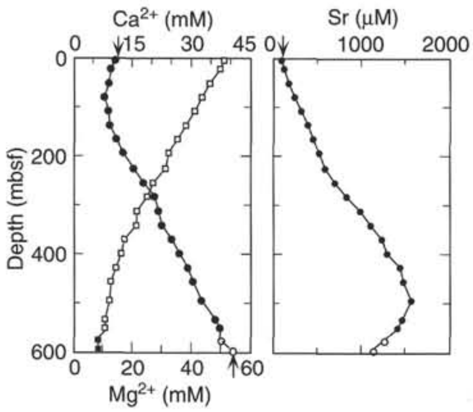

Figure 38. Depth profiles of Ca^{2+} (circles), Mg^{2+} (squares), and Sr in Site 999 interstitial waters. The transition from open to closed or closed to open symbols on a single profile differentiates between Hole 999A and Hole 999B. Arrows indicate mean ocean-bottom-water composition taken from Millero and Sohn (1992).

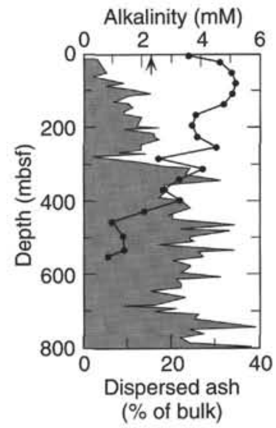

Figure 39. Depth profile of alkalinity (solid circles) for Site 999 interstitial waters. The fraction of bulk sediment composed of dispersed volcanic ash (shaded area) is also plotted with depth to permit evaluation of the effect of ash on pore-water chemistry. Arrow indicates mean ocean-bottom-water alkalinity value taken from Millero and Sohn (1992).

per 10 m of Site 999. The sharp decline in Mn concentrations may reflect surface adsorption or the effect of crystal-chemical partitioning during a period of carbonate precipitation implied from the Ca^{2+} distribution profile (Fig. 38). The broad, but subtle, subsurface maximum for concentrations of dissolved Mn (and Fe) from 240 to 300 mbsf coincides with the pronounced $CaCO_3$ minimum, suggesting a lack of carbonate dilution of detrital Mn. The Fe maximum in the upper 100 m reflects organic-matter degradation in association with a metal oxide electron acceptor. The general coincidence between the initial elevated levels of Fe and Mn is in contrast to the hierarchy of redox reactions often observed in deep-marine sediments (Froelich et al., 1979), suggesting a comparatively rapid progression through the suboxic sequence. The rapid decrease in Fe through 150 mbsf occurs well below the zone of Ca^{2+} decrease, suggesting that the effect of carbonate precipitation and adsorption for Fe is not as significant as for Mn. This dramatic decrease in pore-water Fe at 150 mbsf corresponds with the visual estimate of the first abundant pyrite in the sediment column (see "Lithostratigraphy" section, this chapter), implying an Fe sink caused by bacterial sulfide production. This relationship, however, is not readily apparent in the total sulfur content of the bulk sediment (see "Organic Geochemistry" section, this chapter). Linkages to the abundant precipitation of iron sulfide observed in association with the ash layers may be a factor (see "Igneous Petrology and Volcanology" section, this chapter).

Phosphate concentrations are low and highly variable over the length of the section (Table 8). With one exception (3.3 µM), the concentrations are less than 3 µM and fail to show a systematic increase in the upper 100 mbsf that would be expected with microbial oxidation of organic matter (cf. ammonium and alkalinity; Figs. 37, 39). Variability in the phosphate profile may reflect the comparatively high Fe contents of the associated sediment and the strong capacity of ferric-oxides to scavenge phosphate (Ruttenberg, 1992; Krom and Berner, 1980). As a result, the phosphate profile may be linked intimately to the redox cycling of Fe. The very low levels of dissolved phosphate above and below the ash maximum are consistent with relatively low concentrations of TOC and are maintained by effective adsorption of phosphate onto the surfaces of the abundant calcium carbonate within the host sediment (Walter and Burton, 1986; see "Organic Geochemistry" section, this chapter).

Calcium, Magnesium, and Strontium

Calcium and magnesium show a familiar antithetic relationship (Fig. 38). The profile for Ca^{2+} is dominated by $CaCO_3$ dissolution and precipitation reactions. A subtle, but meaningful, decrease of Ca^{2+} in the upper 75 m indicates carbonate precipitation. This interval of carbonate precipitation may be driven by the effects of bicarbonate production that results from the oxidation of organic matter under oxygen-deficient diagenetic conditions (e.g., bacterial reduction of Mn, Fe, and sulfate). The initial Ca^{2+} decrease is followed downcore by a steady increase that most likely records reactions of carbonate dissolution and recrystallization. There is no perceptible break in slope of the Ca^{2+} profile over the interval of the Miocene carbonate crash. If the carbonate minimum is a dissolution phenomenon, these data speak to the comparatively early timing of the event and the effects of diffusional smoothing.

Concentrations of pore-water Mg^{2+} decrease by approximately a factor of three over 550 m of sediment depth. Similar systematic decreases in Mg^{2+} are observed often in other DSDP/ODP pore-water profiles and commonly are interpreted as reflecting broad-scale diffusion associated with basement alteration (Geiskes, 1983). At Site 999, however, precipitation of dolomite in the sediment column, as well as development of Mg-rich smectites during weathering of the abundant silicic ashes, could provide additional sinks.

Strontium concentrations increase monotonically downcore from values close to those of seawater in the uppermost section to levels in excess of 1500 µM by ~500 mbsf (Fig. 38). This steady increase probably is dominated by the dissolution and reprecipitation of calcite, which has a high initial Sr concentration. Strontium decreases dramatically in the lowest available samples, possibly because of uptake during reverse weathering or $SrSO_4$ precipitation.

Alkalinity

The pore-water alkalinity profile is mediated by organic degradation and ash alteration. The marked increase in alkalinity over the uppermost 100 mbsf is caused by the production of bicarbonate during microbial breakdown of organic matter (Fig. 39). Ash alteration may contribute (see Eq. 2), but its low abundance, as layers and as dispersed matter in the upper 100 m of the sediment column, indicates that this source is minor. As discussed above, the increase in alkalinity will enhance carbonate saturation and facilitate carbonate precipitation, as manifested in the decreasing trend for dissolved Ca^{2+} over the same interval. Minor fluctuations superimposed on a gradual decline in alkalinity deeper downhole may record localized responses to the alteration of glass and silicate components in the ash layers (i.e., smectite formation). The maximum between 170 and 270 mbsf is a likely example of such alteration. The decline in alkalinity below a predominantly organically controlled maximum in the upper part of

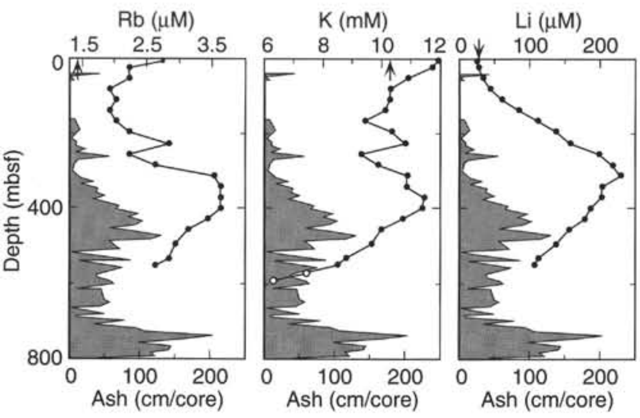

Figure 40. Depth profiles of Rb, K, and Li in Site 999 interstitial waters. The transition from open to closed or closed to open symbols on a single profile differentiates between Holes 999A and 999B. Quantification of the ash component is presented as thickness of ash per core (shaded area) to permit evaluation of the effect of ash on pore-water chemistry. Compare with Figure 41 (see text). Arrows indicate mean ocean-bottom-water composition taken from Millero and Sohn (1992).

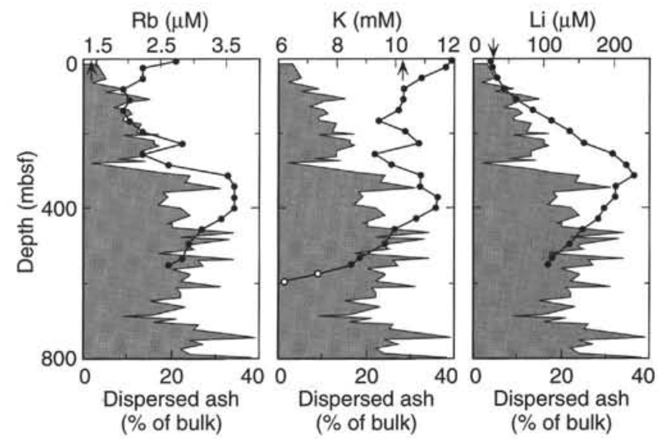

Figure 41. Depth profiles of Rb, K, and Li in Site 999 interstitial waters. The transition from open to closed or closed to open symbols on a single profile differentiates between Holes 999A and 999B. Quantification of the ash component is presented as the percentage of dispersed ash (shaded area) in the sediment column at a given depth to permit evaluation of the effect of ash on pore-water chemistry. Compare with Figure 40 (see text). Arrows indicate mean ocean-bottom-water composition taken from Millero and Sohn (1992).

the section, despite steady carbonate dissolution and recrystallization, reflects the removal of cations and the bicarbonate ion from solution during silicate precipitation. This net decrease (with scatter) is conspicuously independent of the overall distribution of ash layers, or of dispersed ash through the sedimentary column (Fig. 39), but the greatly enhanced microfossil preservation seen near the tops of ash layers attests to highly localized effects not resolved by the pore-water profile.

Rubidium, Potassium, and Lithium

Values for pore-water Rb and K at the top of the sediment column are enriched relative to seawater (Fig. 40). Potassium declines in concentration with increasing depth, but with two subsurface maxima superimposed on this general trend that coincide with similar enrichments in Rb. Downcore variations in the Rb and K concentrations do not mirror the distribution of ash layers within the sediment column to the extent observed at Site 998. The upper sequence of megascopic ash layers in the sedimentary column (from ~170 to 270 mbsf) appears to exert a more direct effect on pore-water chemistry than the underlying, more abundant zone of ash (below ~300 mbsf). This relationship is illustrated by the greater coincidence and relative magnitudes of the observed subsurface Rb and K peaks at the 170–270 mbsf ash zone when compared with the lower ash zone. This differing response is supported by the fact that the upper ashes appear to be substantially more altered than most of the ashes lower than ~300 mbsf (see "Igneous Petrology and Volcanology" section, this chapter). Thus, the more altered nature of the upper ashes may provide a more labile source of cations and silica when compared to the fresher glass observed in the lower ash horizons. However, despite obvious petrographic differences in relative degrees of alteration, bulk chemical analyses of ashes from the entire ash sequence show evidence of considerable chemical alteration (see "Igneous Petrology and Volcanology" section, this chapter).The offset of the Rb and K peaks located between ~300 and 470 mbsf relative to the main peak in Miocene ash layer distribution may simply be a result of the inadequacies of the observed ash frequency or thickness as proxies for the total volume of ash per core. Increases in pore-water concentrations of K and Rb above the major ash interval appear to be a function of the high abundance of dispersed ash in the sediment column over this interval (Fig. 41), as calculated from solid-phase geochemistry (see "Sediment Chemistry" section, below). The dispersed ash signature thus appears to affect pore-water chemical signatures in a similar manner to the megascopic ash layer distribution. Therefore, it appears necessary to quantify this component using solid-phase data (see "Sediment Chemistry" discussion, below).

Although the overall decrease of Rb and K with depth might represent the postulated effects of a basement sink (e.g., Geiskes, 1983), there are clear localized signals that can be reconciled with observed lithologic variations within the sediment column. For example, Rb and K decrease in approximate coincidence with a downcore decrease in the intensity of the Miocene ash signal. This trend could be interpreted simply as reflecting a diminished source effect; however, it is possible that reverse weathering reactions occur that reincorporate cations from the aqueous phase (e.g., clay and/or zeolite precipitation).

The pore-water Li profile exhibits a pronounced subsurface concentration maximum at ~300 mbsf. This maximum is almost 10 times more enriched than the seawater values that characterize the uppermost intervals (Fig. 40). This peak is coincident with the main silica pore-water peak (see discussions below) and is slightly offset from the maxima for Rb and K. Like Rb and K, the subsurface maximum for Li is not coincident with the megascopic ash layer distribution, but it does coincide with a maximum in the dispersed ash component. As observed for Rb and K, but in contrast to the observed behavior for Si (see below), levels of Li decrease steadily below the maximum level, suggesting the combined effects of a diminished source and a loss through silicate reactions. The effect of a large volcanogenic source of Si and Li obscures any detailed relationship between Li and biogenic silica dissolution (e.g., Geiskes, 1983).

Silica

Concentrations of pore-water silica (Fig. 42) appear to be influenced by both the megascopic and dispersed ash component, similar to that observed for Rb, K, and Li. Pore waters from the upper 180 m of section exhibit a very gradual increase in silica levels from seawater values to ~250 μM. A subtle concentration maximum corresponds with the uppermost ash layers. This interval is followed at depth by an increase to 850 μM, which correlates closely with the first main occurrence of ash at 170–270 mbsf. The highly altered nature of the siliceous ash in this interval indicates that the ash is a significant source of pore-water silica by way of silicate and glass weathering

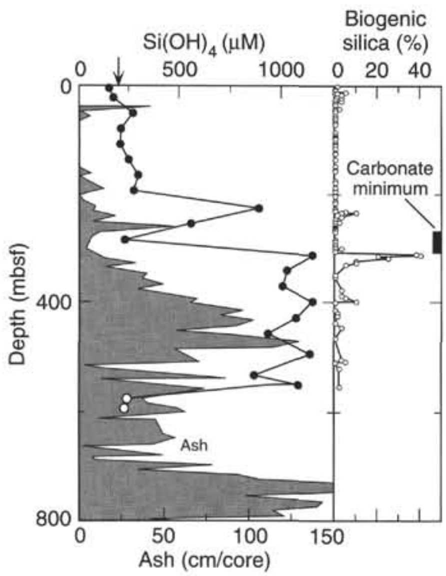

Figure 42. Depth profile of silica in Site 999 interstitial waters. The transition from open to closed or closed to open symbols differentiates between Holes 999A and 999B. Quantification of the ash component is presented as the percentage of dispersed ash (shaded area) in the sediment column at a given depth to permit evaluation of the effect of ash on pore-water chemistry. Arrows indicate mean ocean-bottom-water composition taken from Millero and Sohn (1992). Also plotted is the distribution of biogenic silica as determined from smear-slide analyses.

(see "Igneous Petrology and Volcanology" section, this chapter). Silica concentrations increase sharply downcore to levels > 1150 μM by 310 mbsf, significantly above the peak in ash-layer frequency or ash thickness. Concentrations remain elevated above 800 μM across the peak interval of Miocene ash deposition and do not show the downcore decrease displayed by Rb, K, and Li that are coincident with the decreasing occurrence of discrete ash layers. The occurrence of the main silica peak well above the most abundant ash layer interval is caused by the high abundance of dispersed ash (see below). Feldspars and volcanic glass are significantly more reactive than detrital quartz, and silica would be liberated by weathering reactions involving volcanogenic material such as

$$2.33NaAlSi_3O_8 + 8.64H_2O + 2CO_2 =$$

$$Na_{0.33}Al_{2.33}Si_{3.67}O_{10}(OH)_2 + 2Na^+ + 2HCO_3^- + 3.32H_4SiO_4. \quad (2)$$

Notable increases in the abundance of biogenic silica occur at approximately 220–250 and 300–340 mbsf (Fig. 42; and "Lithostratigraphy" section, this chapter). Additional maxima are present within the uppermost 50 mbsf, and a few others are found below 340 mbsf. There is a striking correspondence between the total distribution of ash (discrete layers plus the dispersed component), variability in the profile for dissolved silica, and the distribution of biogenic silica. Although this may represent an increased biogenic flux, it may instead record enhanced preservation of biogenic silica within ash-rich zones as a consequence of silica buffering and alkalinity production during alteration of ash (see Equation 2). Silica levels may remain buffered at relatively high concentrations below 350 mbsf due to a diffusional contribution from the abundant ashes of Miocene and Eocene age at greater depth, a possible biogenic component, or back-precipitation of a silica-deficient phase. The dramatic decrease in silica concentration approaching 600 mbsf may be a response to a decreased source effect between the two lower main ash intervals.

Interstitial Water Summary

The geochemistry of the interstitial waters at Site 999 is controlled largely by three processes: (1) microbially mediated redox reactions resulting from the progressive breakdown of labile phases of organic carbon, which determine the morphologies of the sulfate, ammonium, Fe, Mn, and alkalinity profiles in the upper 170 mbsf; (2) carbonate dissolution and precipitation reactions, which determine the morphologies of Ca^{2+}, Mg^{2+}, Sr, and, to a lesser extent, alkalinity profiles; and (3) weathering of locally abundant silicic ashes, which governs the behavior of Rb, K, Li, Si, and alkalinity. Although the correlation between pore-water chemistry and the distribution of observed discrete ash layers at this site is less coherent than at Site 998, when dispersed ash within the total sediment column is accounted for the relationship becomes much stronger.

The preservation of pore-water profiles that are regulated by local scale features such as ash distribution indicates that diffusion has not significantly altered the present chemistry of the interstitial waters. This suggests, in turn, a limited role for the basement, perhaps located up to 600 m below the deepest pore-water sample.

Sediment Chemistry

Introduction

At Site 999, the shipboard sediment chemistry program continued at a sampling rate of one sample per core, and analyzed sediment through the entire recovered sequence. Discrete 10-cm^3 samples were taken from particular intervals that visually appeared representative and had no obvious marker beds (i.e., discrete ash layers, turbidites, and other rapid or unusual events were avoided). The samples were analyzed as described in the "Explanatory Notes" chapter (this volume), and the results are presented in Tables 9 and 10.

Quantifying Sedimentary Components (Terrigenous Material and Dispersed Ash)

As at Site 998, the bulk sediment chemistry was used to quantify the relative amounts of terrigenous material and dispersed ash through the sediment column. Although the frequency of ash layer occurrence has been described elsewhere (see "Igneous Petrology and Volcanology" section, this chapter), quantifying the amount of dispersed ash is particularly important to constrain diagenetic reactions, evaluate pore-water profiles, and define the sedimentologic nature of the recovered sequence.

For Site 999, we quantified the terrigenous component by a normative calculation based on concentrations of Cr in a given sample compared to concentrations of Cr in average shale, according to

$$(\%\text{Terrigenous})_{\text{sample}} = 100 \times (\text{Cr}_{\text{sample}}) / (\text{Cr})_{\text{avg shale}}. \quad (3)$$

We chose Cr as the reference element for several reasons.

1. Cr concentrations in ashes recovered at Site 999 are extremely low (frequently below the detection limit of 3 ppm; see "Igneous Petrology and Volcanology" section, this chapter) compared to average shale (Cr ~110 ppm; Taylor and McLennan, 1985).
2. Cr is a refractory element that is unlikely to be affected by diagenetic remobilization.
3. Through the uppermost 70 mbsf, where the sediment is composed exclusively of terrigenous matter and biogenic $CaCO_3$ (see "Lithostratigraphy" section, this chapter), the calculation agrees closely with the calculation by difference (i.e., %Terrigenous = 100 – %$CaCO_3$).

Table 9. Major element chemistry of bulk sediment, Holes 999A and 999B.

Core, section, interval (cm)	Depth (mbsf)	Fe (ppm)	Mn (ppm)	P (ppm)	Ti (ppm)	%Carbonate (ppm)
165-999A-						
1H-3, 77–79	3.77	45716	1305	1500	3817	31
2H-3, 127–129	11.87	35629	1511	588	2770	46
3H-5, 7–9	23.17	36304	2144	816	3081	48
4H-3, 53–55	30.13	41923	2004	1179	3545	34
5H-3, 112–114	40.22	42026	1846	936	3421	35
6H-4, 3–5	50.13	37983	1334	578	3051	42
7H-5, 30–32	61.40	29431	1306	575	2949	48
8H-3, 97–99	68.57	31470	1496	592	2993	49
9H-3, 77–79	77.87	23452	1280	472	2155	57
10H-2, 82–84	85.92	23344	1292	453	2006	60
11H-3, 7–9	96.17	25862	1374	443	2239	56
12H-3, 49–51	106.09	29391	1743	461	2335	50
13H-1, 88–90	112.98	25083	1363	549	2203	57
14H-4, 128–130	127.38	25417	1408	620	2002	59
15H-2, 77–79	133.37	27992	1738	606	2239	51
16H-3, 97–99	144.57	32037	1286	561	2502	46
17H-3, 92–94	154.02	28077	1410	709	2267	50
18H-2, 97–99	162.07	17875	1976	611	1492	67
19H-2, 78–80	171.38	23455	1494	571	1936	57
21H-5, 92–94	195.02	31442	2204	644	2435	48
22X-2, 78–80	199.88	27745	1796	486	1848	54
23X-1, 144–146	202.04	21812	2652	518	1348	63
24X-4, 98–100	215.78	28408	2153	609	2252	50
25X-4, 101–103	225.41	28080	1773	615	2161	48
26X-1, 98–100	230.48	23250	1854	601	2028	53
27X-4, 127–129	244.87	26761	2024	690	1992	53
29X-1, 127–129	259.67	28837	2566	465	1942	55
29X-6, 13–15	266.03	49137	920		3569	11
30X-2, 128–130	270.78	37675	1900	1035	2780	37
30X-7, 18–20	277.18	50005	648		3955	10
31X-5, 126–128	284.86	56429	317		4287	2
32X-5, 89–91	294.09	37250	1443	1294	2976	32
33X-5, 87–89	303.57	25103	1436	679	1942	51
34X-3, 90–92	310.20	30804	1198	730	2362	40
36X-2, 97–99	328.07	25497	1181	600	1867	50
37X-6, 102–104	343.72	21189	1071	547	1957	53
39X-1, 129–131	355.69	13509	980	293	931	71
40X-3, 97–99	367.97	18921	883	408	1463	63
42X-4, 129–131	389.19	13244	920	360	1168	71
43X-3, 77–79	396.77	16062	1056	357	1241	66
45X-4, 99–100	417.59	19121	888	427	1497	62
47X-5, 79–81	438.19	12289	1067	324	948	75
47X-5, 81–83	438.21	12533	1071	339	965	74
48X-5, 119–121	448.29	15028	952	362	1085	71
50X-3, 84–86	464.14	23034	742	403	1991	55
51X-4, 127–129	475.67	15892	801	402	1226	70
52X-1, 101–103	480.51	20290	658	509	1707	57
53X-5, 82–84	495.92	15340	740	304	1098	67
54X-3, 104–106	502.74	19507	855	274	925	69
55X-CC, 7–9	508.37	17664	835	500	1585	62
56X-CC, 6–8	513.88	19068	1001	500	1917	68
57X-CC, 10–12	518.31	17479	867	412	1679	70
58X-5, 30–32	533.90	17916	521	450	1413	57
59X-1, 37–39	537.57	16201	498	367	1324	66
60X-4, 58–60	551.88	15541	479	332	1306	66
61X-3, 92–94	560.42	12117	492	372	1136	75
165-999B-						
5R-2, 24–26	574.30	14205	493	342	1168	71
6R-1, 75–77	577.95	18239	460	633	1774	65
8R-2, 28–30	593.58	15688	549	632	1360	69
9R-5, 93–95	607.10	19531	524	460	1723	62
10R-1, 31–33	611.41	14945	544	612	900	72
11R-3, 98–100	624.15	12037	517	596	895	70
12R-5, 75–77	635.70	10291	459	471	722	72
13R-4, 9–11	644.49	7887	502	418	514	81
15R-2, 72–74	661.32	7981	462	406	442	72
19R-1, 58–61	682.48	5483	374	315	396	84
20R-1, 57–59	685.47	4517	352	254	307	87
21R-3, 117–119	692.07	6216	445	409	305	79
22R-3, 81–83	701.41	7537	5584	340	328	80
23R-1, 102–104	708.22	6355	461	447	180	70
24R-3, 69–71	720.39	10253	1018	448	604	72
26R-5, 84–86	743.14	4271	547	390	157	61
27R-3, 41–43	749.39	9192	717	799	320	72
28R-4, 79–81	760.99	5132	638	575	151	73
29R-5, 93–95	772.33	4869	578	480	143	78
31R-2, 2–4	786.42	4042	1105	308	139	76
32R-2, 46–48	796.26	8347	991	472	913	62
33R-5, 30–32	811.00	5471	607	465	180	87
34R-3, 35–38	817.85	11078	748	500	632	61
36R-2, 63–65	835.83	4998	667	329	280	83
38R-3, 105–107	856.95	5345	786	309	79	67
39R-3, 83–85	866.43	5489	566	438	202	73
40R-4, 53–56	877.23	4897	619	348	83	82
41R-2, 69–71	884.09	6030	749	406	56	77
42R-2, 79–81	888.79	7621	1370	559	354	51
44R-3, 112–114	905.22	11939	763	775	231	54
45R-5, 63–66	917.33	11589	1098	620	733	54
46R-1, 120–122	921.50					47
47R-2, 122–124	932.72	22140	674	641	2124	47
48R-5, 81–83	946.41					57
49R-3, 67–68	952.87	16546	520	700	851	65
50R-4, 97–99	964.27	16507	428	549	1381	70
51R-2, 142–144	971.32					67
52R-3, 4–6	981.14					62
53R-4, 96–98	991.83	19925	498	796	1427	59
54R-3, 116–118	1001.56	16711	475	757	1492	63
55R-5, 23–25	1013.33	26913	519	1069	2002	60
56R-4, 65–67	1021.85	14411	546	804	557	73
57R-3, 65–67	1029.95	4450	733	760	600	77
58R-5, 75–77	1042.15					55
61R-5, 59–61	1061.69	4711	557	141	304	89
62R-CC, 17–19	1066.45					87

Notes: No data indicate samples not analyzed. Data overspecified for calculation purposes. This entire table also appears on CD-ROM (back pocket).

This final point is particularly important; other refractory elements such as Zr and Nb do not yield tolerable results throughout the uppermost sequence (Fig. 43), perhaps reflecting provenance variation or a significant difference between the terrigenous component and the average shale end-member used in the calculations (see below). Although the calculation based on Ti yields a result that agrees closely with the difference calculation, Ti is not used because of the relatively high and variable concentration of Ti in ash at Site 999 (1100–5600 ppm; see "Igneous Petrology and Volcanology" section, this chapter) compared to average shale (Ti = 5995 ppm; Taylor and McLennan, 1985). With the analytical detection limit of 3 ppm for Cr, the detection limit of the terrigenous calculation itself is slightly better than 3% (i.e., 3 ppm/110 ppm).

Given the above calculation of the concentration of terrigenous material based on Cr abundances, the amount of ash dispersed in the sediment (plus other minor components such as Fe oxides and biogenic silica) was calculated by difference, according to

$$(\%\mathrm{Ash})_{\mathrm{sample}} = 100 - \%\mathrm{CaCO_3} - \%\mathrm{Terrigenous}. \quad (4)$$

This calculation yields a maximum estimate for the amount of dispersed ash in a given sample, due to the potential inclusion of oxide and biogenic opal components in the noncarbonate, nonterrigenous fraction. The amount of Fe oxide in a given sample, however, may be approximated from the nonsupported ("excess") Fe fraction, calculated from

$$\text{"excess" Fe} = [\mathrm{Fe_{total}} - \mathrm{Cr_{sample}}(\mathrm{Fe/Cr})_{\mathrm{shale}}]. \quad (5)$$

On a per sample basis, this calculation subtracts Fe, which is supported by the detrital terrigenous component from total Fe. This "excess" Fe is then partitioned into an Fe oxide phase. The calculation was performed for the oxide phases FeO, Fe_2O_3, and Fe_3O_4, with statistically insignificant differences between the results. The results indicate that at Site 999 the amount of Fe oxide in the bulk sediment is less than or equal to approximately 2% (Fig. 44). This value is a relatively large amount of Fe oxide for sediment deposited in this environment, but it is consistent with the strong observed magnetic susceptibility (see "Paleomagnetism" section, this chapter). The amount of biogenic silica in the bulk sediment is also low (averaging less than 5%; see "Lithostratigraphy" section, this chapter).

In summary, we are confident that assigning the result of the "by difference" calculation entirely to ash is a reasonable approximation, and that the estimates of ash abundance are quantitatively accurate. It is important, however, to recognize that such calculations define the amount of terrigenous matter (based on "average shale") and dis-

Table 10. Trace element chemistry of bulk sediment, Holes 999A and 999B.

Core, section, interval (cm)	Depth (mbsf)	Nb (ppm)	Zr (ppm)	Y (ppm)	Sr (ppm)	Rb (ppm)	Zn (ppm)	Cu (ppm)	Ni (ppm)	Cr (ppm)	V (ppm)	Ba (ppm)
165-999A-												
1H-3, 77–79	3.77	9.2	96	16	611	68	124	38	56	80	183	318
2H-3, 127–129	11.87	5.6	72	12	824	50	102	79	51	56	126	324
3H-5, 7–9	23.17	5.1	73	12	826	48	98	32	44	61	131	359
4H-3, 53–55	30.13	8.7	99	16	857	65	115	52	49	77	145	415
5H-3, 112–114	40.22	8.2	94	16	614	67	113	53	52	75	156	347
6H-4, 3–5	50.13	6.4	79	12	797	54	89	42	41	58	120	353
7H-5, 30–32	61.40	6.4	78	12	848	52	102	54	49	55	122	349
8H-3, 97–99	68.57	5.1	73	11	887	47	91	46	40	51	120	301
9H-3, 77–79	77.87	4.5	60	9	914	41	89	41	42	37	83	285
10H-2, 82–84	85.92	3.2	58	10	1000	36	73	44	43	38	79	309
11H-3, 7–9	96.17	5.1	64	10	936	44	81	45	49	36	89	300
12H-3, 49–51	106.09	6.0	75	12	884	50	81	45	40	38	85	304
13H-1, 88–90	112.98	4.8	64	10	919	46	75	44	42	36	83	274
14H-4, 128–130	127.38	3.8	59	10	956	43	77	39	56	37	86	343
15H-2, 77–79	133.37	4.9	65	12	904	49	87	49	60	43	98	385
16H-3, 97–99	144.57	6.6	74	12	937	53	86	49	71	47	110	294
17H-3, 92–94	154.02	4.1	65	10	1044	46	88	47	72	45	97	354
18H-2, 97–99	162.07	2.1	50	8	1141	28	62	39	42	26	60	277
19H-2, 78–80	171.38	3.7	62	9	1095	38	72	41	51	33	84	302
21H-5, 92–94	195.02	4.4	70	11	970	45	80	46	51	44	96	327
22X-2, 78–80	199.88	3.9	67	10	1072	37	68	45	50	32	64	454
23X-1, 144–146	202.04	2.7	58	9	1127	33	57	37	33	31	61	270
24X-4, 98–100	215.78	4.2	68	10	930	44	77	45	54	37	80	318
25X-4, 101–103	225.41	3.0	66	12	978	37	88	58	78	40	92	471
26X-1, 98–100	230.48	4.2	63	11	969	32	74	47	52	33	71	335
27X-4, 127–129	244.87	2.0	61	10	941	36	75	48	58	37	74	461
29X-1, 127–129	259.67	3.1	64	10	1077	36	74	51	55	35	74	452
29X-6, 13–15	266.03	6.6	115	19	517	69	165	76	146	89	258	945
30X-2, 128–130	270.78	5.0	96	19	909	50	113	63	87	54	119	461
30X-7, 18–20	277.18	6.5	114	19	537	72	144	69	114	97	225	650
31X-5, 126–128	284.86	7.1	118	15	399	78	143	77	105	116	245	749
32X-5, 89–91	294.09	4.9	87	14	923	50	97	62	74	61	129	686
33X-5, 87–89	303.57	2.7	63	9	1094	33	88	47	57	34	82	654
34X-3, 90–92	310.20	2.6	74	11	1001	37	104	50	72	40	89	554
36X-2, 97–99	328.07	3.1	72	10	990	36	68	34	42	30	54	585
37X-6, 102–104	343.72	2.4	70	10	997	27	54	48	29	18	64	663
39X-1, 129–131	355.69	1.3	43	5	996	17	36	27	19	12	25	604
40X-3, 97–99	367.97	1.6	50	6	954	21	51	30	24	20	41	558
42X-4, 129–131	389.19	0.8	42	6	956	14	46	34	20	13	33	449
43X-3, 77–79	396.77	0.5	44	5	974	15	44	31	18	13	31	608
45X-4, 99–100	417.59	2.1	48	6	908	22	43	26	22	15	35	455
47X-5, 79–81	438.19	1.2	42	7	1098	10	37	27	13	7	22	452
47X-5, 81–83	438.21	0.2	42	7	1094	11	38	24	13	7	21	458
48X-5, 119–121	448.29	0.6	42	7	963	14	41	27	19	10	29	693
50X-3, 84–86	464.14	3.5	71	10	856	21	50	30	18	12	39	610
51X-4, 127–129	475.67	0.9	45	8	1004	12	35	35	16	9	26	558
52X-1, 101–103	480.51	2.0	64	10	925	21	48	30	18	11	33	632
53X-5, 82–84	495.92	1.2	47	7	1029	15	36	30	20	10	28	648
54X-3, 104–106	502.74	1.2	45	6	1017	18	85	28	30	8	19	511
55X-CC, 7–9	508.37	1.9	52	9	993	21	42	30	18	14	35	599
56X-CC, 6–8	513.88	1.1	49	8	925	17	56	43	15	12	37	643
57X-CC, 10–12	518.31	1.3	54	6	932	16	39	33	18	14	41	704
58X-5, 30–32	533.90	1.1	66	9	986	20	51	34	19	10	39	829
59X-1, 37–39	537.57	1.4	51	7	1093	14	39	29	16	9	28	552
60X-4, 58–60	551.88	1.2	51	6	1126	13	40	28	15	8	24	423
61X-3, 92–94	560.42	0.9	42	5	951	9	36	21	12	6	20	419
165-999B-												
5R-2, 24–26	574.30	5.4	78	6	894	12	31	23	14	5	16	534
6R-1, 75–77	577.95	1.0	59	9	1002	16	66	28	16	12	38	675
8R-2, 28–30	593.58	1.2	55	8	969	18	43	24	15	10	22	753
9R-5, 93–95	607.10	3.6	93	8	1046	14	55	26	13	8	28	815
10R-1, 31–33	611.41		44	8	1124	13	35	25	12	8	26	1120
11R-3, 98–100	624.15	1.2	44	8	996	12	63	95	23	9	32	1220
12R-5, 75–77	635.70	1.0	37	6	927	10	36	30	18	7	18	1029
13R-4, 9–11	644.49	0.5	33	6	915	9	28	32	11	4	14	850
15R-2, 72–74	661.32		26	6	797	8	28	25	20	6	13	810
19R-1, 58–61	682.48		24	6	884	5	24	21	12	0	9	440
20R-1, 57–59	685.47		25	2	860	6	30	26	12	4	7	602
21R-3, 117–119	692.07		26	5	815	8	23	22	10	0	10	729
22R-3, 81–83	701.41	1.5	40	4	844	8	35	25	10	4	9	955
23R-1, 102–104	708.22		28	5	720	8	26	28	18	4	7	1020
24R-3, 69–71	720.39		45	7	997	11	29	32	13	3	16	1135
26R-5, 84–86	743.14		22	5	640	8	18	15	15		4	687
27R-3, 41–43	749.39	0.8	37	12	786	10	33	24	15	4	15	1203
28R-4, 79–81	760.99		25	9	759	8	31	44	11	0	7	854
29R-5, 93–95	772.33		19	8	586	5	19	19	11	0	8	727
31R-2, 2–4	786.42		18	6	549	6	19	143	10	0	6	546
32R-2, 46–48	796.26		42	9	701	10	29	18	7	0	6	547
33R-5, 30–32	811.00		18	7	526	7	19	23	10	0	8	786
34R-3, 35–38	817.85	0.8	35	10	594	11	30	20	10	5	16	992
36R-2, 63–65	835.83		18	6	472	5	18	19	9	0	4	591
38R-3, 105–107	856.95		30	10	817	6	24	41	8	0	7	959
39R-3, 83–85	866.43		22	6	519	4	17	19	8	0	7	728
40R-4, 53–56	877.23	1.2	22	5	546	5	25	19	11	0	6	687
41R-2, 69–71	884.09	1.0	21	6	457	6	22	21	14	5	6	904
42R-2, 79–81	888.79	0.9	24	8	438	8	21	24	16	10	38	696
44R-3, 112–114	905.22	0.6	30	8	545	10	26	33	36	12	22	2609

Table 10 (continued).

Core, section, interval (cm)	Depth (mbsf)	Nb (ppm)	Zr (ppm)	Y (ppm)	Sr (ppm)	Rb (ppm)	Zn (ppm)	Cu (ppm)	Ni (ppm)	Cr (ppm)	V (ppm)	Ba (ppm)
45R-5, 63–66	917.33		26	6	402	8	26	54	22	15	16	1137
46R-1, 120–122	921.50	1.3	25	7	348	9	21	20	17	13	20	1065
47R-2, 122–124	932.72	2.5	40	7	399	11	42	34	37	40	45	1417
48R-5, 81–83	946.41	1.2	46	7	710	8	29	36	25	17	20	1370
49R-3, 67–68	952.87		29	7	464	8	33	31	28	25	32	2384
50R-4, 97–99	964.27	0.6	27	5	437	8	36	51	23	21	31	1222
51R-2, 142–144	971.32	0.5	25	7	506	7	36	25	20	17	29	1826
52R-3, 4–6	981.14	0.9	35	9	586	10	51	33	26	29	48	1951
53R-4, 96–98	991.83	1.6	42	9	584	9	48	35	27	20	37	1814
54R-3, 116–118	1001.56	1.2	42	8	591	11	43	43	27	18	35	2037
55R-5, 23–25	1013.33	1.2	43	10	579	12	55	46	34	34	60	2502
56R-4, 65–67	1021.85	0.5	28	10	557	8	36	28	24	18	30	2393
57R-3, 65–67	1029.95		18	9	556	4	31	25	12	4	10	2488
58R-5, 75–77	1042.15	0.5	30	13	666	8	32	57	13	6	14	2748
61R-5, 59–61	1061.69		14	11	526	4	26	27	14	4	6	1554
62R-CC, 17–19	1066.45		17	13	546	5	29	25	18	4	7	1807

Notes: No data indicate concentrations below detection limit. Data overspecified for calculation purposes. This entire table also appears on CD-ROM (back pocket).

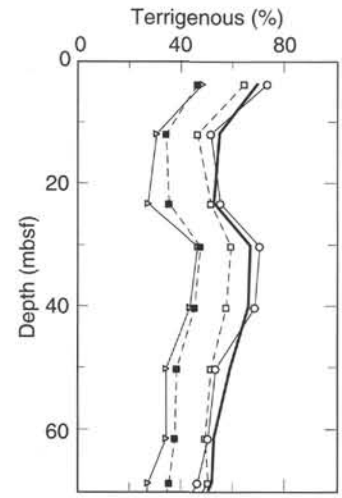

Figure 43. Depth profile of uppermost 70 mbsf of Hole 999A (where the sediment is composed exclusively of carbonate and terrigenous matter) of percentage of terrigenous matter calculated from trace metal abundances (Ti = open squares, Zr = solid squares, Nb = open triangles; see text). Note close correspondence between Cr-based determinations (open circles) and concentrations of noncarbonate fraction (heavy solid line).

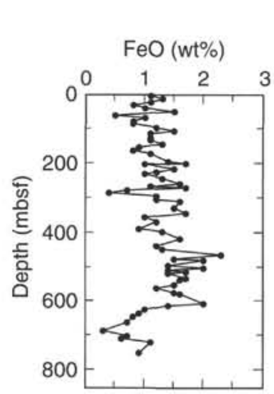

Figure 44. Weight percent of Fe-oxide (as FeO) through the sediment column, calculated by way of normative partitioning.

persed ash in a *bulk* sediment sample. We cannot infer any mechanistic process describing how the terrigenous matter or dispersed ash came to be deposited; in particular, we cannot distinguish between fluvial or eolian processes for either the terrigenous or ash component. This latter point is particularly relevant to the interpretation of ash distribution and accumulation. Although much of the dispersed ash component undoubtedly has been altered to clays, analogous to the alteration of discrete ash layers (see "Igneous Petrology and Volcanology" section, this chapter), the nature of our calculation of dispersed ash still accounts for this altered material because, assuming a closed chemical system, alteration of dispersed ash will not appreciably affect the overall elemental abundances within the bulk.

The results of these calculations indicate that the upper 250 mbsf at Site 999 is characterized by 50%–60% biogenic $CaCO_3$, 30%–40% detrital terrigenous material, and 0%–15% dispersed ash (Fig. 45). From the sediment/water interface to 250 mbsf, the relative proportion of terrigenous material decreases whereas that of ash increases markedly.

The middle Miocene carbonate minimum from 260 to 300 mbsf also marks a change in sediment composition between the upper and lower portions of Site 999. Within the carbonate minimum, the noncarbonate fraction is composed exclusively of terrigenous matter, with essentially zero ash (Fig. 45). The amount of terrigenous matter below the carbonate minimum is much less than immediately above it, and this component continues to decrease to approximately 420 mbsf. From 420 to 430 mbsf, the amount of terrigenous material decreases markedly; below 430 mbsf, it decreases to near-zero values at 650 mbsf and remains low or absent to ~900 mbsf. From 900 to 1030 mbsf, the terrigenous component increases again to a point at which it accounts for ~20% of the bulk. From 1030 mbsf to the bottom of the hole, terrigenous matter again is only a minor component.

The concentration of dispersed ash in the shallowest sediment at Site 999 is very low, but it increases with depth until it constitutes ~15% of the bulk sediment immediately above the middle Miocene carbonate minimum. Below the carbonate minimum, the ash component is greater, composing ~25%–30% of the bulk sediment. When considered as the fraction of the noncarbonate component (Fig. 46), the concentration of dispersed ash increases with depth (with the notable exception of the terrigenous dominated carbonate minimum) until it comprises nearly 100% of the noncarbonate component from 680 to 880 mbsf. Conversely, the terrigenous component decreases through this interval. Deeper in the sequence, where the terrigenous matter increases in concentration (see above) the ash decreases to ~20%–40% of the noncarbonate fraction. These variations in the terrigenous component calculated from solid-phase geochemistry are independently corroborated by an almost exact match in the concentrations of detrital quartz in the sediment as determined by X-ray diffractometry (see "Lithostratigraphy" section, this chapter).

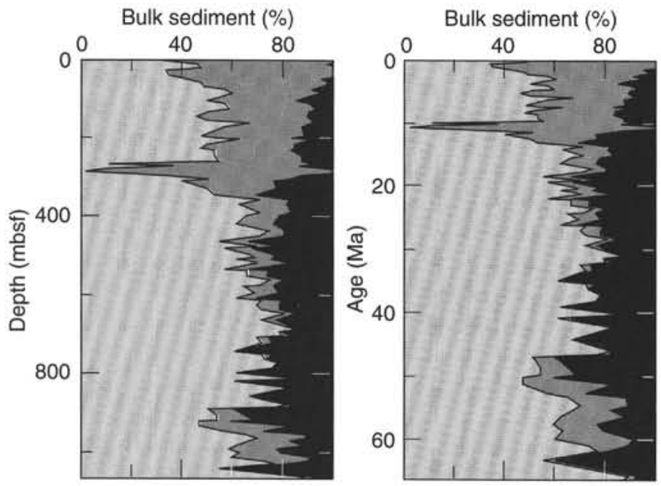

Figure 45. Percentages of carbonate (light gray), terrigenous matter (dark gray), and dispersed ash (black) at Site 999 vs. depth and age.

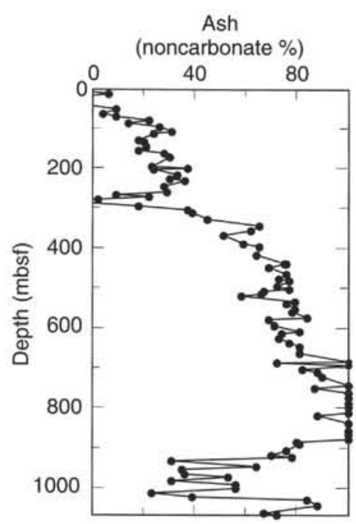

Figure 46. Concentrations of dispersed ash in the noncarbonate fraction vs. depth.

Calculations of the terrigenous and dispersed ash components can be synthesized by presentation as the integrated cumulative percent of each component (Fig. 47), which indicates the continually summed fraction of the total sediment pile that is composed of each of these two components. The value plotted at the surface is the total percentage of the entire sediment column composed of terrigenous material (19%) and dispersed ash (19%). The ash estimate is surprisingly high, but it is consistent with the strong ash impact on pore-water profiles compared with many sections elsewhere. This estimate is also consistent with the great abundance of megascopic ash fall layers. The greatest increase in the terrigenous component is in the carbonate minimum (middle/upper Miocene boundary interval) and in the Pliocene–Pleistocene section, whereas the greatest increase in the ash component occurs below the carbonate minimum. Although these data are affected by both compositional dilution (in the case of both the terrigenous and ash components) and arithmetic closure (in the case of the ash, which is calculated by difference), it is clear that the terrigenous and ash components are behaving independently.

Comparison of the amount of dispersed ash with the total thickness of the ash layers (Fig. 48; see also "Igneous Petrology and Volcanology" section, this chapter) indicates there is broad agreement

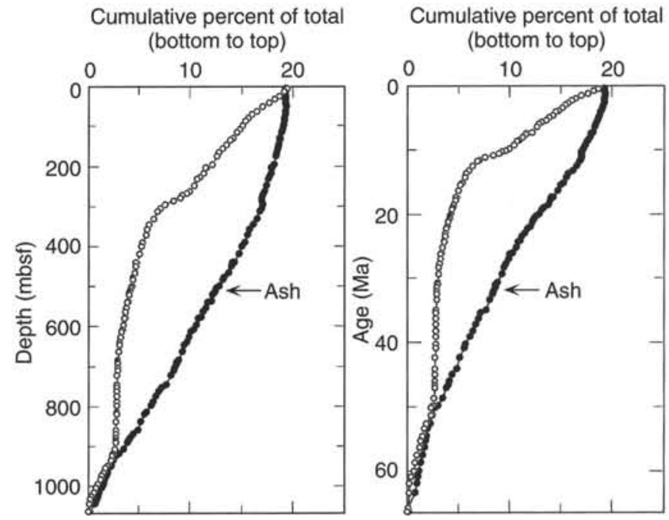

Figure 47. Cumulative percentage of terrigenous matter (open circles) and dispersed ash (solid circles) vs. depth and age. The cumulative percentage is calculated from the bottom upward; thus, values at zero depth (and zero age) represent the total percentage of the respective components at Site 999.

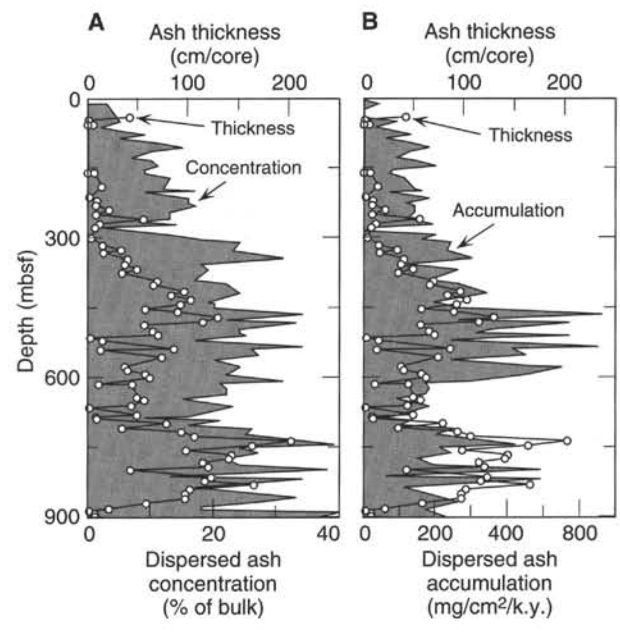

Figure 48. **A.** Concentration of dispersed ash (shaded area) and thickness of discrete ash layers (open circles) vs. depth. **B.** Accumulation of dispersed ash (shaded area) and thickness of discrete ash layers (open circles) vs. age. Note the closer parallel between the profiles in Figure 48B compared with Figure 48A. See text.

between the two approaches. Both show relatively low values from 0 to 250 mbsf as well as in the two deeper episodes (separated at 680–700 mbsf). The ash thickness data, however, more clearly defines these episodes. In particular, the dispersed ash records a plateau of high values with short-term fluctuations from 450 to 600 mbsf, whereas the discrete ash layer thickness data records a sharper maximum at 450 mbsf (Fig. 48). In the deeper volcanic episode (Eocene), the two data sets are more closely matched and record a maximum at 750 mbsf and numerous corresponding fluctuations.

In this context, it is important to recall that the dispersed ash determination cannot resolve the mechanism of ash transport because it is simply an integrated record of the eolian (i.e., resulting from discrete volcanic events) and fluvial inputs (i.e., resulting from the weathering of subaerial volcanic deposits). Thin ash layers that have been destroyed by bioturbation will still contribute to the dispersed amount, yet not be accounted for in the counting of the discrete layers. Because many thin ash layers are still observed (see "Igneous Petrology and Volcanology" section, this chapter), the significance of this process may be minor or localized.

Calculating the accumulation rate of the dispersed ash component (see "Sedimentation Rates" section, this chapter) allows more direct study of the ash flux to the seafloor, because the accumulation rate is unaffected by compositional dilution of the ash by the carbonate and terrigenous matter. The accumulation of the dispersed component (Fig. 48) clearly delineates several episodes of ash deposition, and follows the record of ash thickness more closely than does the concentration of dispersed ash. Most noticeably, the discrete ash layer minimum from 600 to 700 mbsf is well defined in the dispersed accumulation record.

Although the paired records of discrete ash thickness and dispersed ash accumulation closely follow each other overall, contrasts between the records can be interpreted in the context of regional wind patterns and the explosive strength of different volcanic sources. Because the regional surface winds are from the east and northeast (the Trade Winds), and Site 999 is located upwind of the postulated arc sources, only the largest volcanic eruptions are likely to be recorded (see "Igneous Petrology and Volcanology" section, this chapter). More numerous eruptions not large enough to contribute material far upwind of their source nevertheless are still likely to have created proximal, terrestrially exposed volcanic sequences, which may also have contributed to the bulk sediment of the Colombian Basin by way of weathering and fluvial transport. The accumulation record of dispersed ash records both small and large eruptions, whereas the larger eruptions are recorded only by discrete layers. Thus, downhole contrasts between the two records may contribute to our understanding of volcanic eruptive style through time in this region.

The interstitial water profiles of the alkali elements provide important information regarding the chemical weathering of the dispersed ash and the timing of the oceanward fluvial transport of the ash. As discussed above, the alkali metal and silica concentrations in interstitial waters appear to follow the dispersed ash component more closely than the discrete (counted) layers. This indicates that the dispersed ash was still quite chemically reactive upon deposition, because ash that had been strongly altered while terrestrially exposed (i.e., before transport to the deep sea) would not affect the interstitial water profiles as strongly as is observed. Therefore, we conclude that the originally subaerially deposited ash was transported relatively quickly to its current location. This interpretation is supported by the close similarity between the number of discrete ash layers and the accumulation of dispersed ash in the bulk sediment, as described above. Were the terrestrially deposited ash held in the continental reservoir for a substantial period of time (e.g., several millions of years), the records of ash layer deposition and dispersed ash accumulation would be more strongly decoupled.

Provenance Variation

We have argued above that the noncarbonate fraction of the bulk sediment can be approximated by the presence of two distinct components: terrigenous material broadly similar in composition to "average shale" (PAAS of Taylor and McLennan, 1985), and dispersed ash. Potential source variations within the ash component are discussed elsewhere (see "Igneous Petrology and Volcanology" section, this chapter). However, it is also worthwhile to consider whether there are large variations in the provenance of the terrigenous component.

The strongest independent evidence against large variations in the detrital source is the fact that our calculations, which assume only a

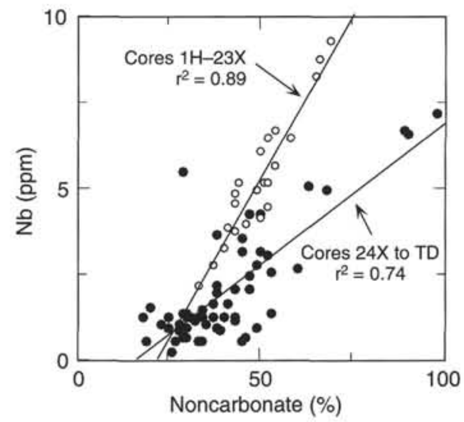

Figure 49. Concentrations of noncarbonate fractions vs. total Nb concentrations. The data fall into two fields: one that is strongly defined and composed of the uppermost sequence, which indicates a terrigenous end member; and (2) another that is more weakly defined and composed of the deeper sequence, which indicates a dispersed ash end-member (see text). TD = total depth.

three-component system, are fully consistent with both the sedimentologic observations of the bulk sediment and inferences made from XRD measurements. In addition, trace metal abundances in the noncarbonate fraction of the bulk sediment indicate only two noncarbonate components. For example, variations in Nb concentrations vs. the percent noncarbonate fraction (Fig. 49) yields one very distinct trend, indicating a noncarbonate component with ~15 ppm Nb (at 100% noncarbonate) and another, more weakly defined component with ~7–8 ppm Nb. The steeper trend defining the 15 ppm Nb end-member encompasses sediment from Cores 165-999A-1H through 23X, where the noncarbonate fraction is dominated by the terrigenous component. The inferred Nb concentration in this end-member closely matches that of average shale (19 ppm; Taylor and McClennan, 1985). Similarly, the shallower trend (with Nb = ~7–8 ppm) defined by sediment from Core 165-999A-24X to the bottom of Hole 999B, where ash dominates much of the noncarbonate fraction, indicates a noncarbonate end-member containing ~7.5 ppm Nb, closely matching the mean ash Nb content of ~8 ppm at this site (see "Igneous Petrology and Volcanology" section, this chapter).

The above considerations give us increased confidence in our hypothesis that there are no large-scale changes in detrital provenance throughout the sequence. Post-cruise statistical study will further test these preliminary observations, and may help resolve some subtleties within this data set. For example, focusing on the relative distribution of the refractory metals in the uppermost 250 mbsf indicates that within the terrigenous regime there may be small-scale variations in provenance (Fig. 50). Paired profiles of Zr/Nb and Ti/Zr show slight respective increases and decreases with depth, each away from the average shale value. Significantly, the increase in Zr/Nb at ~160 mbsf does not coincide with the decrease in Ti/Zr at 70 mbsf. Such variations cannot be the result of simple increases in Zr (the one element common to both ratios) and may indicate subtle fractionation in detrital mineral assemblages. This putative provenance change at 160 mbsf corresponds to the difference in lithologic Subunits IA and IB (see "Lithostratigraphy" section, this chapter), suggesting that further study may indeed resolve provenance changes throughout this interval.

IGNEOUS PETROLOGY AND VOLCANOLOGY

The section drilled at Site 999 includes 1223 silicic ash fall layers, ranging from 0.5 to 26 cm in thickness, with a mean thickness of 3.8 cm (Fig. 51). These discrete ash fall layers total 46.3 m and thus rep-

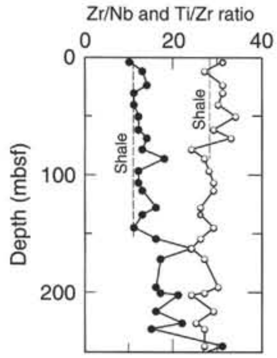

Figure 50. Ratios of Zr/Nb (solid circles) and Ti/Zr (open circles) vs. depth for the uppermost 250 mbsf of Hole 999A. Uppermost ratios are both near that of average shale, although subtle changes at 70 mbsf (for Ti/Zr) and 150 mbsf (for Zr/Nb) may indicate a minor change in provenance.

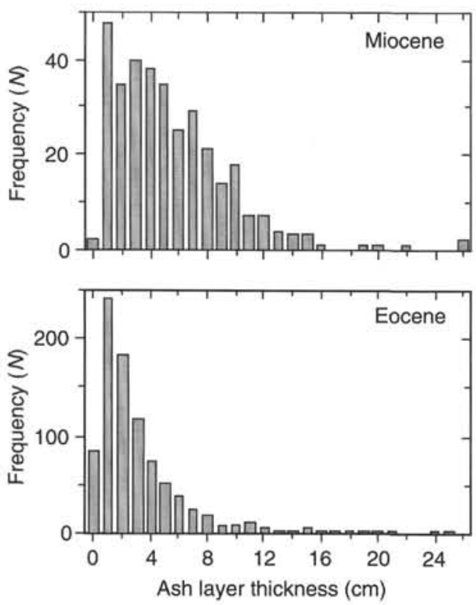

Figure 51. Frequency distribution of the thickness of volcanic ash layers at Site 999 for Miocene and Eocene volcanic episodes. Not shown on the figure is the thickest Miocene ash layer at 32 cm.

resent 4.4% of the total sediment thickness. The distribution of ash layers at Site 999 is given in the Appendix tables on CD-ROM (back pocket, this volume). In addition, dispersed ash is a ubiquitous constituent in the pelagic sediment, as shown by smear-slide analysis and geochemistry, and represents an additional 20% of the drilled section (see "Inorganic Geochemistry" section, this chapter). Fallout of ash at this site was highly episodic. In Figure 52, the distribution of volcanic ash layers downcore is displayed both in terms of frequency of eruptions (i.e., the number of ash layers per million years) as well as the ash accumulation rate (centimeters of ash per million years). The latter value is a more quantitative measure of the ash fallout, as the layers vary greatly in thickness. Typically, the Miocene layers (avg. = 5.5 cm) are thicker than the Eocene layers (avg. = 3.8 cm), but bioturbation of ash layer tops from both episodes results in an underestimate of thickness. The age of ash layers has been assigned on the basis of the following third-order polynomial equation fitted to the depth-vs.-age curve (Fig. 28):

$$\text{Age (Ma)} = (3.7 \times 10^{-8})\,(m^3) - (2.044 \times 10^{-5})\,(m^2) + (4.238 \times 10^{-2})\,(m) - 0.57288, \quad (6)$$

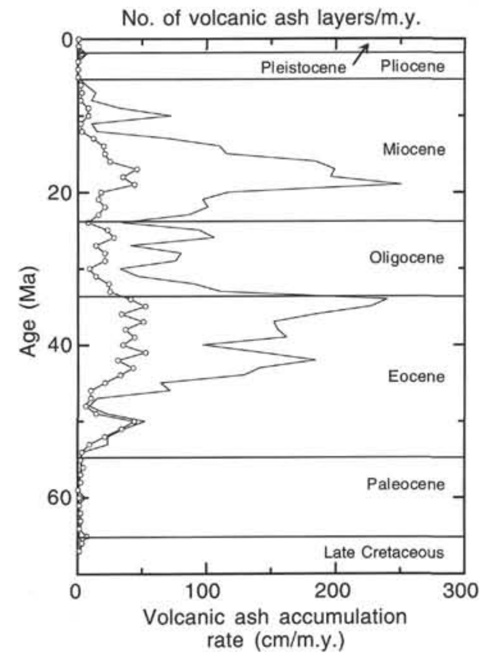

Figure 52. Age distribution of volcanic ash layers at Site 999, shown as ash accumulation rate (centimeters of ash thickness per million years) and as the number of ash layers per million years (open circles).

where m is depth in mbsf. The correlation coefficient for this equation is $r = 0.9988$.

Ash fall layers are rare in the Pliocene–Pleistocene, but there is a major episode of ash fallout in the Miocene. The onset of this episode is relatively sudden at around 23 Ma, reaching its peak at 19 Ma and decreasing after 14 Ma, then trailing off to very low levels in the late Miocene. During the Miocene episode, the frequency of major explosive volcanic events recorded at this site averages one eruption/43 k.y., but it ranges up to about one event/20 k.y. during the climax of this episode. The frequency of ash fallout at Site 999 on the Kogi Rise is about an order of magnitude higher during this episode than observed during the Miocene interval at Site 998 on the Cayman Rise, probably reflecting their different distances from source.

A second major episode of ash fallout occurred in the Eocene (Fig. 52). Following a minor peak in the early Eocene, this episode increased in intensity during the middle Eocene at 48 Ma and reached its climax in the late Eocene at around 34–35 Ma, before falling off very rapidly to low levels at 30 Ma in the early Oligocene. The mean eruption frequency during the Eocene is one eruption/32 k.y., significantly lower than in the Miocene episode. However, the duration of the main Eocene episode is longer (~18 vs. ~12 m.y.). Overall, the sedimentary record at Site 999 indicates that these two Cenozoic episodes of explosive volcanism are of comparable magnitude. Although the Eocene ash layers are more numerous than the Miocene tephra, they are generally thinner, and therefore the accumulation rate of the two episodes is comparable. The Miocene episode at Site 999 is considerably more robust than at Site 998 on the Cayman Ridge, probably reflecting the different distances of these sites from the volcanic source.

At Site 998, we discovered a strong early Eocene episode of volcanism (~50 Ma), which was attributed to a local source on the Cayman Ridge. Ash fallout at this time is relatively subdued at Site 999 (Fig. 52), supporting our view that this episode is localized to the Cayman Ridge area. The earliest record of volcanism affecting Site 999 occurs in Late Cretaceous and early Paleocene times, where ash-bearing clay layers occur interbedded with limestones. These layers are notably different, however, from the typical ash layers described above. They contain a much lower content of volcanic glass shards and lack volcanic phenocrysts; they are rich in carbonate, and some are finely laminated. Unlike the Eocene and Miocene ash layers, which contain clear glass shards, the very minor glass present in the Paleocene and Late Cretaceous ash-bearing claystones is typically brownish in color. Their carbonate content cannot always be attributed to bioturbation, as the basal and top contacts with the limestone are generally sharp. Instead, we propose that these ash-bearing claystone layers represent carbonate dissolution events, which is supported by their regular or rhythmic occurrence. Thus, the evidence from Site 999 indicates that major explosive Central American (?) arc volcanism in the region did not begin until the late Paleocene or early Eocene.

The rate of change of volcanism in the source regions of the Site 999 ash layers can be calculated from the derivative of the accumulation rate (Fig. 53). The two principal episodes show contrasting behavior. The Eocene episode has a relatively gradual and steady onset, at a rate of 50 cm/m.y.^{2}, and a very rapid decline at a rate of up to 130 cm/m.y.^{2}. On the other hand, the Miocene episode has a sharp onset and a more gradual decline in accumulation rate.

The ash layers recovered at Site 999 are often highly bioturbated, and ash has been dispersed above and below the ash layer for distances in excess of 10 cm. Many of the layers have been so extensively disrupted that they now occur as diffuse bands. However, these dispersed ash layers are not included in the data set reported here. Fresh layers are generally gray to brownish gray in color, whereas altered layers are typically dark grey to nearly black because of the high abundance of secondary pyrite and smectite in the ash. The ash layers are composed dominantly (>95%) of clear, silicic glass shards 100–300 µm in size, accompanied by minor crystals of biotite, plagioclase, rare quartz, hornblende, and clinopyroxene. Relatively rare shards of brownish glass of dacitic composition are also present, and they occur together with the more abundant clear glass shards in layers that most likely represent mixed magma eruptions (Fig. 54).

Pyrite coatings on glass shards and spheroidal crystals of pyrite are very common in several of the late Miocene ash layers in the depth range 150–310 mbsf, imparting a dark grey to nearly black color to the layer (Fig. 55). The pyrite occurs as 10- to 20-µm-sized circular patches or overgrowths on the glass shards, only a few micrometers in thickness (Fig. 56). The occurrence and abundance of secondary pyrite is very uneven and does not relate simply to stratigraphic depth. We note, however, that within a given ash layer, pyrite coatings are by far most common on the pale brown to brown glass shards of dacite composition, whereas the clear rhyolitic shards in the same ash layer may be a little affected or unaffected. In addition, there is no clear relationship between glass shard freshness and the degree of pyritization. We suggest that this indicates the nucleation of pyrite on the more iron-rich dacitic glasses during diagenesis. The formation of pyrite is most likely related to reduction of sulfate in the upper parts of the sediment column, and its concentration in the ash layers may be related to their relatively high permeability to interstitial fluids in the sediment, as compared to the surrounding clay- and carbonate-rich normal sediment. Ash layers with high pyrite content are also exceptionally high in nickel, ranging from 200 to 500 ppm. It remains unclear how the high degree of pyrite precipitation has occurred in the ash without alteration of the glass. Furthermore, the great enrichment in nickel remains an unsolved problem. We speculate that the nickel may be derived from a basement source, such as the oceanic plateau crust beneath the sediment pile. One possible scenario is the ascent of sulfur and nickel-enriched fluids along faults such as those that define the Kogi Rise. The intersection of faults with the high permeability ash layers would lead to preferential fluid flow along the layers, resulting in precipitation of pyrite on glass shard surfaces in the relatively fresh ash.

The degree of alteration of ash layers is quite variable downcore (Fig. 57). In the most altered layers, the glass shards are entirely replaced by brown Mg-rich tri-octahedral smectite, whereas in some layers the glass particles show signs of alteration by turning a cloudy or grayish color (Fig. 58). In others, the glass shards remain clear and are apparently unaltered. The Pleistocene volcanic ash layers are essentially unaltered, whereas the late Miocene ash layers are generally highly altered to smectite. Thus, alteration is dominant in the depth range from 150 to 300 m. In the section spanning the great peak of ash abundance in the early to middle Miocene, the ash layers are generally fresh, whereas the Eocene layers are generally altered to a varying degree. It is not clear what factors control this pattern of ash alteration. The presence of pyrite, however, does not correlate simply with alteration of the glass; many of the layers with fresh glass contain high levels of secondary pyrite.

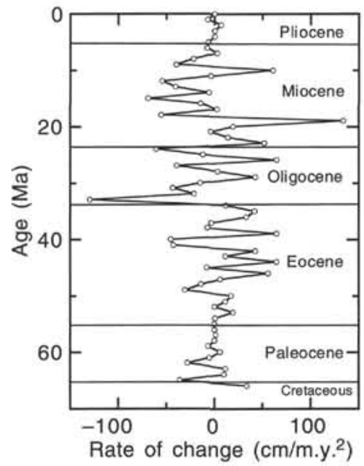

Figure 53. Rate of change in the volcanic ash accumulation at Site 999, derived from the curve shown in Figure 52.

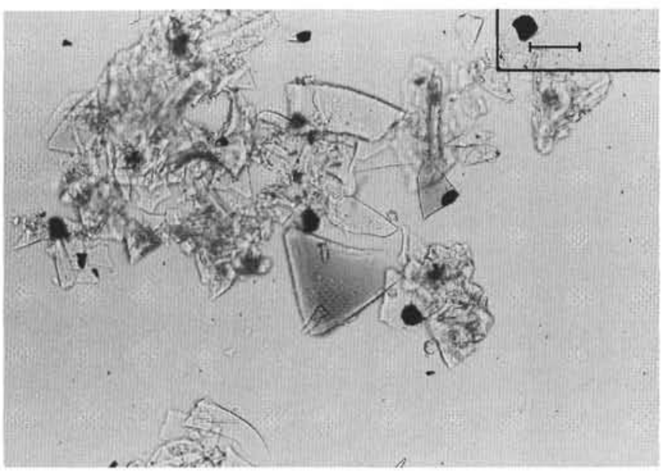

Figure 54. Photomicrograph of silicic (clear) and dacitic (brown) glass shards in the 7-cm-thick early Miocene volcanic ash layer from Sample 165-999A-50X-4, 108 cm. Opaque minerals are pyrite overgrowths on the glass. Scale bar is 40 µm in length.

Glass Shard Morphology

The majority of tephra layers from Site 999 contain clear glass shards that exhibit either thin bubble-wall or pipe-vesicular morphologies (Fig. 59). These are characteristic of the fragmentation of silicic magma by release of juvenile gases as pressure is reduced in the upper parts of volcanic conduits and vents (Heiken and Wohletz, 1985).

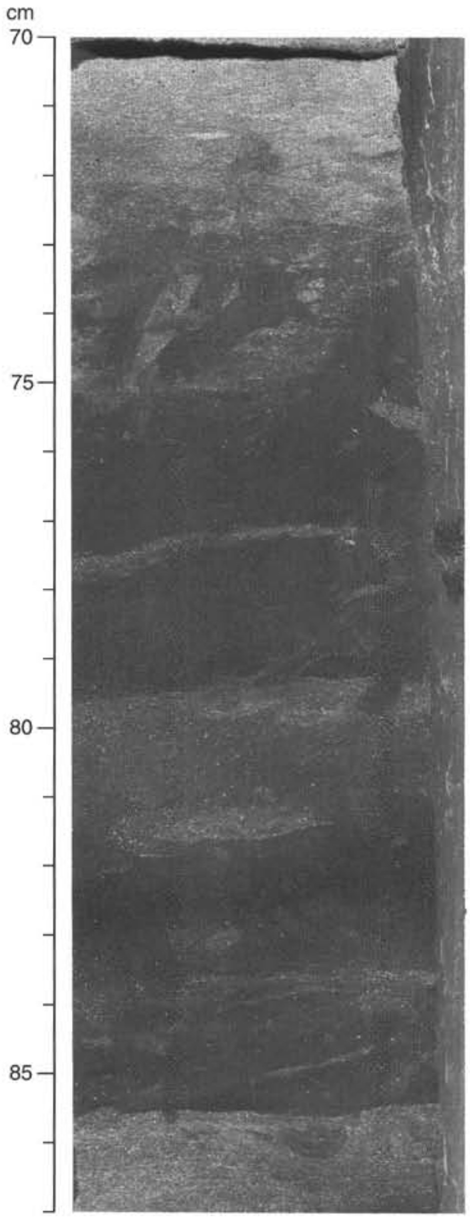

Figure 55. Core closeup photograph of altered dark gray multiple 37-Ma volcanic ash layers that have been bioturbated to a varying degree (Sample 165-999B-30R-3, 70–87 cm).

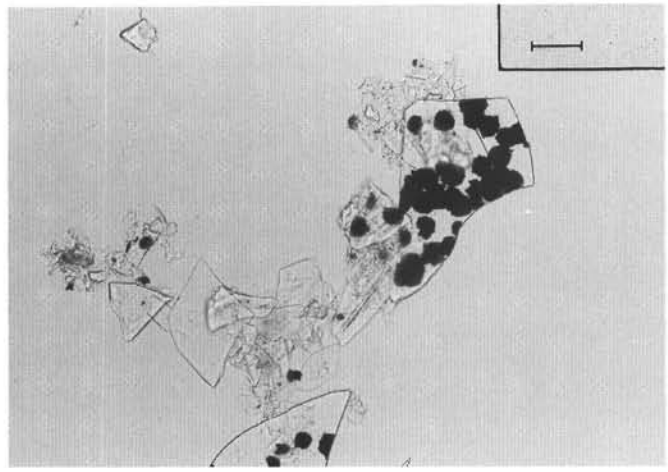

Figure 56. Photomicrograph of silicic glass coated with framboidal pyrite, in a 13-Ma partly altered volcanic ash layer in Sample 165-999A-38X-1, 34 cm. The scale bar is 40 µm in length.

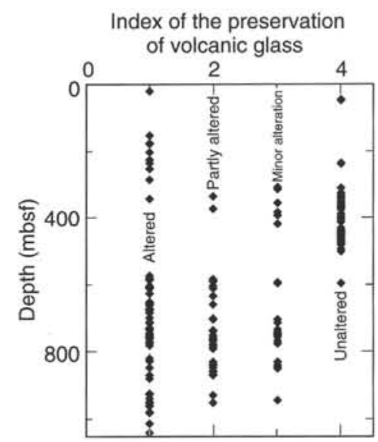

Figure 57. Degree of alteration of glass shards in the volcanic ash layers at Site 999 is generally highest in the depth interval from 150 to 300 mbsf and below 600 mbsf. Altered glasses are those that are completely replaced by smectite. Partly altered layers contain abundant smectite, coexisting with glass. Minor alteration defines layers that contain both clear and cloudy glass shards. Unaltered layers contain clear glass only; however, they may contain pyrite.

However, some layers of early Miocene age contain shards that are distinctly thicker and have a more blocky appearance (e.g., Sample 165-999A-50X-6, 116 cm; Fig. 60). Shards in these layers commonly lack internal gas bubbles, have more rounded edges, and do not have the sharp curvelinear edges that typify the more common bubble wall shards. These glass particles resemble miniature ice cubes in form (Fig. 61). Blocky shard morphology has often been linked to the influence of external water during magmatic fragmentation processes (e.g., Wohletz, 1983; Heiken and Wohletz, 1991) and experimental investigations have reproduced some of the features observed in natural tephra deposits (Wohletz and McQueen, 1984). The occurrence of different shard morphologies may be useful, therefore, for making inferences about the nature of source eruptions defined by distal fall layers of Site 999.

A pilot study was conducted on board using fractal analysis of particle boundaries to quantify the differences in shard morphologies observed in smear slides from tephra layers at Site 999. Images of glass shards between 150- and 300-µm diameter were collected with a video camera under plane polarized light from a petrographic microscope and stored as digital TIFF files. These images were processed and enhanced, and the shard boundaries defined, using NIH 1.58 Image software. Fractal analysis was conducted on individual particles using Image Fractal 1.2, a modified version of NIH Image 1.58 software, which generates incremental particle perimeter measurements by the pixel grid technique.

Fractal analysis is a powerful technique for the quantitative characterization of irregular particle morphology (Orford and Whalley, 1983; Kaye, 1986). It produces a quantitative index of the relative complexity of a particle's outline in two dimensions (Russ, 1992). Sequential measurements of a particle's perimeter are made using a series of measuring "rulers" of increasing size. If the particle outline

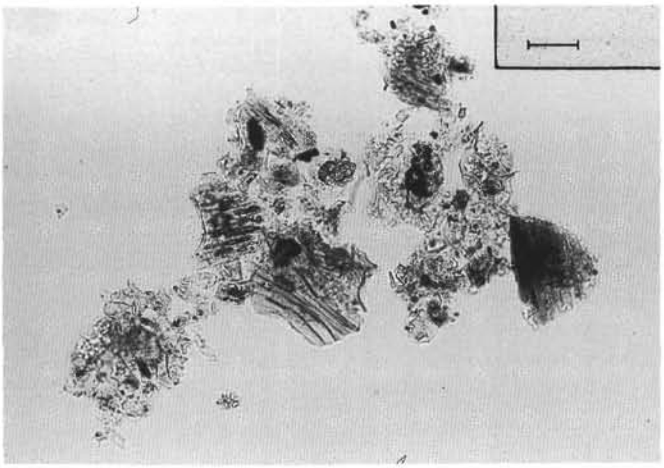

Figure 58. Photomicrograph of a volcanic ash layer with dacitic olive-brown pipe-vesicle glass shards and slightly altered glass (Sample 165-999A-51X-3, 91 cm). The scale bar is 40 µm in length.

A

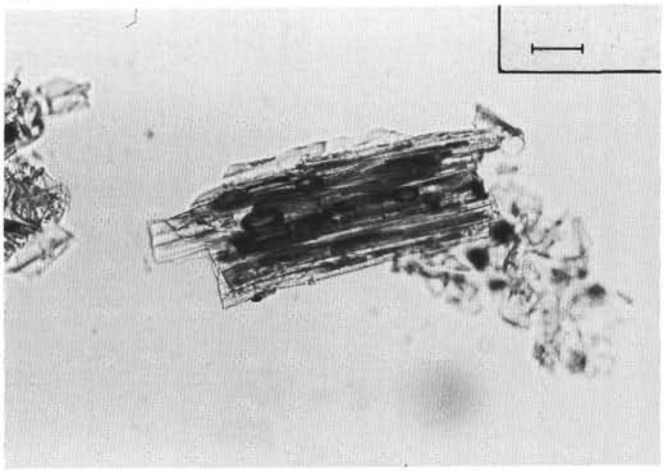

B

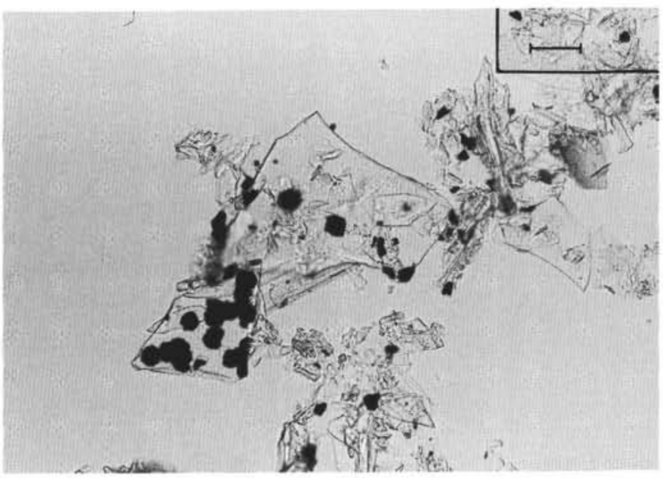

Figure 59. **A.** Photomicrograph of a typical pipe-vesicle glass particle, in 18.5-Ma volcanic ash layer in Sample 165-999A-50X-4, 108 cm. Scale bar is 40 µm in length. **B.** Photomicrograph of partly altered and pitted silicic glass shards with pyrite coating, 13-Ma volcanic ash layer in Sample 165-999A-38X-1, 34 cm. Scale bar is 40 µm in length.

is fractal in character, then a plot of log (perimeter) vs. log (ruler size) will yield an inverse linear relationship (Mandelbrot, 1967). These plots are referred to as Richardson plots. The slope of the line, s, is used to calculate the fractal dimension, F_d, based on the relation, $F_d = 1 - s$. Values of fractal dimension range between 1.0 and 2.0, with higher values corresponding to more complex grain morphologies. Figure 62 shows an example of a bubble-wall shard from a tephra layer in Section 165-999A-26X-6 at 111 cm, and a plot of the fractal analysis results. The boundaries of this particle are sharp and characterized by linear and curvelinear segments. However, fractal data from this particle does not form a single linear trend on a Richardson plot and thus does not constitute a true fractal. Instead, the data form two linear arrays and shows a behavior known as multifractal (Russ, 1994). In this situation, it is possible to calculate two fractal dimensions for the sample: F_{d1} from the linear array beginning at small ruler size, and F_{d2} from the linear array beginning at the inflection of slope and terminating with the largest ruler size (Fig. 62). In general, multifractal behavior suggests that there are two fundamentally different physical processes combining to determine the complexity of a particle's morphology (Russ, 1994). For volcanic particles from explosive eruptions, the boundary of a particle is determined by the breakage of bubbles and the fracturing of rapidly quenched silicate melt. The former will impart strongly curvilinear and complex elements to a particle's morphology on the scale of the average bubble size, whereas the latter will control the overall form of the particle according to the rheological properties of the melt at the time of fragmentation.

Blocky shards would be expected to have a simpler form because the particle boundary is not as complicated by the presence of gas bubbles. Figure 63 shows an example of a blocky shard, and Figure 64 shows the results of a fractal analysis. The morphology of this particle is quite different from the bubble-wall shard in that it lacks the strongly curvilinear elements in the boundary. Fractal analysis results show that this shard also behaves as a multifractal, but there are important differences in the nature of the fractal components. Compared with the bubble-wall shard (Fig. 62), the blocky shard has a lower slope and thus a lower fractal dimension for the first part of the Richardson plot (Fig. 64). This indicates a simpler particle morphology, as can be seen from a comparison of the photographs (Figs. 59B, 60).

Fractal analysis of 21 particles from layers visually identified as dominated by bubble-wall or blocky shard types demonstrates that shard morphologies can be quantitatively subdivided into two groups based on the fractal dimensions of the two multifractal elements, F_{d1} and F_{d2} (Fig. 65). Blocky shards are characterized by F_{d1} values of less than 1.03, indicating a lower complexity in particle morphology on a surficial scale. Bubble-wall shards have F_{d1} values from 1.03 to 1.06 and therefore have a more complex particle boundary superimposed on the overall particle form. Both shard types show a relatively wide range of F_{d2} values from 1.05 to about 1.25, with some suggestion that the overall particle form for bubble-wall shards is more complex.

The variation in shard morphologies of tephra layers at Site 999 may result from differences in the nature of source eruptions. Bubble-wall shards are characteristic of the eruption of volatile-rich siliceous magma where fragmentation results from the bursting of bubbles as magma is converted to viscous and brittle foam as it ascends toward the surface. Source eruptions of this type are likely to be major ignimbrite-forming events associated with caldera collapse and the formation of large-scale co-ignimbrite eruption plumes. However, large siliceous explosive eruptions may also be influenced by the interaction of magma with non-juvenile water. This may occur when magma ascent intersects local aquifers or an eruption occurs through a caldera lake (e.g., Wilson, 1985). It is also likely to be a common phenomenon in the emergent stage of volcanic centers in convergent margins. These phreatomagmatic-style eruptions result in more extensive fragmentation of magma and the formation of blocky shards (Self and Sparks, 1978).

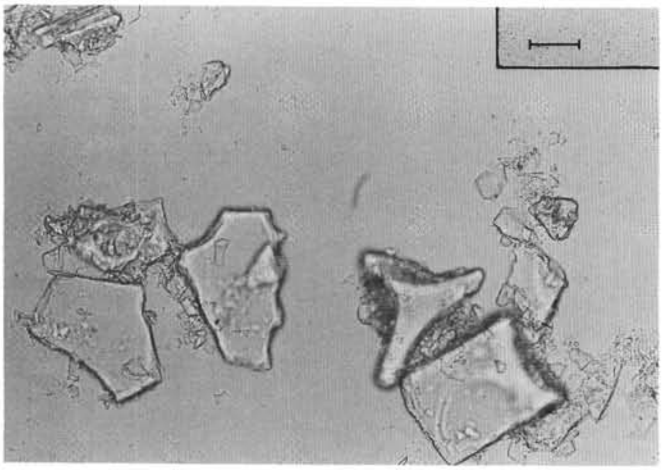

Figure 60. Photomicrograph of silicic glass shards with typical blocky shard morphology (ash layer in Sample 165-999A-45X-2, 97 cm). Scale bar is 40 µm in length.

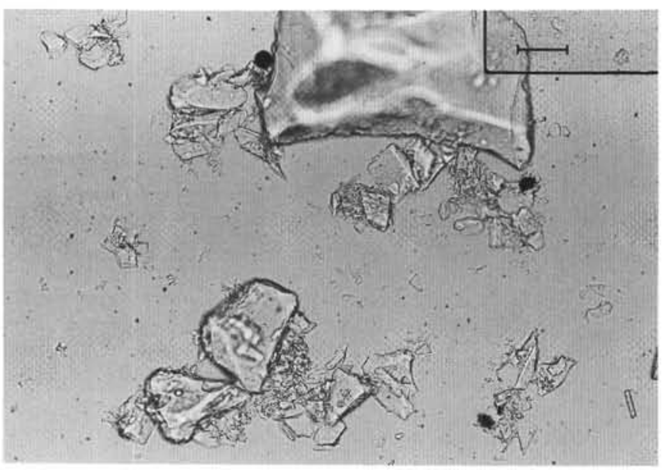

Figure 61. Photomicrograph of silicic glass shards with typical blocky and "ice cube" morphology, and pyrite framboids (ash layer in Sample 165-999A-52X-3, 46 cm). Scale bar is 40 µm in length.

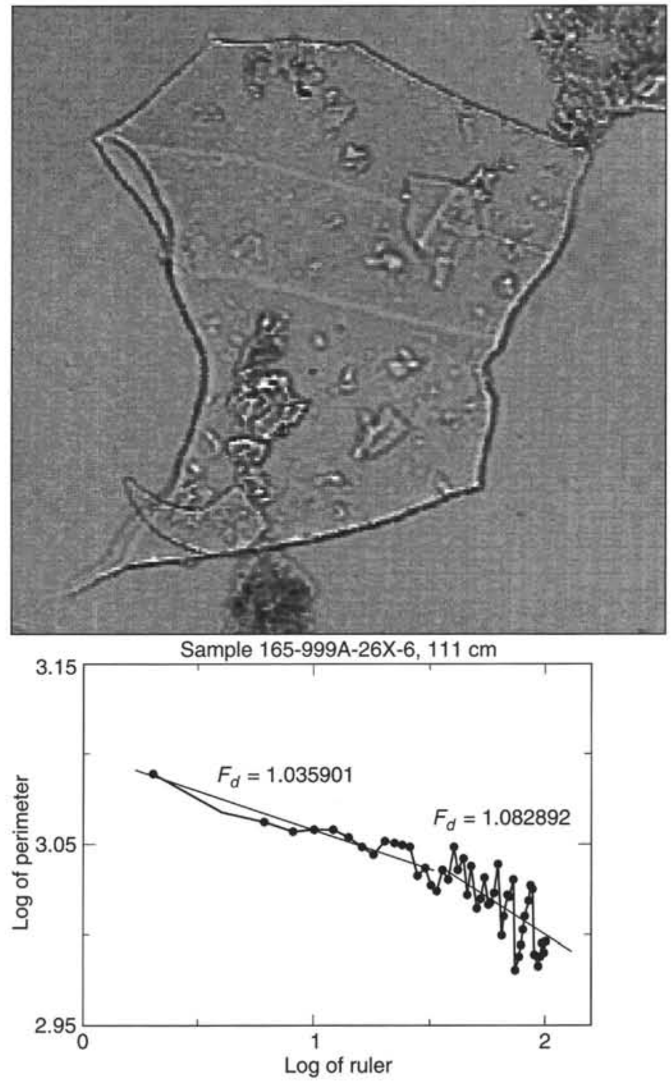

Figure 62. Digital gray-scale image of a bubble-wall shard from Section 165-999A-26X-6 (top). Maximum grain diameter is approximately 350 µm. Log of grain perimeter vs. log of ruler size (Richardson plot) based on the results of fractal analysis of bubble-wall shard (bottom). F_d corresponds to the fractal dimension of the linear segments of the plot (see text for definition of fractal dimension).

Thus, the downcore appearance of early Miocene volcanic ash layers with blocky shard morphology may indicate more frequent phreatomagmatic activity associated with large caldera lakes or shallow-marine emergent volcanic centers. Alternatively, the downcore change in shard morphology may reflect progressive stages of volcanic ash alteration. Below Core 999A-61X, there is a marked increase in the number of altered volcanic ash layers. However, we think that blocky shard morphology is more likely linked to eruption style because of their size characteristics and association with unaltered tephra layers. Many of the blocky shards are thick and lack internal gas bubbles. It is difficult to envisage how such forms could be produced by the degradation of fresh angular shards. Furthermore, in ash layers where alteration has progressed to an advanced state, it is still possible to see clearly the original sharp, angular bubble-wall morphologies.

Tephra layers with blocky shards are also distinct from the more common bubble-wall layers in that they typically contain a much higher proportion of fine-grained equant shards (e.g., Fig. 63). Some of these layers appear to have a bimodal grain-size distribution consisting of a coarse mode with large blocky shards and a fine mode of small equant grains. Such grain-size bimodality may be the result of transport and premature deposition of fine ash as aggregates (Carey and Sigurdsson, 1982). The occurrence of abundant fine-grained components provides additional evidence for the potential importance of phreatomagmatic volcanism, as higher degrees of fragmentation are a consequence of this type of activity (Self and Sparks, 1978).

Geochemistry

The major oxide and trace element chemical composition of Site 999 volcanic ash layers is presented in Tables 11 and 12. Major element concentrations are corrected for carbonate "contamination" on the basis that all C (analyzed by Carlo Erba CNS; see "Organic Geochemistry" section, "Explanatory Notes" chapter, this volume) is

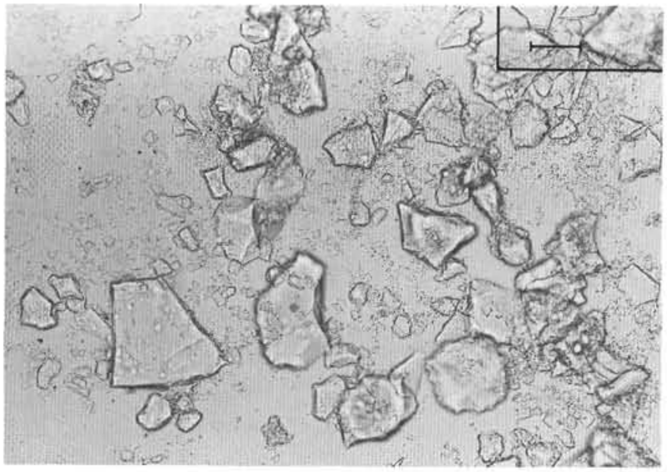

Figure 63. Photomicrograph of poorly sorted ash layer with typical blocky shard morphology, which may be typical of phreatomagmatic explosive eruptions (Sample 165-999A-50X-6, 115 cm). Scale bar is 40 µm in length.

present as $CaCO_3$. Data are then normalized to anhydrous, volatile-free compositions. Trace elements are normalized on a volatile-free basis, and a correction for the effect of strontium contamination due to carbonate is applied. The ash layers exhibit a compositional range that is primarily related to the processes of alteration and mineralization, and secondly due to intrinsic minor variation in magma chemistry. The compositional trends of unaltered ash layers define a relatively coherent trend, suggestive of a common source region, but some scatter around the trend may be the result of either variable sources or a minor alteration that is not detected petrographically (Fig. 66). Ash layers that appear unaltered (i.e., that consist dominantly of clear glass shards) are rhyolitic to dacitic in composition, with 71%–74% SiO_2 and very low MgO content. In terms of trace element content, the ash layers constitute two main groups. One group of ashes is characterized by high Rb/Sr values (>1), high Y, low Ba of 200–400 ppm, and low values of V (4–6 ppm), Cu (6 ppm), and Ni (e.g., ash layers 165-999A-39X-2, 8–11 cm; 48X-1, 14–16 cm; and 50X-1, 74–77 cm). An identical chemical group of ashes is present in the Miocene at Site 998, with Rb/Sr values of 1.7–4.3 and comparable values of other trace elements (Samples 165-998A-20X-2, 9–11 cm; 20X-CC, 32–33 cm; and 28X-4, 123–125 cm). This compositional group represents the most evolved rhyolitic glasses observed at these sites.

A second group of altered ash layers are characterized by a high content of alumina and magnesia, but low alkalies, Rb, Ba, and Y. Their composition reflects the process of conversion of volcanic glass to Mg-rich tri-octahedral smectite. The alteration process is consistent with the loss of the mobile incompatible elements, or large-ion lithophile elements from the glass, notably K, Rb, and Ba. In general, the high-field strength elements are immobile during alteration, including Y, Zr, and Nb. However, contrary to this generalization, the Site 999 altered ash layers show an extreme depletion in Y and also Nb to a lesser extent. Some ash layers have suffered mineralization, primarily with the crystallization of pyrite coatings on glass shards or the crystallization of free pyrite grains. This is reflected in the high sulfur content, up to 3 wt% sulfur in some ash layers (Table 11). The mineralization occurs both in smectite-rich altered ash layers, and in layers that consist mainly of clear and apparently unaltered glass shards. The pyrite mineralization is reflected in high bulk Fe and S values for some of the altered ash layers, and the high degree of correlation of Ni with Fe ($r = 0.845$), as well as high V con-

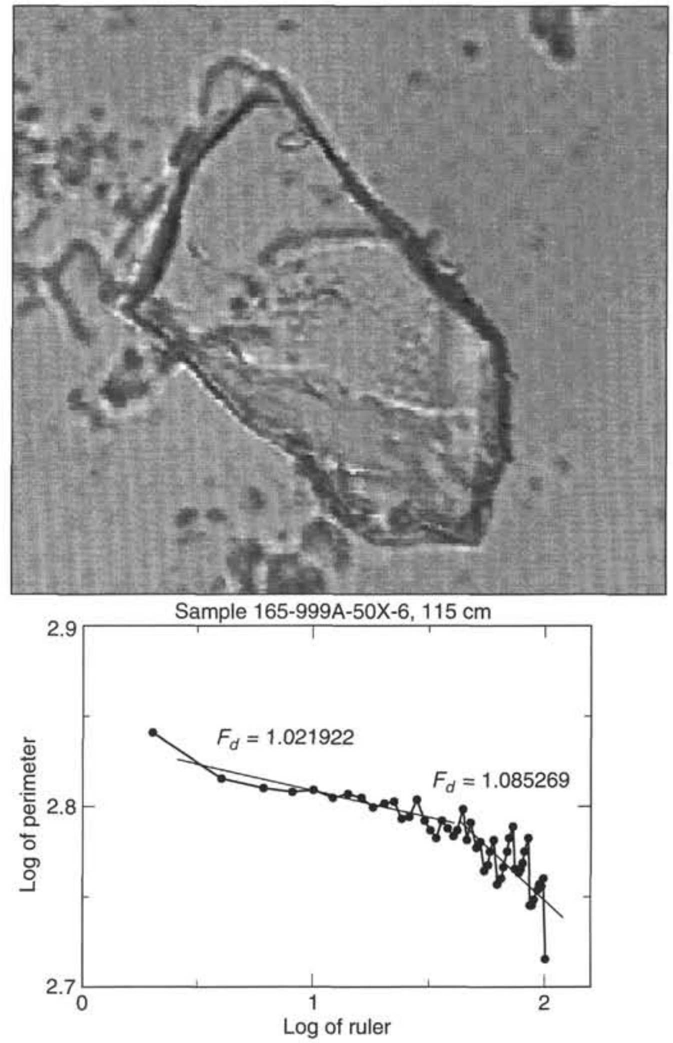

Figure 64. Digital gray-scale image of a blocky shard from Section 165-999A-50X-6 (top). Maximum grain diameter is approximately 300 µm. Log of grain perimeter vs. log of ruler size (Richardson plot) based on the results of fractal analysis of bubble-wall shard (bottom). F_d corresponds to the fractal dimension of the linear segments of the plot (see text for definition of fractal dimension).

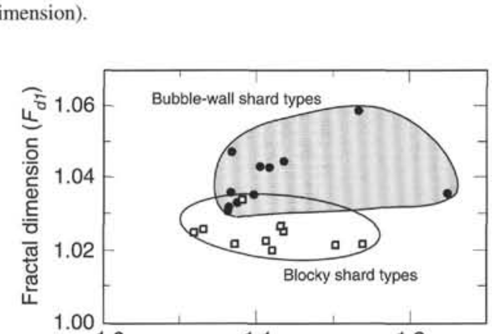

Figure 65. Discrimination of glass shard morphologies (bubble wall and blocky) from tephra layers in Hole 999A based on fractal analysis of particle morphologies. Fractal dimensions, F_{d1} and F_{d2} are the fractal dimensions calculated from Richardson plots of the fractal analyses (e.g., Figs. 62 and 64).

Table 11. Major oxide composition of volcanic ash layers.

Core, section, interval (cm)	SiO_2	TiO_2	Al_2O_3	$*Fe_2O_3$	MnO	MgO	CaO	Na_2O	K_2O	P_2O_5	Total	S	LOI	$CaCO_3$
Uncorrected values (ppm):														
165-999A-														
17H-4, 112–114	55.1	0.94	23.8	9.80	0.04	2.80	2.28	2.40	1.16	0.11	98.430	2.68	11.25	2.80
20H-2, 142–144	57.5	0.78	22.5	8.93	0.04	3.19	2.31	2.84	1.01	0.16	99.260	1.93	8.69	1.02
28X-5, 15–18	60.2	0.82	20.0	6.76	0.04	3.70	3.98	2.72	1.10	0.16	99.480	0.63	9.18	4.68
32X-1, 107–109	58.7	0.66	19.1	9.65	0.03	3.25	3.43	2.59	1.00	0.09	98.500	2.94	9.13	3.92
34X-3, 51–54	58.5	0.78	14.9	7.48	0.16	1.76	8.93	2.92	2.80	0.32	98.550	0.75	8.27	9.33
35X-2, 144–149	70.3	0.30	12.4	2.60	0.09	0.54	6.76	3.08	4.85	0.04	100.960	0.27	10.65	10.22
37X-6, 98–100	65.6	0.52	13.6	4.09	0.11	0.82	7.25	3.17	3.84	0.12	99.120	0.44	9.64	10.25
38X-3, 3–6	66.2	0.51	14.3	3.01	0.11	0.76	6.92	3.29	4.43	0.13	99.660	0.06	9.59	7.89
39X-2, 8–11	73.5	0.19	12.9	1.89	0.07	0.39	2.51	3.42	5.45	0.05	100.370	0.33	6.32	2.61
41X-6, 98–101	62.6	0.55	13.1	4.31	0.14	0.77	12.12	3.01	2.83	0.17	99.600	0.12	12.57	14.66
42X-1, 68–70	68.7	0.55	13.3	3.14	0.15	0.74	6.70	3.65	3.84	0.11	100.880	0.06	10.01	8.06
43X-4, 77–80	68.9	0.29	12.9	2.85	0.09	0.47	7.27	3.53	4.48	0.07	100.850	0.08	9.76	9.72
44X-2, 135–138	67.3	0.56	13.6	3.67	0.15	0.79	6.54	3.35	3.56	0.17	99.690	0.00	9.27	6.58
45X-5, 123–125	70.0	0.50	14.2	3.50	0.09	0.77	2.71	3.47	4.25	0.15	99.640	0.24	6.85	1.24
46X-2, 11–13	58.3	0.57	12.7	4.39	0.15	0.75	18.30	2.73	2.76	0.27	100.920	0.00	15.88	23.32
48X-1, 14–16	70.8	0.11	12.2	3.73	0.07	0.27	2.15	3.32	5.30	0.01	97.960	1.58	7.05	3.17
49X-1, 133–136	70.6	0.50	13.8	2.99	0.12	0.63	3.24	3.78	4.27	0.12	100.050	0.05	7.05	2.81
50X-1, 74–77	73.1	0.09	12.2	2.11	0.05	0.29	3.11	3.55	5.33	0.00	99.830	0.21	7.32	4.58
58X-5, 57–60	71.8	0.34	11.8	2.10	0.06	0.37	7.08	3.07	3.78	0.05	100.450	0.00	8.87	9.50
60X-1, 86–88	63.6	0.99	14.6	6.17	0.14	1.65	7.81	3.22	2.01	0.27	100.460	0.08	9.25	6.24
165-999B-														
6R-1, 28–31	59.3	0.62	17.4	6.86	0.02	3.52	8.32	2.84	0.94	0.06	99.880	0.17	12.96	10
7R-5, 59–62	61.7	0.68	16.5	7.21	0.03	3.83	2.47	2.91	1.21	0.07	96.610	0.55	10.23	1.19
8R-4, 86–89	62.8	0.34	15.1	5.38	0.04	2.97	8.35	2.85	1.98	0.04	99.850	0.16	12.12	10.75
9R-2, 98–102	61.4	1.46	16.7	7.31	0.02	3.16	3.88	3.14	1.79	0.21	99.077	0.215	8.21	2.97
11R-2, 76–79	63.6	0.54	17.1	6.33	0.02	3.76	3.87	2.93	1.40	0.08	99.630	0.18	11.35	3.7
16R-6, 122–125	56.1	0.72	15.1	5.64	0.03	3.07	13.71	2.22	1.18	0.05	97.810	0.341	15.87	18.47
24R-3, 103–107	61.3	1.11	16.4	9.73	0.04	3.38	4.06	2.81	1.34	0.17	100.337	0.16	5.69	1.26
25R-3, 36–39	69.1	0.81	13.6	3.43	0.04	1.18	6.01	3.75	2.45	0.10	100.470	0.17	12.20	6.07
26R-4, 61–63	65.9	0.79	16.3	6.63	0.03	3.09	3.06	3.24	1.52	0.24	100.798	0.311	8.66	1.01
27R-3, 26–29	68.3	0.62	14.2	4.59	0.03	1.89	4.22	3.35	2.05	0.09	99.330	0.174	9.76	13.58
28R-5, 93–96	66.6	0.45	15.8	4.41	0.03	2.32	4.26	3.85	2.04	0.06	99.820	0.16	9.17	3.56
30R-2, 135–138	68.6	0.54	16.2	4.44	0.03	2.77	2.61	3.37	1.89	0.10	100.546	0.04	10.3	1.02
31R-5, 6–9	67.0	0.66	16.6	6.09	0.04	3.88	2.00	2.88	1.35	0.11	100.606	0.2	8.4	0.82
36R-4, 19–21	67.3	0.52	15.7	4.69	0.02	3.21	3.65	3.05	1.61	0.16	99.908	0.05	10.5	2.72
37R-3, 9–11	68.5	0.44	14.9	5.41	0.02	3.13	2.07	3.29	1.84	0.04	99.635	0.11	9.8	0.654
38R-2, 135–137	67.3	0.80	15.2	5.31	0.02	4.51	1.61	2.78	1.43	0.10	99.06	0.05		0.93
Values corrected for carbonate content and loss on ignition:														
165-999A-														
17H-4, 112–114	56.83	0.97	24.55	10.11	0.04	2.89	0.73	2.48	1.20	0.11	99.90			
20H-2, 142–144	58.26	0.79	22.80	9.05	0.04	3.23	1.76	2.88	1.02	0.16	99.98			
28X-5, 15–18	62.09	0.85	20.63	6.97	0.04	3.82	1.40	2.81	1.13	0.17	99.90			
32X-1, 107–109	60.87	0.68	19.81	10.01	0.03	3.37	1.28	2.69	1.04	0.09	99.86			
34X-3, 51–54	62.41	0.83	15.89	7.98	0.17	1.88	3.95	3.11	2.99	0.34	99.55			
35X-2, 144–149	73.65	0.31	12.99	2.72	0.09	0.57	1.08	3.23	5.08	0.04	99.77			
37X-6, 98–100	69.94	0.55	14.50	4.36	0.12	0.87	1.61	3.38	4.09	0.13	99.56			
38X-3, 3–6	69.35	0.53	14.98	3.15	0.12	0.80	2.62	3.45	4.64	0.14	99.77			
39X-2, 8–11	74.30	0.19	13.04	1.91	0.07	0.39	1.06	3.46	5.51	0.05	99.99			
41X-6, 98–101	67.99	0.60	14.23	4.68	0.15	0.84	4.24	3.27	3.07	0.18	99.26			
42X-1, 68–70	71.20	0.57	13.78	3.25	0.16	0.77	2.27	3.78	3.98	0.11	99.87			
43X-4, 77–80	72.07	0.30	13.49	2.98	0.09	0.49	1.91	3.69	4.69	0.07	99.79			
44X-2, 135–138	69.99	0.58	14.14	3.82	0.16	0.82	2.97	3.48	3.70	0.18	99.84			
45X-5, 123–125	70.74	0.51	14.35	3.54	0.09	0.78	2.04	3.51	4.29	0.15	99.99			
46X-2, 11–13	65.38	0.64	14.24	4.92	0.17	0.84	5.87	3.06	3.10	0.30	98.52			
48X-1, 14–16	73.50	0.11	12.67	3.87	0.07	0.28	0.39	3.45	5.50	0.01	99.85			
49X-1, 133–136	71.68	0.51	14.01	3.04	0.12	0.64	1.69	3.84	4.34	0.12	99.98			
50X-1, 74–77	75.10	0.09	12.53	2.17	0.05	0.30	0.56	3.65	5.48	BDL	99.93			
58X-5, 57–60	75.30	0.36	12.37	2.20	0.06	0.39	1.84	3.22	3.96	0.05	99.76			
60X-1, 86–88	65.53	1.02	15.04	6.36	0.14	1.70	4.45	3.32	2.07	0.28	99.91			
165-999B-														
6R-1, 28–31	62.69	0.66	18.40	7.25	0.02	3.72	2.87	3.00	0.99	0.06	99.67			
7R-5, 59–62	64.20	0.71	17.17	7.5	0.03	3.99	1.88	3.03	1.26	0.07	99.84			
8R-4, 86–89	66.68	0.36	16.03	5.71	0.04	3.15	2.47	3.03	2.10	0.04	99.62			
9R-2, 98–102	62.99	1.50	17.13	7.5	0.02	3.24	2.27	3.22	1.84	0.22	99.93			
11R-2, 76–79	65.15	0.55	17.52	6.48	0.02	3.85	1.84	3.00	1.43	0.08	99.94			
16R-6, 122–125	63.13	0.81	16.99	6.35	0.03	3.45	3.78	2.5	1.33	0.05	98.43			
24R-3, 103–107	61.53	1.11	16.46	9.77	0.04	3.39	3.37	2.82	1.34	0.17	100.00			
25R-3, 36–39	71.13	0.83	14.00	3.53	0.04	1.21	2.69	3.86	2.52	0.10	99.91			
26R-4, 61–63	65.75	0.79	16.26	6.61	0.03	3.08	2.49	3.23	1.52	0.24	100.00			
28R-5, 93–96	68.05	0.46	16.14	4.51	0.03	2.37	2.31	3.93	2.08	0.06	99.95			
30R-2, 135–138	68.62	0.54	16.20	4.44	0.03	2.77	2.04	3.37	1.89	0.10	100.00			
31R-5, 6–9	66.90	0.66	16.58	6.08	0.04	3.87	1.54	2.88	1.35	0.11	100.00			
36R-4, 19–21	68.39	0.53	15.95	4.77	0.02	3.26	2.16	3.10	1.64	0.16	99.97			
37R-3, 9–11	69.00	0.44	15.01	5.45	0.02	3.15	1.72	3.31	1.85	0.04	99.99			
38R-2, 135–137	67.93	0.81	15.34	5.36	0.02	4.55	1.63	2.81	1.44	0.10	99.99			

Notes: Shipboard XRF data in weight percent. Shipboard XRF data are uncorrected for carbonate. Total iron reported as $*Fe_2O_3$. LOI = loss on ignition, BDL = below detection limit. This entire table also appears on CD-ROM (back pocket).

Table 12. Trace element concentrations of volcanic ash layers.

Core, section, interval (cm)	Nb	Zr	Y	Sr	Rb	Zn	Cu	Ni	Cr	V	Ba
Uncorrected values (ppm):											
17H-4, 112–114	11.8	201	2	336	11	64	63	449	<3	103	227
20H-2, 142–144	6.1	170	3	361	9	92	43	212	6	78	196
28X-5, 15–18	16.5	314	3	487	12	57	19	198	2	66	154
32X-1, 107–109	8.7	229	2	495	13	155	27	493	6	60	139
34X-3, 51–54	7.1	143	25	646	42	101	55	210	6	120	1235
35X-2, 144–149	5.8	187	32	273	79	46	17	45	4	36	1400
37X-6, 98–100	7.4	147	24	461	57	110	19	55	5	47	1110
38X-3, 3–6	8.4	170	23	460	74	75	11	32	<3	30	1173
39X-2, 8–11	7.2	117	15	120	135	54	6	52	<3	4	479
41X-6, 98–101	6.5	115	24	511	38	95	22	38	<3	39	1055
42X-1, 68–70	6.2	152	41	357	36	109	12	25	<3	27	1141
43X-4, 77–80	6.7	135	27	312	81	57	12	18	<3	22	901
44X-2, 135–138	4.8	106	25	472	45	94	12	11	<3	28	1067
45X-5, 123–125	9.1	180	29	289	64	174	19	77	<3	35	1183
46X-2, 11–13	4.7	112	21	614	35	122	46	71	<3	39	860
48X-1, 135–136	16.1	125	50	100	203	46	6	13	<3	4	315
49X-1, 74–77	4.7	212	45	261	47	87	14	16	<3	16	859
50X-1, 57–60	19.8	172	60	119	148	71	5	36	<3	<4	269
58X-5, 86–88	3.0	174	34	255	43	166	15	5	<3	23	860
60X-1, 90–92	6.6	145	32	632	20	78	23	26	<3	112	410
6R-1, 28–31	10.5	307	<1	696	9	109	30	42	<3	41	133
7R-5, 59–62		382	<1	2771	1	84	44	33	<3	56	3389
8R-4, 86–89	7.2	165	4	511	25	44	18	22	<3	31	375
9R-2, 98–102	12.7	241	19	1154	18	167	53	25	<3	166	117
11R-2, 76–79	7.4	334	<1	1081	11	72	23	32	<3	32	100
14R-6, 136–138	1.2	144	<1	1101	18	93	32	25	<3	44	219
16R-6, 122–126	9.1	300	3	3607	8	84	34	43	<3	50	1316
24R-3, 103–107	2.0	84	17	850	15	101	79	55	<3	282	55
25R-3, 36–39	5.5	169	12	1948	18	63	18	15	<3	72	192
26R-4, 61–63	10.8	267	10	1378	13	67	15	13	<3	37	443
27R-3, 26–29	10.0	281	10	1556	16	71	16	16	<3	28	164
28R-5, 93–96	26.7	246	2	1247	16	50	21	11	<3	20	197
29R-6, 7.74–193	7.7	193	35	1406	19	93	18	13	<3	59	131
30R-2, 14–275	14.0	275	18	1152	13	69	16	13	<3	47	240
31R-5, 4.7–242	4.7	242	42	889	10	73	9	6	<3	22	354
33R-2, 5.69–329	5.7	329	4	1640	15	48	49	10	<3	19	1784
34R-3, 5.35–175	5.4	175	2	1349	16	39	13	11	<3	39	577
35R-2, 4.54–290	4.5	290	29	1385	11	37	14	3	<3	22	166
36R-4, 6.99–168	7.0	168	10	1501	9	75	23	7	<3	31	122
37R-3, 2.52–232	2.5	232	1	1653	12	48	11	12	<3	24	149
38R-2, 8.94–191	8.9	191	22	1177	10	69	11	6	<3	38	104
Values corrected for carbonate content and loss on ignition:											
17H-4, 112–114	13.4	229	2	342	11	72	71	514	1	116	234
20H-2, 142–144	6.7	187	3	383	9	101	47	233	6	85	207
28X-5, 15–18	18.6	353	3	480	11	63	20	223	1	72	132
32X-1, 107–109	9.7	256	2	499	12	173	29	554	6	65	121
34X-3, 51–54	7.9	160	28	601	43	113	60	239	4	133	1341
35X-2, 144–149	6.6	217	37	162	88	50	16	50	2	37	1575
37X-6, 98–100	8.4	168	27	381	61	125	18	61	3	49	1214
38X-3, 3–6	9.5	193	26	411	81	84	9	34	<3	30	1290
39X-2, 8–11	7.7	125	16	92	145	58	5	56	<3	3	497
41X-6, 98–101	7.7	136	29	395	38	113	21	42	<3	39	1182
42X-1, 68–70	7	173	47	290	37	124	10	26	<3	27	1259
43X-4, 77–80	7.5	153	31	213	89	63	10	18	<3	20	970
44X-2, 135–138	5.3	118	28	440	48	105	11	10	<3	28	1165
45X-5, 123–125	9.8	194	31	294	68	188	20	83	<3	37	1269
46X-2, 11–13	5.7	141	27	421	31	159	52	90	<3	38	945
48X-1, 135–136	17.5	135	55	63	221	49	5	13	<3	2	317
49X-1, 74–77	5	230	49	244	50	94	14	16	<3	16	915
50X-1, 57–60	21.8	188	66	63	161	77	4	38	<3	1	257
58X-5, 86–88	3.2	197	39	148	44	189	13	2	<3	21	913
60X-1, 90–92	7.3	163	36	628	19	87	24	28	<3	125	412
6R-1, 28–31	12.8	376	<3	835	10	133	36	51	<3	50	152
7R-5, 59–62	<3	423	<3	2947	1	90	45	33	<3	56	3706
8R-4, 86–89	8.7	200	5	575	28	52	21	26	<3	36	429
9R-2, 98–102	14.0	265	21	1225	18	184	57	26	<3	182	97
11R-2, 76–79	8.3	381	<3	1108	7	79	23	34	<3	32	32
14R-6, 136–138	0.8	163	<3	1033	9	104	30	23	<3	42	84
16R-6, 122–126	12.3	406	4	4866	10	113	45	58	<3	67	1770
24R-3, 103–107	2.0	86	18	821	12	105	82	57	<3	298	6
25R-3, 36–39	6.4	200	14	2292	21	74	21	17	<3	85	218
26R-4, 61–63	11.5	287	10	1316	6	68	11	10	<3	33	367
27R-3, 26–29	12.0	338	12	1825	17	84	18	18	<3	32	164
28R-5, 93–96	30.1	276	2	1388	17	56	23	12	<3	22	213
29R-6, 7.74–193	8.8	219	40	1583	21	105	20	14	<3	66	140
30R-2, 14–275	15.7	308	20	1281	14	77	18	14	<3	52	262
31R-5, 4.7–242	5.1	262	46	970	11	80	10	6	<3	24	385
33R-2, 5.69–329	6.4	369	5	1838	17	54	55	11	<3	21	2001
34R-3, 5.35–175	5.9	193	2	1476	17	43	14	12	<3	42	628
35R-2, 4.54–290	5.0	323	32	1511	11	40	14	2	<3	23	161
36R-4, 6.99–168	7.9	191	11	1696	10	85	26	8	<3	35	133
37R-3, 2.52–232	2.8	258	1	1826	13	53	12	13	<3	26	158
38R-2, 8.94–191	9.0	192	22	1183	10	69	11	6	0	38	104

Note: This entire table also appears on CD-ROM (back pocket).

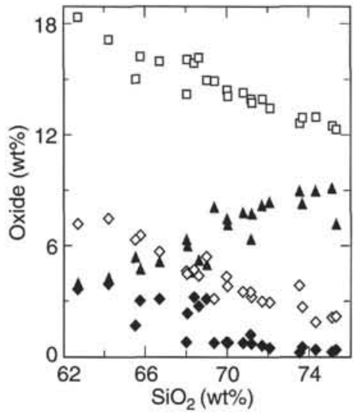

Figure 66. Major oxide trends of unaltered and glass-rich volcanic ash layers from Site 999. The trends show a range from dacitic to rhyolitic compositions. Open squares = Al_2O_3, open diamonds = Fe_2O_3, solid diamonds = MgO, and solid triangles = $Na_2O + K_2O$.

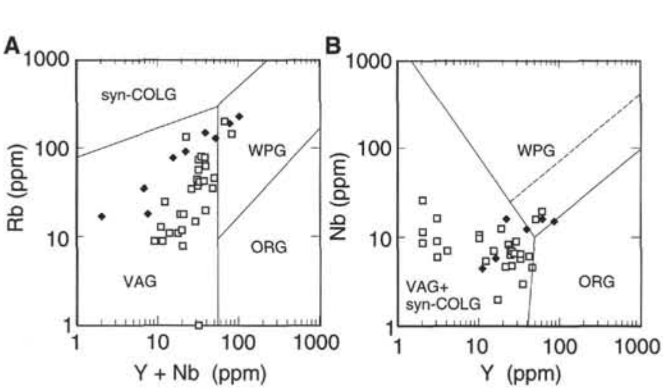

Figure 67. **A.** Volcanic ash layers from Sites 998 (solid diamonds) and 999 (open squares) plotted in granite Rb/(Nb+Y) discrimination diagram of Pearce et al. (1984), with the fields of volcanic arc silicic rocks (VAG), syn-collisional granites (syn-COLG), within-plate granites (WPG), and ocean-ridge granites (ORG). The altered volcanic ash layers define a separate group at very low Nb+Y and Rb values, due to leaching. The fresh volcanic glasses generally fall within the field of volcanic arc silicic rocks, but some layers trend into the field of within-plate granites. **B.** Volcanic ash layers from Sites 998 (solid diamonds) and 999 (open squares) are shown in the granite Nb-Y discrimination diagram of Pearce et al. (1984); fields same as in Figure 67A. Dashed line is the field boundary for ORG from anomalous ridges. The altered volcanic ash layers define a separate group at very low Rb values, due to leaching. The fresh volcanic glasses generally fall within the field of volcanic arc silicic rocks.

tent in the pyrite-rich ashes, indicates that these trace metals are substituting for iron in the pyrite. Altered ash layers, dominated by smectite, are characterized by high alumina content and decreased levels of silica, alkalis, and alkaline earths, caused by leaching during the glass alteration. These signatures are strongly reflected in the pore-water chemistries of the ash-rich zones in the sediment (see "Inorganic Geochemistry" section, this chapter).

We have used trace element discrimination diagrams to attempt to characterize the tectonic setting of the source regions of the unaltered Miocene volcanic ash layers. The elements Rb, Nb, and Y have been considered as the most efficient trace element discriminants for granitic rocks (Pearce et al., 1984). As shown in Figure 67, the vast majority of the silicic ash layers plot in the field of volcanic arc granites, but trend into the field of within-plate granites. A potential source volcanic center for the Miocene ash layers at Site 999 is the Atitlan I caldera in Guatemala (Newhall, 1980). This center produced voluminous pyroclastic flows or ignimbrites in Miocene time, including five or more Maria Tecun welded ash flow tuffs. These large eruptions have been estimated to be on the order 500 km^3 and were produced in a series of caldera-forming events (C.G. Newhall, pers. comm., 1996). The fourth of these (Tmt-4) is K/Ar dated as 11.6 ± 0.5 Ma. The pale reddish brown ignimbrites contain up to 50% broken and corroded quartz, plagioclase, sanidine, biotite, and hornblende phenocrysts. Comparisons are difficult at this stage, however, because the land-based data are few in number, and those that exist are on crystal-rich, whole-rock ignimbrite samples, whereas the ash fall layers are essentially glasses that have been depleted in crystals during atmospheric sorting. The Atitlan ignimbrites are dacites to rhyolites, with Rb/Sr values that increase from about 0.2 to greater than unity as SiO_2 increases from 68% to 77% (Newhall, 1980), or very close to the trends determined at Sites 998 and 999.

Discussion

The source of Site 999 Miocene ash fallout is most likely the same as that of contemporaneous ash fall layers at Site 998 on the Cayman Rise. Site 999 is currently about 700 km east of the major volcanic sources in Costa Rica and Nicaragua of the Central American arc, and in the Miocene these sources were most likely at a comparable distance from the site. Before the initiation of subduction in the Central American arc, the Caribbean Plate, like the Farallon Plate, was moving east-northeast at a rate of about 8 cm/yr (Duncan and Hargraves, 1984). However, at the time of Miocene volcanism in the region, the motion of the Caribbean Plate with respect to the Chortis Block had ceased or slowed down considerably because of the onset of subduction in the Middle America Trench. Thus, the present distance to the Central American arc is probably also representative for Miocene times.

The magnitude (total erupted volume) of explosive eruptions can be roughly gauged from the thickness vs. distance relationship of ash fallout downwind from the volcanic source. Ash fallout that produces a layer of five to tens of centimeters thick about a thousand kilometers from source is from an event that is of the same scale as the 50–100 km^3 rhyolitic eruption of the Roseau ignimbrite in the Lesser Antilles at 28 k.y. (Carey and Sigurdsson, 1980; Sigurdsson et al., 1980), or the Los Chocoyos eruption from the Atitlan caldera at 84 k.y. (Hahn et al., 1979). The magmatic activity that sustained this rate of emission of rhyolitic tephra for a period of several million years must be regarded as of batholith proportions, and of the type typical for either a continental crustal setting or a volcanic arc at a continental margin, such as the northern part of the Central American arc on the Chortis Block. The ancient Chortis terrane originated from the Mexican subcontinent, near Acapulco, based on lead isotopic evidence (Kesler et al., 1990). The block includes pre-Mesozoic metamorphic rocks with radiometric ages up to 305 Ma (Horne et al., 1976). The thick Miocene ignimbrite sequence that covers much of Central America is commonly referred to as the Padre Miguel Group in Guatemala and the Chalatanango Formation in El Salvador (Horne et al., 1990).

Site 999 is also downwind from volcanoes in the southern part of the Central American arc, in Costa Rica and Panama, and these regions must also be evaluated as potential sources of the Miocene tephra fallout at this site. There are, however, marked contrasts in the crustal structure and volcanic products of the northern and southern parts of the Central American arc. There is a sharp division between the northern and southern geologic terranes at the Santa Elena Fault Zone in northernmost Costa Rica and its seaward continuation in the Hess Escarpment. Unlike the northern Chortis block, which developed on continental crust, the southern Chorotega and Choco blocks developed on oceanic crust, and include much of Costa Rica and Panama.

Evidence of volcanic activity in the southern Central American arc can be found in numerous formations throughout this area. In Costa Rica, volcaniclastic sediments and volcanics of Paleocene to early Miocene age are contained in the Rio Lari, Tuis, and Senosri formations of the Limon Basin (Escalante, 1990). Farther to the southeast, in the Canal Basin, upper Eocene to upper Oligocene deposits of tuffaceous siltstones/sandstones are present in the Bohio and Caimito formations. In western Colombia, there are also Eocene tuffs up to 2 km thick (Morti tuffs) and Oligocene–Miocene tuffs of almost 1.5-km thickness (Pacific tuffs). Lower Miocene ash-fall layers were deposited at the time of radiolarian and diatom sedimentation in the Napipi and Sierra formations (H. Duque-Caro, pers. comm., 1996). Other important volcaniclastic deposits of mostly middle to late Miocene age include the Punta Carballo, Pacacua, Turrucares, Coris (with abundant detrital quartz), Curre, and Venado formations in Costa Rica and the Culebra, Cucaracha, and Gatun formations in the Canal Basin of Panama.

In summary, the arc volcanism associated with the Chorotega and Choco blocks probably began in Paleocene to Eocene time, but it greatly intensified in the late Cenozoic, especially in Costa Rica and on the Pacific side of central Panama. The initiation of this intense episode in Panama may be the San Pedro Formation of late to middle Miocene age, and the Aguacate Formation in Costa Rica. However, the scale of Miocene volcanism in the southern region is orders of magnitude lower than on the Chortis block, and the nature of the magmas erupted on the Chorotega and Choco blocks is typically andesitic, rather than the dominantly rhyolitic Miocene activity of the Chortis block. These southern terrains, therefore, are unlikely sources of the Miocene tephra layers observed at Sites 999 and 998. The geochemical evidence, the geologic history of the Central American arc, and the volcanotectonic relations indicate that the Miocene ash fallout recorded in sediments recovered at Sites 998 and 999 records an episode of explosive volcanism on the Chortis Block to the west.

The origin of the silicic magmatism that produced the Miocene ash fallout layers may be related to the reconfiguration of plates in the Pacific Ocean. Major plate reorganization occurred at the time of the breakup of the southern Farallon Plate at around 25 Ma, forming the Cocos and Nazca Plates, and the Galapagos Spreading Center (Mattson, 1984; Atwater, 1989). The east-trending Galapagos Spreading Center intervenes between these plates, imparting a northeast component to the Cocos Plate and thus changing the direction of subduction under the Chortis Block from a more or less eastern to northeast direction in the early Miocene or late Oligocene. Studies of the Middle America Trench convergent plate boundary off Guatemala also show that the configuration of the forearc basin changed greatly before the Miocene, with major uplift of the shelf and development of the present arc-trench system (von Huene, 1989). Before this time, the Chortis Block had been moving in an eastward direction, with strike-slip motion along the Motagua Fault system. With the rearrangement of the Pacific plates and the onset of a more northeasterly component on the Chortis Block, strike-slip motion was hindered and a higher rate of subduction occurred at the plate margin in the Middle America Trench beneath the Chortis Block. Thus, the rearrangement of plate configurations in the Pacific may have brought about increased subduction under the Chortis Block, resulting in enhanced magma production and a pulse of explosive volcanic activity at the surface, as manifest in the abundant Miocene ash fall layers found in Leg 165 sediments in the Caribbean. The volcanic front on the Chortis Block, located farther inland in the Miocene, has moved progressively closer toward the Pacific coast in late Tertiary times and during the Quaternary (Carr and Stoiber, 1990).

PHYSICAL PROPERTIES

The physical properties program at Site 999 included multisensor track (MST) and thermal conductivity measurements of whole-round cores, and *P*-wave velocity, index properties, electrical resistivity, and vane shear strength measurements of split cores. Methods for these measurements are described in the "Physical Properties" section of the "Explanatory Notes" chapter (this volume).

The high recovery at Site 999 allowed us to obtain a complete suite of physical properties data. MST *P*-wave velocity, magnetic susceptibility, and GRAPE data were recorded at 1-cm intervals for Cores 165-999A-1H to 21H (down to a depth of about 197 mbsf) and for Cores 165-999B-59R to 62R (the K/T boundary and Cretaceous cores). In all other cores, measurements were made at 5-cm intervals. MST *P*-wave velocity data were not recorded in the part of Hole 999A cored with the XCB or in the part of Hole 999B cored with the RCB. MST natural gamma-ray measurements were made at 10-cm intervals to a depth of about 1048 mbsf, and at 5-cm intervals below this depth. Thermal conductivity was measured on Sections 1, 3, and 5 of each core in Hole 999A to a depth at which induration prevented insertion of the needles (around 197 mbsf). On the split core, *P*-wave velocity was measured and samples for index properties were taken at a sampling interval of one per section in all cores, whereas one measurement per section of electrical resistivity and vane shear strength was taken in Hole 999A to the depth at which induration prevented insertion of the needles for electrical resistivity (around 197 mbsf) and the vane for shear strength (around 84 mbsf).

Multisensor Track

Data from the MST measurements are presented in Figure 68 and Tables 13 through 16. The magnetic susceptibility shows a relatively high background signal in the uppermost 130 m of the hole due to the higher amount of terrigenous and volcaniclastic material when compared with Site 998. Susceptibility peaks in the upper 130 mbsf and between 400 and 560 mbsf are related to pronounced single ash layers (see "Lithostratigraphy" section, this chapter). The peaks in magnetic susceptibility correspond to local low values in GRAPE density, whereas the GRAPE data indicate a relatively high overall density in the same intervals. There is a zone of low susceptibility values between 158 and 178 mbsf, interpreted as an interval with less volcanic/volcaniclastic input. Two zones of lower susceptibility at 220–225 mbsf and 295–325 mbsf are due to the relatively high amount of biosiliceous components (see "Lithostratigraphy" section, this chapter). The Miocene carbonate crash (see "Lithostratigraphy" section, this chapter) is documented by higher magnetic susceptibilities, as already shown for Site 998.

As at Site 998, the GRAPE densities are close to those determined from index properties in Hole 999A, except in the uppermost 200 mbsf, where the high water content causes an overestimation of density by the GRAPE. Boyce-correction is only included in the processing of Hole 999B. GRAPE densities are shifted to lower values relative to index property data downhole. This is to be expected because the cores below 400 mbsf do not fill the liner, and the GRAPE processing assumes a core diameter corresponding to a filled liner.

P-wave velocity data correspond well to the data collected on the split core (see below). The natural gamma radiation shows a general correlation with the magnetic susceptibility (especially for the Miocene carbonate crash interval, Fig. 68) and is relatively high compared to Site 998 for the Neogene interval. For older sediments, the natural gamma radiation is generally low. For Section 165-999B-59R-3 to Core 165-999B-62R, the MST measurements were done in 1-cm intervals for magnetic susceptibility and GRAPE devices, and in 5-cm intervals for the natural gamma device, to collect high-resolution data across the K/T boundary (Fig. 69). The magnetic susceptibility data of the Cretaceous sediments show a well-pronounced cyclicity in decimeter scale, whereas the susceptibility pattern of the Paleocene sediments is more irregular. The white limestones near the boundary (see "Lithostratigraphy" section, this chapter) are characterized by relatively high GRAPE densities (Fig. 69).

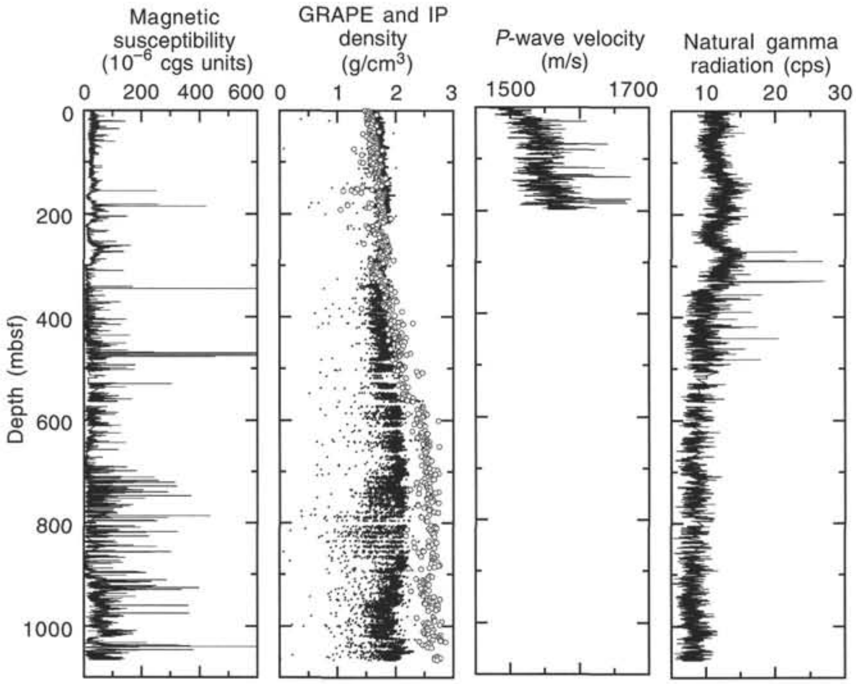

Figure 68. Multisensor track data showing magnetic susceptibility, GRAPE density (shaded symbols) with index properties density (open circles) for comparison, *P*-wave velocity, and natural gamma radiation vs. depth.

Table 13. Gamma-ray attenuation porosity evaluator (GRAPE) data for Site 999.

Core, section, interval (cm)	Depth (mbsf)	Raw counts	DAQ period (s)	Density (g/cm³)
165-999A-				
1H-1, 3	0.03	22,683	31.553	
1H-1, 4	0.04	22,630	31.557	
1H-1, 5	0.05	22,883	31.536	
1H-1, 6	0.06	22,658	31.555	
1H-1, 7	0.07	22,515	31.567	
1H-1, 8	0.08	22,440	31.573	
1H-1, 9	0.09	22,594	31.56	
1H-1, 10	0.1	22,491	31.569	
1H-1, 11	0.11	22,622	31.558	
1H-1, 12	0.12	22,781	31.545	

Notes: Raw counts are not reported for Hole 999B. DAQ = data acquisition. Density = bulk density, no Boyce correction applied. The data in this table differ from the raw data in that (1) all columns do not appear, (2) depths have been added, (3) columns have been labeled, and (4) unsuccessful measurements have been deleted.

Only part of this table is produced here. The entire table appears on CD-ROM (back pocket).

Table 14. Magnetic susceptibility data for Site 999.

Core, section, interval (cm)	Depth (mbsf)	Raw mean susc. (10^{-6} cgs)	SD susc.	Drift corr.	DAQ period (s)
165-999A-					
1H-1, 5	0.05	14.4	0.320803	0	5
1H-1, 10	0.1	14.8	0.32	0	5
1H-1, 15	0.15	13.6	0.355295	0	5
1H-1, 20	0.2	14	0	0	5
1H-1, 25	0.25	12.8	0.235775	0	5
1H-1, 30	0.3	12.8	0.235775	0	5
1H-1, 35	0.35	12.4	0.326787	0	5
1H-1, 40	0.4	12.8	0.273924	0	5
1H-1, 45	0.45	14	0	0	5
1H-1, 50	0.5	15.85	0.32	–0.1	5

Notes: Susc. = susceptibility, SD = standard deviation, corr. = correction, DAQ = data acquisition. The data in this table differ from the raw data in that (1) all columns do not appear, (2) depths have been added, (3) columns have been labeled, (4) unsuccessful measurements have been deleted, (5) magnetic susceptibility values have been averaged, and (6) data from Cores 165-999A-11H through 61X are not reported.

Only part of this table is produced here. The entire table appears on CD-ROM (back pocket).

Thermal Conductivity

Thermal conductivity data were collected at the same locations where the velocity measurements were made (Table 17; Fig. 70). The thermal conductivity increases from around 1.0 W/(m·K) near the top of the cored interval, where porosities are about 80%, to around 1.3 W/(m·K) at 197 mbsf, where porosities have fallen to about 62% (see below).

P-wave Velocity

P-wave velocity measurements from split cores were made along the axis of the core (DSV1) as well as perpendicular to the axis (DSV2) by the Digital Sonic Velocimeter down to a depth of around 106 mbsf (Table 18; Fig. 71A). Unlike Site 998, the DSV1 (perpendicular to the core/bedding) vs. DSV2 (parallel to the core/bedding) shows an anisotropy of the velocity data for the uppermost 100 mbsf of Hole 999A (Fig. 71B). The higher velocity data measured parallel to the bedding are probably a result of the relatively higher amount of clay at this site compared with Site 998. Between 106 and 364 mbsf, the sediments are more indurated. For this interval, the *P*-wave velocities were measured in half cores parallel to bedding by the Hamilton Frame. Below 364 mbsf, the Hamilton Frame was used to measure *P*-wave velocities perpendicular to bedding on discrete samples. The change of measuring device at around 106 mbsf and around 364 mbsf seems to have no influence on the continuity of the data.

The laboratory data were corrected to in situ stress (Table 18; Fig. 71A) by the empirical relation derived by Urmos et al. (1993; see "Physical Properties" section, "Site 998" chapter, this volume). It is questionable whether this correction, being derived for a pure carbonate lithology, is valid for the mixed lithology sediments of Hole 999A. Unfortunately, no log data were obtained in Hole 999A for comparison. For the entire logged section of Hole 999B, however, the log velocities correspond well to the uncorrected laboratory velocities rather than the corrected ones.

Table 15. Multisensor track *P*-wave data for Site 999.

Core, section, interval (cm)	Depth (mbsf)	*P*-wave velocity (m/s)	Raw mean time	Raw SD time	Raw mean displ.	Raw SD displ.	Mean signal level	DAQ period (s)
165-999A-								
1H-1, 8	0.08		30.4	0.02	43	0	3	5
1H-1, 9	0.09		44.4	7.8044	42	0	26	5
1H-1, 10	0.1	1508	50.7	0.0245	42	0	175	5
1H-1, 11	0.11	1510	50.5	0	41	0	178	5
1H-1, 12	0.12	1517	50.3	0.0245	40	0	180	5
1H-1, 13	0.13	1513	50.4	0.0316	39	0	181	5
1H-1, 14	0.14	1506	50.5	0.02	39	0	181	5
1H-1, 15	0.15	1505	50.6	0.0245	39	0	183	5
1H-1, 16	0.16	1504	50.6	0	39	0	183	5
1H-1, 17	0.17	1504	50.6	0	39	0	182	5

Notes: SD = standard deviation, displ. = displacement, DAQ = data acquisition. The data in this table differ from the raw data in that (1) all columns do not appear, (2) depths have been added, (3) columns have been labeled, and (4) unsuccessful measurements have been deleted.

Only part of this table is produced here. The entire table appears on CD-ROM (back pocket).

An overall increase in velocity with depth is seen from around 1500 m/s near the seafloor to ~4200 m/s at 800 mbsf. At about 575 mbsf, the velocity shifts from 2000 to >2800 m/s, which correlates with the boundary of lithologic Units IV to V (see "Lithostratigraphy" section, this chapter). Below 570 mbsf, the velocity data show a high variance, which is caused by the higher lithologic variability of the sediments compared with Hole 999A (above 570 mbsf). Clayey intervals exhibit lower velocities (<3000 m/s), and higher velocity values occur in more indurated limestones (>4000 m/s).

Index Properties

Index properties samples were taken from split cores at those locations where the velocity measurements were made (Table 19; Fig. 72). Wet and dry weights and wet and dry volumes were measured and used to calculate wet-bulk density, grain density, water content, porosity, and dry-bulk density (see "Explanatory Notes" chapter, this volume).

Porosity decreases from about 80% near the seafloor to around 14% at a depth of 700 mbsf, and remains approximately constant to 900 mbsf. Below 900 mbsf, porosity rises again to about 25% (Fig. 72). In Hole 999A, wet-bulk density values correlate with the amount of foraminifers and the occurrence of biogenic opal, and thus helped in defining the lithologic subunits (see also "Lithostratigraphy" section, this chapter, and Figs. 8, 9). The lithologic change from sediments containing less than 10% foraminifers to sediments with more than 10% foraminifers in an interval around 230 mbsf is marked by low densities and high porosities. Two zones of lower densities (and magnetic susceptibility values) and lower porosities at 220–225 mbsf and at 295–325 mbsf (Fig. 72) coincide with sediments containing a higher amount of biogenic opal (up to 40%). According to Boyce (1973), low density layers are caused by biogenic opaline silica and an open radiolarian structure combined with dissolution of fine-grained calcareous material. The zone of slightly lower porosity at 400–415 mbsf correlates with slightly lower dry-bulk densities (Table 19) and reflects the increased occurrence of ash layers (see also "Igneous Petrology and Volcanology" section, this chapter).

Electrical Resistivity

Electrical resistivity data (Table 20; Fig. 73) were collected at the same locations where the velocity measurements were made. The electrical resistivity increases from around 0.4 Ωm near the seafloor to around 1.35 Ωm at 210 mbsf. The formation factor, *F*, corresponding to the resistivity was calculated from $F = R_o/R_w$, where R_o is the resistivity of the sediment and R_w is the resistivity of the pore water. The pore-water resistivity was assumed to be that of seawater at 20°C (0.206 Ωm). The porosity, Ø, was calculated from the formation factor by Archie's equation

$$Ø = (a/F)^{1/m}, \tag{7}$$

where *F* is a formation factor, and *a* and *m* are lithology-dependent constants. For the entire site, the relationship of porosity to the formation factor results in Archie coefficients of 1.2 and 2.33 for *a* and *m*, respectively, with a correlation coefficient of 0.62. The resulting porosity data, when compared with index properties–derived porosity values, indicate differences of less than 10% (Fig. 73).

Vane Shear Strength

The ODP motorized minivane was used to measure undrained shear strength in split-core sections (Table 21; Fig. 74). The measurements were made at the same depths used for *P*-wave velocity determination. Overall, shear strength increases with depth from 2 kPa at seafloor to ~60 kPa down to 43 mbsf, below which the shear strength varies from 20 to 40 kPa.

Gammaspectral Scanning of the Cretaceous/Tertiary Boundary Section[3]

To identify the spectral gamma-ray signature of the K/T boundary sections penetrated during Leg 165, core sections containing the K/T boundary section of Hole 999B were measured by the natural gamma radiation detector on the shipboard multisensor track (see "Explanatory Notes" chapter, this volume, for details of the procedure). The data were compared to the natural gamma-ray spectrometry (NGT) log for Hole 999B (see "Downhole Measurements" section, this chapter).

The total gamma radiation (SGR) and K plus Th (CGR) data for Hole 999B are plotted in Figure 75, where the level of the K/T boundary is tentatively indicated, as reported in the "Lithostratigraphy" and "Biostratigraphy" sections (this chapter). The lowermost 20 m of the Paleogene has a relatively high natural gamma-ray intensity, so that a decrease in the gamma-ray intensity is seen when crossing from Paleogene into Cretaceous sediments.

Laboratory measurements of K, Th, and U in cores from the K/T boundary section of Hole 999B are plotted in Figure 76. If the K/T boundary is represented by the thin clay band near the bottom of Section 165-999B-59R-CC (see "Lithostratigraphy" section, this chapter), corresponding to a depth near 101 cm on Figure 76, the boundary is characterized by low K relative to Th and U. This is shown in Figure 77, where the K/(Th+U) value is plotted for the core data as well as the log data of Hole 999B. The downhole logging data for Hole 999B show the same characteristic K/(Th+U) pattern as the laboratory data.

DOWNHOLE MEASUREMENTS

Operations

After drilling to a total depth of 1066.4 mbsf in Hole 999B, the borehole and drilling equipment were prepared for wireline logging. A pill of sepiolite mud was pumped down the drill pipe to sweep the

[3]D.E. Paulsen, Department of Automation, Technical University of Denmark b. 322, DK-2800 Lyngby, Denmark; I.L. Lind, Department of Geology and Geotechnical Engineering, Technical University of Denmark b. 322, DK-2800 Lyngby, Denmark.

Table 16. Natural gamma-ray (NGR) data for Site 999.

Core, section, interval (cm)	Depth (mbsf)	GR (cps)	Win 1	Win 2	Win 3	Win 4	Win 5	DAQ period (s)
165-999A-								
1H-1, 5	0.05	11.8	6.4	3.8	1.35	0.15	0.1	20
1H-1, 15	0.15	13.1	6.85	4.05	1.5	0.35	0.35	20
1H-1, 25	0.25	12.2	6.35	3.95	1.3	0.2	0.4	20
1H-1, 35	0.35	11.75	6.3	3.25	1.3	0.4	0.5	20
1H-1, 45	0.45	11.55	5.5	3.75	1.4	0.55	0.35	20
1H-1, 55	0.55	12.15	6.2	4.25	1.1	0.4	0.2	20
1H-1, 65	0.65	11.95	5.65	4.1	1.5	0.5	0.2	20
1H-1, 75	0.75	11.95	5.9	4.25	0.85	0.35	0.6	20
1H-1, 85	0.85	11.75	5.85	3.65	1.2	0.6	0.45	20
1H-1, 95	0.95	13.7	6.55	4.6	1.75	0.4	0.4	20

Notes: Win 1 through Win 5 = counts per second in each of five energy windows, corresponding to Schlumberger practice for spectral natural gamma-ray logs. DAQ = data acquisition. The data in the table differ from the raw data in that (1) all columns do not appear, (2) depths have been added, (3) columns have been labeled, and (4) unsuccessful measurements have been deleted.

Only part of this table is produced here. The entire table appears on CD-ROM (back pocket).

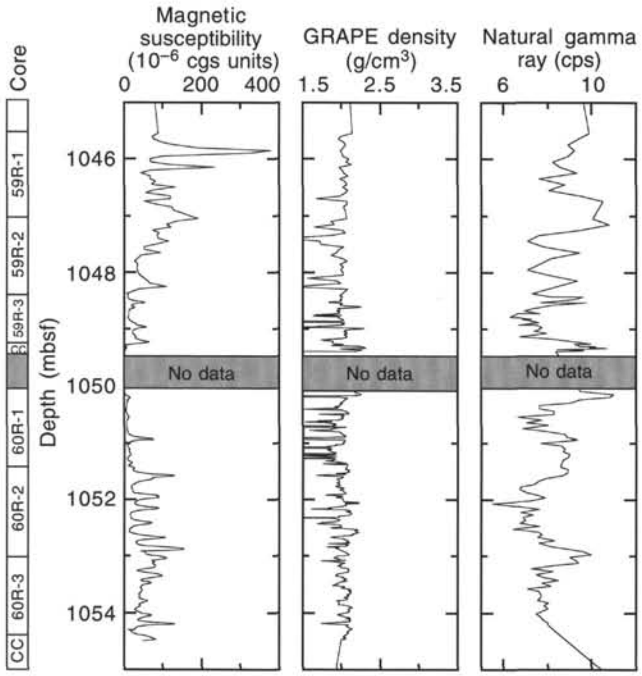

Figure 69. Multisensor track data showing magnetic susceptibility, GRAPE, and natural gamma radiation vs. depth for Cores 165-999B-59R and 60R (K/T boundary cores). Note that the data gap is only an artifact of ODP's core logging nomenclature. Currently, other data (e.g., FMS) indicate that little or no real data gap exists between Sections 165-999B-59R-CC and 60R-1.

hole of cuttings not removed by circulated seawater. A complete wiper trip was waived because of the excellent hole conditions and significant time constraints. The drill pipe was tripped to the surface and the bit removed at the rig floor. The drill pipe was then returned to the borehole after a successful reentry attempt and set at 554.2 mbsf, which was 28 m below the casing shoe. Before the beginning of each logging run, the drill pipe was set to 554.2 mbsf to aid the tools as they passed into a narrower part of the borehole at 540 mbsf. After each tool had passed the constriction, the drill pipe was pulled up to 527.6 mbsf to provide more open hole available for logging. The first of three logging runs began in Hole 999B at 2045 UTC on 23 January 1996, and all logging runs were completed at 1700 UTC on 24 January, corresponding to a total logging time of 21.75 hr (Table 22).

The Quad combo tool string included, from top to bottom, the telemetry cartridge, natural gamma spectrometry, long-spaced sonic, compensated neutron, lithodensity, and dual induction resistivity

Table 17. Thermal conductivity measured on whole-round core sections for Site 999.

Core, section, interval (cm)	Depth (mbsf)	Thermal conductivity (W/[m·K])
165-999A-		
1H-3, 33-33.1	3.33	1.046
1H-5, 33-33.1	6.33	1.01
2H-3, 33-33.1	10.93	1.113
2H-5, 33-33.1	13.93	1.054
3H-1, 33-33.1	17.43	0.95
3H-3, 33-33.1	20.43	1.05
3H-5, 33-33.1	23.43	1.094
4H-1, 33-33.1	26.93	1.017
4H-5, 33-33.1	32.93	1.089
5H-3, 33-33.1	39.43	1.091

Only part of this table is produced here. The entire table appears on CD-ROM (back pocket).

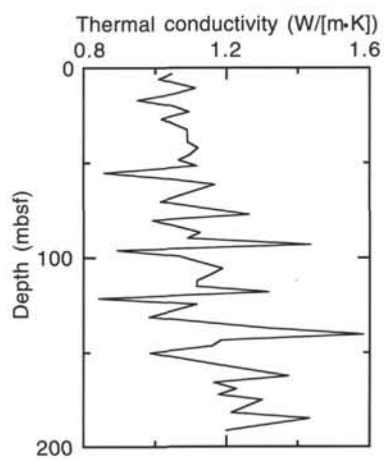

Figure 70. Thermal conductivity vs. depth measured on whole cores.

tools, creating a tool string 33 m long. The Quad combo tools were run down to the bottom of the hole to a depth of 1067.1 mbsf, as measured by the downhole logging equipment. During the downward trip, the far-spaced transmitter (12-ft spacing between transmitter and receiver) in the long-spaced sonic tool was determined to be malfunctioning. All digital sonic data acquisition was determined to be normal. Only the analog DTLF channel was not collected.

A repeat section between 1067.1 and 970.8 mbsf was run first to insure adequate data collected in the K/T boundary region. The tool string was lowered again to the bottom of the hole and logged upward at a speed of 300 m/hr. (Table 22). As the tools were pulled upward,

Table 18. DSV (DSV1 and DSV2) and Hamilton Frame (DSV3) velocities measured at discrete intervals for Site 999.

Core, section, interval (cm)	Depth (mbsf)	DSV1 (km/s)	DSV2 (km/s)	DSV3 (km/s)	Urmos correction (km/s)	Corrected velocity (m/s)
165-999A-						
1H-1, 33–33.1	0.330		1.580		0.000	1580
1H-2, 33–33.1	1.830	1.539			0.003	1542
1H-2, 33.1–33.2	1.831		1.553		0.003	1556
1H-3, 33–33.1	3.330	1.547			0.005	1552
1H-3, 33–33.1	3.330		1.562		0.005	1567
1H-4, 33–33.1	4.830		1.586		0.007	1593
1H-4, 33.1–33.2	4.831	1.565			0.007	1572
1H-5, 33–33.1	6.330	1.532			0.009	1541
1H-5, 33–33.1	6.330		1.551		0.009	1560
1H-6, 32.9–33	7.329	1.547			0.010	1557

Note: DSV = Dalhousie University/Bedford Institute of Oceanography Digital Sonic Velocimeter.

Only part of this table is produced here. The entire table appears on CD-ROM (back pocket).

the depth to the end of casing was measured at 525.1 mbsf, which is 1.1 m shallower than the depth calculated by the driller. The final Quad combo run was completed by acquiring data in the drill pipe and casing through 12.6 m above the seafloor.

During the first run with the Quad combo, the wireline heave compensator (WHC) shut down unexpectedly. The WHC was immediately powered down, and all vital operating parameters were checked. No problems were detected with the WHC, so it was restarted and was operational for the remainder of the logging.

The geochemical tool string included telemetry, natural gamma spectrometry, aluminum activation clay, and induced gamma-ray spectrometry tools, which created a tool string 17.13 m long. Logging data were recorded from 1065.1 to 521.8 mbsf as the tool string moved uphole at 200 m/hr (Table 22). A 50.3-m repeat section was logged from 1065.1 to 1014.8 mbsf.

The Formation MicroScanner (FMS) included telemetry, natural gamma spectrometry, and FMS sections. To assist the tool in descending to total depth more quickly, downward pressure was applied to the tool by pumping seawater down the drill pipe. High-resolution data were collected with the FMS between 1067.1 and 537.8 mbsf. A 52.3-m repeat section from 1067.1 to 1014.8 mbsf was run for quality control and to collect duplicate information over the interval suspected of containing K/T boundary sediments.

Log Quality

In general, the data from all three tool strings appear to be of high quality and rarely were the data degraded by borehole washouts. It was necessary, however, to adjust several data points where the HLDT tool had recorded erroneous density and PEF values. In addition, sonic velocities were unrealistically low or high in several intervals (probably because of cycle skipping). Unrealistic velocities were replaced with interpolated values. Additional processing (including depth shifting) of logging data was conducted onshore by the Borehole Research Group. The results are presented in Figures 78 through 80; in compilation figures at the end of this chapter; and on CD-ROM in the back pocket of this volume. Detailed information regarding shore-based log processing is given in the "Downhole Measurements" section of the "Explanatory Notes" chapter (this volume).

Logging Units

Four logging units were identified in Hole 999B (Figs. 78–80), based on log responses and analyses of recovered cores; these should not be confused, however, with the lithologic units defined earlier ("Lithostratigraphy" section, this chapter). The boundaries between adjacent logging units were placed at significant inflection points resulting from simultaneous variations on at least several of the logs. These units display consistent log responses or distinct overall trends.

The lithologies for unrecovered intervals can be inferred from the logs, based on the broad assumption that the logging tools respond to varying proportions of the primary constituents in samples actually recovered (e.g., carbonate, hemipelagic clay, volcanic ash, altered volcanogenic material, and biogenic silica) and to their relative porosity.

Logging Unit 1 (527–563 mbsf)

Logging Unit 1 is characterized by the lowest and least variable values of sonic velocity (1.9–2.0 km/s) and resistivity (1 Ωm) in the entire logged interval (Fig. 78). The bulk density and PEF value, which is a lithologic indicator, are both low relative to logging Unit 2, but, because the caliper arms were closed at 550 mbsf, these logs were not recorded through most of this unit. The Th/U value also exhibits several peaks (Fig. 80).

Logging Unit 1 corresponds to the base of the lithologic Unit III, which consists of clayey calcareous chalks with interbedded abundant ash layers (see "Lithostratigraphy" section, this chapter). The boundary between logging Units 1 and 2 corresponds to the lithologic Unit III/Unit IV boundary and is marked by a step increase in sonic velocity, bulk density, and resistivity values. The distinct logging response is consistent with the abrupt change in lithification at 563 mbsf, where the chalk and clay of lithologic Unit III become the clayey limestone that distinguishes lithologic Unit IV. The low values of the iron indicator ratio (IIR) are consistent with the generally less-altered nature of volcanic ash reported for lithologic Unit III (see "Lithostratigraphy" and "Igneous Petrology and Volcanology" sections, this chapter). Thorium concentrations in volcanic ash are typically high relative to uranium and potassium, and therefore increases in Th/U, can be used to discriminate ash layers from nonvolcanogenic clays. In general, the entire logged interval is characterized by extreme variability in Th/U, which is consistent with coring results that indicate the nearly ubiquitous presence of distinct ash layers.

Logging Subunit 2a (563–644 mbsf)

The abrupt increase in the velocity, density, and resistivity values defining the top of this unit is coupled with an increased variability in the amplitude of these curves. The average value is relatively constant. The average sonic velocity is approximately 2.6 km/s, and bulk density and resistivity vary from about 2.10 to 2.25 g/cm^3 and from 2.0 to 2.2 Ωm, respectively. Natural gamma-ray counts have a constant average value slightly higher than in Unit 1, which seems to be primarily due to a higher content of potassium. The Th/U value continues to show maxima at the about the same frequency observed in logging Unit 1.

Figure 79 displays geochemical data in the form of elemental ratios: the lithology indicator ratio, LIR = Si/(Si+Ca); the iron indicator ratio, IIR = Fe/(Si+Ca); and the porosity indicator ratio, PIR = H/(Si+Ca). The LIR is used to assess the relative amounts of carbonate and silica, the IIR serves to identify iron-rich clay intervals, and the PIR indicates the relative amount of bound and unbound water in the formation. Relative to logging Subunit 2b, the LIR, IIR, and PIR are higher and more variable and generally decrease downhole. The aluminum concentration is consistently low down to 600 mbsf, where Al concentrations increase gradually to the bottom of logging Subunit 2a.

Logging Subunit 2a corresponds exactly to lithologic Subunit IVA, described as clayey calcareous limestone with common thin ash layers (see "Lithostratigraphy" section, this chapter). The boundary between logging Subunits 2a and 2b corresponds to the simultaneous change in slope of several logging curves.

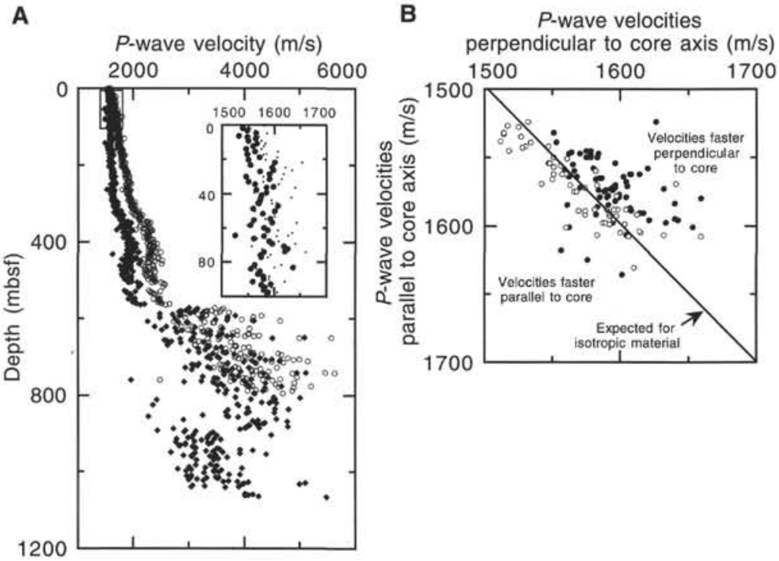

Figure 71. **A.** *P*-wave velocities for Site 999 (solid circles are DSV measurements parallel to core axis, dots are DSV measurements perpendicular to core axis, and solid diamonds are Hamilton Frame measurements). Open circles refer to depth-corrected values. Below 600 mbsf, this depth correction is too large (see text). **B.** Anisotropy of *P*-wave velocities DSV1 vs. DSV2 for the upper 100 m of Holes 998A (open circles) and 999A (solid circles). The higher velocities perpendicular to the core axis for Hole 999A are thought to arise from the higher amount of clay.

Table 19. Index properties measured at discrete intervals for Site 999.

Core, section, interval (cm)	Depth (mbsf)	Water content (bulk wt%)	Bulk density (g/cm^3)	Grain density (g/cm^3)	Dry density (g/cm^3)	Porosity (%)
165-999A-						
1H-1, 32–34	0.32	54.70	1.48	2.65	0.67	78.92
1H-2, 32–34	1.82	54.07	1.54	2.80	0.71	81.36
1H-3, 32–34	3.32	51.78	1.51	2.71	0.73	76.42
1H-4, 32–34	4.82	49.76	1.55	2.81	0.78	75.50
1H-5, 32–34	6.32	48.49	1.53	2.82	0.79	72.56
1H-6, 32–34	7.32	49.25	1.55	2.72	0.79	74.52
2H-1, 32–34	7.92	49.21	1.53	2.83	0.78	73.51
2H-2, 32–34	9.42	51.31	1.68	2.73	0.82	83.99
2H-3, 32–34	10.92	48.62	1.52	2.72	0.78	72.17
2H-4, 32–34	12.42	47.66	1.61	2.81	0.84	74.77

Only part of this table is produced here. The entire table appears on CD-ROM (back pocket).

Table 20. Electrical resistivity measured at discrete intervals for Hole 999A.

Core, section, interval (cm)	Depth (mbsf)	Resistivity (Ωm)
165-999A-		
1H-1, 33–35	0.33	0.432
1H-2, 33–35	1.83	0.401
1H-3, 33–35	3.33	0.537
1H-4, 33–35	4.83	0.590
1H-5, 33–35	6.33	0.553
1H-6, 33–35	7.33	0.499
2H-1, 33–35	7.93	0.467
2H-2, 33–35	9.43	0.536
2H-3, 33–35	10.93	0.611
2H-4, 33–35	12.43	0.320

Only part of this table is produced here. The entire table appears on CD-ROM (back pocket).

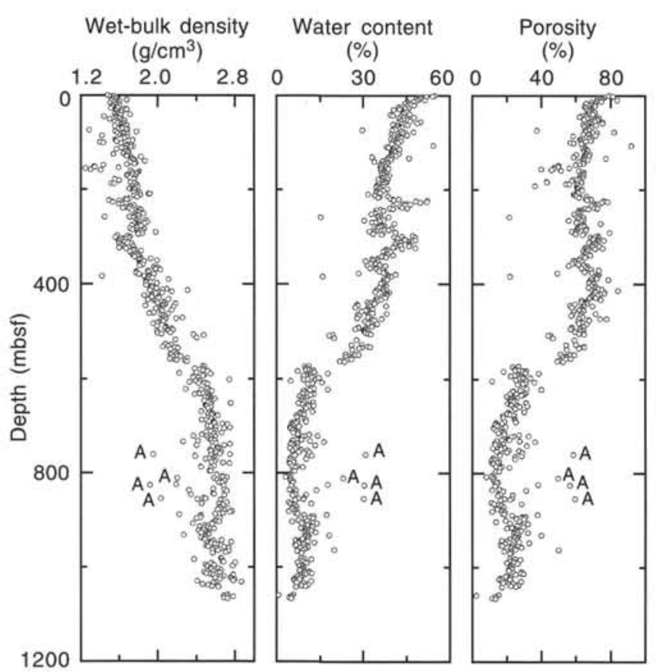

Figure 72. Wet-bulk density, water content, and porosity vs. depth. The letter "A" refers to samples from ash layers.

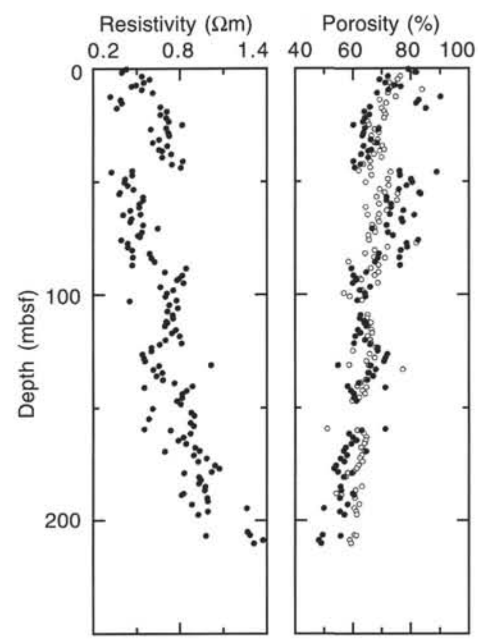

Figure 73. Electrical resistivity and a comparison of Archie porosity (solid circles) and porosity from index properties (open circles) vs. depth.

Table 21. Undrained and residual shear strength from miniature vane shear measurements for Site 999.

Core, section, interval (cm)	Depth (mbsf)	Undrained shear strength (kPa)	Residual shear strength (kPa)
165-999A-			
1H-1, 33–33.1	0.33	2.5	1.1
1H-2, 33–33.1	1.83	3.6	2.2
1H-3, 33–33.1	3.33	7.4	5.1
1H-4, 33–33.1	4.83	9.1	4.6
1H-5, 33–33.1	6.33	10.4	6.3
1H-6, 33–33.1	7.33	15	10
2H-1, 33–33.1	7.93	5.7	3.8
2H-2, 33–33.1	9.43	14.2	8.9
2H-3, 33–33.1	10.93	10.7	5.7
2H-4, 33–33.1	12.43	13.5	6.3

Only part of this table is produced here. The entire table appears on CD-ROM (back pocket).

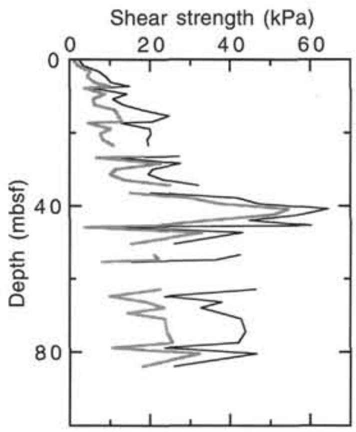

Figure 74. Undrained shear strength (solid line) and residual shear strength (shaded line) vs. depth.

Logging Subunit 2b (644–688 mbsf)

Logging Subunit 2b is defined by uniformly increasing velocity (2.75 to >3.5 km/s), density (2.25–2.4 g/cm^3), and resistivity (2.2–4 Ωm), and a steady decrease in PIR and IIR values. These logging responses are interpreted as an increase in lithification (decrease in porosity), which indicates a gradual transition in lithology from clayey limestone (lithologic Subunit IVA) to limestone with clay (lithologic Subunit IVB). This logging transition also corresponds to the steady increase in carbonate concentration from 610 to 688 mbsf ("Lithostratigraphy" section, this chapter). The transition is complete by 680 mbsf and is marked by minimum values of LIR, IIR, PIR, and aluminum concentrations from 680 to 688 mbsf. Logging Subunit 2b is also characterized by the conspicuous absence of extreme Th/U maxima and relatively low potassium concentrations, indicating an additional lithologic change. This logging response is consistent with the observation of thinner ash layers (>10 cm) and smaller quantities of ash in this interval ("Lithostratigraphy" section, this chapter). An exception occurs at 650–653 mbsf where there is a maximum of Th/U; however, no thick ash layer has been reported for this interval.

Logging Subunit 3a (688–719 mbsf)

The high values of sonic velocity, density, and resistivity reached at the base of logging Subunit 2b are maintained through logging Subunit 3a. However, the sonic velocity and resistivity curves show greater variability (3.0–3.5 km/s and 3–4.5 Ωm, respectively). The

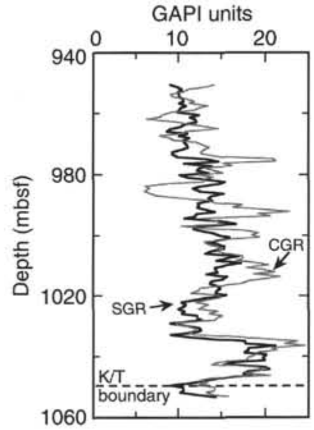

Figure 75. Logging data for Hole 999B. Total natural gamma-ray (SGR) and the K plus Th signal (CGR) over the depth interval containing the K/T boundary. The K/T boundary is near a decrease in natural gamma-ray intensity when crossing from Paleogene into Cretaceous sediments.

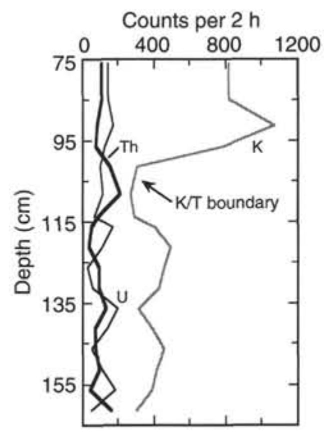

Figure 76. K, Th, and U data from laboratory measurements of spectral gamma-ray intensity over the interval 165-999B-59R-3, 76 cm, to 60R-1, 55 cm. The depth scale is chosen so that the plot refers to the top of Section 165-999B-59R-3.

bulk density curve is more constant and displays an average value of about 2.35 g/cm^3.

A slight increase is observed in the natural gamma-ray counts, associated with a steady increase in potassium concentration and a return of distinct maxima in the Th/U value. Several Th/U maxima appear to correspond to ash layers observed in the cores ("Lithostratigraphy" section, this chapter).

Logging Subunit 3a corresponds to the top 30 m of lithologic Subunit IVC, which is distinguished by an increase in clay content and the amount and thickness of the ash layers ("Lithostratigraphy" section, this chapter). The generally elevated, but highly variable, logging responses of Subunit 3a indicate distinct alternations in the extent of lithification, consistent with thicker ash layers within well-lithified limestone. FMS images show this interval as generally high-resistivity bands, punctuated by isolated low-resistivity bands. This image is interpreted as distinct low-resistivity ash layers within resistive limestone. The logging response within Subunit 3a indicates that the change in the physical properties of the limestone/clay portion of the sediment that characterizes lithologic Subunit IVB are maintained for an additional 30 m into lithologic Subunit IVC.

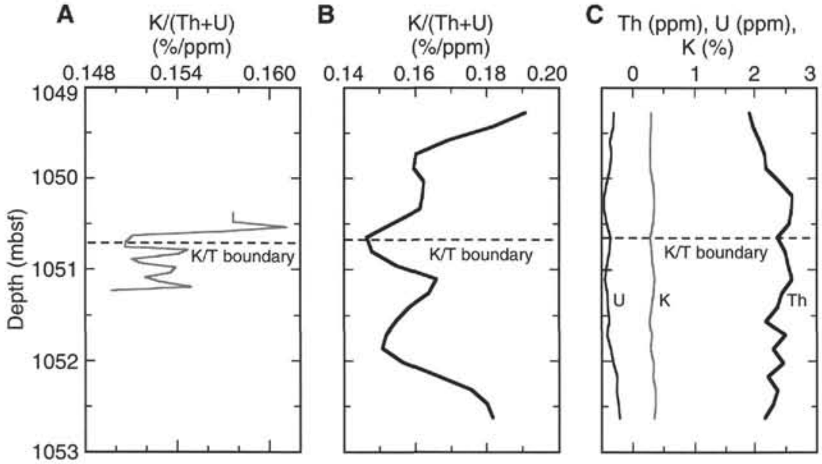

Figure 77. **A.** K/(Th+U) data from laboratory measurements. **B.** K/(Th+U) data from the downhole NGT log. **C.** K, Th, and U data from downhole log. The depth scale of laboratory data has been adjusted to match that of the logging data.

Table 22. Time schedule (UTC) for logging operations at Hole 999B, including a listing of the tools used during each logging run.

Time (UTC)	Activity
23–24 Jan. 1996	
Drillers' TD = 3905.3 mbrf (1066.4 mbsf), WD = 2838.9 mbrf, casing shoe = 3365.1 mbrf (526.2 mbsf)	
1915	Make up cable. Quad combo assembled and prepared for logging.
2045	Run in hole with Quad combo (DIT/HLDT/CNT/SDT/NGT/TCC/LEH-QT).
2115	Begin logging 96.3-m section (1067.1–970.8 mbsf). Pull pipe up 25.5 m to 527.6 mbsf. Run full pass (1067.1–12.6 mbsf).
0155	Quad combo pulled out of drill string.
0245	Quad combo disassembled and removed from rig floor.
0330	GLT assembled and prepared for logging.
0405	GLT lowered into the drill string.
0700	Begin logging 50.3-m repeat section (1065.1–1014.8 mbsf). Pull pipe up 25.5 m to 527.6 mbsf. Run full pass (1065.1–521.8 mbsf).
1000	GLT pulled out of drill string.
1100	GLT disassembled and removed from rig floor.
1115	FMS assembled and prepared for logging.
1125	RIH with FMS.
1315	Begin logging 52.3-m repeat section between (1067.1–1014.8 mbsf). Pull pipe up 25.5 m to 527.6 mbsf. Run full pass (1067.1–537.8 mbsf).
1500	FMS pulled out of drill string.
1600	FMS disassembled and removed from rig floor.
1700	End logging operations.

Note: TD = total depth, WD = water depth.

Logging Subunit 3b (719–859 mbsf)

The logging Subunit 3b/3a boundary is defined by a step decrease in velocity (2.75 km/s), density (2.25 g/cm^3), and resistivity (2.5 Ωm) and increases in the LIR, PIR, and PEF values. The natural gamma-ray counts maintain the relatively high values observed at the base of Subunit 3a (>10 API), with several intervals above 15 API units. Logging Subunit 3b corresponds to the portion of lithologic Subunit IVC below 719 mbsf, where the consistent logging response indicates an overall decrease in lithification (increase porosity), presumably caused by a distinct increase in the concentration of ash and or clay (i.e., overall elevated gamma ray and an extreme drop in resistivity). The logging response is consistent with the reported increase in the number of ash layers below 719 mbsf ("Lithostratigraphy" section, this chapter). Thick ash layers are also responsible for two distinct anomalies within logging Subunit 3b at 790–795 and ~857 mbsf. The upper anomaly (790–795 mbsf) is defined by the absolute maximum in gamma-ray counts (>20 API) caused by elevated concentrations of thorium, potassium, and uranium. In addition, absolute maxima in LIR, IIR, and PIR and minima in velocity, density, resistivity, and PEF are observed (Figs. 78–80). This anomaly occurs within the Core 165-999B-31R interval (785–795 mbsf), where recovery is only 59%, but where very dark ash layers are common at the base (see core photos in Section 4). FMS images reveal numerous, closely spaced, low-resistivity layers between 790 and 797 mbsf, which we interpret as an unusually ash-rich interval. The FMS data allow better estimates of the depth and thickness of such zones where core recovery is often low.

The second anomaly at 857 mbsf is marked by minima in velocity, density, resistivity, and PEF. This anomaly corresponds to Core 165-999B-38R (853–863 mbsf, 58% recovery) where a 40-cm-thick ash layer has been reported along with several thinner ash layers ("Lithostratigraphy" section, this chapter). The FMS data reveal a distinct interval of low resistivity between 856.58 and 857.72 mbsf and indicate that the 40-cm-thick ash layer that was recovered may represent only a portion of an ash layer that is over 1 m thick (Fig. 81). Interestingly, this interval does not appear to be associated with an extreme gamma-ray response, although a large excursion in Th/U is present at about 852 mbsf (Fig. 80).

At the base of logging Subunit 3a, aluminum concentrations become extremely variable from 837 to 859 mbsf, whereas most other logs show distinct changes from 850 to 859 mbsf and mark the lower boundary of this unit.

Logging Subunit 3c (859–887 mbsf)

Logging Subunit 3c is characterized by highly variable but steadily increasing velocity (3–4 km/s) and resistivity (2.5–5 Ωm), a step increase in density (~2.4 g/cm^3), and a uniform decrease in gamma-ray counts (10–5 API) mainly due to lower potassium and thorium concentrations. The aluminum concentration, LIR, IIR, and PIR curves all display uniformly low values beginning at 859 mbsf.

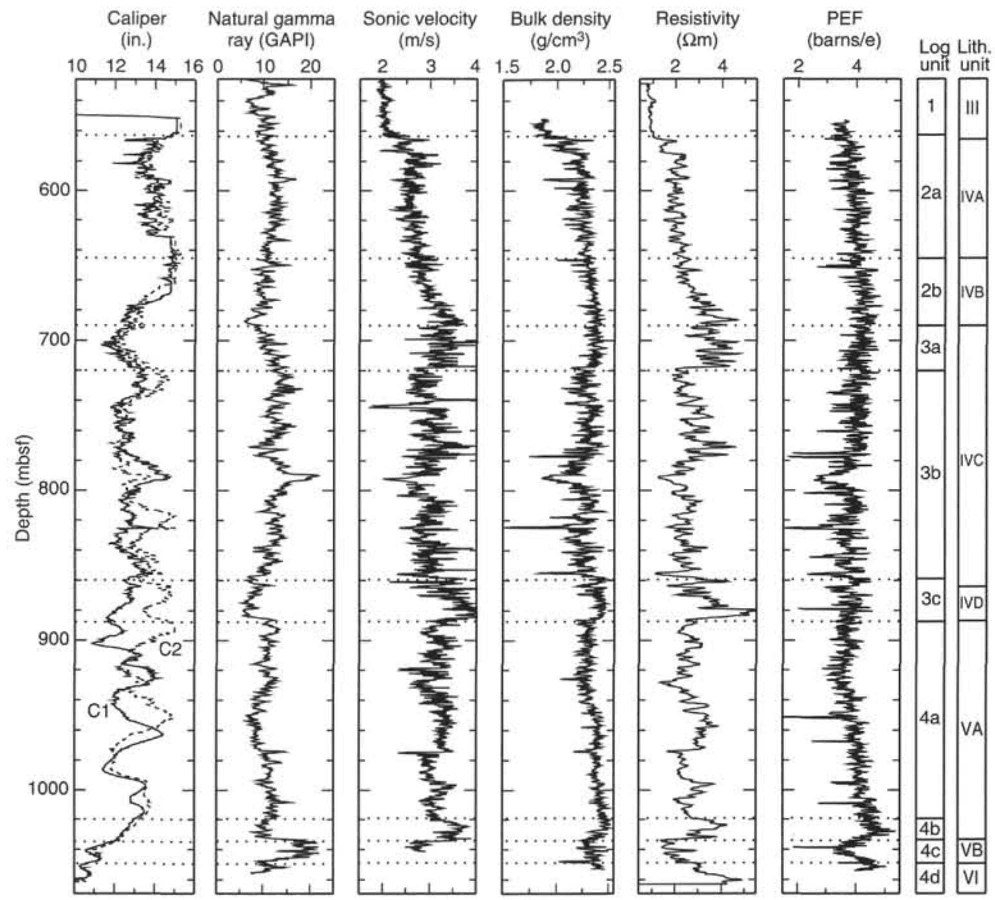

Figure 78. Selected downhole logs from Quad combo (QC) and FMS tool strings for the interval from 525 to 1070 mbsf in Hole 999B: calipers from the FMS (C1 perpendicular to C2), total natural gamma ray (QC up to 1035 mbsf and FMS below), sonic velocity (QC), bulk density (QC), resistivity, and photoelectric effect (PEF) (QC). Depth intervals of logging units are marked by dotted lines. The lithologic units are defined in the "Lithostratigraphy" section (this chapter). Sonic velocity, resistivity, and density reflect the porosity of the formation and therefore the degree of lithification or cementation. In general, sections with high concentrations of volcanogenic material correspond to relative minima in velocity, density, resistivity, and PEF, and maxima in gamma ray.

Logging Subunit 3c corresponds to lithologic Subunit IVD (866–887 mbsf), which consists of calcareous limestone with clay, and is further distinguished by a reduction in the abundance and thickness of volcanic ash layers ("Lithostratigraphy" section, this chapter). The logging response is consistent with the lithologies reported, including the increased carbonate content of the limestone, and suggests that the upper boundary of lithologic Subunit IVD may extend up to 850–860 mbsf.

The lower boundary of logging Subunit 3c, which represents the boundary between the major logging and lithologic units, corresponds to abrupt changes in the majority of the logging curves.

Logging Subunit 4a (887–1019 mbsf)

The upper boundary of logging Subunit 4a is defined by a step decrease in velocity, density, and resistivity and an increase in aluminum concentration, LIR, IIR, PIR, and natural gamma-ray counts. In general, the logging curves gently undulate throughout Unit 4, reaching alternate broad, co-varying minima/maxima over approximately 50-m wavelengths; however, they are punctuated by several more abrupt changes. The two orthogonal calipers on the FMS tool indicate that the borehole is both elliptical in shape and regularly undulating in diameter (see caliper curves in Fig. 78). A change of borehole shape can result from a lithologic change, and, if the hole diameter becomes too large (>15 in), it can influence the log response on certain tools regardless of lithology. At Site 999, the caliper rarely exceeded 15 in, however, and the geochemical and sonic velocity logs, which are relatively less sensitive to borehole diameter, co-vary with logs such as density, which require contact with the borehole wall. Thus, we interpret the broad undulations to reflect real variations in physical properties and/or lithology.

Logging Subunit 4a corresponds to most of lithologic Subunit VA, which is characterized by lithologies that range in composition from almost pure claystone to limestone end-members ("Lithostratigraphy" section, this chapter). The logging response in this unit can be explained by the varying contributions of these end-member lithologies with varying amounts of ash. For example, at approximately 920–930 mbsf, the LIR, IIR, PIR, and aluminum concentrations show broad maxima and velocity, density, and resistivity curves show significant minima. The gamma-ray counts are elevated and variable, but no large anomalies are present. This interval corresponds to extremes in lithologic and physical properties with the lowest carbonate concentration within lithologic Subunit VA, high magnetic susceptibility, and a peak in relative quartz abundance. The logging response is similar to that of a thick clay or ash layer, but without an extreme gamma-ray response. In addition, the FMS image does not show a distinct banded appearance, as it often does with thick ash layers in carbonate. Instead the FMS reveals an interval of relatively

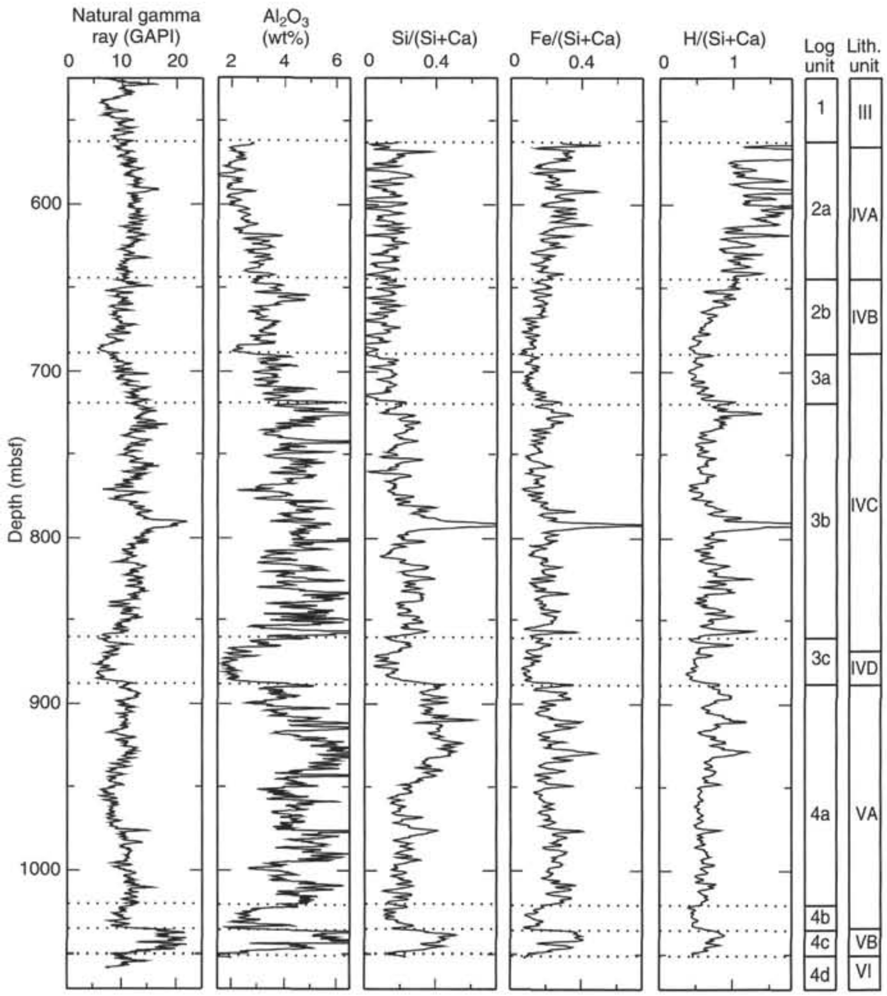

Figure 79. Selected downhole logs from the geochemical tool string for the interval from 525 to 1070 mbsf in Hole 999B: total gamma ray (from QC and FMS), Al_2O_3, Si/(Si+Ca), Fe/(Si+Ca), and H/(Si+Ca), which are known as the lithology indicator ratio (LIR), iron indicator ratio (IIR), and porosity indicator ratio (PIR), respectively. Depth intervals of logging units are marked by dotted lines. The lithologic units are defined in the "Lithostratigraphy" section (this chapter). The relative abundances of the elements Ca, Si, Al, and Fe serve to identify the primary constituents that distinguish the major lithologies recovered from Hole 999B (e.g., carbonate pelagic clay, and volcanogenic material including clay).

low resistivity composed of diffuse bands along with irregular-shaped high-resistivity zones. The observation of radiolarian/foraminifer-rich layers within this zone (see "Lithostratigraphy" and "Biostratigraphy" sections, this chapter) is consistent with the logging response, but significant amounts of clay must also be present. A similar anomaly occurs at 975 mbsf with the addition of a sharp increase in gamma-ray counts and significant maxima in potassium and thorium. As observed on the resistivity curve, the FMS data, which are higher resolution, show a sharp increase in the abundance and thickness of low-resistivity layers below 975 mbsf. This logging response correlates to a distinct claystone interval observed in Core 165-999-51R (970–980 mbsf) and indicates that a clay-rich interval extends to 995 mbsf. This interval corresponds to the late Paleocene thermal maximum event described in the "Lithostratigraphy" sections of the "Site 999" and "Site 1001" chapters (this volume).

Logging Subunit 4b (1019–1034 mbsf)

Logging Subunits 4b, 4c, and 4d display extreme continuations of the minimum-maximum undulations in logging curves that characterized Subunit 4a. In Subunit 4b, velocity and resistivity abruptly increase, and density and PEF reach an absolute maximum. Gamma-ray counts are below 10 API, with distinct minima (nearly absolute minima) observed in LIR, IIR, PIR, and aluminum concentrations.

Logging Subunit 4b corresponds to the bottom 15 m of lithologic Subunit VA. This interval coincides with the highest carbonate concentrations reported from lithologic Subunit VA and the logging response is identical to that observed in Subunit 3c (lithologic Subunit IVD). Therefore, this interval is interpreted as a thickly bedded limestone with little contribution from clay and or ash.

Logging Subunit 4c (1034–1048.5 mbsf)

Logging Subunit 4c is characterized by extreme minima and maxima of the opposite sense from the overlying logging Subunit 4b. The LIR and IIR both reach absolute maxima in this interval, and gamma-ray counts reach 15–20 API. FMS images show a distinct change to relatively low-resistivity bands punctuated by rare high-resistivity bands.

Logging Subunit 4c corresponds exactly to lithologic Subunit VB, characterized by abundant claystone and by extremely low carbonate content, which is consistent with the observed logging response ("Lithostratigraphy" section, this chapter).

Logging Subunit 4d (1050–1065 mbsf)

Some of the data have not been recorded in this unit because of the length of the various tool strings (up to 33 m long). Gamma-ray values reach a minimum at 1048.5 mbsf and then begin to rise. Logging Subunit 4d corresponds to lithologic Unit VI, which consists of limestone with clay and includes the K/T boundary. The sequence comprising the K/T boundary, consisting of massive limestone

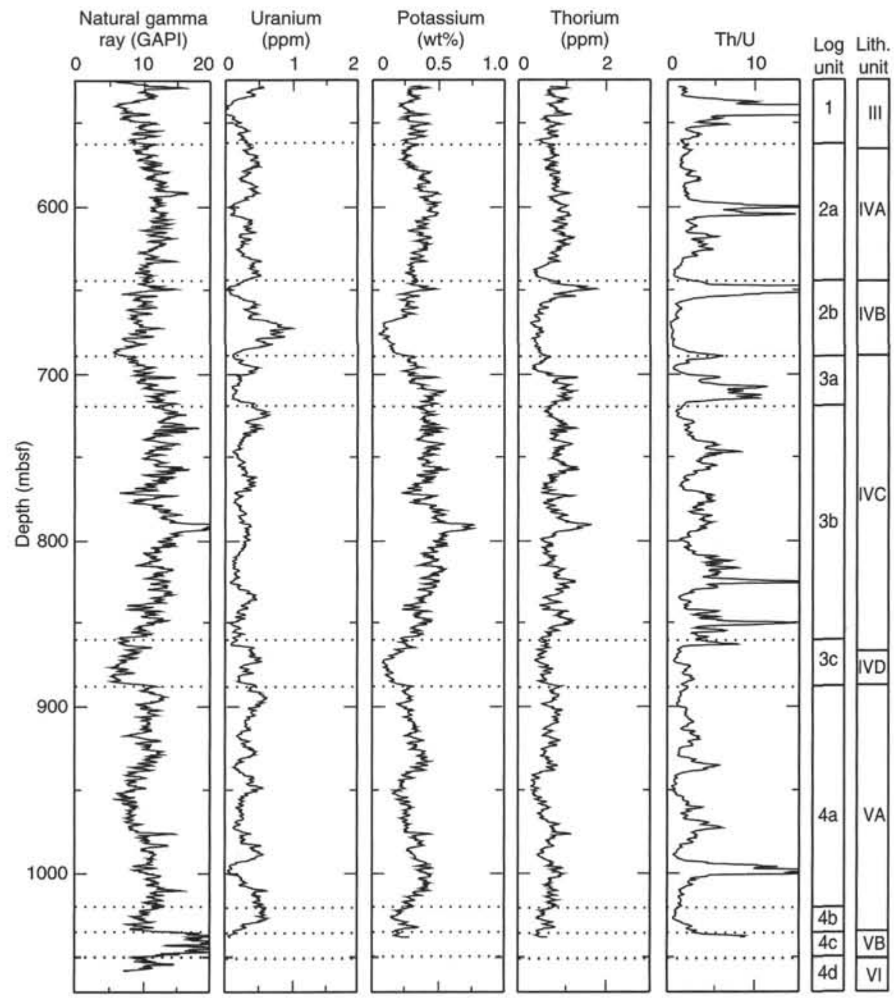

Figure 80. Downhole logs from the natural gamma-ray spectrometry tool on the Quad combo tool string for the interval from 525 to 1035 mbsf and on the FMS tool string from 1035 to 1070 mbsf in Hole 999B: total gamma ray, uranium, potassium, thorium, and thorium-uranium ratio. Depth intervals of logging units are marked by dotted lines. The lithologic units are defined in the "Lithostratigraphy" section (this chapter). At Site 999, maxima in the above element ratios correlate with discrete ash fall layers and other intervals with a relatively high clay content.

bounded by clay-rich intervals, is clearly displayed on FMS images as a distinct high-resistivity band approximately 23 cm thick bounded by thin low-resistivity layers ("Lithostratigraphy" section, this chapter). The sequence observed on the FMS data was critical for evaluating the completeness of K/T recovery and is discussed in the "Summary and Conclusions" section, this chapter (Fig. 85).

Acoustic Velocities

Compressional velocity data derived from the sonic log, which extends from 527 to 1044 mbsf, were merged with compressional velocities measured on split cores by the Digital Sonic Velocimeter or with a Hamilton Frame apparatus from 0 to 518 mbsf (see "Physical Properties" section, this chapter). The laboratory velocity data were corrected to in situ stress by the empirical relation derived by Urmos et al. (1993) (Table 17; Fig. 69). The merged velocities were integrated over the entire interval cored at Site 999 (0.0–1066.4 mbsf) to produce a plot of two-way traveltime vs. depth (Fig. 82). The three curves displayed in Figure 82 use uncorrected laboratory velocity, corrected laboratory velocity, and the average of uncorrected and corrected velocity merged with velocities derived from downhole logging measurements. The resultant traveltime vs. depth below seafloor curve derived from the "average" laboratory velocities (Fig. 82) is used to tie the cored sequences at Site 999 to seismic reflection data over the site. A summary of these correlations is shown in Figure 84 and is discussed in the "Summary and Conclusions" section, this volume.

SUMMARY AND CONCLUSIONS

Introduction

Site 999 is located at a depth of 2827.8 mbsl, near the crest of an unnamed bathymetric high, approximately 150 km northeast of Mona Rise and south of the Hess Escarpment in the Colombian Basin. We have proposed the name Kogi Rise for this feature. The location of Site 999 is above the influence of coarse sediment deposition by gravity flow from the Hess Escarpment and the Magdalena Fan complex to the southeast, although significant contributions from fine-grained terrigenous material (e.g., nepheloid clays) could be expected. Site 999 was targeted for its potential to sample a long record of tropical ocean history within the realm of the Mesozoic–Cenozoic Tethys Sea, including its final demise in the late Neogene with the closing of the Central American Seaway. The thick, turbidite-free sequence on the Kogi Rise was also an excellent prospect to recover an undisturbed K/T sequence relatively proximal to the Chicxulub impact crater.

A 1066.4-m-thick upper Maastrichtian through Pleistocene sedimentary section was cored, including a K/T boundary interval at approximately 1050.2 mbsf (Fig. 83). Preliminary paleontologic data suggest that the boundary sequence is nearly complete at this site, although confirmation of an impact-derived boundary clay will have to await shore-based analyses. Comparison of lithostratigraphy and logging data from the Formation MicroScanner (FMS) indicates that about 10 cm of the K/T boundary impact deposit were not recovered

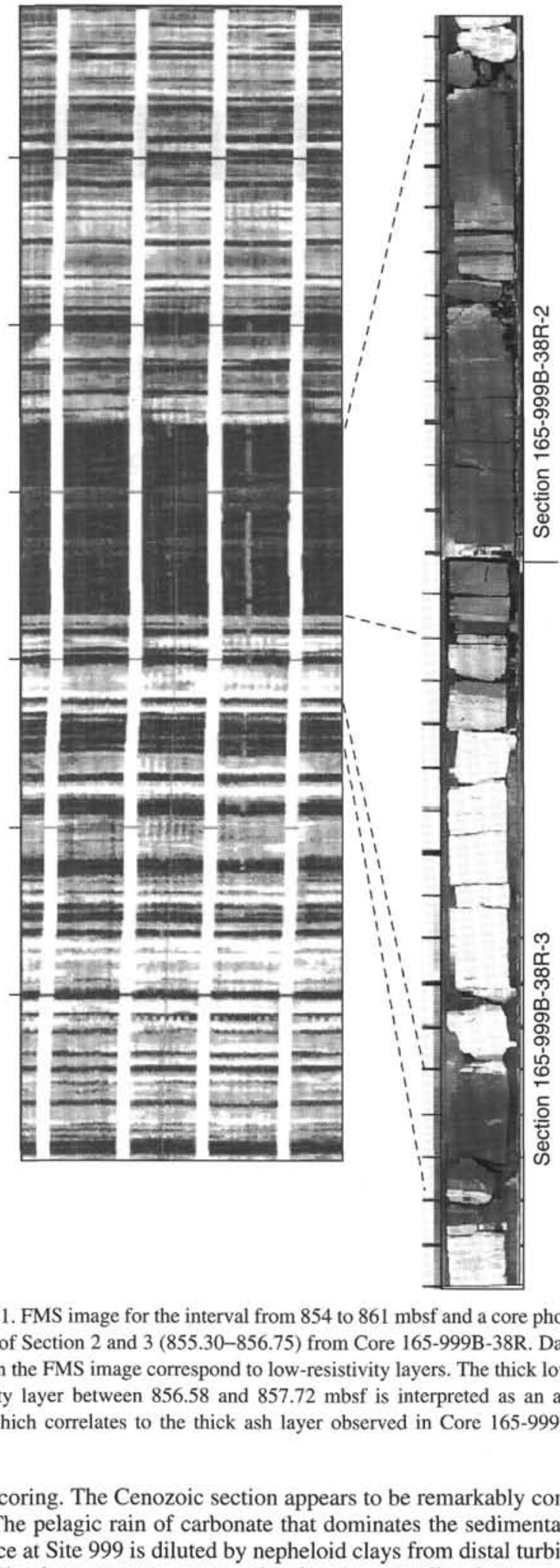

Figure 81. FMS image for the interval from 854 to 861 mbsf and a core photo for part of Section 2 and 3 (855.30–856.75) from Core 165-999B-38R. Dark layers on the FMS image correspond to low-resistivity layers. The thick low-resistivity layer between 856.58 and 857.72 mbsf is interpreted as an ash layer, which correlates to the thick ash layer observed in Core 165-999B-38R.

during coring. The Cenozoic section appears to be remarkably complete. The pelagic rain of carbonate that dominates the sedimentary sequence at Site 999 is diluted by nepheloid clays from distal turbidites and/or deep-water currents, volcanic ash, and eolian dust.

Volcanic Ash Record

The most striking feature of the sedimentary section at Site 999 is the persistence of ash fall deposits, particularly in the lower to middle Miocene and middle to upper Eocene parts of the section. Volcaniclastic sedimentation is a major component of the deposits cored at Site 999, including >1200 discrete ash fall layers (4.4% of the section; see "Igneous Petrology and Volcanology" section, this chapter) and dispersed ash (~20% of the section; see "Inorganic Geochemistry" section, this chapter). The sediments contain an excellent record of two major episodes of explosive volcanic activity, which we attribute to the Central American arc to the west (Fig. 51). The early to middle Miocene episode was also observed at Site 998 on the Cayman Rise, but on the Kogi Rise the volcanic ash sedimentation rate from this episode was higher by about an order of magnitude, indicating that the Colombian Basin was closer to the principal fallout axis of the Miocene volcanic source. These Miocene ash layers are from very large silicic ignimbrite-forming eruptions, of the type that inject tephra into the lower stratosphere and lead to its eastward transport in winds that are prevalent above the tropical tropopause (~15 to 17 km). The Miocene episode has a peak volcanic ash layer sedimentation rate of 2.5 m/m.y. and peak frequency of about one major eruption (>500 km^3) every 20 k.y. The source of this volcanic fallout may lie in the great ignimbrite eruptions that occurred on the Chortis Block in the Miocene, particularly in Guatemala, where widespread and thick ignimbrite deposits of this age have been documented (Reynolds, 1980).

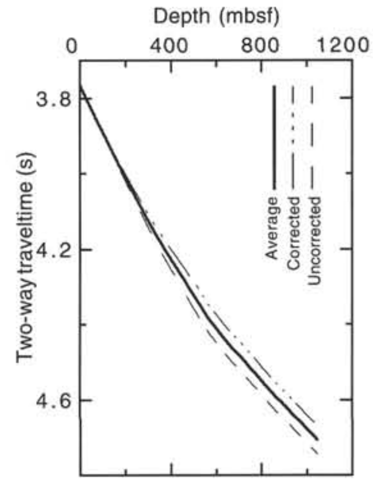

Figure 82. Two-way traveltime vs. depth calculated from the sonic log in Hole 999B and laboratory velocity data from Hole 999A.

Another major volcanic episode is preserved in the middle to upper Eocene sediments. At Site 999 this episode is somewhat larger than the Miocene event, whereas at Site 998 it is much more subdued. This spatial distribution suggests that the principal fallout axis of the Eocene activity is south of the Miocene fallout, and thus its volcanic source may lie further south in the Central American arc. The peak Eocene eruption frequency and ash sedimentation rate is comparable to the Miocene, but the duration of this episode is somewhat longer than the Miocene episode (duration of 18 m.y. vs. 12 m.y.).

At Site 998 we observed an early Eocene volcanic episode (peak at ~50 Ma), which we consider to be derived from the local Cayman Ridge volcanic arc on the basis of sedimentary features. This activity may be represented by a minor ash peak observed at 50 Ma and a marked increase in the noncarbonate mass accumulation rate (MAR) at Site 999 (Fig. 34). Thus, these results confirm that ash fallout from the Cayman Ridge was not widespread to the south, as is to be expected from prevailing west-to-east atmospheric (stratosphere) dispersal and the plate-tectonic configuration of the Caribbean in Eocene time. However, nepheloid clays generated by volcaniclastic turbidites associated with this early Eocene volcanic activity may be partly responsible for the increased noncarbonate MARs observed at both sites.

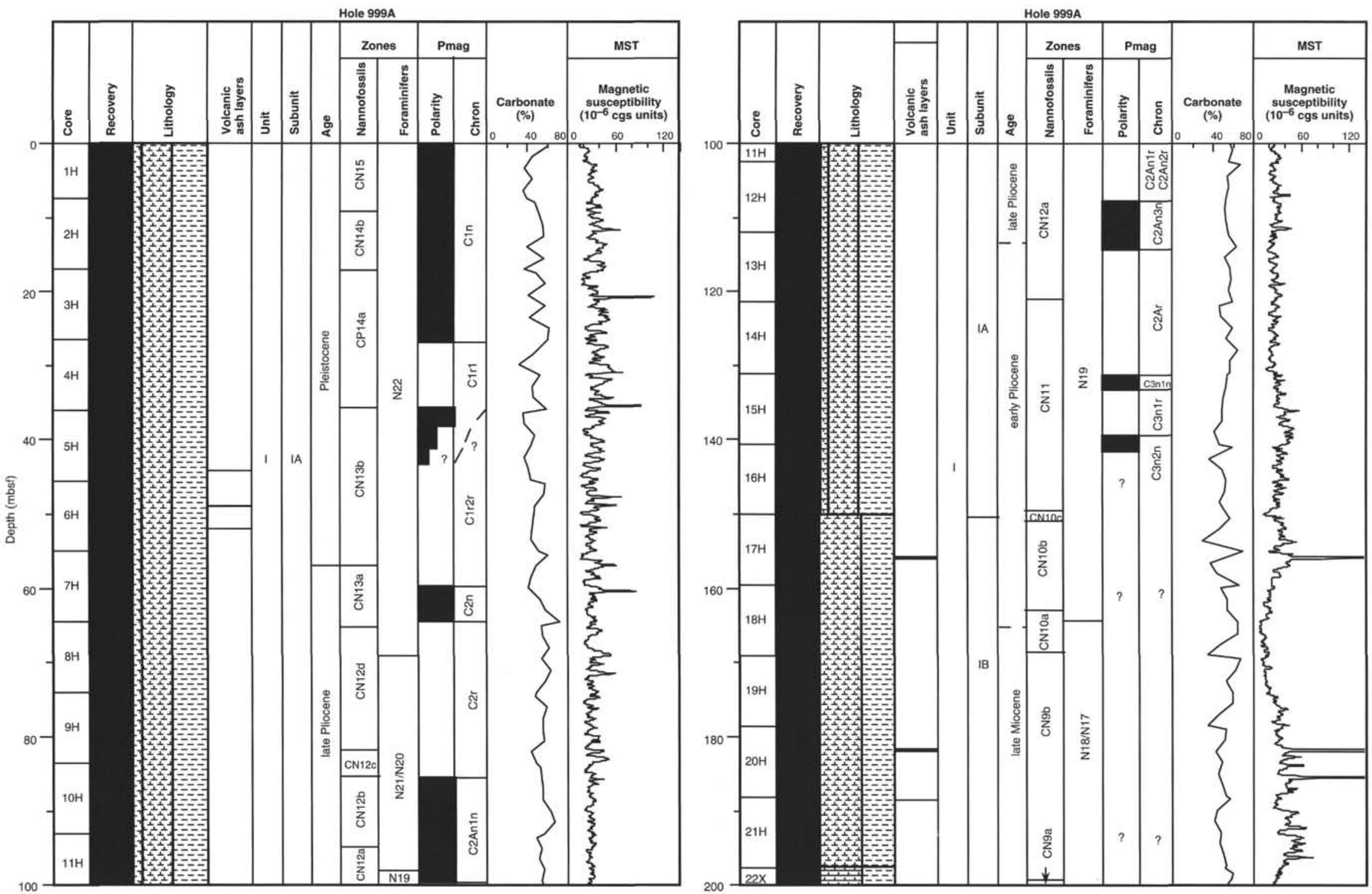

Figure 83. Site 999 summary column for core recovery, lithology, volcanic ash layer occurrence, lithologic unit and subunit boundaries, ages, nannofossil and foraminiferal datum boundaries, magnetic reversal boundaries with a preliminary interpretation of chron correlations, carbonate percentages, MST magnetic susceptibilities, and, for Hole 999B, *P*-wave velocities from downhole measurements.

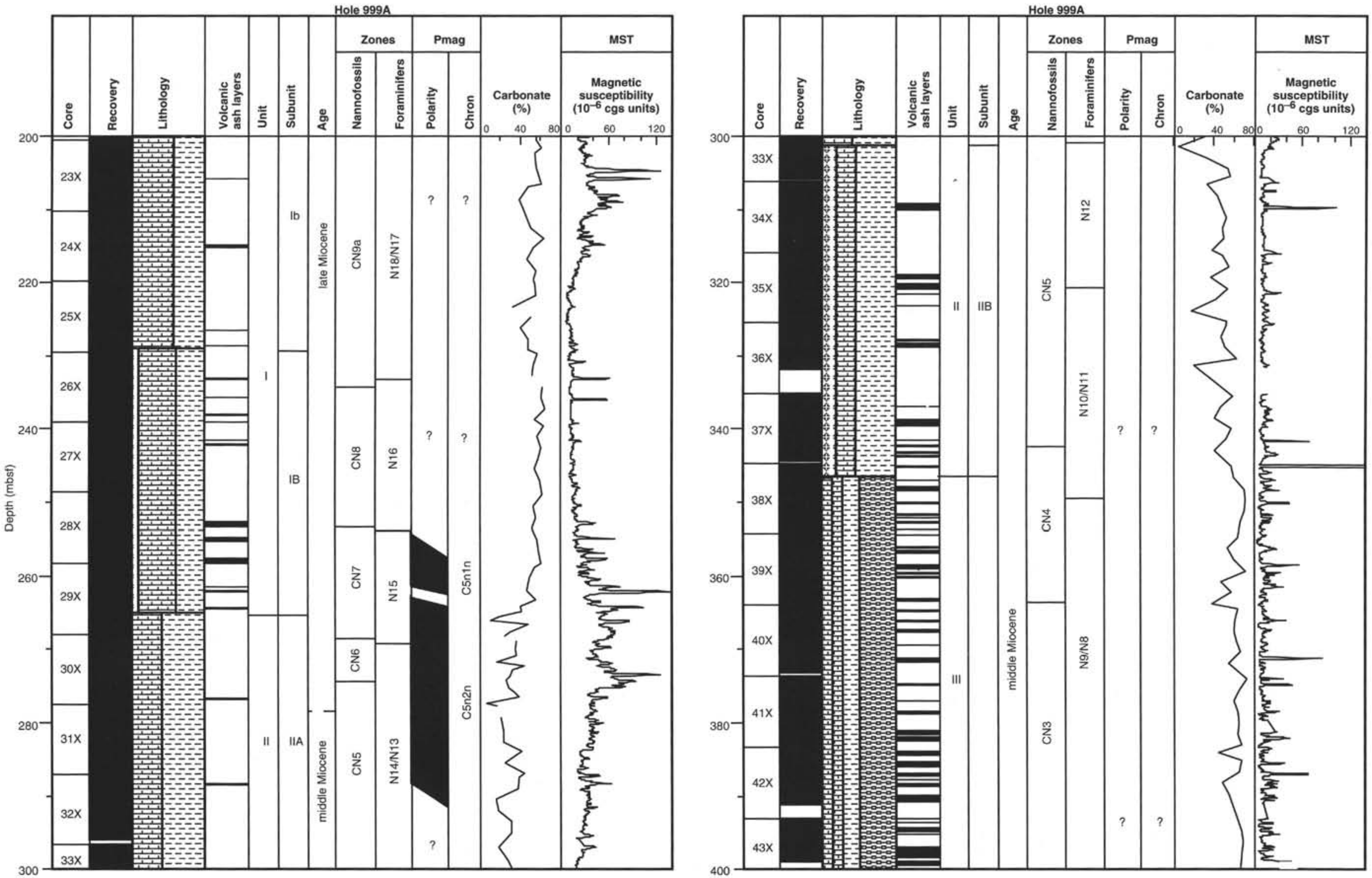

Figure 83 (continued).

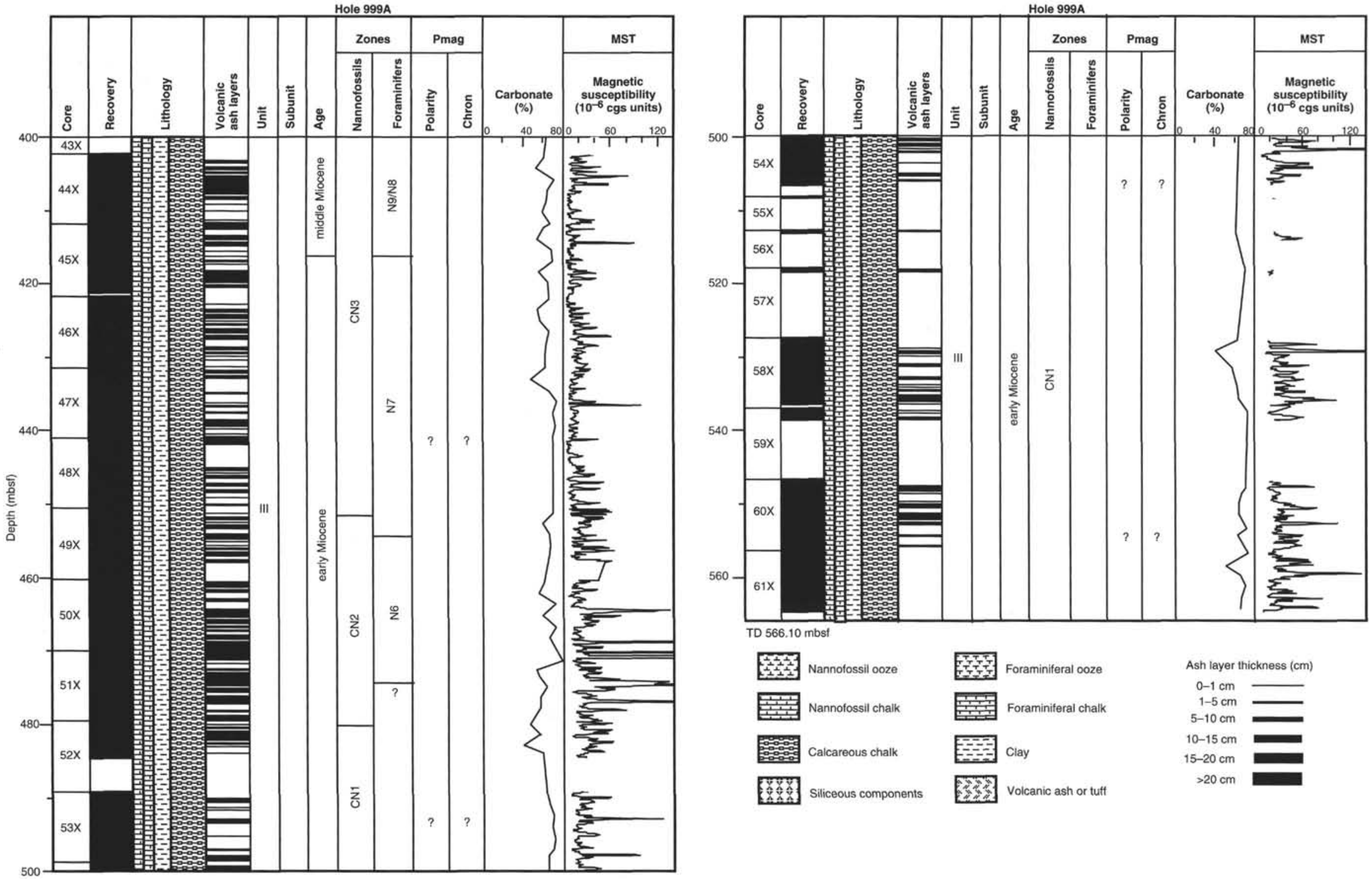

Figure 83 (continued).

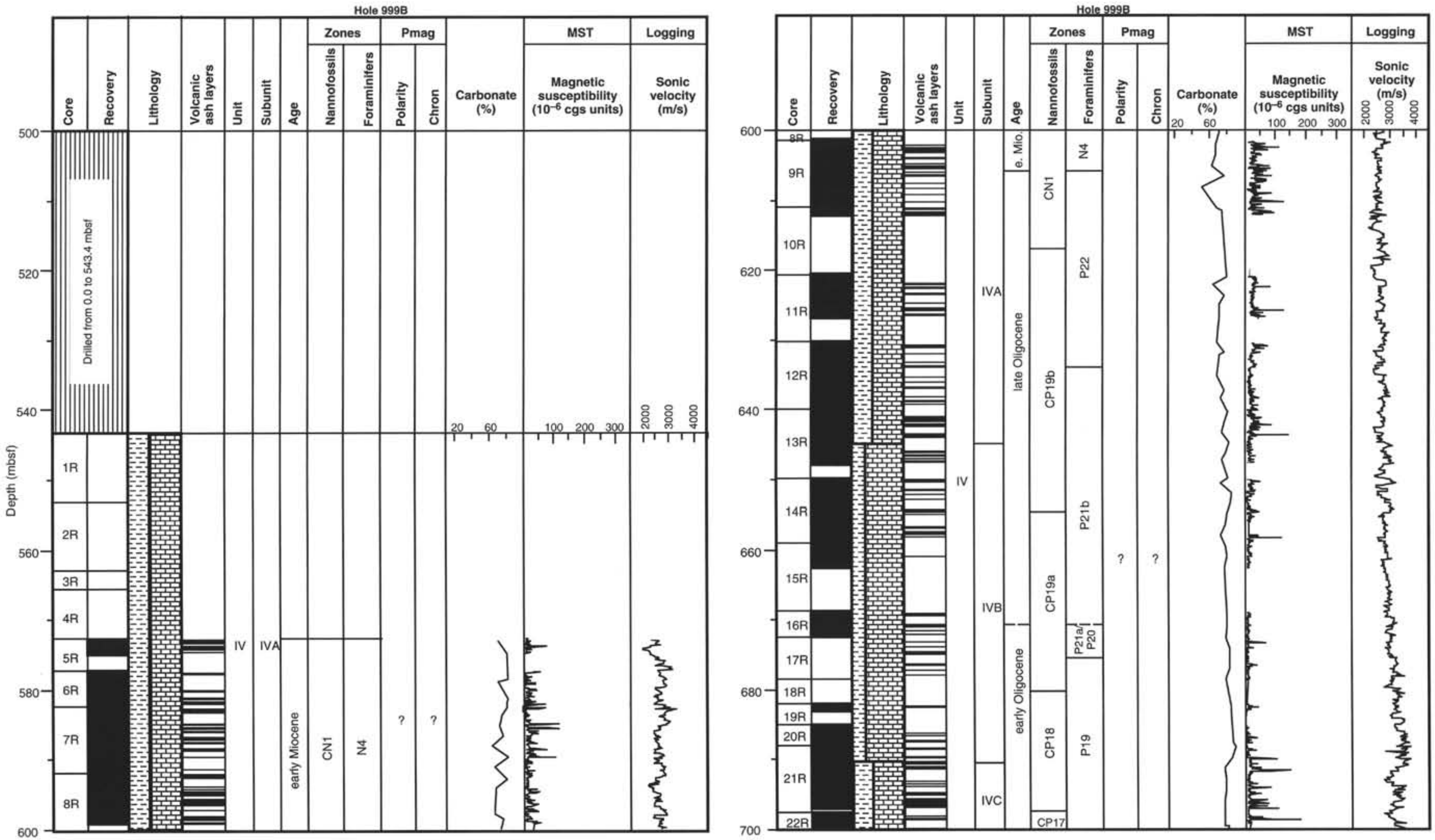

Figure 83 (continued).

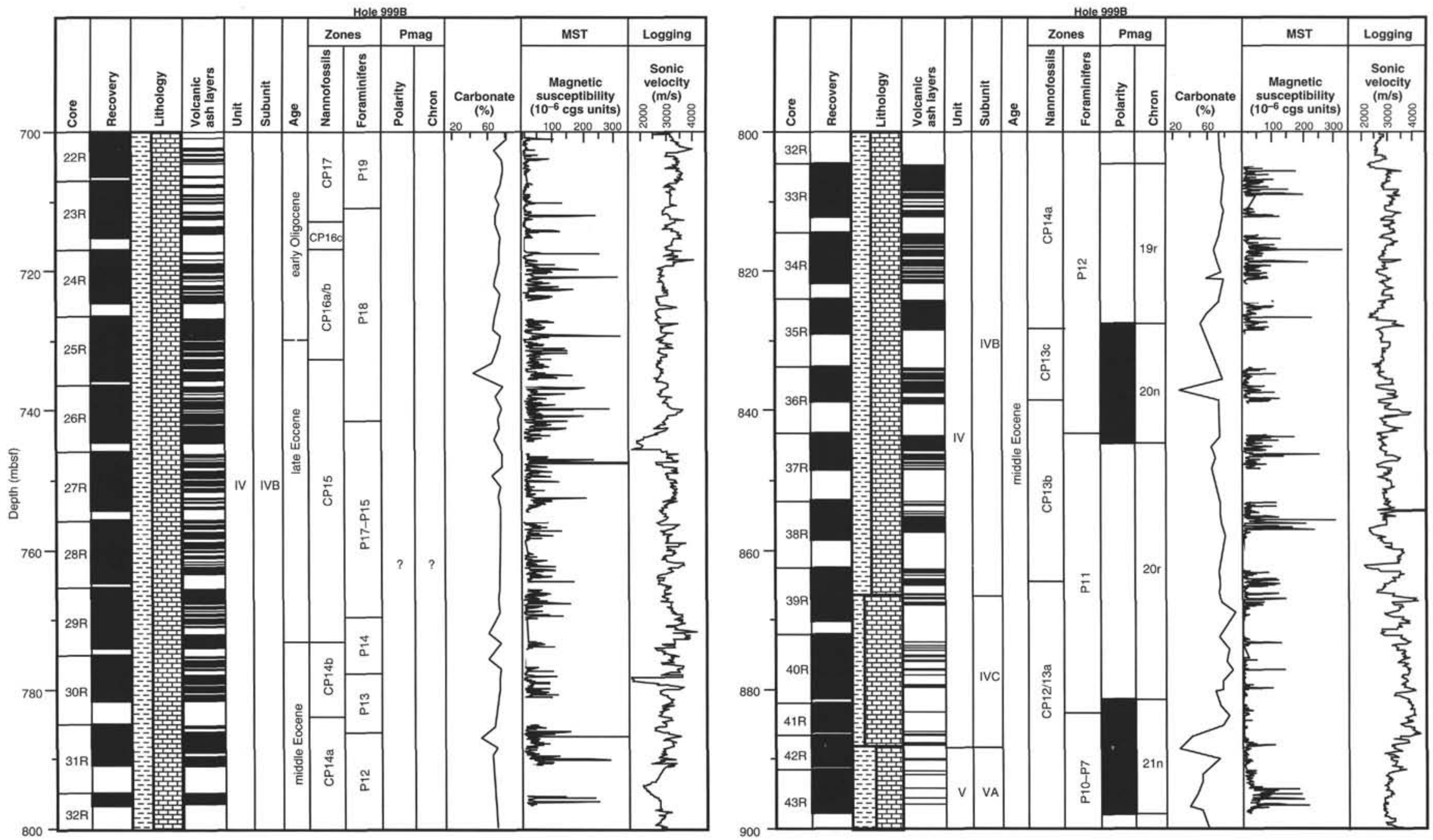

Figure 83 (continued).

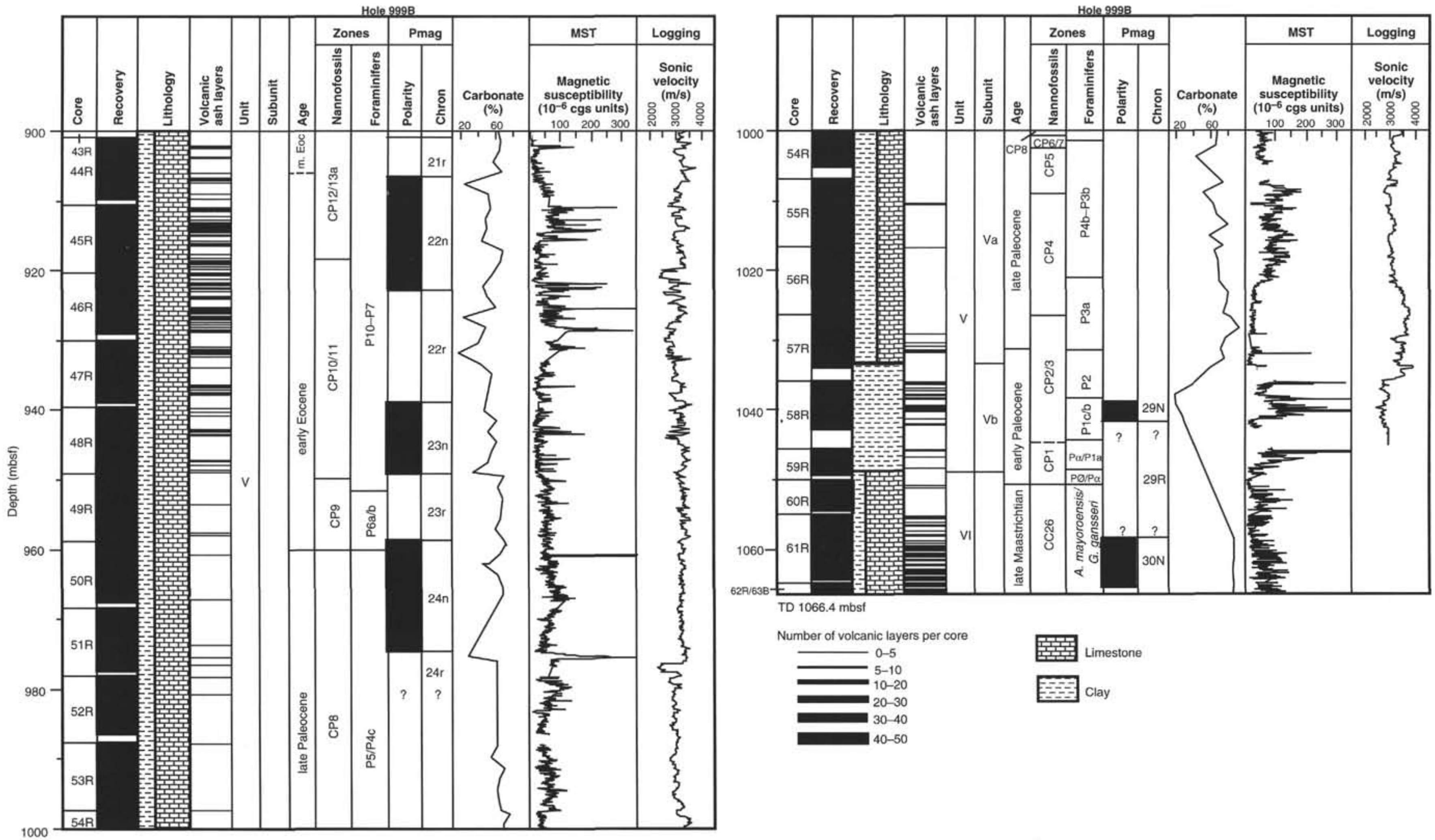

Figure 83 (continued).

Inorganic Geochemistry

In addition to the dominant carbonate deposition at Site 999, the solid-phase sediment geochemistry shows the effects of two components: a terrigenous fraction, which has been quantified on the basis of the Cr variation in the bulk sediment, and a component that consists of dispersed volcanic ash. Important variations in the abundance of these components with time reveal the changing roles of the geologic processes that influence sediment provenance and deposition in the Colombian Basin.

During the Paleocene and early Eocene, both the terrigenous input and dispersed volcanic ash were important contributors to sedimentation (10%–20% of total sediment each). However, from middle Eocene to middle Miocene times, the terrigenous component was greatly subdued, whereas the dispersed volcanic input increased in keeping with the independent ash layer evidence of the Eocene and Miocene volcanic episodes. The high abundance of the terrigenous component (30%–40%) in the last 12 m.y. is a striking feature of the geochemical profile, and most likely relates to major orogenic-tectonic events on the South American continent.

The reactive organic content of sediments at Site 999, although still low, is generally higher than at Site 998, and this has led to a relatively more reducing environment at Site 999, with greater rates of sulfate reduction and higher abundances of pyrite. These relationships may reflect the higher accumulation rates at Site 999. The trends for sulfate, Fe, and Mn concentrations observed downcore are governed, therefore, by redox-controlled reactions related to organic degradation (Fig. 37).

The abundance of both dispersed ash and discrete ash layers has had a profound effect on the pore-water chemistry at this site ("Inorganic Chemistry" section, this chapter). The variation in many cations shows a better correlation with the abundance of dispersed ash than the discrete layers. Over most of the pore-water profile, the Ca^{2+} and Sr concentrations increase systematically with depth as a function of carbonate dissolution and recrystallization, whereas Mg decreases systematically, possibly due to Mg uptake during alteration of volcanic glass to smectite or due to dolomitization (Fig. 38). Glass weathering also has a strong influence on the pore-water profile. Thus, the downcore variations in the Rb and K pore-water contents generally follow the abundance of ash layers, but concentration peaks are offset from peaks in the abundance of megascopic ash layers. Pore-water alkalis do not mirror the megascopic ash distribution to the same extent as observed at Site 998. The coincidence of silica, Rb, and K (and, to some extent, Li) with ash layers is strongest in the intervals of extensively altered ash, whereas they show lower values in pore waters within zones of fresh ash. The mobilization of silica during the transformation of the volcanic ash to smectite is reflected both in the pore-water chemistry and in the occurrence of biogenic silica within enrichment intervals, but this most likely reflects enhanced preservation of the microfossils caused by the high dissolved silica concentration, and not an increased input of biogenic siliceous matter (Fig. 42).

As mentioned previously, the solid-phase geochemistry of Site 999 indicates that dispersed ash played a major role in the composition of sediment throughout the Cenozoic section, representing some 20% of the total sediment at the site and locally as much as 30% ("Inorganic Geochemistry" section, this chapter). These high levels are reflected in the ash-dominated pore-water profiles. This chemically identified ash component is likely to occur in two ways in the sediment, both as dispersed glass shards and associated volcanic phenocryst minerals, and as the clay alteration products of volcanic ash. Dispersed ash is frequently observed in sediment smear slides at this site, although not at the >25% level, as indicated by the chemical mass balance. Thus, a significant portion of the clays contained in the sediment are likely to be volcanic glass alteration products, as is observed in the altered megascopic ash layers, where Mg-rich tri-octahedral smectite is a major component.

The transport of this dispersed volcanic ash component to the site probably occurred by either atmospheric processes, such as ash fallout, or by fluvial and marine processes, such as turbidite generation from the continental shelf and slope of adjacent subaerial volcanic regions in Central America and northern South America followed by deposition in the Colombian Basin.

The correlation of dispersed ash abundance with the accumulation rate of megascopic ash layers is one test of the relative importance of these two transport processes. The amount of dispersed ash does not appear to correlate simply with the variation in the abundance of megascopic ash layers in the drilled section, where large peak abundances occur in the Miocene and Eocene. The poor correlation with the ash layer frequency suggests another transport and depositional mechanism of the dispersed ash. This mechanism could be a nepheloid layer produced by turbidites that spread across the basins surrounding the Kogi Rise. Information on this process comes from Site 154, located in the Colombian Basin to the southwest of Site 999, in a region affected by major turbidite deposition (Edgar, Saunders, et al., 1973). This site recovered a late Neogene volcanic-terrigenous sequence, consisting of sands, silts, and clays with glass fragments and a volcanic mineral assemblage as the dominant constituent. The seismic stratigraphy of the Colombian Basin also indicates large-volume clastic sedimentation to the basin as unconfined volcanogenic and carbonate turbidite flows, ponding around basement highs such as the Kogi Rise. Bowland (1993) has proposed that the Eocene to late Miocene turbidites were derived from volcanic and carbonate provinces on the Nicaraguan Rise and in Central America. Another important source of nepheloid clays would have been the distal turbidites of the Magdalena Fan complex to the southeast of Kogi Rise. Some of the turbidite sediment would have been resuspended into the nepheloid layer and deposited as hemipelagic drape on elevated areas such as the Kogi Rise.

Correlation Between Seismic Stratigraphy and Lithostratigraphy

The "average" two-way traveltime vs. depth curve ("Downhole Measurements" section, this chapter; Fig. 82) was used to tie the cored sequences at Site 999 (given in depth below seafloor) to seismic reflection data over the site (given as two-way traveltime in seconds [s TWT]) (Fig. 84).

Reflectors are most often interference patterns caused by the impedance effects of many thin beds, but exceptions include the sediment/basement interface or, sometimes, thick chert layers. A log-generated synthetic seismogram can offer additional constraints on depth-TWT correlations if the synthetic seismogram matches the observed reflection character. The correlations presented in Figure 84 are the best estimates available until an adequate synthetic seismogram can be produced.

Beneath the Kogi Rise (Site 999), the acoustic basement horizon is smooth and continuous, and of a variable reflection amplitude at approximately 5.0 s TWT (Figs. 3, 4, "Seismic Stratigraphy" section, this chapter). This horizon is interpreted as the top of the interbedded basaltic sills, flows, and volcaniclastic sediment that represents the carapace of an oceanic plateau, presumably Coniacian in age (88–89 Ma). The total depth at Hole 999B of 1066.4 mbsf corresponds to 4.722 s TWT. The depth to acoustic (volcanic) basement at Site 999 lies at 4.936 s TWT, corresponding to 1400 mbsf, if the average velocity (3113 m/s) recorded by downhole sonic log measurements throughout the top portion of seismic Unit CB5 is extended to acoustic basement. This total depth is in agreement with predrilling estimates based on semblance type velocity analysis of MCS data reported in Bowland (1993) (see "Seismic Stratigraphy" section, this chapter).

The seismic interval immediately overlying volcanic basement (seismic Unit CB5) extends to 4.556 s TWT and consists of continuous, parallel, high-amplitude reflections concordant with acoustic

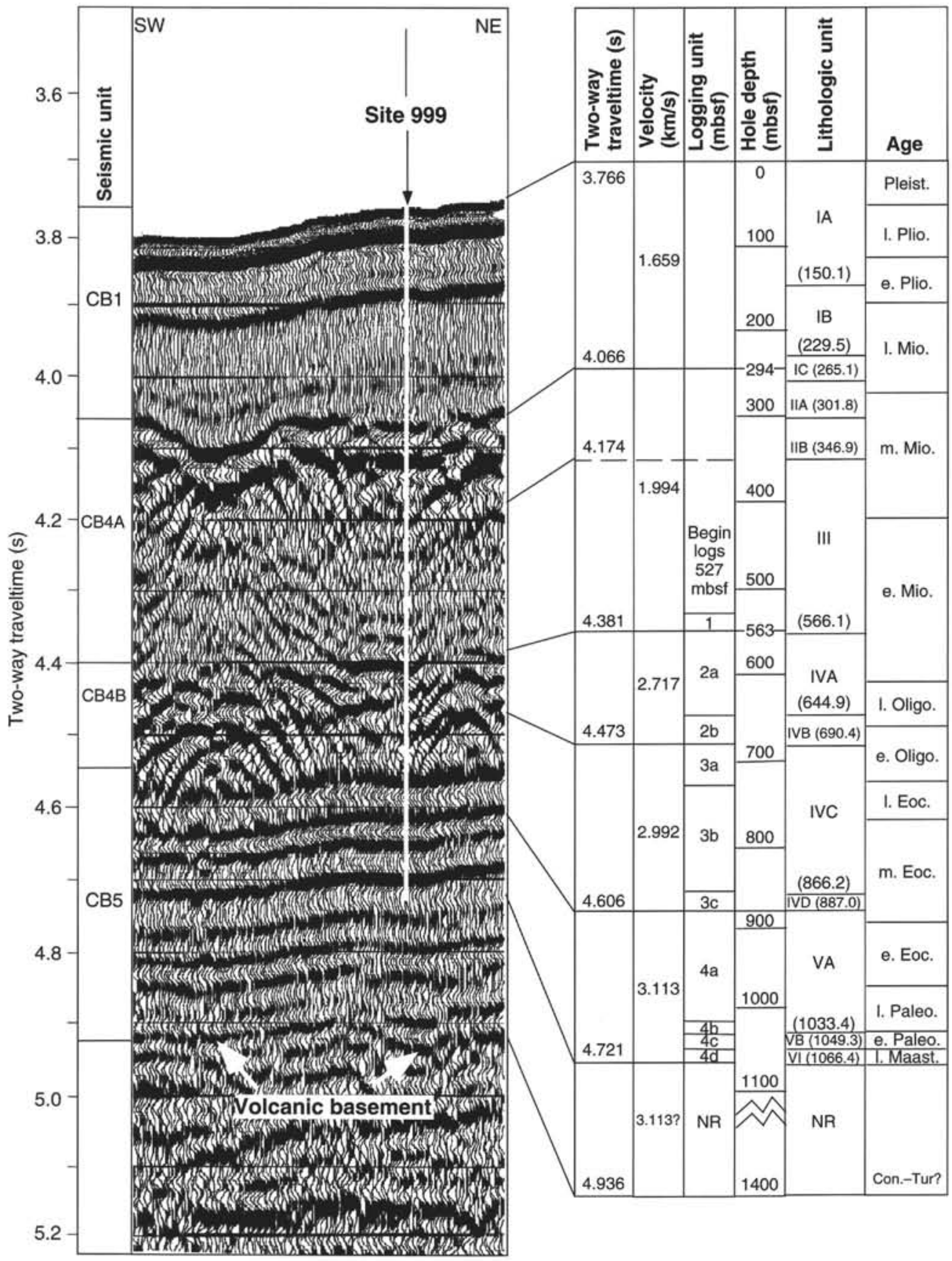

Figure 84. Summary of correlations between seismic stratigraphy, depths, logging units, lithologic units, and ages at Site 999. The location of Site 999 marked on this profile is 800 m west of the actual site location determined by GPS. Correlations with the reflection seismic record were constrained by calculations of two-way traveltime vs. depth derived from compressional velocities measured by downhole logging and laboratory instruments (see Fig. 82 in "Downhole Measurements" section, this chapter). Velocities shown are averages derived from the downhole sonic tool within each major logging unit. In the interval from the seafloor to the first logged depth (~527 mbsf), average velocities from laboratory measurements are given for seismic Units CB1 and CB4-A. The total depth at Hole 999B of 1066.4 mbsf corresponds to 4.722 s TWT. The depth of volcanic basement is approximately 1400 mbsf if average velocities measured within seismic Unit CB5 are extended to 4.936 s TWT. A 6-km portion of IG2901 MCS Line CT1-12a is displayed with a vertical exaggeration of 15 times. (See "Underway Geophysics and Pre-Site Survey" section, "Explanatory Notes" chapter, this volume, for seismic processing and display parameters and Fig. 3, "Seismic Stratigraphy" section, this chapter).

basement. Seismic Unit CB5 was interpreted as a sheet drape deposit consisting of pelagic material before drilling began (Fig. 3, "Seismic Stratigraphy" section, this chapter). The reflection at 4.556 s TWT marking the boundary between seismic Units CB4 and CB5 corresponds to 810 mbsf (ranging from 756 to 864 mbsf; Fig. 82). Thus, the change in reflection character at this depth corresponds to the lower portion of logging Subunit 3b and lithologic Subunit IVC. This corresponds with the interval in the lower middle Eocene where zones of silicification or incipient chertification and disseminated chert nodules occur (Cores 165-999B-36R and 37R, 833.7–852.9 mbsf). One may suspect that such a distinctive change in reflection amplitude correlates to logging Subunit 3c (860–888 mbsf), where a dramatic change in logging response including absolute maxima in velocity (>4.0 km/s), resistivity (>5 Ωm), and density (2.5 g/cm^3) is consistent with a change in the physical properties of the sediment that could produce large impedance contrasts that create this series of reflections. Logging Subunit 3c corresponds exactly to lithologic Subunit IVD, which is a well-indurated limestone with low amounts of clay and ash relative to the surrounding intervals.

Seismic Unit CB4 extends from 4.066 to 4.556 s TWT and consists of two subunits (CB4-A and CB4-B) separated at 4.4 s TWT. Lithologic Units II and III and portions of Unit IV correlate to this seismic interval. The interpretation of Unit CB4 by Bowland (1993) as mainly hemipelagic and biogenic pelagic deposits, probably laid down above the level of turbidite deposition, but not above the influence of nepheloid layers (hemipelagic clay), is consistent with coring results.

The thin lower subunit (CB4-B) is characterized by chaotic, discontinuous, and relatively high-amplitude reflections throughout the interval. The top of CB4-B correlates with the boundary between logging Unit 1/lithologic Unit III and logging Subunit 2a/lithologic Subunit IVA at 563 mbsf. Significant and abrupt changes in the physical properties of the sediment occur at this depth as measured in situ by downhole logs and by shipboard laboratory instruments (step increases in velocity, density, and resistivity and decreases in porosity; see "Downhole Measurements" and "Physical Properties" sections, this chapter). This boundary marks the downhole lithologic change from chalk to limestone (see "Lithostratigraphy" section, this chapter).

The upper subunit (CB4-A) displays a high-amplitude, hummocky-mounded to chaotic and disrupted seismic facies followed by a relatively transparent interval. The seismic character at the top of seismic Unit CB4 at 249 mbsf may be the result of significant variations in porosity associated with increased lithification of clayey calcareous sediments and the large increase in biosiliceous material that distinguishes lithologic Subunit IC. Laboratory measurements show significant variations in sediment porosity beginning at 225 mbsf (lithologic Subunit IC) and extending to approximately 350 mbsf (lithologic Unit II/III boundary) (Fig. 72, "Physical Properties" section, this chapter). Bowland (1993) noted the downhole increase in biosiliceous sediments at DSDP Site 502, and he related the observed seismic character to undercompaction of the open, mechanically interlocked, siliceous-microfossil framework of the sediment. The seismically transparent nature of the lower portion of CB4-A is consistent with the relatively uniform velocity and density profiles observed within the depth range, corresponding to the clayey calcareous chalks of lithologic Unit III (4.174–4.381 s TWT) (see "Downhole Measurements" and "Physical Properties" sections, this chapter).

The reflection-free character of seismic Unit CB1 extending from 0 to 249 mbsf is indicative of a relatively homogenous interval containing no significant impedance contrasts other than at the seafloor. This interval correlates to the unlithified nannofossil clayey mixed sediments with foraminifers characterizing lithologic Unit I. The high-amplitude event at approximately 3.9 s TWT is most likely the bubble pulse from the air gun seismic source (see "Underway Geophysics and Pre-Site Survey" section, "Explanatory Notes" chapter, this volume).

Cretaceous/Tertiary Boundary

The K/T boundary was cored at approximately 1050.2 mbsf in Hole 999B (Section 165-999B-60R-1; Fig. 85). The overlying Paleocene sedimentary rocks in Core 165-999B-59R are moderately bioturbated clayey limestones, with three dark gray, 1- to 4-cm ash layers that are highly altered to smectite and burrowed. Other dark gray to greenish wispy bands in the clayey calcareous limestone are claystone. At the base of Section 165-999B-59R-3, the clayey limestone grades into olive brown claystone. A smear slide from this interval (165-999B-59R-3, 85 cm) is of a carbonate-rich claystone containing a brownish colored glass particle up to 150 μm across, rounded to subrounded, along with minor opaque minerals, abundant recrystallized foraminifers, and tiny biotite flakes. This claystone band grades down to the base of the section and into the next section (165-999B-59R-CC), becoming progressively more laminated and more clay-rich downward. The claystone in Section 165-999B-59R-CC contains planktonic foraminifers of Danian age, from Zone Pα (Fig. 85), and nannofossils most likely from Subzone CP1a, as well as some reworked Cretaceous species.

The claystone in the upper part (0–5 cm) of Core 165-999B-59R-CC, is dark greenish gray in color with a faint lamination. A smear slide (165-999B-59R-CC, 3 cm) of this carbonate-rich claystone shows that it consists of clay and very fine grained carbonate, with common large opaque grains, and tiny, pale brown flakes of a biotite-like mineral. Apatite is also present as minute prismatic crystals. From a depth of 5–15 cm in the core catcher, there is a massive white to light gray and very indurated limestone, speckled with a bluish or greenish tinge or staining in the upper part, and with stylolites in the lower part. At the base of the limestone, there is a 1-mm-thick, dark gray claystone band, which marks the bottom of Core 165-999B-59R.

The white, highly indurated limestone in Section 165-999B-59R-CC is also present in the top of the first section in Core 165-999B-60R. This fine-grained and marble-like limestone bed contains lowermost Danian foraminifers of the P0/Pα Biozone (undifferentiated), as well as reworked Cretaceous species. Two 1-mm, thin, dark gray clay bands occur within the white limestone. A smear slide of the 1-mm-thick, dark gray, claystone band in Sample 165-999B-60R-1, 7 cm, shows this to be very fine grained, carbonate-rich clay, with very small particles of brown glass and small biotite flakes.

Below the very sharp base of the limestone in the top of Section 165-999B-60R-1, there is a 4-mm-thick, brownish to dark greenish gray, laminated claystone band that contains fine carbonate, clay, brown glass and silicate mineral fragments, and opaque minerals. A smear slide from Sample 165-999B-60R-1, 10–11 cm, contains very fine grained, carbonate-rich claystone, also with small biotite-like flakes. This claystone contains a Maastrichtian nannofossil assemblage of the CC26 Biozone, including *Micula murus,* a species that is restricted to the last 1.2 m.y. of the Cretaceous. Thus, the current evidence indicates that the K/T boundary occurs between this 4-mm-thick, clay-rich interval and the light gray to white limestone above, and therefore entirely within Section 165-999B-60R-1. The 4-mm-thick clay grades downward into clayey calcareous limestone of late Maastrichtian age, with foraminifers characteristic of the uppermost Maastrichtian *Abathomphalous mayaroensis* biozone (Fig. 85). A smear slide from Sample 165-999B-60R-1, 13 cm, in the base of a 2-cm-thick claystone that marks the transition, shows a more carbonate-dominated sediment, overlying the moderately bioturbated clayey calcareous limestone of Late Cretaceous age.

The litho- and biostratigraphic record indicates that the K/T boundary at Site 999 occurs between the white basal Paleocene limestone and the upper Maastrichtian calcareous limestone in the upper part of Section 165-999B-60R-1, that is, most likely within the 2-cm-thick claystone layer separating these two lithologies. Shipboard and downhole logging data obtained on the K/T boundary are summarized in Figure 85, including magnetic susceptibility and gamma-ray intensity measurements of the core, as well as downhole FMS data. The image reveals alternating low- and high-resistivity bands that can be correlated with claystone (dark areas in Fig. 85) and limestone (light areas), respectively. In the upper part of Figure 85, the individual beds of claystone and limestone can be correlated between the FMS image and the lithology in Sections 165-999B-59R-3 and 59R-CC, and in the topmost part of Section 165-999B-60R-1. However, the claystone recovered at the K/T boundary is about 8–10 cm thinner than the corresponding dark (high resistivity) interval shown in the FMS log at this level, representing the boundary deposit. Therefore, it is probable that the upper part of the boundary clay was lost by drilling erosion below the highly indurated limestone.

Preliminary paleomagnetic analysis indicates that the lowermost Paleocene sediments are normally magnetized, consistent with the

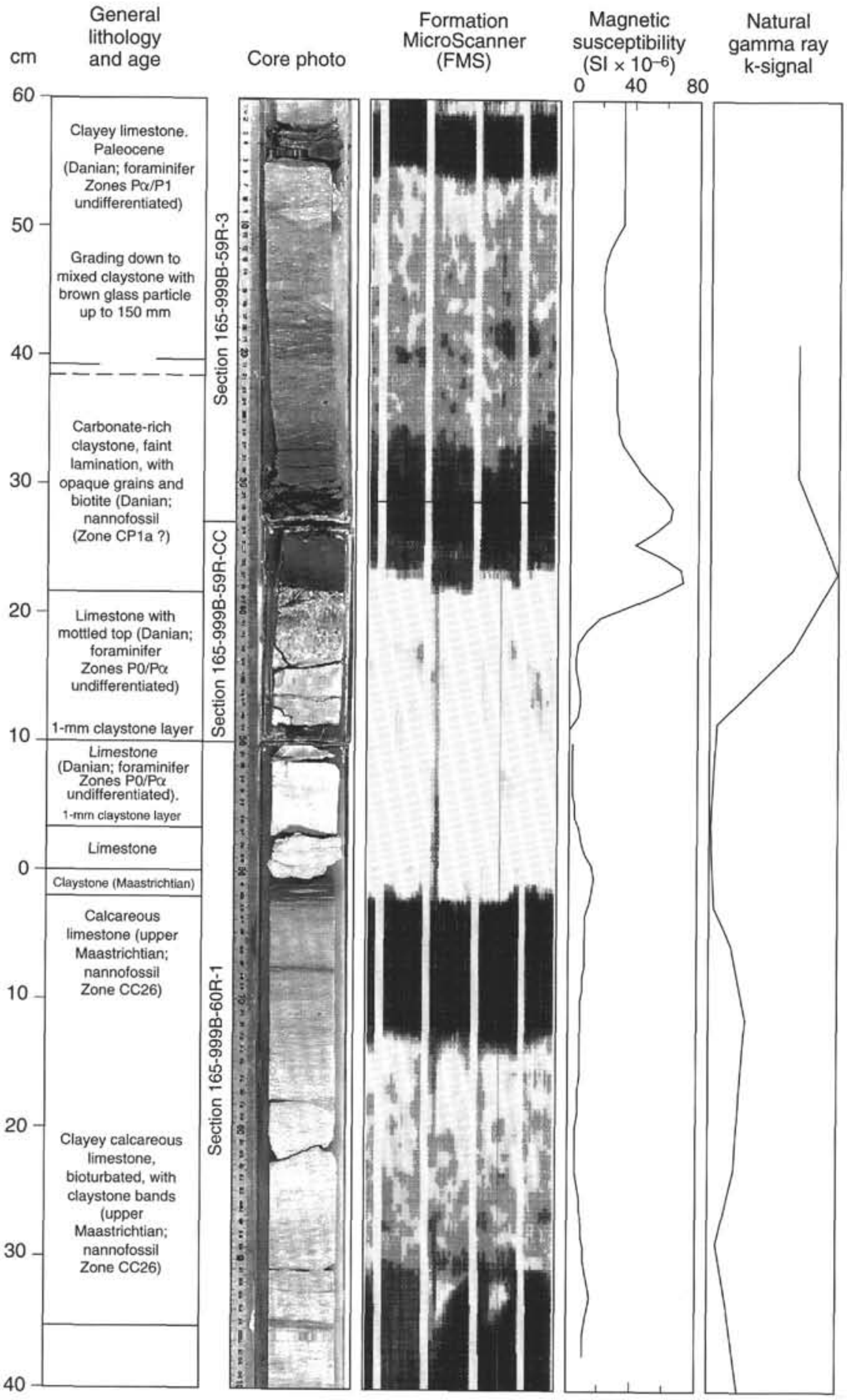

Figure 85. An overview of the Cretaceous/Tertiary boundary at Site 999. At left is a lithostratigraphic summary of the boundary. The second column from left shows a photograph of the core sections including and adjacent to the boundary (Sections 165-999B-59R-3, 59R-CC, and 60R-1). In the center is an image of the boundary from the Formation MicroScanner (FMS) log of the hole. In this image, the limestone above the boundary appears light gray (a low-conductivity layer), whereas the claystone above and below the boundary is dark (high-conductivity layers). The FMS image shows a claystone layer at the base of the limestone that is about 8 cm thicker than the recovered claystone deposit. We propose that this represents the portion of the boundary deposit that was not recovered. On the right are scans of magnetic susceptibility and the K-signal from the natural gamma ray of the drilled sections, which include the boundary deposit (see "Physical Properties" section, this chapter).

C29N polarity zone, whereas the clayey limestone below the boundary is reversely magnetized and thus probably correlates with Chron C29R. Wispy claystone seams occur throughout the upper Maastrichtian clayey limestone (smear slides 165-999B-60R-1, 42 cm, and 60R-1, 68 cm). At a depth of 82–84 cm (smear slide 165-999B-60R-1, 84 cm), there is an altered but crystal-rich volcanic ash layer, with abundant brownish smectite, relatively coarse grained, with phenocrysts of hornblende, plagioclase, rare biotite, and minor opaque grains.

In general, the Cenozoic sedimentary record on the Kogi Rise is very complete, with no significant unconformities apparent. This may stem from the relatively isolated nature of the Kogi Rise as a long-lived topographic feature, and the absence of turbidites in the entire succession also suggests that preservation of the strata may be complete. From data obtained in the FMS log, therefore, it is possible to infer that the K/T boundary deposit thickness at this site is only about 10 cm. A compilation of the thickness of the K/T boundary ejecta deposit worldwide shows a systematic trend of decreasing thickness as a function of distance from the Chicxulub crater source; however, the data are strongly biased toward Northern Hemisphere locations (Hildebrand and Stansberry, 1992). On the basis of this trend, ejecta deposit thickness at Site 999, at a paleodistance of some 1000 km south or southeast of the source, should be on the order of 50 cm, assuming an axisymmetric distribution (Fig. 86). We suggest

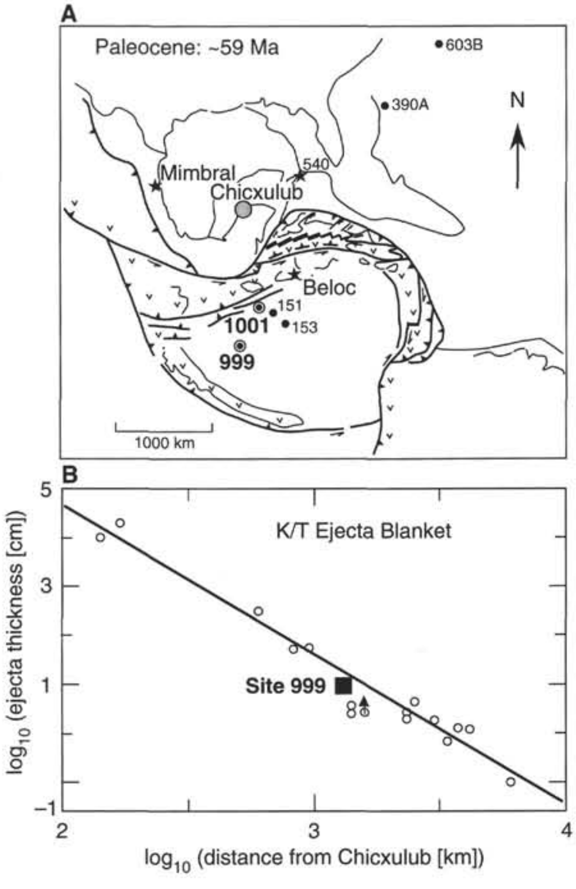

Figure 86. Locations of sites with K/T boundary sections in the vicinity of Chicxulub (**A**), and the relationship between the thicknesses of K/T boundary sections and their distances from Chicxulub (**B**). Data for other sites from Hildebrand and Stansberry (1992).

that the greatly reduced thickness of the boundary deposit at this site, by a factor of at least 5, may be a reflection of an oblique impact (Schultz and Gault, 1990; Schultz and D'Hondt, 1995), which would also account for some features observed in the impact site (see "Synthesis" chapter, this volume).

Paleogene Radiolarian- and Foraminifer-Rich Layers

The upper Paleocene–lower Eocene interval at Site 999 contains numerous distinctive sandy units, ranging in thickness from 1 to 13 cm, composed mostly of radiolarians and planktonic foraminifers in varying proportions (Subunit VA; see "Lithostratigraphy" section, this chapter). These foraminifer- and radiolarian-rich layers are present in the upper Maastrichtian, but sharply increase in frequency in the upper Paleocene (Core 165-999B-55R), peak in the interval that includes the Paleocene/Eocene boundary (Cores 165-999B-52R to 46R), and then rapidly decline in frequency in the upper lower Eocene (Core 165-999B-45R; Fig. 17). They typically have sharp lower and upper contacts, although some have a thin clay-rich band delineating both contacts. The sandy units typically lack any evidence of grading and therefore a turbidite origin is discounted. Winnowing by currents at a time of enhanced deep/intermediate water flow and/or at a time when an unobstructed, deep-water connection between the Pacific and Caribbean facilitated circulation between the two basins, are two favored hypotheses to account for the enrichment in radiolarian and foraminifer shells. An increased flux rate of these zooplankton groups caused by enhanced productivity is a third hypothesis to be considered.

The upper Paleocene–lower Eocene sandy units end abruptly at about the level of a major increase in volcanic ash deposition at Site 999, most likely derived from silicic volcanoes to the west, in the Chortis Block of Honduras, Guatemala, Nicaragua, El Salvador, and northern Costa Rica. This explosive silicic activity may signal widespread volcanism all along the Central American arc, including the Panama–Costa Rica arc. Construction and shoaling of the Panama–Costa Rica arc, in particular, may have altered water-mass circulation through the Pacific-Caribbean portal of Tethys, a hypothesis supported by the abrupt end of the winnowed deposits close to the onset of a major peak of volcanic activity in the region. Alternatively, warm, saline, deep- and intermediate-water masses produced on nearby margins or carbonate platforms may have contributed to heightened current activity through the Caribbean region. The late Paleocene–early Eocene was a time of high eustatic sea levels and warm global climates (e.g., Zachos et al., 1994), and perhaps the flooded margins of Tethys were intermittent source areas for the production of deep and intermediate waters to the world ocean, as has been proposed for the latest Paleocene (e.g., Kennett and Stott, 1990).

Late Paleocene Thermal Maximum

In the uppermost Paleocene, there is an anomalous 39-cm interval of dark greenish gray, finely laminated, carbonate-poor claystone within a unit of moderately bioturbated clayey calcareous mixed sedimentary rock (Section 165-999B-51R-5, 88–127 cm; lithologic Subunit VA; see "Lithostratigraphy" section, this chapter). This distinctive unit shows up in the logging data at about 976 mbsf as a strong peak in natural gamma, Al, and Si, and as lows in sonic velocity, bulk density, and resistivity (logging Subunit 4a; see "Downhole Measurements" section, this chapter). The foraminiferal evidence places the dark band within the uppermost Paleocene (Zone P5). We suggest that this layer correlates with the very rapid oceanographic and climatic changes identified as the late Paleocene thermal maximum (Zachos et al., 1993). Abrupt and extreme warming of both surface and deep waters in the southern high latitudes was associated with a mass extinction of benthic foraminifers. A fundamental change in the mode of deep-sea circulation possibly is responsible for this short-lived event. Kennett and Stott (1990), Zachos et al. (1993), and Bralower et al. (1995) have proposed that deep- and intermediate-water masses produced in the low latitudes by the sinking of warm, saline waters rapidly spread to the high latitudes, reduced surface to deep thermal gradients, and caused a major perturbation in marine productivity. The extinction of benthic foraminifers has been attributed, in part, to lower dissolved oxygen contents of the warm deep waters (Kennett and Stott, 1991; Thomas, 1990, 1992). Based on a preliminary study of benthic foraminifers in Cores 165-999B-50R to 52R, the extinction event occurs within or near the dark laminated claystone interval (the highest sample examined, which contained *Gavelinella beccariiformis,* is 165-999B-51R-5, 144–145 cm).

Middle/Late Miocene Carbonate Crash

A sharp reduction in carbonate content and a marked increase in magnetic susceptibility and in terrigenous mass accumulation rates (Figs. 31, 32) distinguish an interval through the uppermost middle Miocene and lowermost upper Miocene thought to be correlative to the late Miocene carbonate crash of the central and eastern equatorial Pacific (Farrell et al., 1995; Lyle et al., 1995; Pisias et al., 1995). This distinctive interval was also recognized at Site 998 on the Cayman Rise. In the Caribbean, the carbonate-poor interval begins in the late middle Miocene, within nannofossil Zone CN5 and near the top of foraminifer Zone N12 (approximately 11.8–12 Ma), and ends in the early late Miocene, within nannofossil Zone CN7 (approximately 10.0 Ma; Figs. 12, 13). The event in the eastern equatorial Pacific has been attributed to changes in the deep-water chemistry and to the exchange of deep waters between the Pacific and Atlantic caused by the progressive uplift of the Panamanian sill during late Miocene time. Questions concerning the possible synchroneity of the event on both sides of the Isthmus of Panama as well as the linkages to changing thermohaline circulation will be addressed in shore-based research.

Uplift of the Northern Andes and Magdalena Fan Deposition

The Magdalena River drains the Andes of northern Colombia, including the Cordillera Central and Cordillera Oriental. A large deep-sea fan complex radiates away from its point source along the continental margin, and deposits of the Magdalena Fan reach widely across the floor of the Colombian Basin. Uplift events in the Cordillera Central of Colombia occurred in the middle Eocene, at the end of the Oligocene, at the end of the Miocene, and in the late Pliocene and most of the Pleistocene (Shagam, 1975). However, most of the late-stage deformation and uplift of the northern Andes has occurred from the late Miocene to the recent (Benjamin et al., 1987; Case et al., 1990). At Site 999, there is evidence for progressively increasing influence of the Magdalena Fan on the deposition of nepheloid clays on the Kogi Rise since late Miocene times. Following the large increase in noncarbonate (terrigenous) MARs during the middle/late Miocene carbonate crash and the subsequent marked decrease, there is a steady trend of increasing terrigenous MARs beginning about 8 Ma (nannofossil Subzone CN9a), with the greatest terrigenous MARs occurring in the Pliocene–Pleistocene (Figs. 31, 32). The detrital clays chlorite and kaolinite occur in detectable abundances in whole-rock XRD analyses from about 220 mbsf to the top of Hole 999A (Fig. 7). Recent drilling results from the Ceara Rise in the western equatorial Atlantic have documented an increase in terrigenous MARs (from the Amazon Fan) beginning at 8–10 Ma and particularly after 5 Ma (Curry, Shackleton, Richter, et al., 1995). This was accompanied by a major change in clay mineralogy and has been interpreted as the record of accelerated uplift of the northern Andes since the late Miocene.

Central American Seaway

Near-shore marine records from Costa Rica, Panama, and Colombia, and deep-sea records from both sides of the Isthmus of Panama document the closing of the Central American Seaway in mid-Pliocene time (~3.5 Ma; Saito, 1976; Keigwin, 1978, 1982a; Duque-Caro, 1990; Coates et al., 1992). With an open Central American Seaway, the oceanic divergence created by the westward-flowing North Equatorial Current from the Atlantic and the eastward-flowing Equatorial Countercurrent from the Pacific around 10°–12°N latitude could have produced seasonal upwelling in the central Caribbean basin. Closure of the seaway disrupted the exchange of surface-water masses between the Pacific and the Caribbean and altered the distribution of productivity in both regions. Farrell et al. (1995) document a major change in the distribution of opal accumulation in the eastern equatorial Pacific at 4.4 Ma, attributed to the closure of the seaway.

At Site 999, sinistrally coiled *Neogloboquadrina pachyderma*, typically a polar/subpolar species, occur with *Globigerina bulloides*, a cool-water species associated with seasonal upwelling in the low to mid-latitudes, in Cores 165-999A-23X to 18H. Upsection, in Cores 165-999B-17H to 15H, the sinistral form of *N. pachyderma* is gradually replaced by warmer water, dextrally coiled forms. The top of this "*pachyderma*" interval occurs in the early Pliocene, about 4.5 Ma (Chron C3n2n?). This is suggestive of the Caribbean equivalent of the change in opal deposition in the eastern equatorial Pacific, denoting a major reorganization of circulation and productivity. Another proxy for productivity is the degree of bioturbation, which is extensive in the upper Miocene and lower Pliocene and decreases to more moderate levels in the upper Pliocene and Pleistocene (see "Lithostratigraphy" section, this chapter).

REFERENCES

Atwater, T., 1989. Plate tectonic history of the northeast Pacific and western North America. *In* Winterer, E.L., Hussong, D.M., and Decker, R.W. (Eds.), *The Eastern Pacific Ocean and Hawaii.* Geol. Soc. Am., Geol. of North America Ser., N:21–72.

Aubry, M.-P., 1989. *Handbook of Cenozoic Calcareous Nannoplankton* (Book 3): *Ortholithae (Pentaliths and Others). Heliolithae (Fasciculiths, Sphenoliths, and Others):* New York (Micropaleontology Press).

Backman, J., and Hermelin, J.O.R., 1986. Morphometry of the Eocene nannofossil *Reticulofenestra umbilicus* lineage and its biochronological consequences. *Palaeogeogr., Palaeoclimatol., Palaeoecol.,* 57:103–116.

Benjamin, M., Johnson, N.M., and Naeser, C.W., 1987. Recent rapid uplift in the Bolivian Andes: evidence from fission-track dating. *Geology,* 15:680–683.

Berggren, W.A., Kent, D.V., Swisher, C.C., III, and Aubry, M.-P., 1995. A revised Cenozoic geochronology and chronostratigraphy. *In* Berggren, W.A., Kent, D.V., and Hardenbol, J. (Eds.), *Geochronology, Time Scales and Global Stratigraphic Correlations: A Unified Temporal Framework for an Historical Geology,* Spec. Publ.—Soc. Econ. Paleont. Mineral., 54:129–212.

Berner, R.A., 1978. Sulfate reduction and the rate of deposition of marine sediments. *Earth Planet. Sci. Lett.,* 37:492–498.

Biju-Duval, B., Mascle, A., Montadert, L., and Wanneson, J., 1978. Seismic investigation in the Colombia, Venezuela and Granada Basins, and on the Barbados Ridge for future IPOD drilling. *Geol. Mijnbouw,* 57:105–116.

Blow, W.H., 1969. Late middle Eocene to Recent planktonic foraminiferal biostratigraphy. *In* Brönnimann, P., and Renz, H.H. (Eds.), *Proc. First Int. Conf. Planktonic Microfossils, Geneva, 1967:* Leiden (E.J. Brill), 1:199–422.

Bolli, H.M., and Saunders, J.B., 1985. Oligocene to Holocene low latitude planktonic foraminifera. *In* Bolli, H.M., Saunders, J.B., and Perch-Nielsen, K. (Eds.), *Plankton Stratigraphy:* Cambridge (Cambridge Univ. Press), 155–262.

Bowin, C., 1976. Caribbean gravity field and plate tectonics. *Spec. Pap.—Geol. Soc. Am.,* 169.

Bowland, C.L., 1984. Seismic stratigraphy and structure of the western Colombian Basin, Caribbean Sea [M.S. thesis]. University of Texas, Austin, TX.

————, 1993. Depositional history of the western Colombian Basin, Caribbean Sea, revealed by seismic stratigraphy. *Geol. Soc. Am. Bull.,* 105:1321–1345.

Bowland, C.L., and Rosencrantz, E., 1988. Upper crustal structure of the western Colombian Basin, Caribbean Sea. *Geol. Soc. Am. Bull.,* 100:534–546.

Boyce, R.E., 1973. Physical properties—summary. *In* Edgar, N.T., Saunders, J.B., et al., *Init. Repts. DSDP,* 15: Washington (U.S. Govt. Printing Office), 1067–1068.

Bralower, T.J., and Mutterlose, J., 1995. Calcareous nannofossil biostratigraphy of Site 865, Allison Guyot, Central Pacific Ocean: a tropical Paleogene reference section. *In* Winterer, E.L., Sager, W.W., Firth, J.V., and Sinton, J.M. (Eds.), *Proc. ODP, Sci. Results,* 143: College Station, TX (Ocean Drilling Program), 31–74.

Bralower, T.J., Zachos, J.C., Thomas, E., Parrow, M., Paull, C.K., Kelly, D.C., Premoli Silva, I., Sliter, W.V., and Lohmann, K.C., 1995. Late Paleocene to Eocene paleoceanography of the equatorial Pacific Ocean: stable isotopes recorded at Ocean Drilling Program Site 865, Allison Guyot. *Paleoceanography,* 10:841–865.

Burke, K., Cooper, C., Dewey, J.F., Mann, P., and Pindell, J.L., 1984. Caribbean tectonics and relative plate motions. *In* Bonini, W.E., Hargraves, R.B., and Shagram, R. (Eds.), *The Caribbean-South American Plate Boundary and Regional Tectonics,* Mem.—Geol. Soc. Am., 162:31–63.

Carey, S., and Sigurdsson, H., 1980. The Roseau ash: deep-sea tephra deposits from a major eruption on Dominica, Lesser Antilles arc. *J. Volcanol. Geotherm. Res.,* 7:67–86.

————, 1982. Influence of particle aggregation on deposition of distal tephra from the May 18, 1980 eruption of Mount St. Helens volcano. *J. Geophys. Res.,* 90:2948–2958.

Carr, M.J., and Stoiber, R.E., 1990. Volcanism. *In* Dengo, G., and Case, J.E. (Eds.), *The Caribbean Region.* Geol. Soc. Am., Geol. of North Am. Ser., H:375–391.

Case, J.E., Shagam, R., and Giegengack, R.F., 1990. The geology of the northern Andes; an overview. *In* Dengo, G., and Case, J.E. (Eds.), *The Caribbean Region,* Geol. Soc. Am., Geol. of North Am. Ser., H:177–200.

Chaisson, W.P. and Leckie, R.M., 1993. High resolution Neogene planktonic foraminifer biostratigraphy of Site 806, Ontong Java Plateau (western equatorial Pacific). *In* Berger, W.H., Kroenke, L.W., Janecek, T., et al., *Proc. ODP, Sci. Results,* 130: College Station, TX (Ocean Drilling Program), 137–178.

Chaisson, W.P., and Pearson, P.N., in press. Planktonic foraminifer biostratigraphy at ODP Site 925, western tropical Atlantic: the last 12 m.y. *In* Curry, W.B., Shackleton, N.J., Richter, C., Bralower, T.J., et al., *Proc. ODP, Sci Results,* 154: College Station (Ocean Drilling Program).

Coates, A.G., Jackson, J.B.C., Collins, L.S., Cronin, T.M., Dowsett, H.J., Bybell, L.M., Jung, P., and Obando, J.A., 1992. Closure of the Isthmus of Panama: the near-shore marine record of Costa Rica and western Panama. *Geol. Soc. Am. Bull.,* 104:814–828.

Cullen, J., and Prell, W.L., 1984. Planktonic foraminifera of the northern Indian Ocean: distribution and preservation in surface sediments. *Mar. Micropaleontol.,* 9:1–52.

Curry, W.B., Shackleton, N.J., Richter, C., et al., 1995. *Proc. ODP, Init. Repts.,* 154: College Station, TX (Ocean Drilling Program).

Diebold, J.B., Driscoll, N.W., Abrams, L., Buhl, P., Donnelly, T.W., Laine, E.P. , and Leroy, S., 1995a. A regional geophysical survey of the Venezuelan Basin and Beata Ridge: implications for interpretations of stratigraphy and tectonics. *Eos,* 76:614.

————, 1995b. Tectonic model for the origin and evolution of the rough/smooth basement in the Venezuelan Basin. *Eos,* 76:615.

Diebold, J.B., Stoffa, P.L., Buhl, P., and Truchan, M., 1981. Venezuela Basin crustal structure. *J. Geophys. Res.,* 86:7901–7923.

Duncan, R.A., and Hargraves, R.B., 1984. Plate tectonic evolution of the Caribbean region in the mantle reference frame. *In* Bonini, W.E., Hargraves, R.B., and Shagam, R. (Eds.), *The Caribbean-South American Plate Boundary and Regional Tectonics.* Mem.—Geol. Soc. Am., 162:81–94.

Duque-Caro, H., 1990. Neogene stratigraphy, paleoceanography, and paleobiogeography in northwest South Amica and the evolution of the Panama Seaway. *Palaeogeogr., Palaeoclimatol., Palaeoecol.,* 77:203–234.

Edgar, N.T., Ewing, J.I., and Hennion, J., 1971. Seismic refraction and reflection in Caribbean Sea. *AAPG Bull.,* 55:833–870.

Edgar, N.T., Saunders, J.B., et al., 1973. *Init. Repts. DSDP,* 15: Washington (U.S. Govt. Printing Office).

Emiliani, C., Gartner, S., and Lidz, B., 1972. Neogene sedimentation of the Blake Plateau and emergence of the Central American isthmus. *Palaeogeog., Palaeoclimat., Palaeoecol.,* 11:1–10.

Escalante, G., 1990. The geology of southern Central America and western Colombia. *In* Dengo, G., and Case, J.E. (Eds.), *The Caribbean Region.* Geol. Soc. Am., Geol. of North Am. Ser., H:201–230.

Ewing, J., Antoine, J., and Ewing, M., 1960. Geophysical measurements in the western Caribbean Sea and in the Gulf of Mexico. *J. Geophys. Res.,* 65:4087–4126.

Farrell, J.W., Raffi, I., Janecek, T.R., Murray, D.W., Levitan, M., Dadey, K.A., Emeis, K-C., Lyle, M., Flores, J.-A., and Hovan, S., 1995. Late Neogene sedimentation patterns in the eastern equatorial Pacific Ocean. *In* Pisias, N.G., Mayer, L.A., Janecek, T.R., Palmer-Julson, A, and van Andel, T.H. (Eds.), *Proc. ODP, Sci. Results,* 138: College Station, TX (Ocean Drilling Program), 717–756.

Froelich, P.N., Klinkhammer, G.P., Bender, M.L., Luedtke, N.A., Heath, G.R., Cullen, D., Dauphin, P., Hammond, D., Hartman, B., and Maynard, V., 1979. Early oxidation of organic matter in pelagic sediments of the eastern equatorial Atlantic: suboxic diagenesis. *Geochim. Cosmochim. Acta,* 43:1075–1090.

Gieskes, J.M., 1983. The chemistry of interstitial waters of deep sea sediments: interpretation of deep-sea drilling data. *In* Riley, J.P., and Chester, R. (Eds.), *Chemical Oceanography* (Vol. 8): London (Academic), 221–268.

Hahn, G.A., Rose, W.I., and Meyers, T., 1979. Geochemical correlation of genetically related rhyolitic ash-flow and air-fall ashes, central and western Guatemala and the equatorial Pacific. *Spec. Pap.—Geol. Soc. Amer.,* 180:101–112.

Hay, W.W., and Beaudry, F.M., 1973. Calcareous nannofossils--Leg 15, Deep Sea Drilling Project. *In* Edgar, N.T., Saunders, J.B., et al., *Init. Repts. DSDP,* 15: Washington (U.S. Govt. Printing Office), 625–683.

Heiken, G., and Wohletz, K., 1985. *Volcanic ash:* Berkeley (Univ. of California Press).

————, 1991. Fragmentation processes in explosive volcanic eruptions. *In* Fisher, R.V. and Smith, G.A. (Eds), *Sedimentation in Volcanic Settings.* Spec. Publ.—Soc. Econ. Palentol. Mineral., 45:19–26.

Hildebrand, A., and Stansberry, J.A., 1992. K/T boundary ejecta distribution predicts size and location of Chicxulub crater. *Lunar Planet. Sci.,* 23:537–538. (Abstract)

Holcombe, T.L., Ladd, J.W., Westbrook, G., Edgar, N.T., and Bowland, C.L., 1990. Caribbean marine geology: ridges and basins of the plate interior. *In* Dengo, G., and Case, J.E. (Eds.), *The Caribbean Region.* Geol. Soc. Am., Geol. of North Am. Ser., H:231–260.

Horne, G.S., Clark, G.S, and Pushkar, P., 1976. Pre-Cretaceous rocks of northwestern Honduras: basement terrane in Sierra de Omoa. *AAPG Bull.,* 60:566–583.

Horne, G.S., Finch, R.C., and Donnelly, T.W., 1990. The Chortis Block. *In* Dengo, G., and Case, J.E. (Eds.), *The Caribbean Region.* Geol. Soc. Am., Geol. of North Am. Ser., H:55–76.

Houtz, R.E., and Ludwig, W.J., 1977. Structure of Colombia Basin, Caribbean Sea from profiler-sonobuoy measurements. *J. Geophys. Res.* 82:4861–4867.

Jenkins, D.G., and Orr, W.N., 1972. Planktonic foraminiferal biostratigraphy of the eastern equatorial Pacific—DSDP Leg 9. *In* Hays, J.D., et al., *Init. Repts. DSDP,* 9: Washington (U.S. Govt. Printing Office), 1059–1193.

Kaneps, A.G., 1979. Gulf stream: velocity fluctuations during the late Cenozoic. *Science,* 204:297–301.

Kaye, B.H., 1986. Image analysis procedures for characterizing the fractal dimension of fine particles. *Proc. Particle Technol. Conf., Nurnberg, Germany,* 8:15–28.

Keigwin, L.D., Jr., 1978. Pliocene closing of the Isthmus of Panama, based on biostratigraphic evidence from nearby Pacific Ocean and Caribbean Sea cores. *Geology,* 6:630–634.

————, 1982a. Isotopic paleoceanography of the Caribbean and the east Pacific: role of the Panama uplift in late Neogene time. *Science,* 217:350–353.

————, 1982b. Neogene planktonic foraminifers from Deep Sea Drilling Project Sites 502 and 503. *In* Prell, W.L., Gardner, J.V., et al., *Init. Repts. DSDP,* 68: Washington (U.S. Govt. Printing Office), 269–288.

Kennett, J.P., and Srinivasan, M.S., 1983. *Neogene Planktonic Foraminifera: A Phylogenetic Atlas:* Stroudsburg, PA (Hutchinson Ross).

Kennett, J.P., and Stott, L.D., 1990. Proteus and Proto-oceanus: ancestral Paleogene oceans as revealed from Antarctic stable isotopic results: ODP Leg 113. *In* Barker, P.F., Kennett, J.P., et al., *Proc. ODP, Sci. Results,* 113: College Station, TX (Ocean Drilling Program), 865–880.

————, 1991. Abrupt deep-sea warming, paleoceanographic changes and benthic extinctions at the end of the Paleocene. *Nature,* 353:225–229.

Kesler, S.E., Levy, E., and Cecilia Martin, F., 1990. Metallogenic evolution of the Caribbean region. *In* Dengo, G., and Case, J.E. (Eds.), *The Caribbean Region.* Geol. Soc. Am., Geol. of North Am. Ser., H:459–482.

Krom, M.D., and Berner, R.A., 1980. Adsorption of phosphate in anoxic marine sediments. *Limnol. Oceanogr.,* 25:797–806.

Ludwig, W.J., Houtz, R.E., and Ewing, J.I., 1975. Profiler-sonobuoy measurements in Colombian and Venezuelan Basins, Caribbean Sea. *AAPG Bull.,* 59:115–123.

Lyle, M., Dadey, K.A., and Farrell, J.W., 1995. The late Miocene (11–8 Ma) eastern Pacific carbonate crash: evidence for reorganization of deep-water circulation by the closure of the Panama Gateway. *In* Pisias, N.G., Mayer, L.A., Janecek, T. R., Palmer-Julson, A., and van Andel, T.H. (Eds.), *Proc. ODP, Sci. Results,* 138: College Station, TX (Ocean Drilling Program), 821–838.

Mandelbrot, B.B., 1967. How long is the coast of Britain? Statistical self-similarity and fractional dimension. *Science,* 156:636–638.

Martens, C.S., and Berner, R.A., 1974. Methane production in the interstitial waters of sulfate-depleted marine sediments. *Science,* 185:1167–1169.

Mattson, P.H., 1984. Caribbean structural breaks and plate movements. *Mem.—Geol. Soc. Am.,* 162:131–152.

Millero, F.J., and Sohn, M.L., 1992. *Chemical Oceanography:* Boca Raton (CRC Press).

Newhall, C.G., 1980. Geology of the Lake Atitlan Area, Guatemala [unpubl. dissertation]. Dartmouth College, Hanover.

Okada, H., and Bukry, D., 1980. Supplementary modification and introduction of code numbers to the low-latitude coccolith biostratigraphic zonation (Bukry, 1973; 1975). *Mar. Micropaleontol.,* 5:321–325.

Orford, J.D., and Whalley, W.B., 1983. The use of fractal dimension to quantify the morphology of irregular-shaped particles. *Sedimentology,* 30:644–668.

Parker, F.L., and Berger, W.H., 1971. Faunal and solution patterns of planktonic foraminifera in surface sediments of the South Pacific. *Deep-Sea Res. Part A,* 18:73–107.

Parker, F.L., and Berger, W.H., 1971. Faunal and solution patterns of planktonic foraminifera in surface sediments of the South Pacific. *Deep-Sea Res. Part A,* 18:73–107.

Pearce, J.A., Harris, N.B.W., and Tindle, A.G., 1984. Trace element discrimination diagrams for the tectonic interpretation of granitic rocks. *J. Petrol.,* 25:956–983.

Perch-Nielsen, K., 1985. Cenozoic calcareous nannofossils. *In* Bolli, H.M., Saunders, J.B., and Perch-Nielsen, K. (Eds.), *Plankton Stratigraphy:* Cambridge (Cambridge Univ. Press), 427–554.

Perch-Nielsen, K., McKenzie, J.A., and He, Q.X., 1982. Biostratigraphy and isotope stratigraphy and the "catastrophic" extinction of calcareous nannoplankton at the Cretaceous/Tertiary boundary. *In* Silver, L.T., and Schultz, H. (Eds.), *Geological Implications of Impacts of Large Asteroids and Comets on the Earth.* Spec. Pap.—Geol. Soc. Am., 190:353–371.

Pisias, N.G., Mayer, L.A., and Mix, A.C., 1995. Paleoceanography of the eastern equatorial Pacific during the Neogene: synthesis of Leg 138 drilling results. *In* Pisias, N.G., Mayer, L.A., Janecek, T.R., Palmer-Julson, A., and van Andel, T.H. (Eds.), *Proc. ODP, Sci. Results,* 138: College Station, TX (Ocean Drilling Program), 5–21.

Prell, W.L., Gardner, J.V., et al., 1982. *Init. Repts. DSDP,* 68: Washington (U.S. Govt. Printing Office).

Raffi, I., Backman, J., Rio, D., and Shackleton, N.J., 1993. Plio-Pleistocene nannofossil biostratigraphy and calibration to oxygen isotopes stratigraphies from Deep Sea Drilling Project Site 607 and Ocean Drilling Program Site 677. *Paleoceanography,* 8:387–408.

Reynolds, J.H., 1980. Late Tertiary volcanic stratigraphy of northern Central America. *Bull. Volcanol.,* 43:601–607.

Russ, J.C., 1992. *The Image Processing Handbook:* Ann Arbor (CRC Press).

————, 1994. *Fractal Surfaces:* Ann Arbor (CRC Press).

Ruttenberg, K.C., 1992. Development of a sequential extraction method for different forms of phosphorus in marine sediments. *Limnol. Oceanogr.,* 37:1460–1482.

Saito, T., 1976. Geologic significance of coiling direction in the planktonic foraminifer *Pulleniatina. Geology,* 4:305–309.

Sato, T., Kameo, K., and Takayama, T., 1991. Coccolith biostratigraphy of the Arabian Sea. *In* Prell, W.L., Niitsuma, N., et al., *Proc. ODP, Sci. Results,* 117: College Station, TX (Ocean Drilling Program), 37–54.

Schultz, P.H., and D'Hondt, S., 1995. The Chicxulub impact angle and its consequences.. *Ann. Mtg.—Geol. Soc. Amer.,* 27:A349. (Abstract)

Schultz, P.H., and Gault, D.E., 1990. Prolonged global catastrophes from oblique impacts. *Spec. Pap.—Geol. Soc. Am.,* 247:239–261.

Self, S., and Sparks, R.S.J., 1978. Characteristics of widespread pyroclastic deposits formed the interaction of silicic magma and water. *Bull. Volcanol.,* 41:196–212.

Shagam, R., 1975. The northern termination of the Andes. *In* Nairn, A.E.M., and Stehli, F.G. (Eds.), *The Ocean Basins and Margins, The Gulf of Mexico and the Caribbean* (Vol. 3): New York (Plenum), 325–420.

Sigurdsson, H., Sparks, R.S.J., Carey, S.N., and Huang, T.C., 1980. Volcanogenic sedimentation in the Lesser Antilles arc. *J. Geol.,* 88:523–540.

Sissingh, W., 1977. Biostratigraphy of Cretaceous calcareous nannoplankton. *Geol. Mijnbouw,* 56:37–50.

Stevenson, F.J., and Cheng, C.N., 1972. Organic geochemistry of the Argentine Basin sediments: carbon-nitrogen relationships and Quaternary correlations. *Geochim. Cosmochim. Acta,* 36:653–671.

Stoffa, P.L., Mauffret, A., Truchan, M., and Buhl, P., 1981. Sub-B″ layering in the southern Caribbean: the Aruba Gap and Venezuela Basin. *Earth Planet. Sci. Lett.,* 53:131–146.

Takayama, T., and Sato, T., 1987. Coccolith biostratigraphy of the North Atlantic Ocean, Deep Sea Drilling Project Leg 94. *In* Ruddiman, W.F., Kidd, R.B., Thomas, E., et al., *Init. Repts. DSDP,* 94 (Pt. 2): Washington (U.S. Govt. Printing Office), 651–702.

Taylor, S.R., and McLennan, S.M., 1985. *The Continental Crust: Its Composition and Evolution:* Oxford (Blackwell Scientific).

Thomas, E., 1990. Late Cretaceous through Neogene deep-sea benthic foraminifers (Maud Rise, Weddell Sea, Antarctica). *In* Barker, P.F., Kennett, J.P., et al., *Proc. ODP, Sci. Results,* 113: College Station, TX (Ocean Drilling Program), 571–594.

————, 1992. Cenozoic deep-sea circulation: evidence from deep-sea benthic foraminifera. *In* Kennett, J.P., and Warnke, D. (Eds.), *The Antarctic Paleoenvironment: A Perspective on Global Change.* Am. Geophys. Union, Antarct. Res. Ser., 56:141–165.

Toth, D.J., and Lerman, A., 1977. Organic matter reactivity and sedimentation rates in the ocean. *Am. J. Sci.,* 277:465–485.

Urmos, J., Wilkens, R.H., Bassinot, F., Lyle, M., Marsters, J.C., Mayer, L.A., and Mosher, D.C., 1993. Laboratory and well-log velocity and density measurements from the Ontong Java Plateau: new in-situ corrections to laboratory data for pelagic carbonates. *In* Berger, W.H., Kroenke, L.W., Mayer, L.A., et al., *Proc. ODP, Sci. Results,* 130: College Station, TX (Ocean Drilling Program), 607–622.

von Huene, R., 1989. The Middle America convergent plate boundary, Guatemala. *In* Winterer, E.L., Hussong, D.M., and Decker, R.W. (Eds.), *The Eastern Pacific Ocean and Hawaii,* Geol. Soc. Am., Geol. of North Am. Ser., N:535–550.

Walter, L.M., and Burton, E.A., 1986. The effect of orthophosphate on carbonate mineral dissolution rates in seawater. *Chem. Geology,* 56:313–323.

Weaver, P.P.E., and Raymo, M.E., 1989. Late Miocene to Holocene planktonic foraminifers from the equatorial Atlantic, Leg 108. *In* Ruddiman, W., Sarnthein, M., et al., *Proc. ODP, Sci. Results,* 108: College Station, TX (Ocean Drilling Program), 71–91.

Wilson, C.J.N., 1985. The Taupo eruption, New Zealand II. The Taupo Ignimbrite. *Philos. Trans. R. Soc. London A,* 314:229–310.

Wohletz, K.H., 1983. Mechanisms of hydrovolcanic pyroclast formation: grain size, scanning electron microscopy, and experimental studies. *J. Volcanol. Geotherm. Res.,* 17:31–63.

Wohletz, K.H., and McQueen, R.G., 1984. Experimental studies of hydromagmatic volcanism. In *Explosive Volcanism; Inception, Evolution, and Hazards:* Washington (Nat. Acad. Press), 158–169.

Zachos, J.C., Lohmann, K.C., Walker, J.C.G., and Wise, S.W., 1993. Abrupt climate change and transient climates during the Paleogene: a marine perspective. *J. Geol.,* 101:191–213.

Zachos, J.C., Stott, L.D., Lohmann, K.C., 1994. Evolution of Early Cenozoic marine temperatures. *Paleoceanography,* 9:353–387.

Ms 165IR-104

NOTE: Core-description forms ("barrel sheets") and core photographs can be found in Section 4, beginning on page 403. Forms containing smear-slide data can be found in Section 5, beginning on page 821. Thin-section descriptions are given in Sections 6 and 7, beginning on page 851. See Table of Contents for material contained on CD-ROM.

SHORE-BASED LOG PROCESSING
HOLE 999B

Bottom felt: 2838.9 mbrf (used for depth shift to seafloor)
Total penetration: 1066.4 mbsf
Total core recovered: 397.8 m (73%)

Logging Runs

Logging string 1: DIT/SDT/HLDT/CNTG/NGT
Logging string 2: ACT/GST/NGT
Logging string 3: FMS/GPIT/NGT (2 passes)
Wireline heave compensator was used to counter ship heave.

Bottom-Hole Assembly

The following bottom-hole assembly/pipe/casing depths are as they appear on the logs after differential depth shift (see "Depth shift" section) and depth shift to the seafloor. As such, there might be a discrepancy with the original depths given by the drillers on board. Possible reasons for depth discrepancies are ship heave, use of wireline heave compensator, and drill string and/or wireline stretch.

DIT/SDT/HLDT/CNTG/NGT: Bottom-hole assembly at ~525 mbsf
ACT/GST/NGT: Bottom-hole assembly at ~525 mbsf
FMS/GPIT/NGT: Did not reach bottom-hole assembly

Processing

Depth shift: Original logs have been interactively depth shifted with reference to NGT from ACT/GST/NGT run and to the seafloor (−2838.9 m).

Gamma-ray processing: Data have been processed to correct for borehole size and type of drilling fluid.

Acoustic data processing: The array sonic tool was operated in standard depth-derived, borehole compensated, long spacing (8–10 and 10–12 ft) mode. The sonic tool partially failed before entering the borehole; this resulted in good analog waveforms from the 8- and 10-ft spacing only. A noncompensated velocity was calculated from the 8-ft-spacing reading. Digital waveforms were recorded as normal and are included on the CD-ROM for further processing.

Geochemical processing: The elemental yields recorded by the GST tool represent the relative contribution of only some of the rock-forming elements (iron, calcium, chlorine, silicon, sulfur, hydrogen, gadolinium, and titanium—the last two computed during geochemical processing) to the total spectrum. Because other rock-forming elements are present in the formation (such as aluminum, potassium, etc.), caution is recommended in using the yields to infer lithologic changes. Instead, ratios are more appropriate to determine changes in the macroscopic properties of the formation.

List of oxide factors used in geochemical processing:
SiO_2 = 2.139
$CaCO_3$ = 2.497
FeO* = 1.358
TiO_2 = 1.668
K_2O = 1.205
Al_2O_3 = 1.889
FeO* = computed using an oxide factor that assumes a 50:50 combination of Fe_2O_3 and FeO factors.

Quality Control

Invalid density data were recorded at 651, 789, 878, 948, 952, 968, 977, 982, 997, 1013, 1089, and 1053 mbsf. The spikes occurred because of instability of the long-spacing detector, possibly because of borehole conditions.

Data recorded through the bottom-hole assembly, such as the spectral gamma-ray data above 525 mbsf, should be used qualitatively only because of attenuation on the incoming signal. Invalid gamma-ray data were recorded at 520–524 mbsf during the DIT/SDT/HLDT/CNTG/NGT run.

Hole diameter was recorded by the hydraulic caliper on the HLDT tool (CALI) and the caliper on the FMS string (C1 and C2).

Details of standard shore-based processing procedures are found in the "Explanatory Notes" chapter (this volume). For further information about the logs, please contact:

Cristina Broglia
Phone: 914-365-8343
Fax: 914-365-3182
E-mail: chris@ldeo.columbia.edu

Zhiping Tu
Phone: 914-365-8336
Fax: 914-365-3182
E-mail: ztu@ldeo.columbia.edu

Hole 999B: Natural Gamma Ray Logging Data

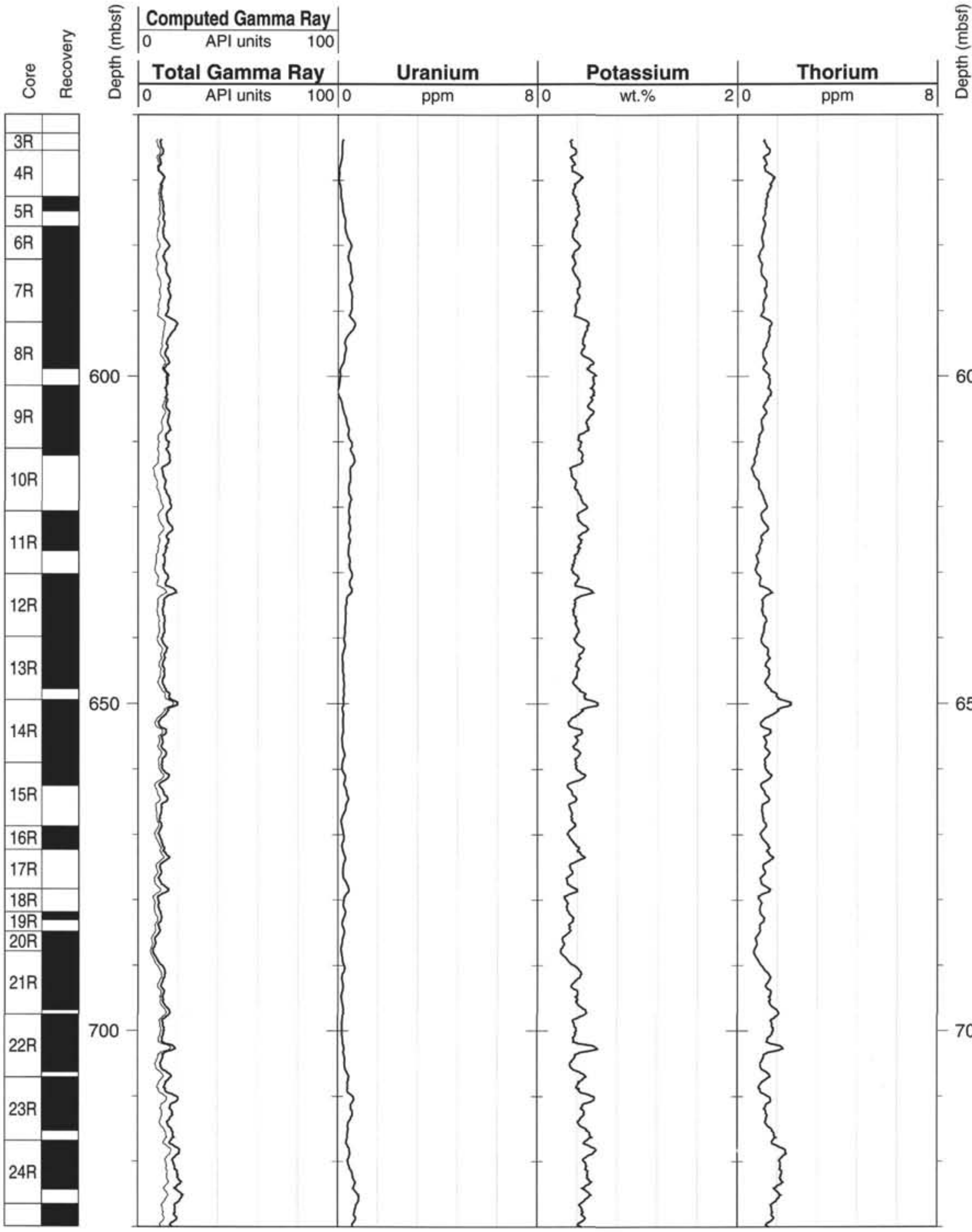

Hole 999B: Natural Gamma Ray Logging Data (cont.)

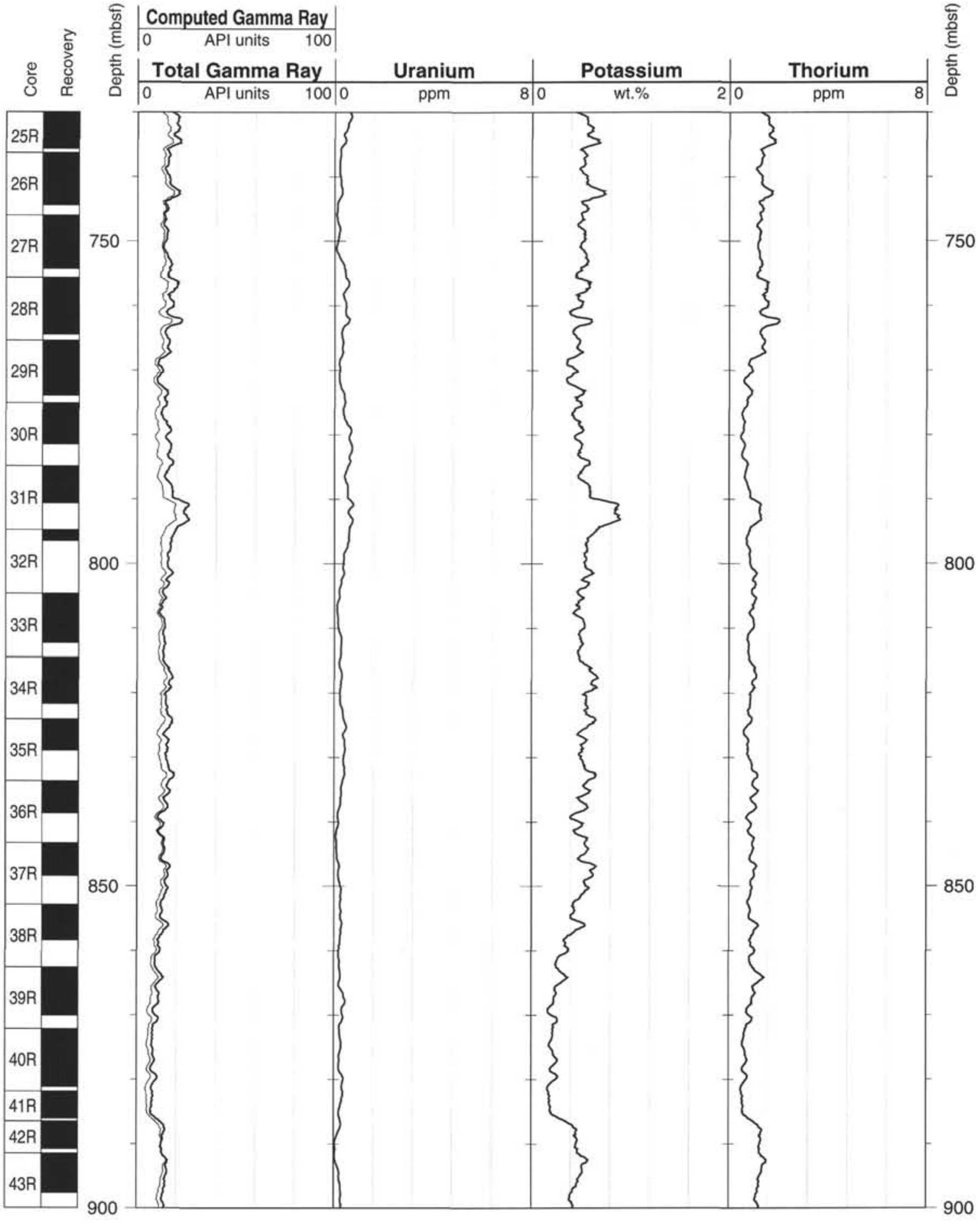

Hole 999B: Natural Gamma Ray Logging Data (cont.)

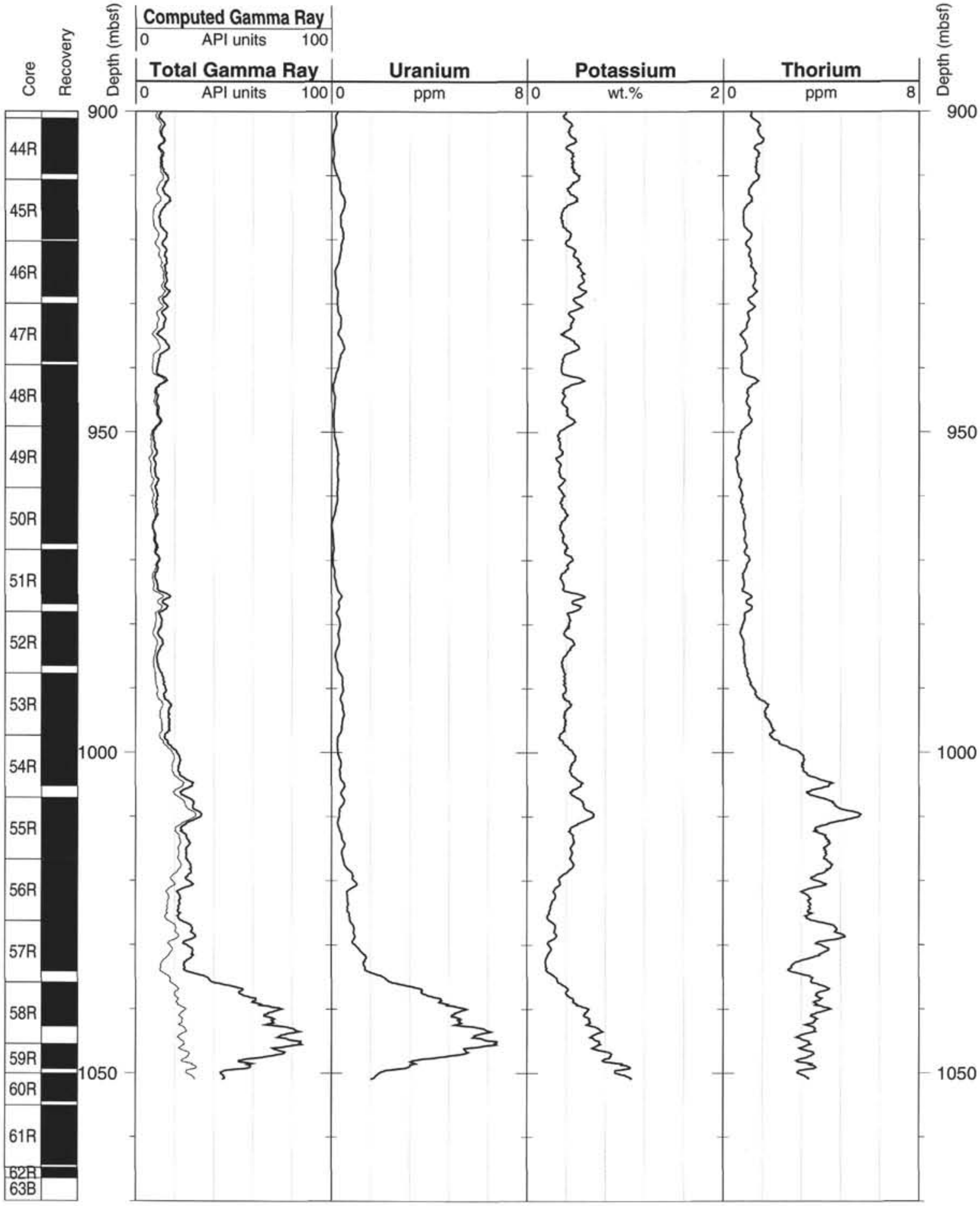

Hole 999B: Natural Gamma Ray-Density-Porosity Logging Data

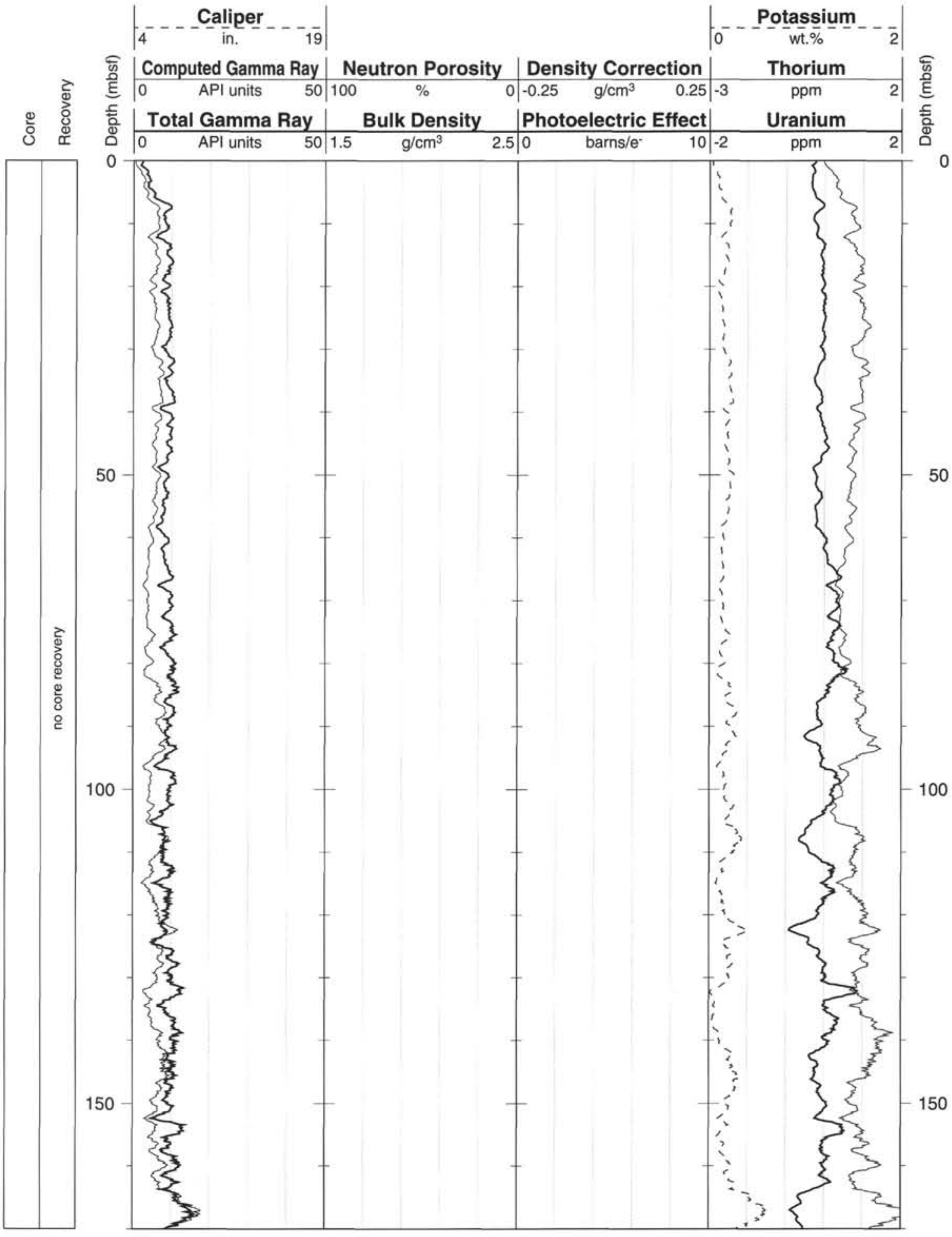

Hole 999B: Natural Gamma Ray-Density-Porosity Logging Data (cont.)

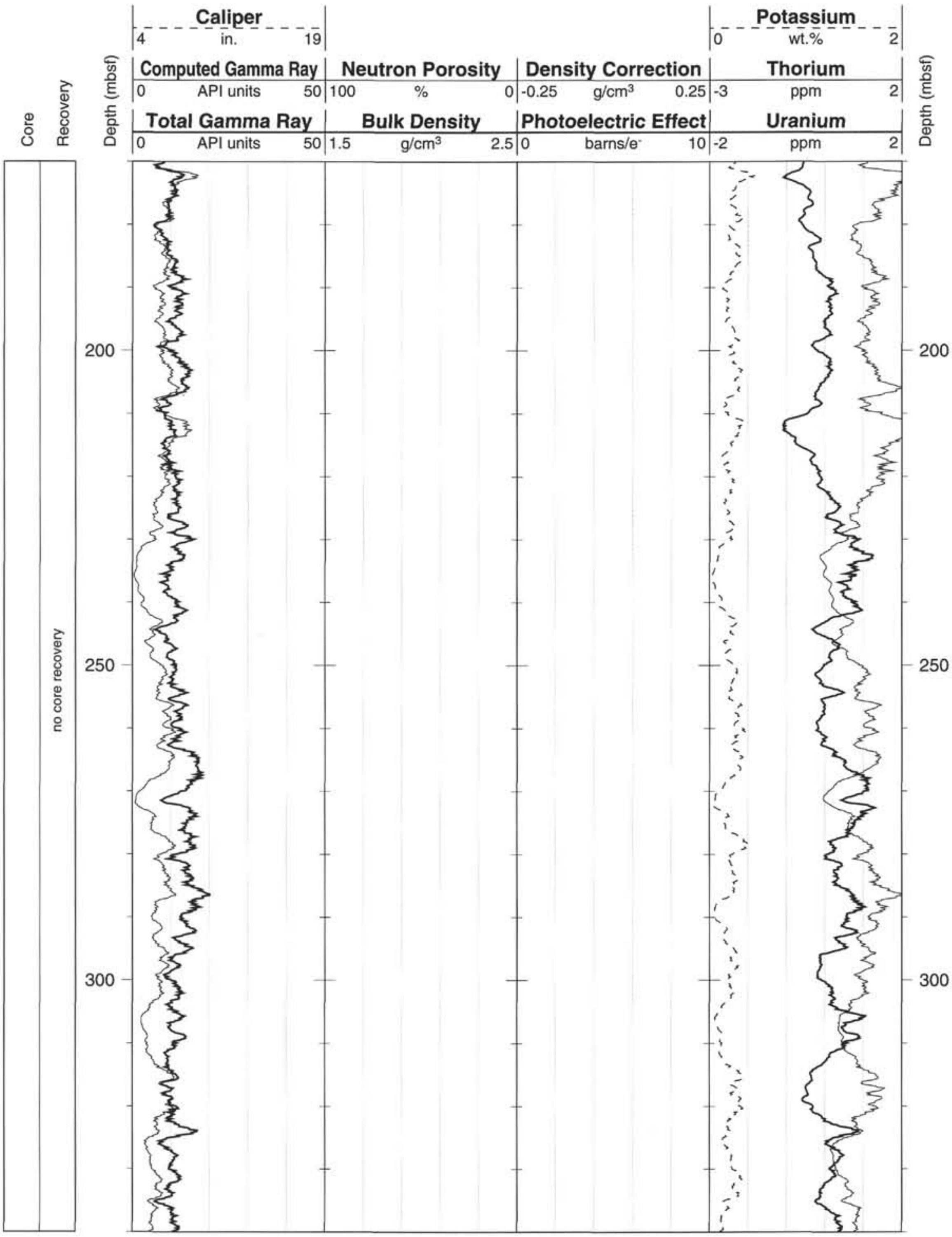

Hole 999B: Natural Gamma Ray-Density-Porosity Logging Data (cont.)

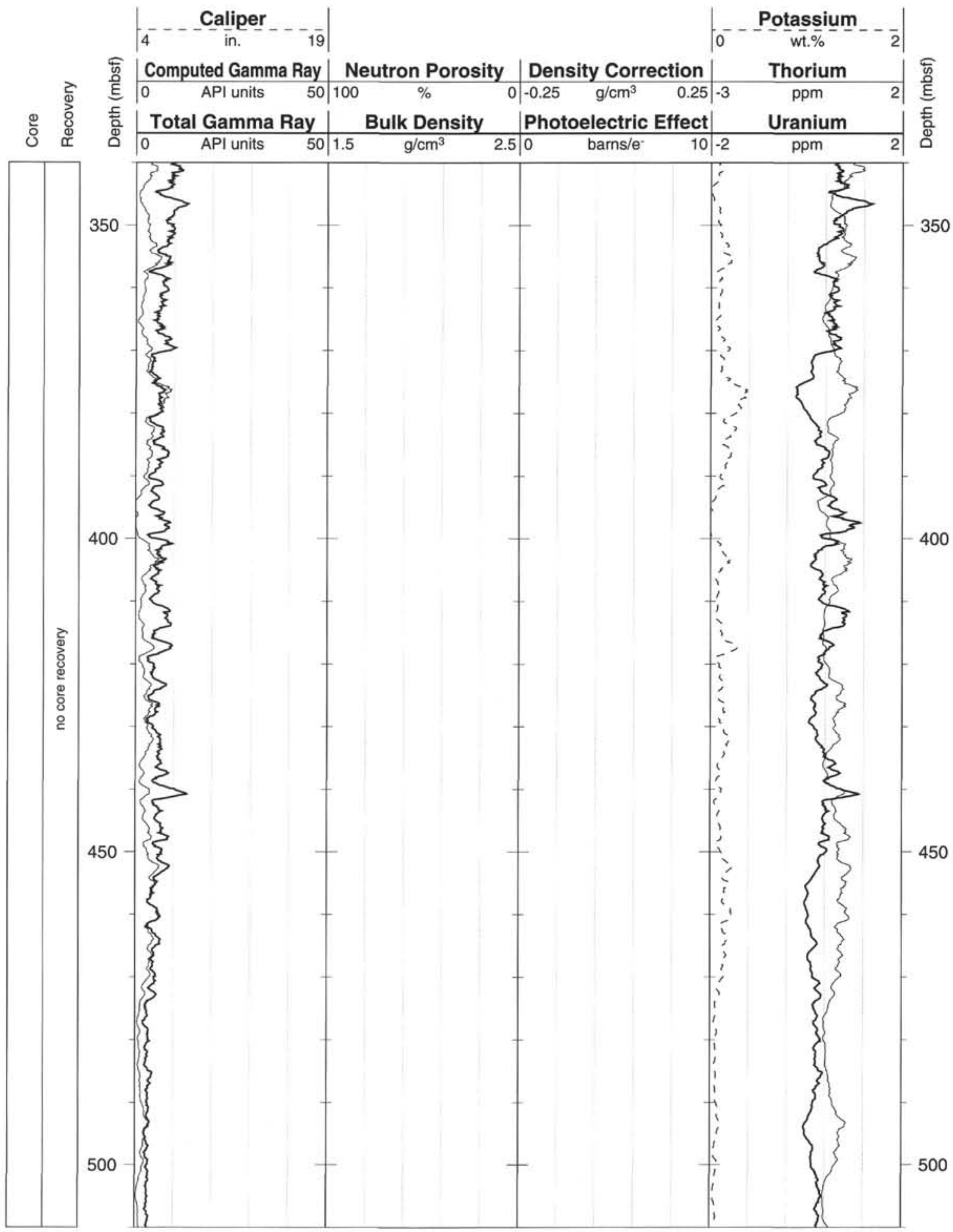

Hole 999B: Natural Gamma Ray-Density-Porosity Logging Data (cont.)

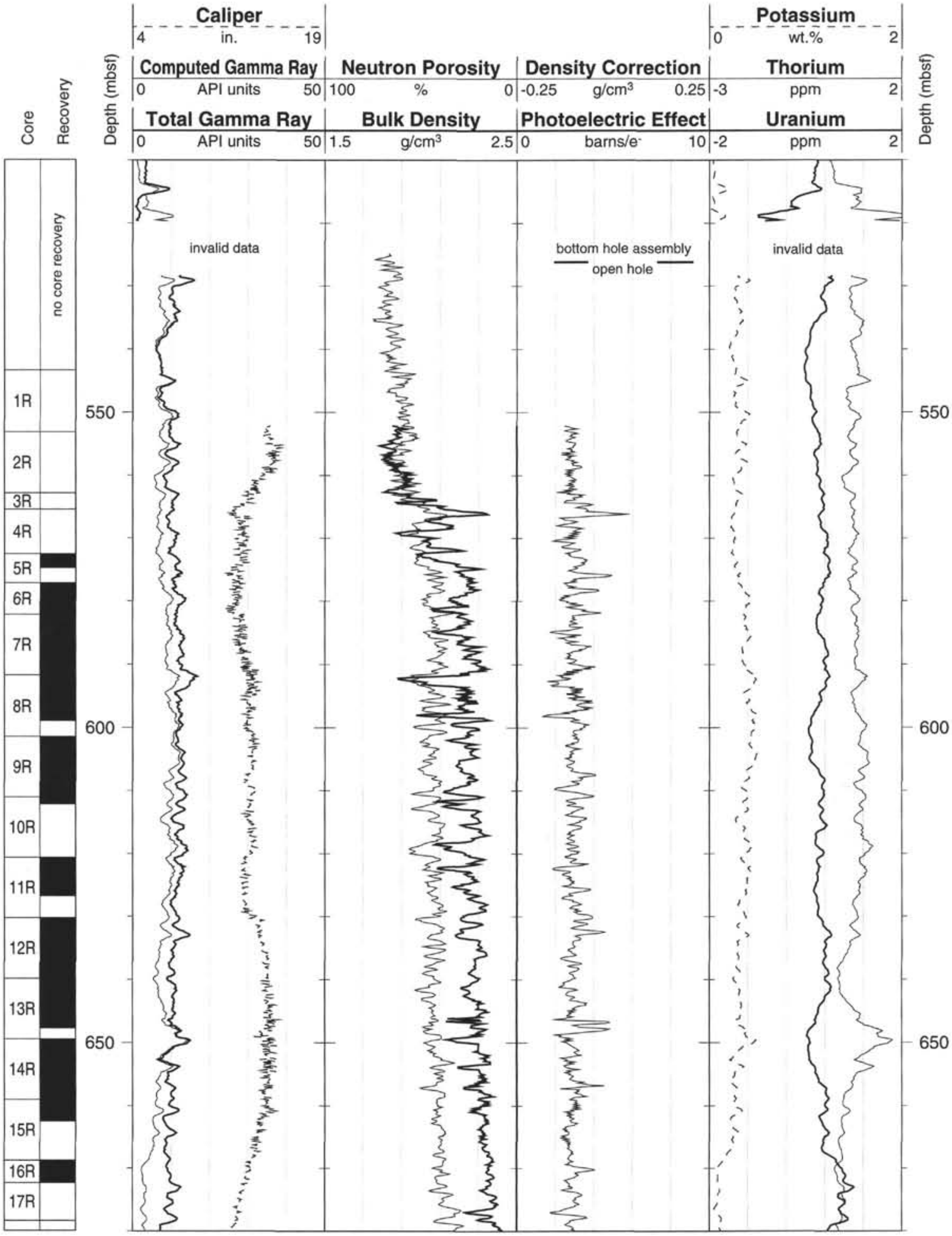

Hole 999B: Natural Gamma Ray-Density-Porosity Logging Data (cont.)

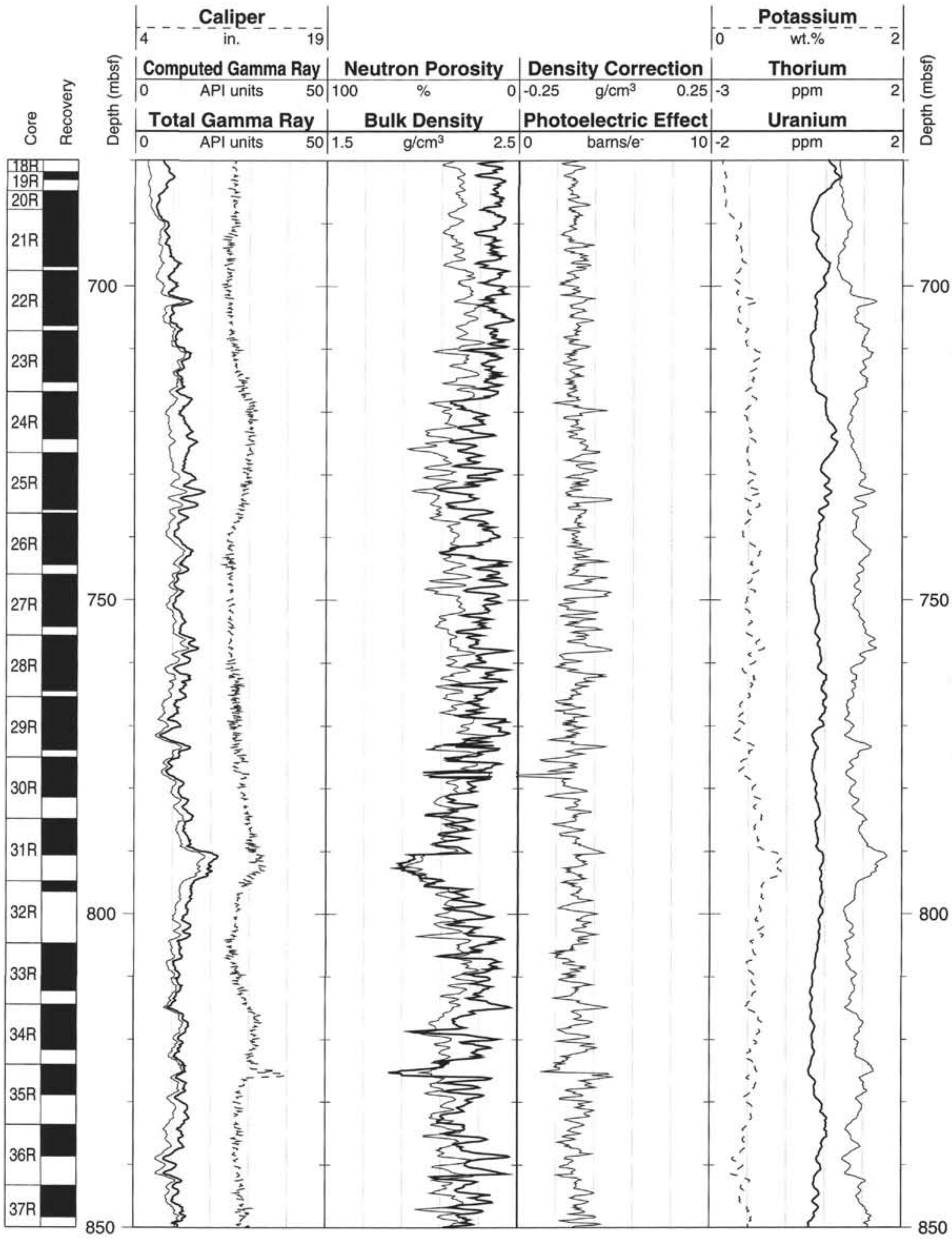

Hole 999B: Natural Gamma Ray-Density-Porosity Logging Data (cont.)

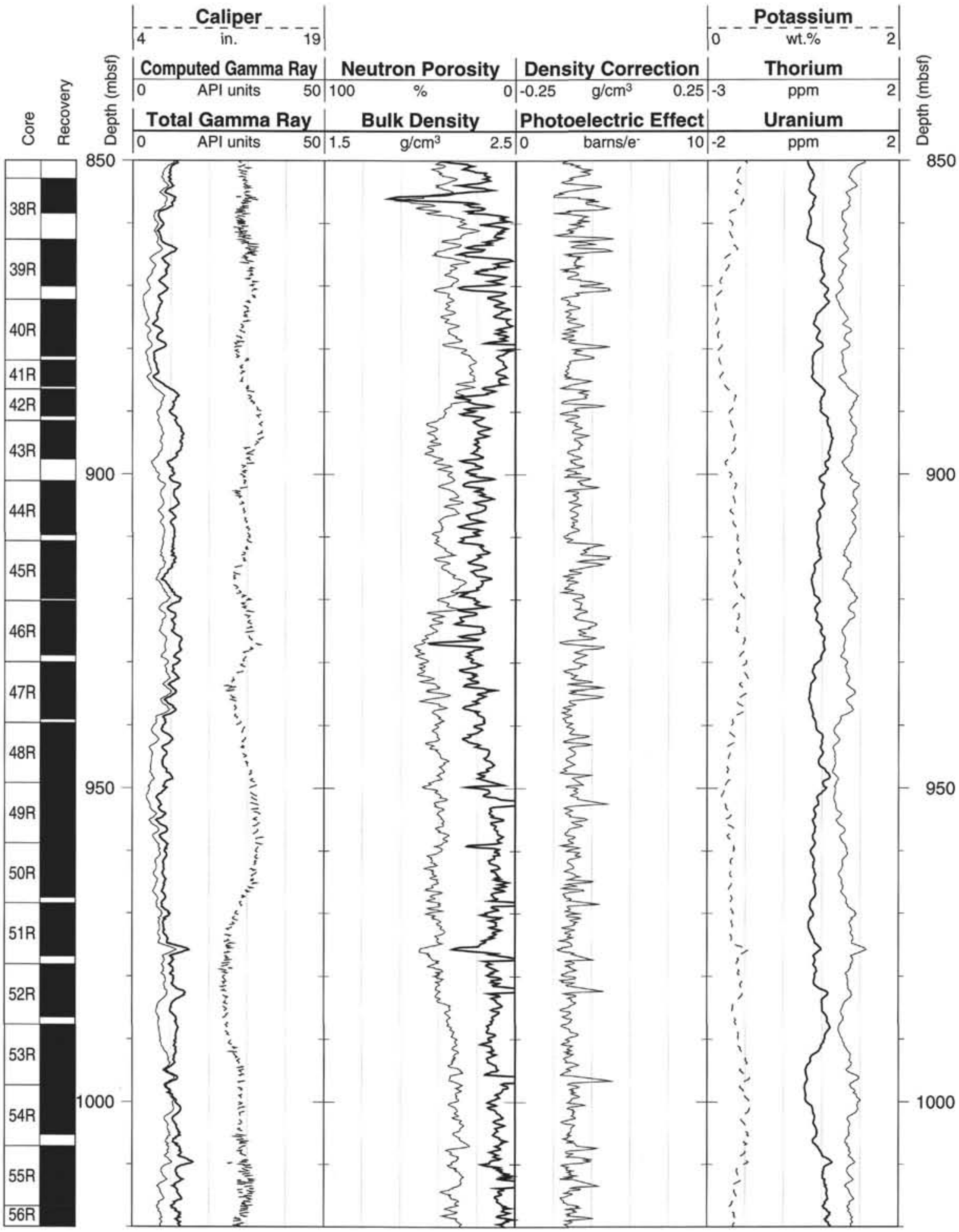

Hole 999B: Natural Gamma Ray-Density-Porosity Logging Data (cont.)

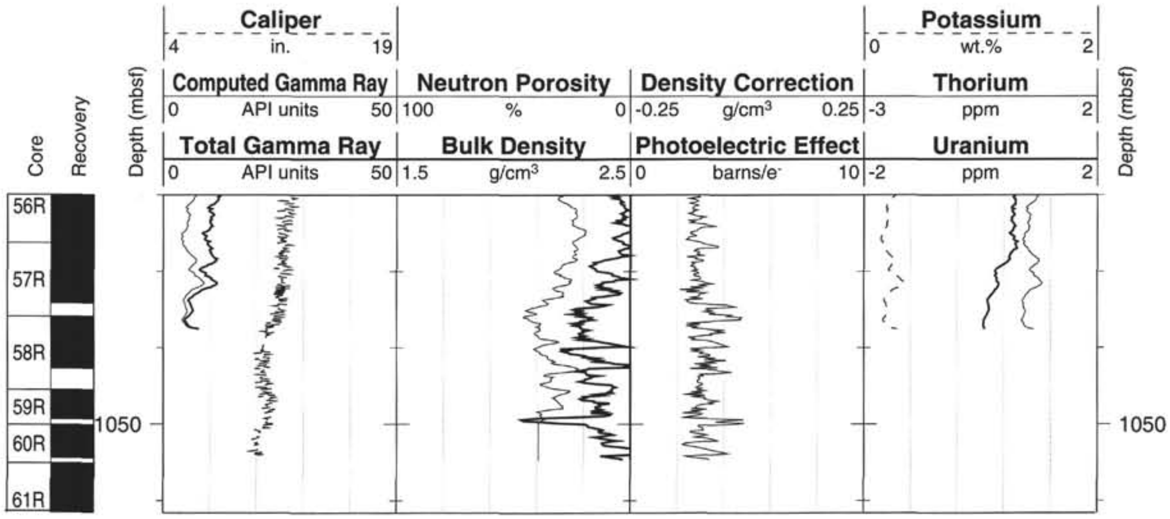

Hole 999B: Natural Gamma Ray-Resistivity-Sonic Logging Data

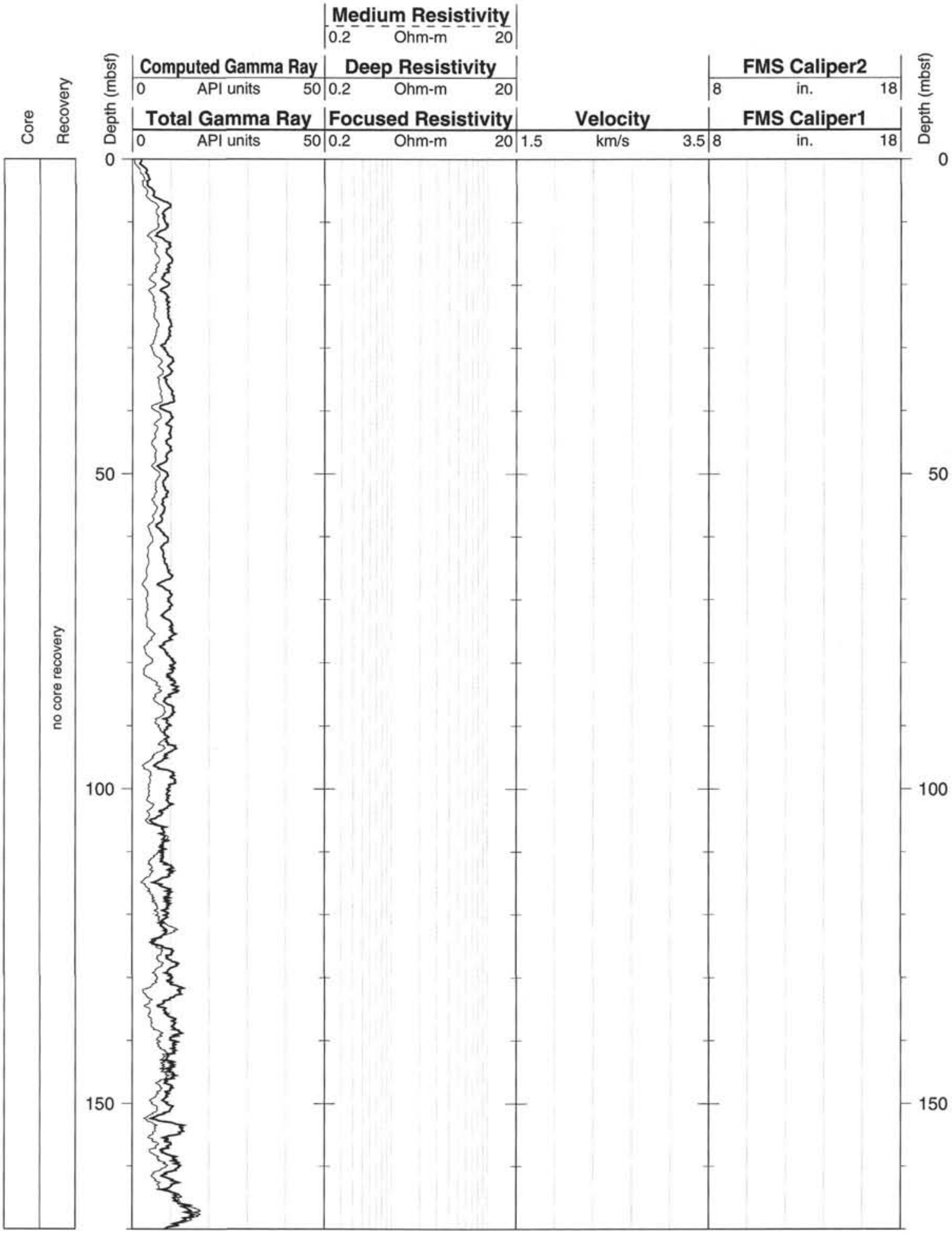

Hole 999B: Natural Gamma Ray-Resistivity-Sonic Logging Data (cont.)

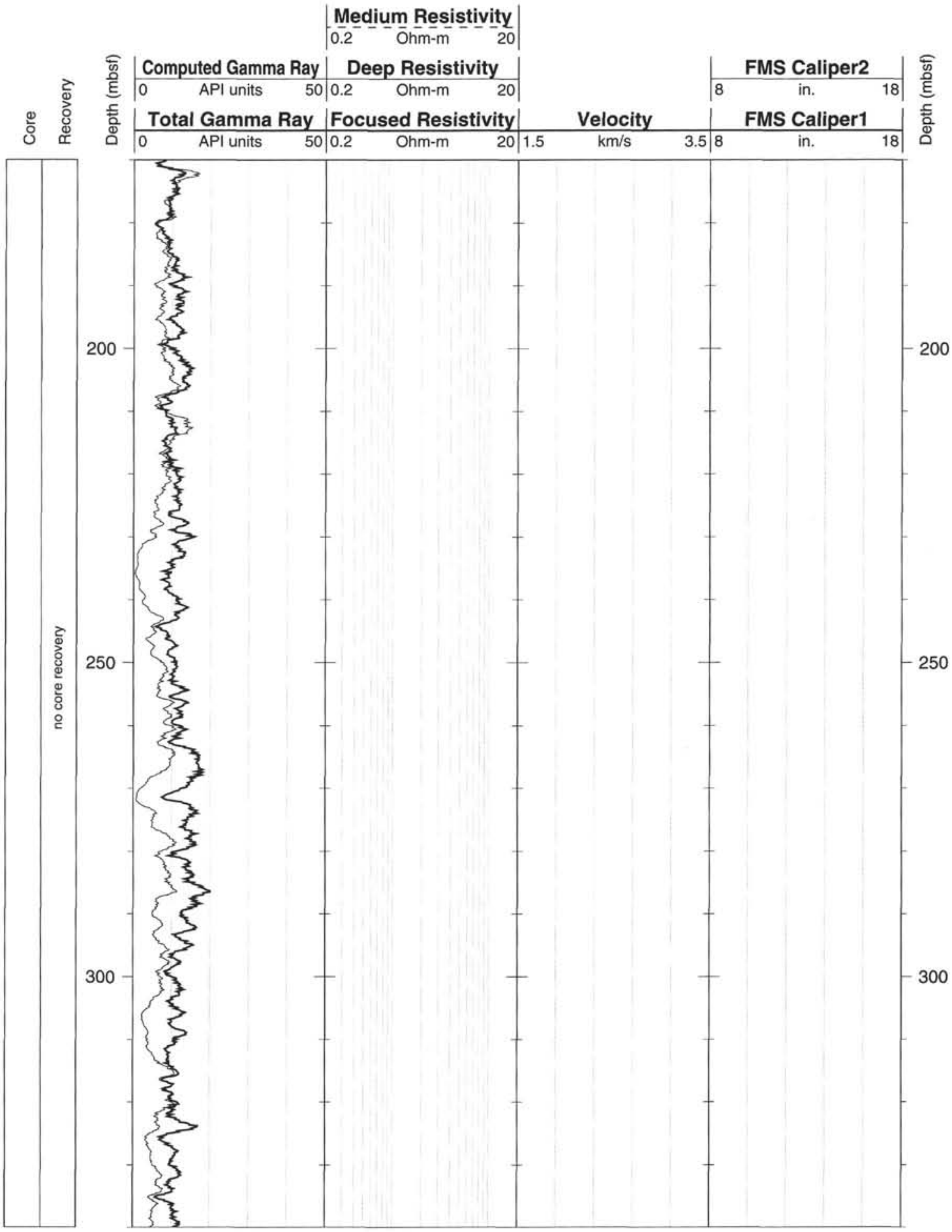

Hole 999B: Natural Gamma Ray-Resistivity-Sonic Logging Data (cont.)

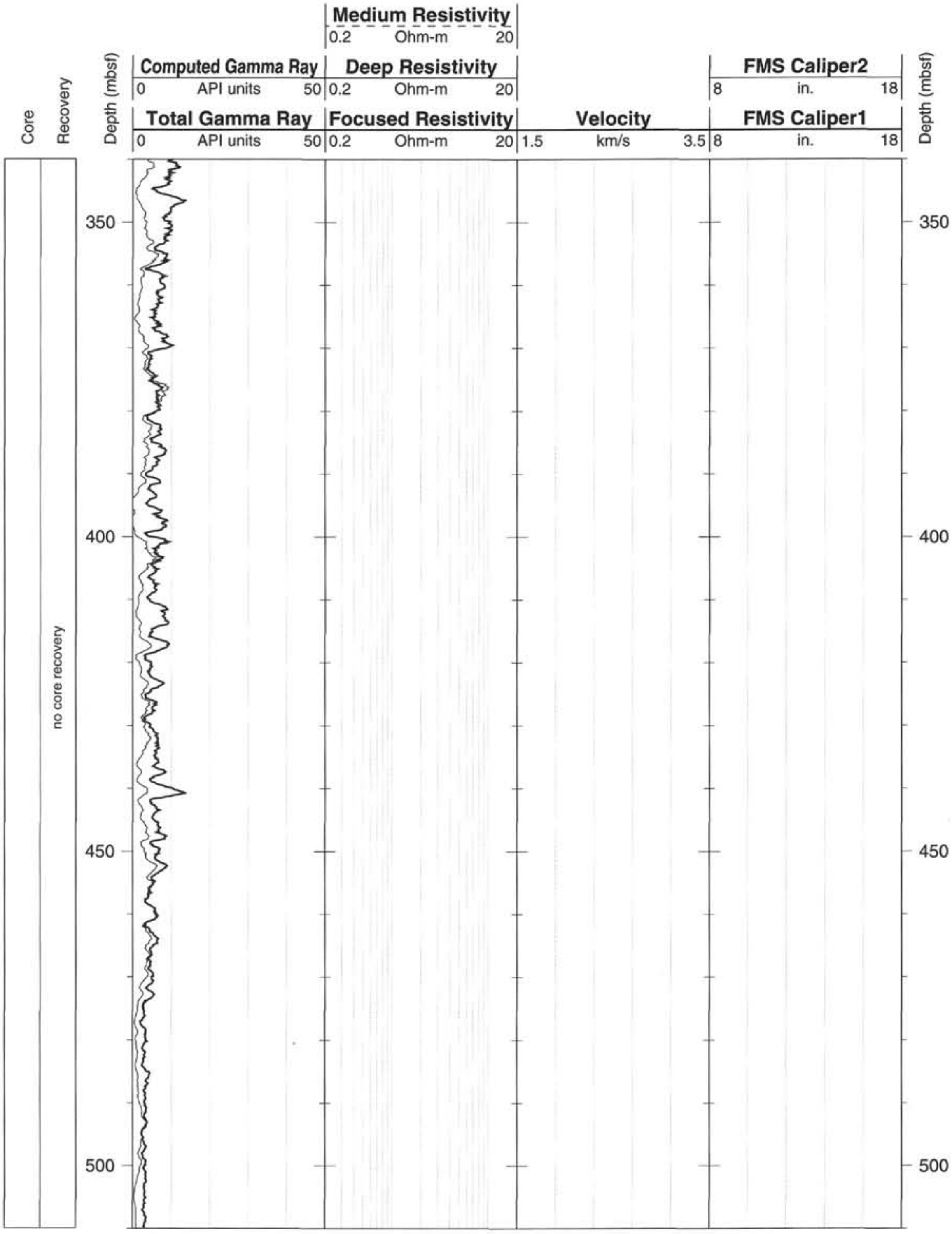

Hole 999B: Natural Gamma Ray-Resistivity-Sonic Logging Data (cont.)

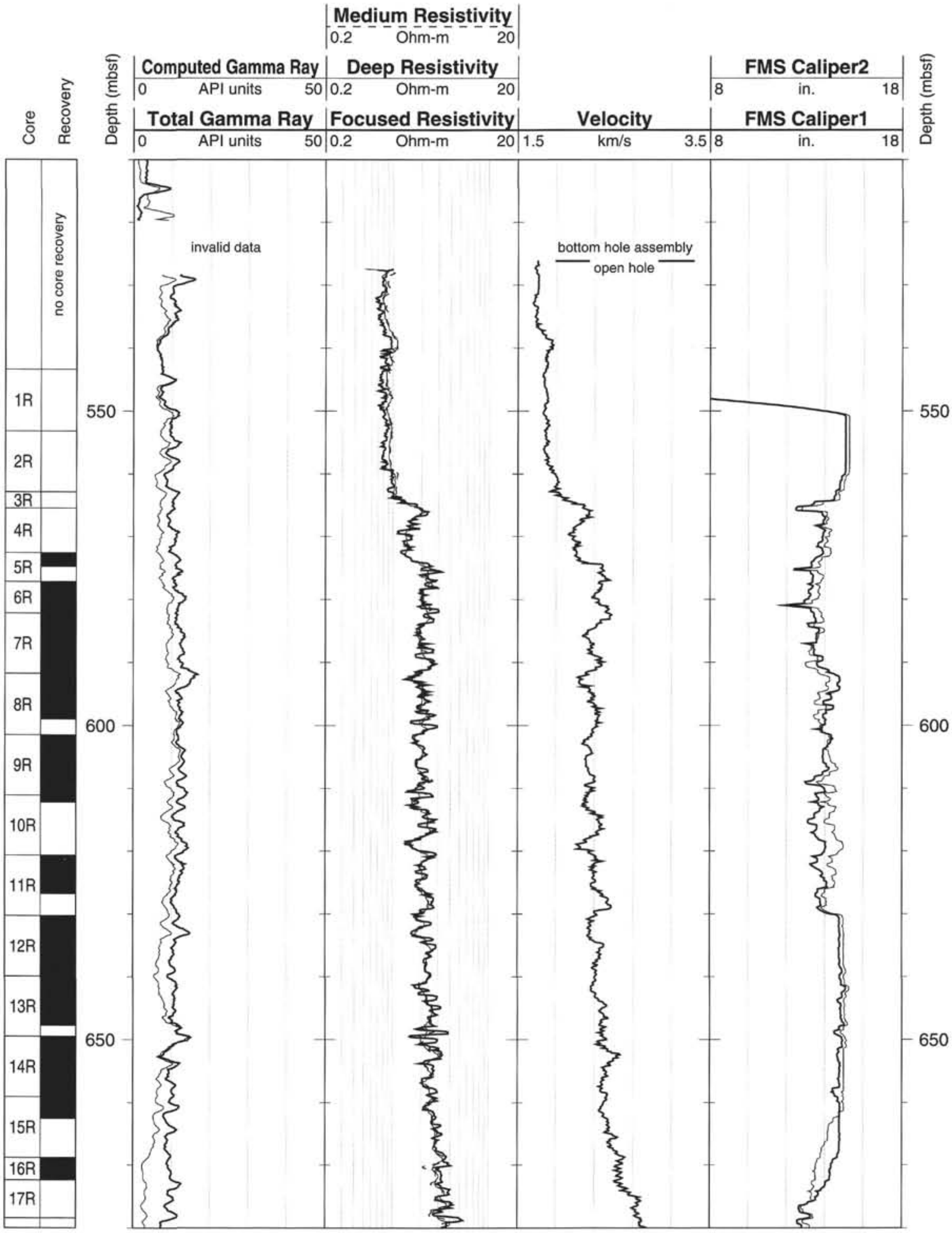

Hole 999B: Natural Gamma Ray-Resistivity-Sonic Logging Data (cont.)

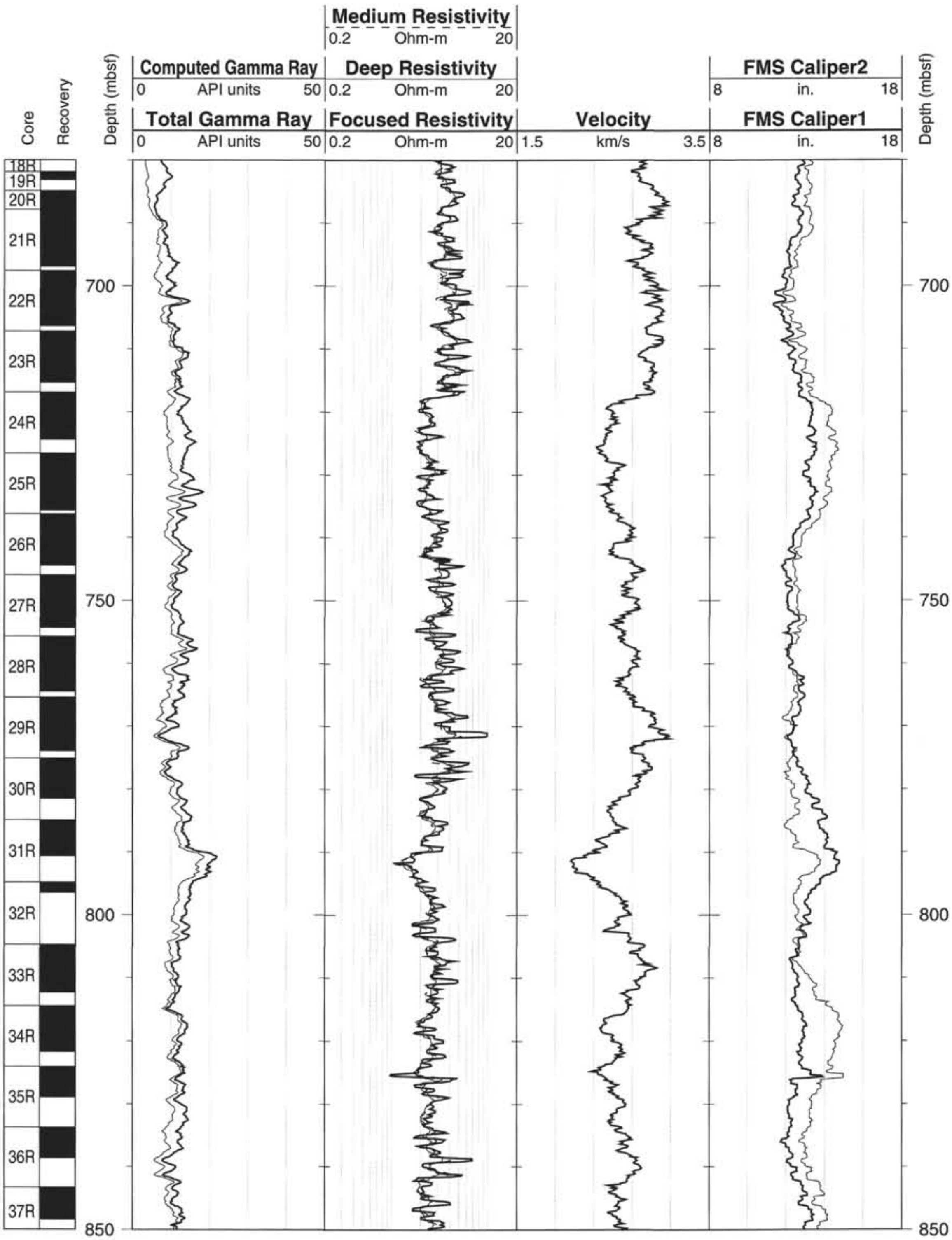

Hole 999B: Natural Gamma Ray-Resistivity-Sonic Logging Data (cont.)

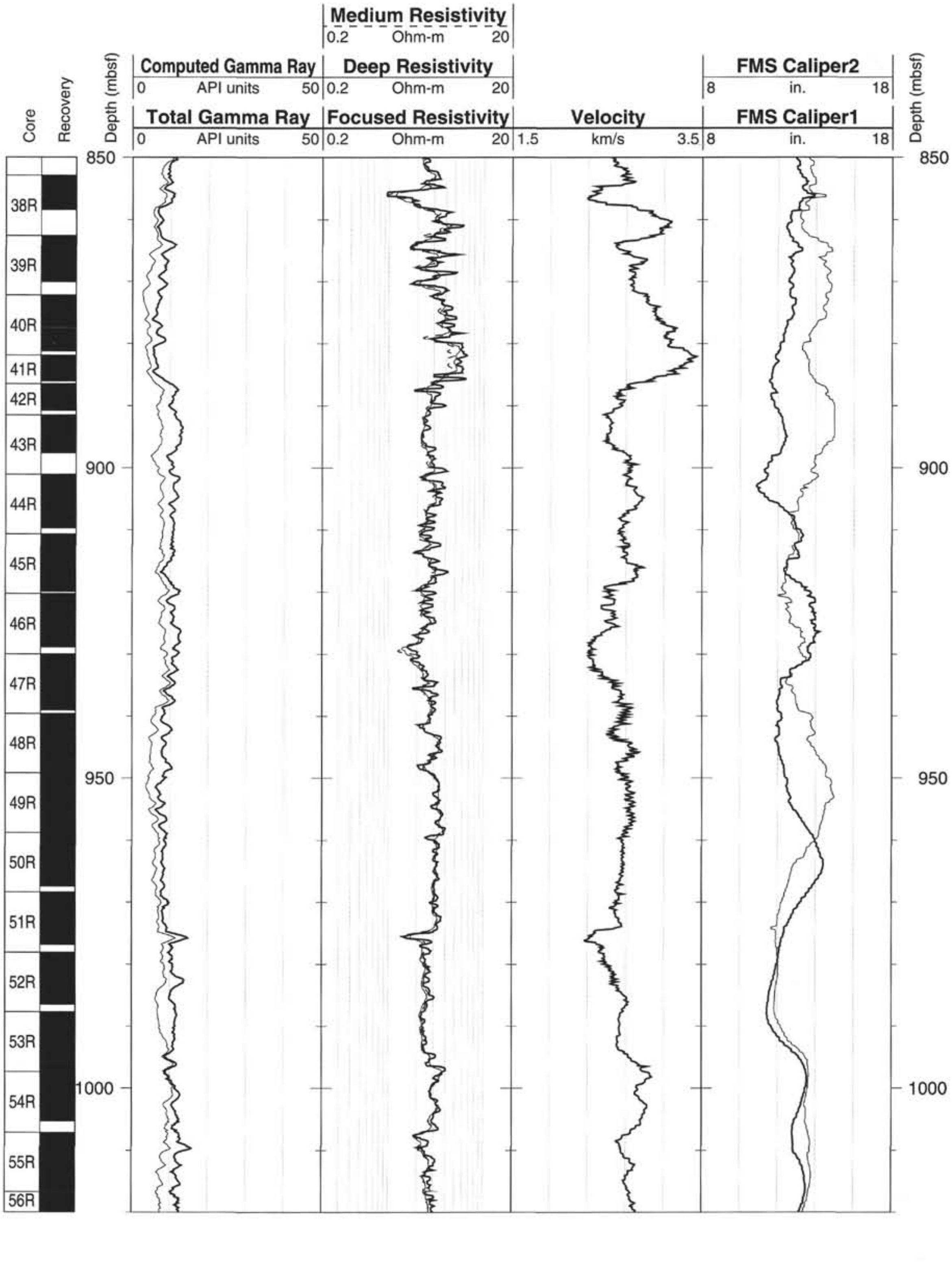

Hole 999B: Natural Gamma Ray-Resistivity-Sonic Logging Data (cont.)

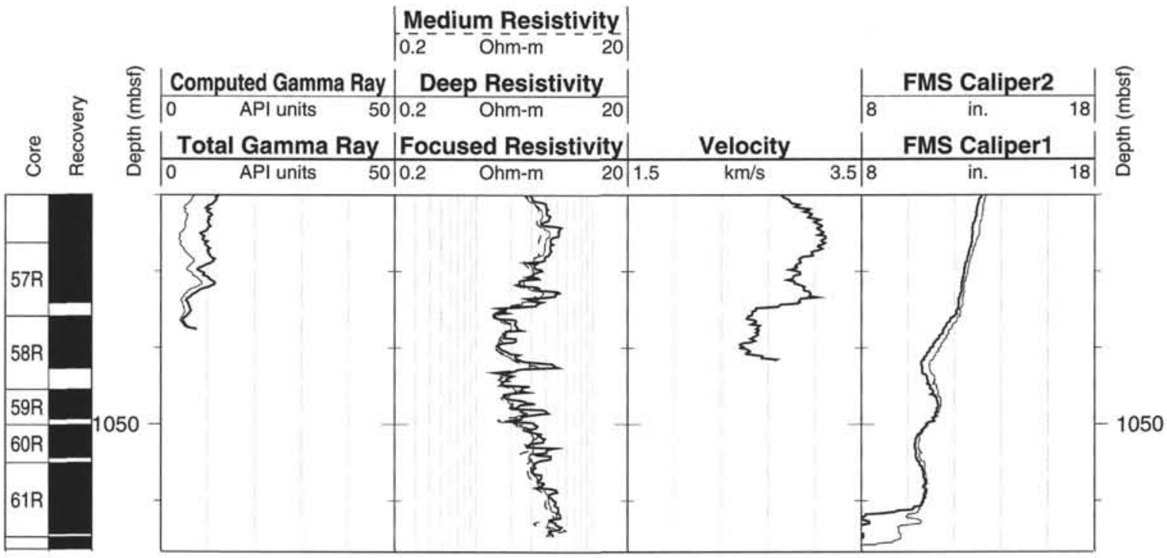

Hole 999B: Geochemical Logging Data

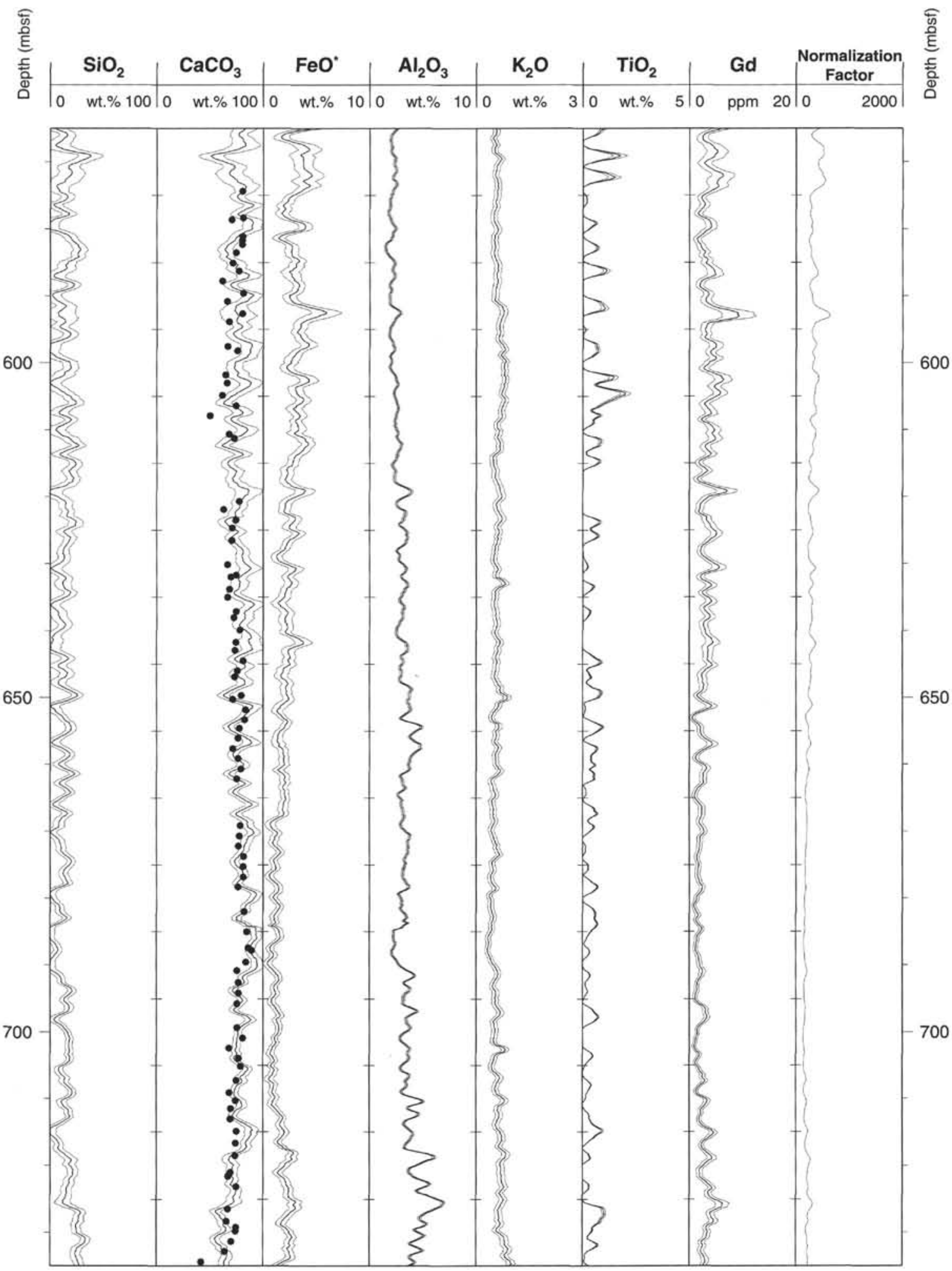

Hole 999B: Geochemical Logging Data (cont.)

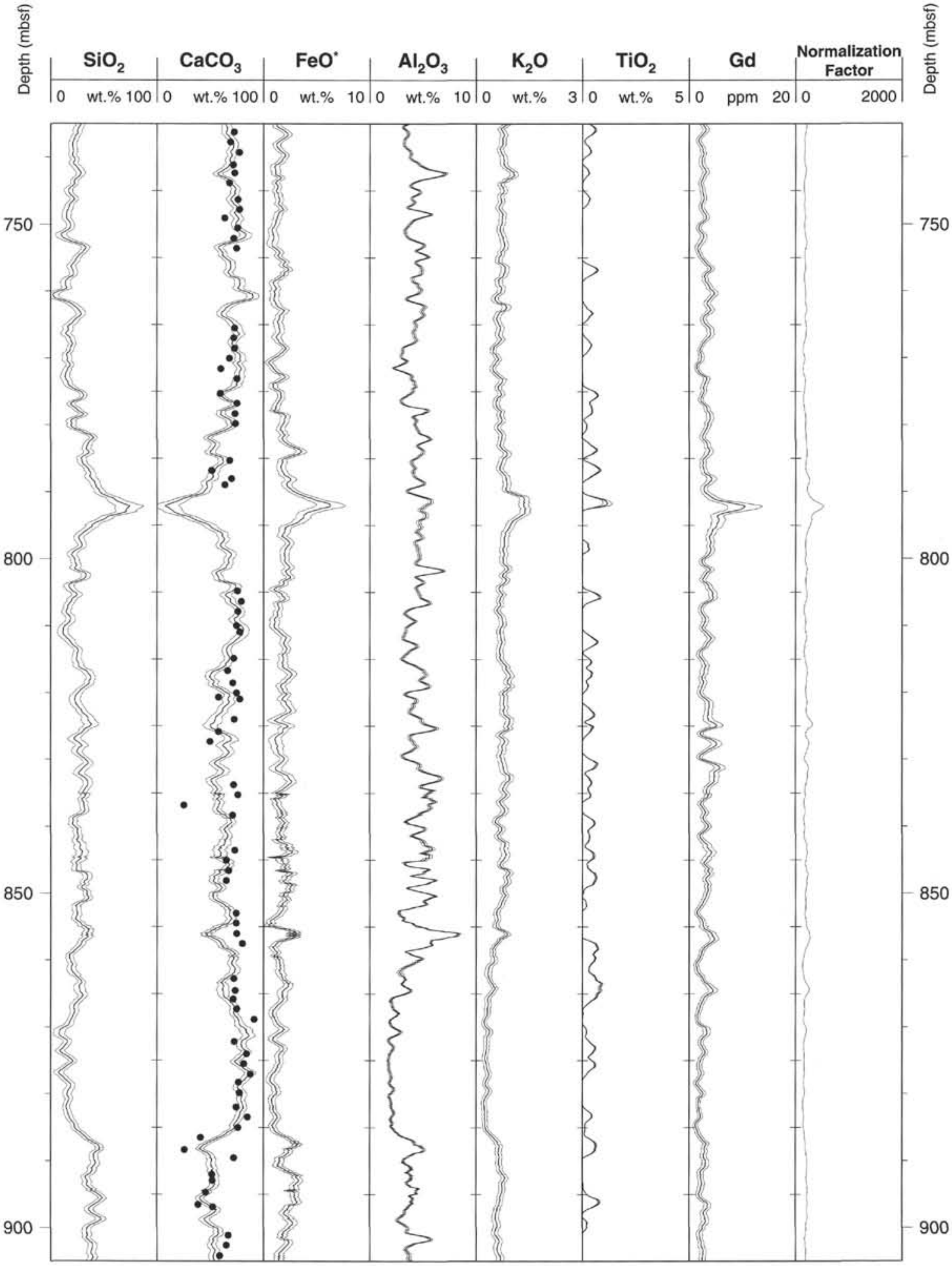

Hole 999B: Geochemical Logging Data (cont.)